



THÈSE

En vue de l'obtention du

DOCTORAT DE L'UNIVERSITÉ DE TOULOUSE

Délivré par :

Université Toulouse 3 Paul Sabatier (UT3 Paul Sabatier)

Présentée et soutenue par :

Wan-Yu TSAI

Le mercredi 1 juillet 2015

Ion Adsorption in Porous Carbon : from Fundamental
Studies to Supercapacitor Applications

École doctorale et discipline ou spécialité :

ED SDM : Sciences et génie des matériaux - CO034c

Unité de recherche :

CIRIMAT UMR CNRS 5085 (Institut Carnot)

Directeur/trice(s) de Thèse :

Pr. Patrice SIMON et Dr. Pierre-Louis TABERNA

Jury :

C. VIX-GUTERL	Directrice de recherche	IS2M, Université de Haut-Alsace	Rapporteur
T. BROUSSE	Professeur	IMN, Ecole Polytechnique de Nantes	Rapporteur
P. BARBOUX	Professeur	Chimie ParisTech (ENSCP)	Examineur
J.M. TARASCON	Professeur	Collège de France	Examineur
T. TZEDAKIS	Professeur	LGC, UPS Toulouse	Examineur
P. SIMON	Professeur	CIRIMAT, UPS Toulouse	Directeur de thèse
P.L. TABERNA	Chargé de recherche	CIRIMAT, UPS Toulouse	Co-directeur de thèse

Progress is made by trial and failure; the failures are generally a hundred times more numerous than the successes; yet they are usually left unchronicled.

– William Ramsay

Acknowledgements

First, I would like to express my special appreciation and thanks to my main supervisor Prof. Patrice Simon for offering me this opportunity to work under his supervision. Thanks for his expertise, guidance and supports, I have progressed a lot professionally and personally.

I would like also to thank sincerely my co-supervisor Dr. Pierre-Louis Taberna, not only for his expertise, but also for his encouragements, patience, and understanding. The numerous discussions we had and all the salient points he pointed out have been a great help for advancing the research work.

I would like to thank Dr. Cathie Vix-Guterl and Prof. Thierry Brousse who accepted to refer my thesis manuscript, and Prof. Philippe Barboux, Prof. Jean-Marie Tarascon, and Prof. Théo Tzedakis who agreed to be jury members for my oral defense. The discussion during the defense and the advices given by all the juries are interesting, and would be very useful for me in the future. I would like also to thank European Research Council for financing my PhD and the director of institute Carnot CIRIMAT, Dr. P. Tailhades, for providing the laboratory.

I would like to acknowledge all the people from different groups that I had the chance to work with during these three years. I would like to thank Prof. Yury Gogotsi, Dr. John K. McDonough and Dr. Carlos R. Pérez from Drexel University (Philadelphia, USA); Prof. Rodney S. Ruoff, Dr. Shanthi Murali, and Dr. Li Li Zhang from University of Texas at Austin (USA); Prof. Frédéric Favier, and Dr. Pengcheng Gao from Université de Montpellier (France) for experimental supports and scientific discussions. Special thanks to Prof. Claire Grey, Dr. John M. Griffin, and Dr. Alexander C. Forse from Cambridge University (UK) for the fruitful scientific discussion and collaboration in Cambridge and in Toulouse.

I would like to thank Prof. Isamu Moriguchi, and Dr. Koki Urita from Nagasaki University (Japan) who hosted me in their lab for in-situ experiments. The exchange was interesting and challenging. I would like also to thank Chiharu and Yuki for making my stay convivial and cheerful in Nagasaki. Apart from experimental aspects, I would like to thank Prof. Mathieu Salanne, Dr. Clarisse Péan from Université Pierre et Marie Curie (France), and Dr. Céline Merlet from Cambridge University for broadening my horizons in the modelling world. Special thanks to Clarisse for the all the discussions from theoretical point of view, and her warm support.

I would like to express my gratitude to the colleagues for administrative assistance, Mdm. S. Berkouk, Prof. B. Viguier and Prof. E. Benoist from Ecole Doctorale, Mdm. C. Stasiulis from the Service des Relations Internationales, Nicole, Murielle, Nabila, Maryse, Sandrine, and Christiane from CIRIMAT. Special thanks to Marie-Claire for her technical support, and always being smiley and encouraging.

I would like to thank my former and current team member: Dr. Patrick Rozier, Barbara Daffos, Rongying, Etsuro, Julie, Peihua, Jeremy, Lorie, Efi, Yohan, Léo, Zifeng, Kevin, Yinghui, Cyril, Eider, Laurent... It was a great pleasure to work under such a nice and professional environment. Special thanks to Barbara, who has always been supportive and helpful in all the aspects; also to Etsuro, Koki and Laurent, without them, the struggle against EQCM alone in Room 62 could have been extremely long and difficult. I would like to thank Julie and Rongying who trained me and taught me with patience when I just joined the team. I would like to address my gratitude especially to Rongying, who shared her scientific and personal experiences with me, took care of me as an elder sister and comforted me when I missed home.

Thanks to all the PhD students, post-doctoral researchers, interns, permanents, engineers, technician, and IT personnel I met during my PhD, who helped to complete these three years. Thanks Claire for those artistic nights we spent together, though short but I enjoyed a lot. Thanks Rafael for his understanding and his Franglish office ambience. Thanks Congcong for always being smiley, positive and encouraging. Un grand Merci à Pauline, for her presence and support. The art workshops and several short weekends in Peyrusse-le-Roc were awesome and definitely essential to conquer EQCM!

I would like to address my great appreciation to Prof. Tri-Rung Yew from National Tsing Hua University (Taiwan). Without her guidance and encouragement, I could not have gone so far. I would like also to thank my dear "EMPTY" for their support and concern no matter where they are.

Un grand Merci à Laurent for always being patient, warm and understanding in every aspect. Je remercie également Suzanne et Olivier, who made France my second home.

Lastly, I would like to thank my mom, my brother, Wan-jui, and Rice Ball. Without their constant support and consideration, I could not have achieved all these. 謝謝你們!

Contents

General Introduction	1
Chapter I: Bibliography	5
1. Supercapacitors	5
1.1 Why supercapacitors?.....	5
1.2 Fundamentals of Supercapacitors	7
1.2.1 Brief history	7
1.2.2 Different types of supercapacitors	9
1.2.3 How does an electric double layer capacitor (EDLC) work?	10
1.3 Applications.....	15
2. State-of-the-art of the materials used in carbon/carbon supercapacitors	17
2.1 General material design concept for high performance supercapacitor	17
2.2 Carbon electrode materials	18
2.2 Electrolytes	24
3. State-of-the-art of the EDL study: pore size vs electrolyte ion size.....	26
4. State-of-the-art of the charging mechanism and ion transport: from modelling and in-situ techniques point of view	33
4.1 Theoretical Approaches.....	33
4.1.1 Solvent-free environment: room temperature ionic liquids (RTILs).....	34
4.1.2 Solvent-containing electrolytes.....	38
4.2 In-situ Experimental Approaches	40
4.3 What do we know today about charging mechanism?	45
5. Objectives of the thesis	46
5.1 Study of carbon microstructure effect on capacitive storage	46
5.2 In-situ EQCM study on ion dynamics and charging mechanisms in confined carbon micropores	46
6. Reference.....	47

Chapter II: Materials studied and experimental set-ups57

1. Introduction	57
2. Commercial Activated Carbons	57
3. Electrolytes.....	60
4. Electrochemical Characterization of Supercapacitors.....	64
4.1 Electrochemical characterization techniques.....	64
4.1.1 Cyclic voltammetry (CV)	64
4.1.2 Chronoamperometry	66
4.1.3 Electrochemical Impedance Spectroscopy (EIS).....	67
4.2 Set-ups	70
4.2.1 Swagelok® Cells.....	70
4.2.2 Cavity Micro-Electrode (CME)	72
5. Reference.....	75

Chapter III: Study of carbon microstructure effect on capacitive storage ..77

1. Introduction	77
2. Characteristics of ionic liquid-mixture ((PIP ₁₃ FSI) _{0.5} (PYR ₁₄ FSI) _{0.5}).....	79
3. Hierarchy silicon carbide-derived carbon (SiC-CDC) in organic electrolyte and IL mixture.....	80
3.1 Electrochemical characterization of SiC-CDC in conventional organic electrolyte (NEt ₄ BF ₄ /AN).....	83
3.2 Electrochemical characterization of SiC-CDC in IL eutectic mixture	87
4. Activated Graphene (a-MEGO) in IL mixture	95
4.1 Electrochemical characterization of activated graphene in IL mixture	98
4.2 Removal of surface functional group by vacuum annealing	102
5. Conclusions	107
6. Reference.....	109

Chapter IV: In-situ EQCM Study on Ion Dynamics in Confined Carbon Micropores111

1. Introduction	111
2. Electrochemical quartz crystal microbalance (EQCM)	118
2.1 EQCM Principle	118
2.2 EQCM set-up.....	123
2.3 Calibration (sensitivity constant, C_f)	125
2.4 Theoretical mass change, apparent molecular weight, and solvation number	126
3. In-situ EQCM study of charge mechanism and the solvation effect at the electrode/electrolyte interface	128
3.1 Different experimental parameters	128
3.2 Neat EMI-TFSI.....	130
3.2.1 CDC-1nm.....	130
3.2.2 CDC-0.65nm.....	134
3.3 Solvated EMI-TFSI	136
3.3.1 CDC-1nm.....	136
3.3.2 CDC-0.65nm.....	138
4. Discussions.....	141
5. Conclusions	143
6. Reference.....	143

Chapter V: Further understanding of the EDL structure by combining in-situ EQCM with in-situ NMR Spectroscopy145

1. Introduction	145
2. In-situ nuclear magnetic resonance (NMR) spectroscopy	147
2.1 Brief NMR principle.....	147
2.2 In-situ NMR experimental.....	150

2.2.1 NMR details	150
2.2.2 Quantification of the adsorbed species at zero applied potential.....	151
2.2.3 In-situ NMR cell set-up	153
3. In-situ NMR results	155
3.1 At zero potential	155
3.2 Under polarization	156
3.3 Quantitative information.....	157
4. In-situ EQCM results	160
4.1 Primary in-situ EQCM information.....	161
4.2 Quantitative/Qualitative interpretation	164
5. Discussions.....	167
6. Conclusions	168
7. Reference.....	170
General Conclusions and Perspective	173
Résumé de Thèse	177

General Introduction

General Introduction

The major challenge our society is currently facing is the dwindling fossil energy on earth and the great ecological impact and climate change caused by consuming this fossil energy. As a result, research has been focused on developing renewable and sustainable solutions to obtain non-exhaustive energy resources, such as solar energy, wind energy, wave power, geothermal energy, bioenergy, tidal power, etc. In principle, these methods involve converting different forms of energy (e.g. heat, nuclear, radiant energy, etc.) which exist naturally into electrical energy (energy conversion systems). However, the production cannot always timely meet the demand, thus highlighting the need for the energy storage systems.

Energy is commonly stored in the form of chemical energy (e.g. batteries) or mechanical energy (e.g. flywheel or hydroelectricity), but conversion of energy into electricity is often achieved with great loss. In this context, although the major electrical charge storage device today is secondary batteries, electrochemical double layer capacitors (EDLCs), also known as supercapacitors, are very interesting since they store and deliver electrical energy directly without converting into different forms. Basically, in supercapacitors, the charge is stored through non-faradaic electrostatic attraction between the electrolyte ions and the porous carbon electrode surface; hence the response time for storing and releasing the charges is much faster compared to that of batteries. This charge storage process is highly reversible thus giving supercapacitor a high cycle life ($>10^6$ cycle).^{[1][2]}

Although supercapacitors own high power capability (15 kW/kg), they suffer from a relatively low energy density (6 Wh/kg) as compared to batteries. Therefore, the main challenge today for supercapacitors is to increase their energy density.^[3] Although efforts have been put on seeking for novel electrode and electrolyte materials, the performance improvement was little due to the lack of fundamental understanding about the charge storage mechanisms. An important discovery has been reported by our team in 2006^[4], using carbide-derived carbons (CDCs) with finely-controlled pore size distribution; it was found that the capacitance increased dramatically when the carbon pore size was decreased below the solvated ion size, suggesting that ions could lose a part of their solvation shell to access these confined nanopores. Following this study, numerous works have been devoted to understanding the origin of the anomalous increase in capacitance, and the physics of ion adsorption and ionic transport in confined microporous carbons.

The aim of this thesis is to improve the energy and power performance of EDLCs, which can be achieved mainly from two different aspects: (1) searching for new electrolytes and electrode materials to increase the energy density, and improving the electrode/electrolyte interface and electrode microstructure to enhance the power performance. (2) Improving fundamental understanding of the double layer charging at the electrode/electrolyte interface in confined pores of porous carbons by using an in-situ electrochemical technique.

In **the first chapter**, bibliography covering different aspects will be presented: basic principles of supercapacitors, concept for improving supercapacitor performance from material point of view, different types of electrolytes and active materials used in current supercapacitors and their corresponding pros and cons. From fundamental point of view, EDL studies and the relationship between pore size and ion size during the past 10 years will be reviewed; different investigations conducted by using both theoretical and in-situ experimental approaches will be discussed, and current understanding on EDL charging mechanism will also be summarized.

The second chapter describes the active materials and electrolytes tested in this work. Different electrochemical methods and cell configurations used to characterize the supercapacitors in this work will also be presented.

The third chapter investigates carbons with different microstructures in (PIP₁₃FSI)_{0.5}(PYR₁₄FSI)_{0.5} ionic liquid mixture electrolyte under different operation temperatures. The aim is to build high performance supercapacitors that allow operation under wide temperature range by optimizing the carbon/electrolyte interface and to increase the magnitude and quality of charge storage.

Improving fundamental understanding of the charging mechanism is the most efficient way to enhance supercapacitor performance. Therefore, **the fourth chapter** is devoted to studying the charging mechanism and ion transport at molecular scale during supercapacitor operation. Charging of different carbons in neat and solvated ionic liquid electrolytes will be investigated by electrochemical quartz crystal microbalance (EQCM) in real time.

In **the fifth chapter**, in-situ EQCM is coupled with in-situ NMR spectroscopy to study the same electrode/electrolyte system. By incorporating the advantages of both techniques, one should be able to get a clearer picture of the supercapacitor charge storage.

Lastly, the results obtained in this work will be summed up in the general conclusions part, and the perspectives inspired by this work will also be addressed.

- [1] B. E. Conway, *Electrochemical Supercapacitors: Scientific Fundamentals and Technological Applications*, Springer, **1999**.
- [2] F. Beguin, E. Frackowiak, Eds. , *Carbons for Electrochemical Energy Storage and Conversion Systems*, CRC Press, **2009**.
- [3] P. Simon, Y. Gogotsi, *Nat. Mater.* **2008**, 7, 845.
- [4] J. Chmiola, G. Yushin, Y. Gogotsi, C. Portet, P. Simon, P. L. Taberna, *Science* **2006**, 313, 1760.

Chapter I: Bibliography

1. Supercapacitors

1.1 Why supercapacitors?

More and more attention has been put on the “energy issue” due to the limiting fossil fuels on earth and the climate change, such as global warming and ozone depletion, caused by the combustion of fossil fuels. As a result, much effort has been put in finding renewable and sustainable energy resources to produce electricity, such as wind energy or solar energy. However, the production cannot always timely meet the consumption as the sun won’t shine all the time and the wind won’t blow when we request; hence it is of great importance to develop efficient energy storage and conversion devices to be able to utilize electricity whenever and wherever we need. Electrochemical energy storage systems are currently one of the most researched systems in view of achieving sustainable solutions.

Ragone plot, shown in Figure I-1,^[1] is commonly used to present and compare the performance of different energy storage systems.^[2] As shown in this plot, batteries, electrochemical capacitors, and capacitors are the three main energy storage systems which

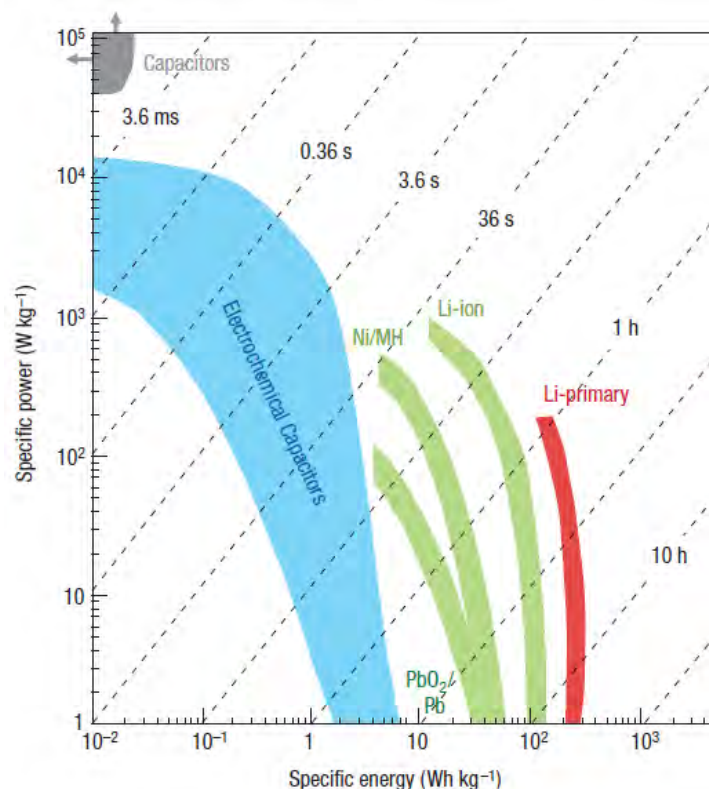


Figure I-1: Specific power versus specific energy, also called a Ragone plot, for various electrical energy storage devices. If a battery is used in an electric vehicle, the specific power shows how fast one can go, and the specific energy shows how far one can go on a single charge. Times shown are the time constants of the devices, obtained by dividing the energy density by the power.^[1]

can be used for storing energy, and each system provides different characteristics in terms of specific power and energy. Specific energy tells the amount of energy that can be stored in the device, and specific power gives information on how fast the device is able to deliver its energy. The dashed lines in Figure indicate the time needed to withdraw all the energy stored in the device. Although batteries have been popular for the past decades and great efforts have been made to develop high-performance Li-ion and other advanced secondary batteries, they still suffer from slow power delivery or uptake. Faster and higher-power energy storage systems are needed in a number of applications. Therefore, electrochemical capacitors, which are power devices that can be fully charged or discharged in seconds, started to attract much more attention recently.^[3,4]

As shown in Ragone plot (Figure I-1), electrochemical capacitors, also commonly known as supercapacitors, ultracapacitors or electrochemical double layer capacitors (EDLCs), fill the gap between batteries and conventional capacitors. They can deliver very high power density (15 kW/kg) with a lower stored energy than batteries (6 Wh/kg). Batteries, such as Li-ion batteries, generally have high energy densities (up to 200 Wh/kg), however, with low power capability (up to 1 kW/kg).^[1] These characteristics are defined from the way that the energy is stored in the energy storage systems. Owing to the simple *non-faradaic*, electrostatic attraction between the electrolyte ions and the charges at the surface of the active material in the supercapacitor, the response time for storing and releasing the charge stored is much faster as compared to batteries, in which faradaic reactions in the bulk of electroactive materials are the main mechanisms for its operation as a chemical storage device. Moreover, the charge storage process is highly reversible as compared to other energy storage devices which involve faradaic reactions, thus EDLCs are able to sustain few millions of cycles. Accordingly, supercapacitors are particularly attractive for applications where high power is needed for a few seconds. They can also be seen as a complement to Li-ion batteries in applications where both high energy (Li-ion batteries) and high power delivery (supercapacitors) have to be achieved. Table I-1 summarizes the characteristics of the three types of energy storage systems.

Table I-1: Comparison of typical capacitor, carbon based supercapacitors, and battery characteristics^[4]

Characteristics	Capacitors	Carbon EDLC	Battery
Examples	Al, Ta oxide, condenser	Activated carbon in H ₂ SO ₄ or NEt ₄ BF ₄ /AN	Lead acid, Ni-Cd, and Ni-MH
Storage mechanism	Electrostatic	Electrostatic	Chemical
E (Wh/kg)	< 0.1	1 – 10	~20 – 150
P (kW/kg)	>> 10	0.5 – 10	< 1
Discharge time (t _d)	10 ⁻⁶ – 10 ⁻³ s	Seconds to minutes	0.3 – 3 h
Charging time (t _c)	10 ⁻⁶ – 10 ⁻³ s	Seconds to minutes	1 – 5 h
Efficiency (t _d /t _c)	~ 1.0	0.85 – 0.99	0.7 – 0.85
Cycle life (cycles)	>> 10 ⁶	> 10 ⁶	~ 1500
	>> 10 yr	> 10 yr	~ 3 yr
V _{max} determined by:	Dielectric thickness	Electrode/electrolyte stability	Thermodynamics of phase reactions
Self-discharge	Low	Moderate	Low

1.2 Fundamentals of Supercapacitors

1.2.1 Brief history

Although the first capacitor, which was named “Leyden jar” and stores the static electricity between two electrodes inside and outside of a glass jar (Figure I-2), was invented independently in 1745 by German cleric Ewald Georg von Kleist and by Dutch scientist Pieter van Musschenbroek, the nature of electricity kept poorly understood until late 19th century.^[3] The mechanism of electrical charge storage in capacitors was then studied and the first model of double layer capacitance was devised by von Helmholtz in 1853.^[5] In 1957, The first patent applying the concept of double layer capacitor for practical purposes was filed by Becker, who used porous carbon coated on a metallic current collector immerse in an aqueous electrolyte.^[6]

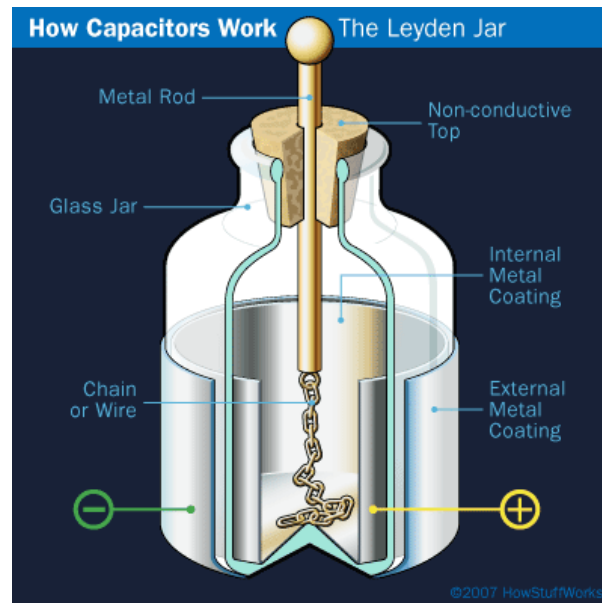


Figure I-2: Schematic of the Leyden jar ^[7]

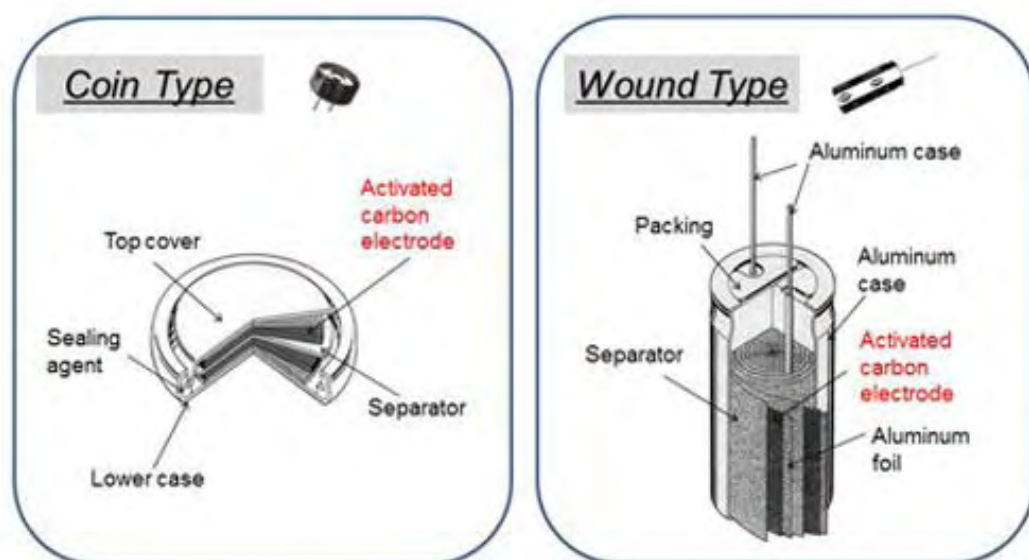
In 1969, the SOHIO Corporation in Cleveland patented and produced the first commercial EDLCs consisting of porous carbon paste electrode in sulfuric acid electrolyte separated by ion-permeable separator.^[8] SOHIO also built EDLC cells in non-aqueous electrolyte which provides higher operating voltages^[9]; however the poor sales led to licensing the technology to NEC (Japan).

In 1971, NEC further developed and marketed the EDLCs successfully for memory back-up applications which require low power and low voltage, and this can be considered as the starting point for EDLC use in commercial devices.^[10] Different applications in mobile electronics, transportation (especially in electric vehicles), military and aerospace systems boosted further research.

To date, supercapacitors are widely used in different applications where high power is demanded. The global supercapacitor market is estimated to reach \$2.10 billion in 2020.^[11] Current major manufacturers include: Maxwell Technologies Inc. (U.S.), Nippon electrical Co. (Japan), Nesscap Co. Ltd. (Korea), Cap-XX (Australia), etc. Most of the commercial supercapacitors are based on porous activated carbons in organic salt dissolved in either acetonitrile or propylene carbonate solvents. Table I-2 lists the characteristics of some commercial supercapacitors (data is collected from official websites individually). Figure I-3 shows two structure examples of commercial supercapacitor.

Table I-2: Examples of commercially available EDLCs

Manufacturer	Cell/module Voltage (V)	C (F)	Specific Energy (Wh/kg)	Specific Power (kW/kg)
Maxwell	2.85	3400	7.4	14
Nesscap	2.7	3000	5.6	6.2
Batscap	2.7	2600	5.3	18
Ioxus	2.7	3000	6.3	10.1
Nippon Chemi-Con	2.5	2300	2.0	-

Figure I-3: Examples of different structures of supercapacitors^[12]

1.2.2 Different types of supercapacitors

To date, different types of supercapacitors have been developed. Depending on the mechanisms of charge storage and the active materials used, they can be generally sorted into three groups: First group includes the most common devices using carbon-based active materials with high specific surface area (SSA).^[13,14] Due to the low cost and ease of preparation of carbon materials, more than 95% of commercial supercapacitors utilize activated carbon as electrodes. Second group of supercapacitors, known as pseudo-capacitors or redox supercapacitors, uses fast and reversible redox reactions at the surface of active

materials. Metal oxides such as RuO_2 , Fe_3O_4 or MnO_2 and electronically conducting polymers have been studied for this group of supercapacitors in the past decades. Hybrid capacitors, belonging to the third group, involves the combination of a capacitive or pseudo-capacitive electrode with a battery electrode, are recently under attraction since they benefit from both the capacitor and the battery properties.

This thesis work focuses on the first group of supercapacitors where the capacitive charge stored in the so-called “double layer” at the electrode-electrolyte interface, which gives this type of supercapacitors the name “electric double layer capacitors (EDLCs)” and no redox reaction is involved. For second and third group of supercapacitors, detail information could be found in references.^[3,15-19]

1.2.3 How does an electric double layer capacitor (EDLC) work?

Dielectric Capacitors

Starting with the basic concept of “capacitors” where a dielectric material is sandwiched by two conductive plates. Two oppositely-charged conductive plates are separated by a dielectric material, as shown in Figure I-4.

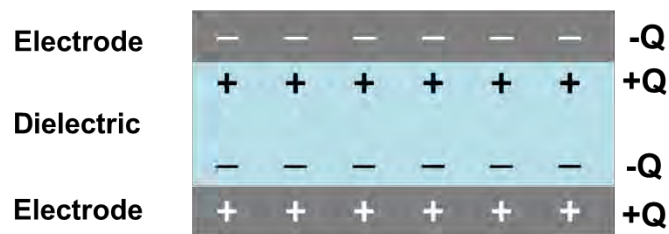


Figure I-4: Schematic of dielectric capacitor

By applying an external bias voltage, the charges are stored by electrostatic attraction between the polarized dielectric and charges residing on each plate. In order to maintain the charge separation, the dielectric material sandwiching in between the two conductive plates must be an electrical insulator. A capacitor is assumed to be self-contained, isolated, and with no net electrical charges between the positive and negative electrodes. The conductive plates thus hold equal and opposite charges on their respective in an ideal case surfaces, resulting in the development of an electric field in the dielectric. The amount of charge (Q in Coulomb) stored is determined by the capacitance C (in Farads) and the voltage difference V (in Volt) across the capacitor using Equation I-1.

$$Q = C \cdot V \quad (\text{Equation I-1})$$

Increase in charge storage lead to the increase of the electric field across the dielectric. Ability of a capacitor to store energy in an electric field is quantified as the term ‘Capacitance’ by following equation (Equation I-2):

$$C = \frac{\epsilon_o \epsilon_r A}{d} \quad (\text{Equation I-2})$$

where ϵ_o and ϵ_r are the vacuum permittivity (8.854×10^{-12} F/m) and the dielectric constant of the material between plates (for vacuum $\epsilon_r = 1$), A is the area of the plates in meter square, and d stands for the distance of separation between two parallel plates in meter.

Electric Double Layer (EDL) Theory

For charge storage in supercapacitors, the capacitance concept is the same as the basic capacitors except that the conductive plates are replaced by different active materials, usually non-metallic conductive materials (such as porous carbons) laminated on metallic current collectors, and the dielectric material is replaced by a polymeric separator fully immersed in the electrolyte. The electronic charges move through the external circuit from the positive to the negative active material while applying a voltage difference across the cell. The cations and anions in the electrolyte are then attracted by their opposite charges and move towards to negative and positive electrodes respectively due to the electrostatic force. The charges are then separated and stored at the electrolyte/electrode surface, which is the so-called “electric double layer (EDL)”.

“Electric double layer” was first stated by Helmholtz in 1853^[5,20] that when charged electrodes are immersed in electrolyte solutions, co-ions (ions that carry the same sign of charge as electrode) will be repelled from the electrode surface while attracting counter-ions (ions with opposite sign to that of the electrode). Two compact layers of charges are formed at the electrode/electrolyte interface separated by a distance H (Figure I-5a), which is a similar concept as planar dielectric capacitor.

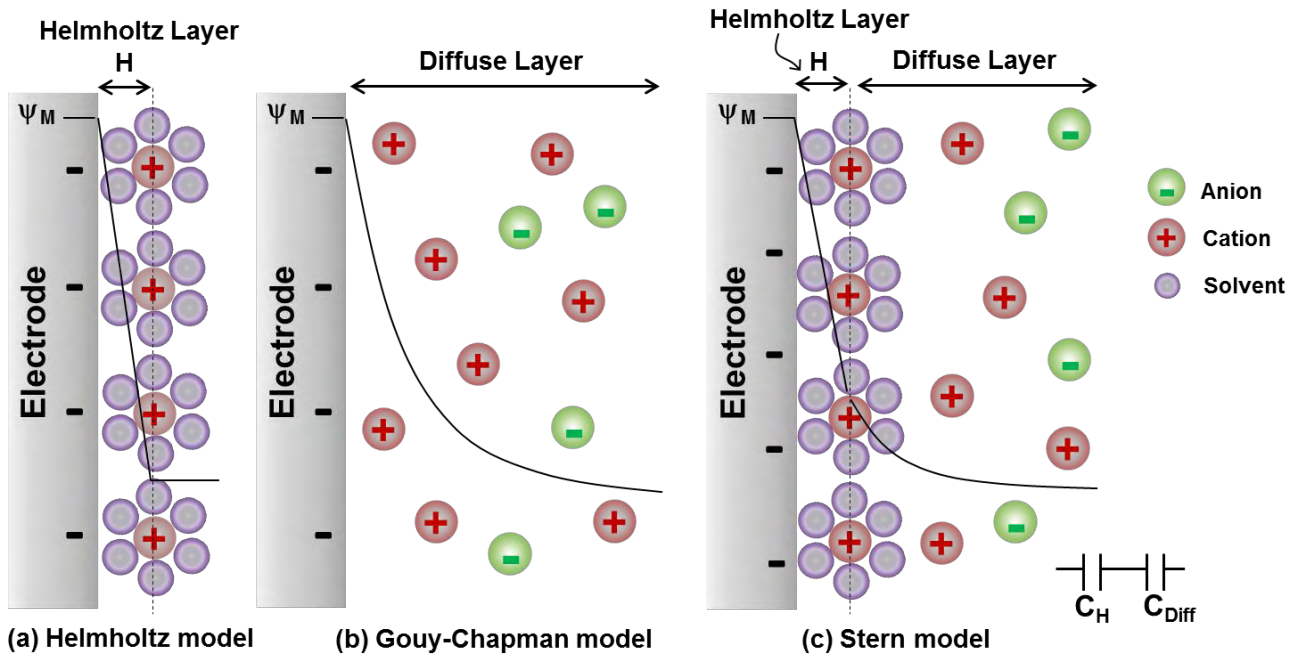


Figure I-5: Schematics of the electric double layer structure showing the arrangement of solvated anions and cations near the electrode/electrolyte interface in the Stern layer and the diffuse layer. (a) Helmholtz model, (b) Gouy-Chapman model, and (c) Stern model

The Helmholtz model was modified by Gouy in 1910^[21] and Chapman in 1913^[22] taking into account that the ions are mobile in the electrolyte solutions and are driven by the coupled influences of diffusion and electrostatic forces, resulting in the so-called “diffuse layer” shown in Figure I-5b. However, the Gouy-Chapman model overestimates the double layer capacitance since it assumed that ions are point charges^[3]. In 1924, Stern^[23] overcame this problem by combining both Helmholtz compact layer and the Gouy-Chapman diffuse layer in his model (Figure I-5c). The resulting double layer capacitance (C_{dl}) can be seen as a capacitance conjugated of two capacitances generated from Helmholtz layer (C_H) and diffusion layer (C_{Diff}), as shown in Figure I-5c, and can be expressed by:

$$\frac{1}{C_{dl}} = \frac{1}{C_H} + \frac{1}{C_{Diff}} \quad (\text{Equation I-3})$$

In general, double layer capacitance on a carbon surface is about $5 - 35 \mu\text{F}/\text{cm}^2$ which depends mainly on the choice of electrolyte. Since the electrolyte concentration is generally well above 0.1 M, the diffusion layer can be ignored.^[3]

Figure I-6a is a simple schematic of an electric double layer capacitor (EDLC) using porous carbon as active material, and the electric double layer at the *negative* electrode is also shown. Figure I-6b gives the corresponding equivalent circuit. C_{dl} is double layer capacitance,

and R_{Ely} , R_C , and R_L are the resistance of the bulk electrolyte, contact resistance between active material film and current collectors, and leakage resistance, respectively. The internal resistance of current collector is assumed negligible.

The capacitance of EDLCs can be described by the same equation as basic capacitor (Equation I-2), while A is the accessible surface area to ions, and d stands for the distance between the center of the ion and the carbon surface. The equivalent circuit of a supercapacitor can also be simplified and presented as in Figure I-6c which is composed by a parasitic inductance (L), an equivalent series resistance (R_S), a capacitance (C), and a Faradaic leakage resistance (R_F).

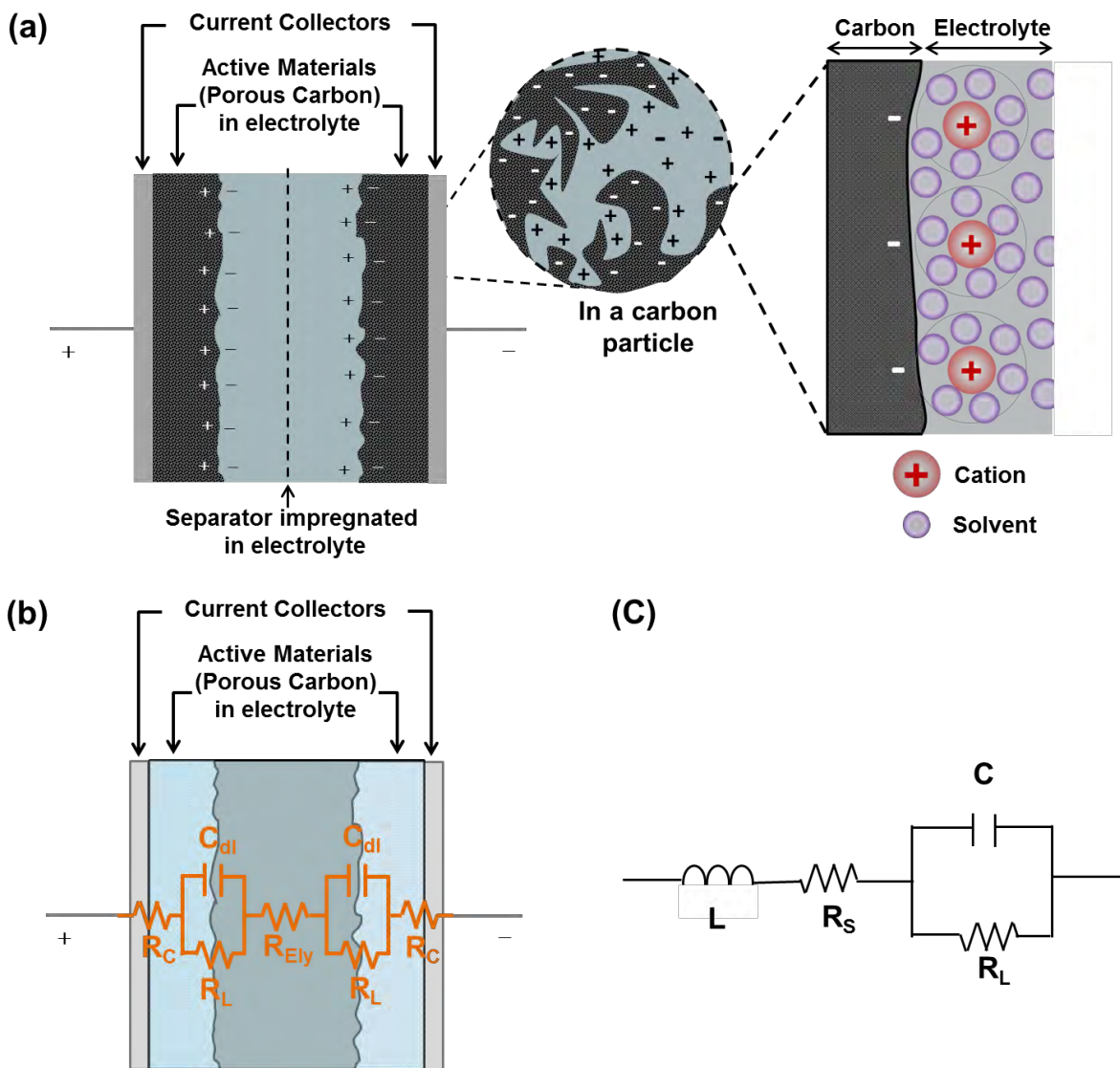


Figure I-6: Schematic of an EDLC: (a) configuration of an EDLC and the zoomed view at the negative electrode-electrolyte interface, (b) corresponding equivalent circuit, and (c) the simplified equivalent circuit

The global capacitance of capacitors is calculated from both electrodes:

$$\frac{1}{C} = \frac{1}{C_+} + \frac{1}{C_-} \quad (\text{Equation I-4})$$

Where C stands for the overall capacitance of the device, while C_+ and C_- are the capacitances of positive and negative electrode, respectively. Taking an EDLC with two electrodes of the same weight and same single electrode capacitance, e.g. 100 F/g, for example, the overall capacitance of the device becomes 25 F/g (considering Equation I-4 and twice the amount of electrode material), which was reduced by a factor of four compare to single electrode capacitance. Therefore, it is important to precise which capacitance it is referred to during discussion. In this thesis work, all the capacitance shown in the result chapters is presented as single electrode capacitance.

The maximum energy (E , in Watt hours) and the power (P , in Watt) of capacitors that one can extract from the device could be calculated by following equations:

$$E_{\max} = \frac{1}{2} CV_{\max}^2 \quad (\text{Equation I-5})$$

$$P_{\max} = \frac{V_{\max}^2}{4R} \quad (\text{Equation I-6})$$

Where C is the overall capacitance of the cell (in Farad), V is the voltage difference between the plates (in Volt), and R is the equivalent series resistance of the cell (in Ohm).

From Equation I-5 and 6, one can know that the energy and the power of supercapacitors are determined by the double-layer capacitance (C), series resistance (R) which is mainly attributed to bulk electrolyte resistance and the interfacial resistance between current collector/active material film, and the cell voltage (V) which is mainly limited by electrolyte electrochemical window. Therefore, the approach for improving the power and energy of supercapacitors is to (1) decrease the internal resistance and interfacial between current collectors and active materials (2) to search electrolytes with higher electrochemical window, and (3) to increase the double-layer capacitance by optimizing the parameters in Equation I-2, such as using high specific surface area porous materials or by optimizing the pore structure to decrease the distance between AM and ions. The concept for improving energy and power density of EDLCs, and fundamental understandings of EDL charging are the core of this thesis work. The state-of-the-art of these aspects will be discussed in detail later in this chapter.

1.3 Applications

As mentioned previously, the *non-faradaic* nature makes EDLCs highly attractive to high power applications. Initially supercapacitors were used as back-up power devices for volatile clock chips and complementary metal-oxide-semiconductor (CMOS) computer memories. But many other applications have emerged over the past 40 years, including portable wireless communication, heavy-duty systems^[24], enhanced power quality for distributed power generation systems and industrial actuator power sources.^[25] For example, Ireland just announced to deploy supercapacitors in their smart grid systems for better energy distribution management.^[26]

In the past 10 years, supercapacitors have been involved intensely in transportation-related field. For instance, in 2006, supercapacitors have been used to power the emergency doors (16 per plane) in an Airbus A380, which proves their performance and safety.^[1,27] Today, one of the most promising applications is their use as high-efficiency energy storage for electric vehicles (EVs) and hybrid electric vehicles (HEVs) for recovering the braking energy and fast start-up of the engine.^[28] Buses powered by supercapacitors are also available in different cities in the world.^[29-31]

In 2014, Guangzhou (China) started to use supercapacitor powered trams where they are charged at stops (Figure I-7b). Charging takes between 10 to 30 seconds and are enough to run for 4 km. Braking energy recovery system is also used on this tram with more than 85 % of recovery efficiency. In the same year, Maxwell also won the energy Storage North America (ESNA) Innovation Awards for an electric rail project aiming for Philadelphia area the involvement of supercapacitors provides an energy efficient solution.^[32] Figure I-7 shows some examples where supercapacitors are involved in transportations.

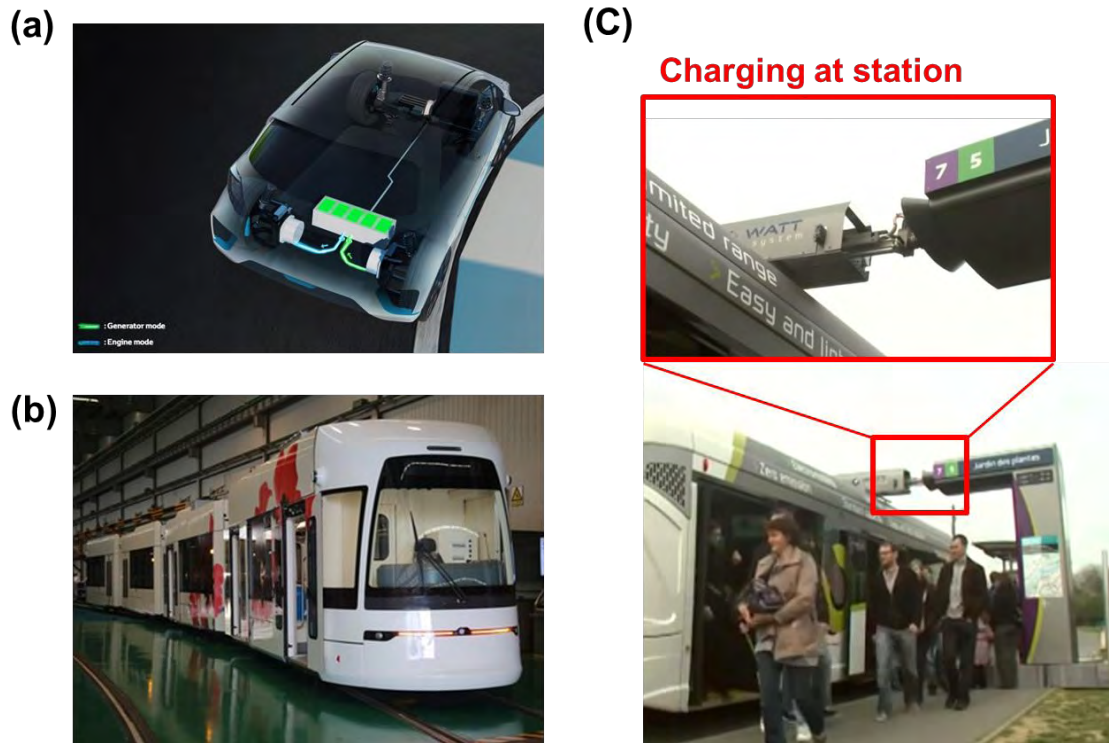


Figure I-7: (a) Combination of super capacitor and motor-generator proposed for Yaris Hybrid-R (Toyota)^[33]; (b) Supercapacitor-powered tram in Guangzhou, China^[34]; (c) Supercapacitor-powered bus for airport transportation in Nice, France ^[29]. The charging of the supercapacitors takes place while waiting for the passengers to get on/off the bus (as shown in the red frame zone)

2. State-of-the-art of the materials used in carbon/carbon supercapacitors

2.1 General material design concept for high performance supercapacitor

The main challenge today for supercapacitors is to increase their energy density without sacrificing their power performance. There have been vast researches dedicated into finding new electrolyte and electrode materials, and new concepts for charge storage. All the important factors for building high performance supercapacitors are imbedded in the specific energy and specific power equations, shown previously in Equation I-2, 5, and 6, recalled below:

$$E_{\max} = \frac{1}{2} \cdot C \cdot V_{\max}^2 = \frac{1}{2} \cdot \left(\frac{\epsilon_0 \epsilon_r A}{d} \right) \cdot V_{\max}^2 \quad (\text{Equation I-7})$$

$$P_{\max} = \frac{V_{\max}^2}{4 \cdot ESR} \quad (\text{Equation I-8})$$

From equations listed above, the energy density of supercapacitors can be enhanced by increasing capacitance of the electrode/electrolyte pair (C) and the electrochemical window of the system (V_{\max}). In general, the electrochemical window is determined by the nature of electrolytes. Increasing electrochemical window is an efficient way to enhance supercapacitor performance as it has a square relationship with both energy and power densities. This is the reason why that researches have shifted from aqueous electrolytes (~ 1 V), to organic electrolytes (~ 2.85 V), and further to room temperature ionic liquids (>3 V). While working on the aforementioned parameters, at the same time, the resistance (R) of the cell (which was affected by ionic conductivity of the electrolytes, electronic conductivity of the carbons, and the contact between electrode/current collectors or between carbon particles) should be kept as small as possible in order to maintain high power density.

The capacitance (C), as depicted in Equation I-7, can be improved by increasing the charge storage surface area (A), decreasing the distance between ion center and carbon electrode surface (d), or modifying the permittivity of the EDL which is mainly determined by solvents or electrolytes. It is commonly assumed that the specific surface area (SSA) of the carbon is the same as the surface area of electrode/electrolyte interface; hence the trend for designing supercapacitor electrode materials is to increase the SSA of the carbons, mainly by elaboration of microstructures or porosity creation (e.g. CO_2 or KOH activation). However, the correlation between capacitance and SSA is not so straightforward since electrode electrical conductivity and other pore characteristics such as pore size, pore size distributions,

porosity, pore shape and pore structure are highly associated to each other.^[35-37] For example, creating porosity by activation often results in widening in pore size distributions (PSD), and decrease in electrical conductivity.^[38] It is difficult to modify solely one parameter without changing the others, and all of them play a different role in the charging process. On the other hand, to play with the factor d requires tailored electrode pore size and fundamental understanding on the charge storage mechanism at molecular scale (will discuss in detail in the following sections). The poor control on pore characteristics, and the complicated relationship between pore characteristics and charging performance hinder both fundamental understanding of EDL charging mechanism and electrode design of better performance. To date, studies have shown that energy density is mainly dependent on micropores (pore size < 2 nm) and the best pore size depends on the electrolyte ions. However, mesopores (2 – 50 nm) and/or macropores (> 50 nm) are equally important for power performance. Therefore, it is also important to develop synthesis strategies which can finely control the porous structure and tailor the required pore size and PSD.


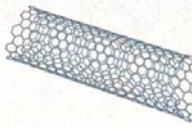

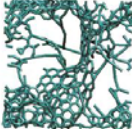


2.2 Carbon electrode materials

As mentioned in the previous section, the choice of electrode materials for supercapacitors requires high specific surface area (SSA) which offers high capacitance thus high energy density (Equation I-7) and good electrical conductivity (~ 1 S/cm). Carbon-based materials have been widely studied as supercapacitor electrode materials^[39] since they are light, abundant, highly conductive, thermally and chemically stable, and they possess open porosity and high SSA. Moreover, one of the most interesting properties of carbon is its versatility that enables different microstructures to be produced and a wide variety of physical and chemical properties to be achieved, allowing them to be used in different types of applications.

Nowadays, activated carbons (AC) are the material of choice for commercial supercapacitors because of their high SSA, relatively facile process and low cost.^[13,40] Carbide-derived carbons (CDCs)^[41-45], templated carbons^[46-48], onion-like carbons (OLCs)^[49-51], carbon nanotubes (CNTs)^[52-55], carbon nanohorns^[57,58], carbon fabrics^[59-62], carbon fibers^[63-65], and graphene^[66-70] have also been investigated. Table I-3 summarizes of the different categories of carbon materials used in supercapacitors.^[71] In this section, different

carbon materials used in supercapacitors will be briefly summarized and discussed regarding their synthesis methods, characteristic structures and electrochemical performances.

Table I-3: Different carbon structures used in EDLCs with onion-like carbon (OLC), carbon nanotubes, graphene, activated carbons, and carbide-derived carbons ^[71]

Material	Carbon onions	Carbon nanotubes	Graphene	Activated carbon	Carbide derived carbon	Templated carbon
Dimensionality	0-D	1-D	2-D	3-D	3-D	3-D
Conductivity	High	High	High	Low	Moderate	Low
Volumetric Capacitance	Low	Low	Moderate	High	High	Low
Cost	High	High	Moderate	Low	Moderate	High
Structure						

0-D: Onion-Like Carbons (OLCs)

Onion-like carbons (OLCs) are zero-dimension carbons with concentric graphitic shells (Figure I-8a-c). Currently there are two ways for large-scale production of OLCs: one is by annealing diamond powder at 1200 – 1800 °C in vacuum or inert gas^[49,51], and the other one is by laser excitation of carbon precursor molecules (ethylene)^[72]. OLCs have open surface structure and are free of micropores with particle size ranges from 5 to 15 nm. Since all the surface area is fully ion accessible without ion transport limitation as in a microporous network, OLCs presents high power capability.^[49,73] Micro-supercapacitors based on these OLCs^[73] showed impressive rate capability (up to 200 V/s) and relaxation time constant (26 ms). Yet the low SSA (500 – 600 m²/g) of this material gives a poor energy performance and low capacitance (~ 30 F/g). Chemical activation at the outer shells of OLCs shows increases in both SSA (~ 800 m²/g) and capacitance (122 F/g) in aqueous electrolyte.^[50]

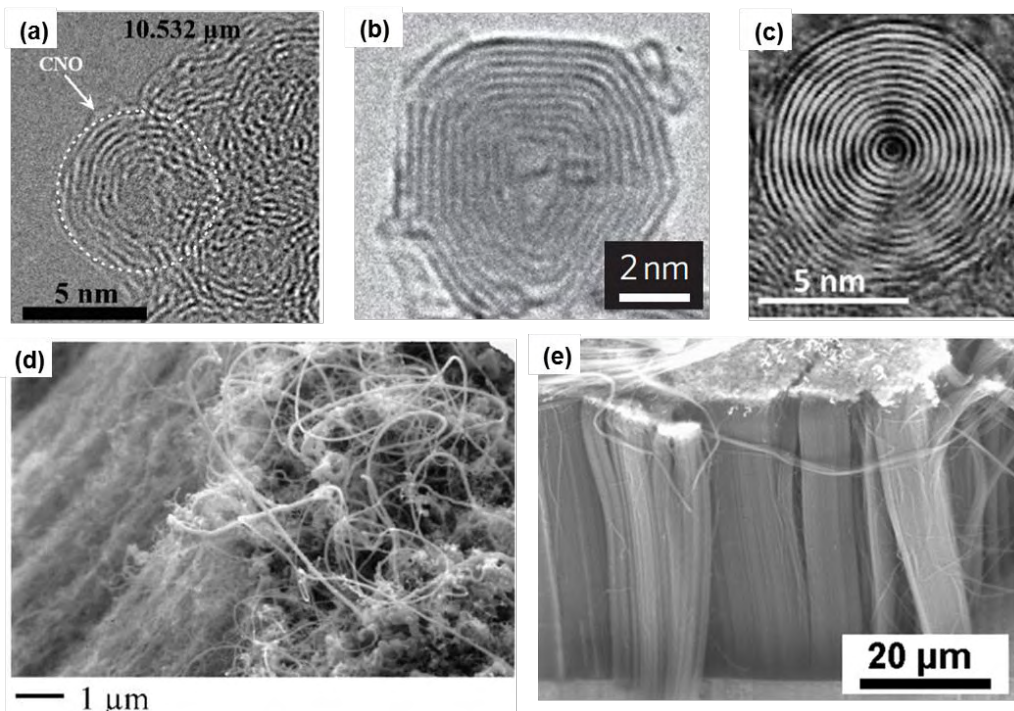


Figure I-8: TEM images of OLCs (a) growth with laser excitation at $10.532 \mu\text{m}$ ^[72], (b) produced by annealing nanodiamond powders at $1800 \text{ }^\circ\text{C}$ (Lattice spacing between the bent graphitic layers in the onion is close to 0.35 nm) ^[73], and (c) synthesized via arc discharge between two carbon electrodes in water ^[74]; SEM images of (d) CNTs synthesised in the CVD system ^[75] and (e) vertical aligned CNTs generated by Fe:Co (2:3) catalyst with additional Al_2O_3 layer ^[53]

1-D: Carbon nanotubes (CNTs)

One dimensional carbon nanotubes are highly attractive electrode materials owing to their superior electrical conductivity, and excellent thermal and mechanical stability. As OLCs, CNTs have mainly exohedral surface with moderate SSA $120 - 500 \text{ m}^2/\text{g}$ (single wall CNTs can go up to $1000 \text{ m}^2/\text{g}$). As a result, they generally present a lower capacitance ($50 - 80 \text{ F/g}$) than activated carbon in organic electrolytes ^[71], but are attractive candidates for high power devices. Most common method to produce CNTs is by chemical vapor deposition (CVD), as shown in Figure I-8d. Current trend is to grow CNTs vertically on conductive substrate (Figure I-8e) which allows efficient electron pathway between current collectors and CNTs and fast ionic transport. ^[53,76] CNTs are also commonly used as substrate for composite electrodes by decorating a thin layer of pseudocapacitive materials on the surface ^[77-79] since raw CNTs suffer from the same energy limitation as OLCs.

2-D: Graphene

Graphene is a single, atomic-thick, tightly-packed layer of carbon atoms bonded in hexagonal lattice. It has drawn tremendous attention during the past decade since its first successful creation in the lab by mechanical exfoliation using adhesive tape.^[70-82]

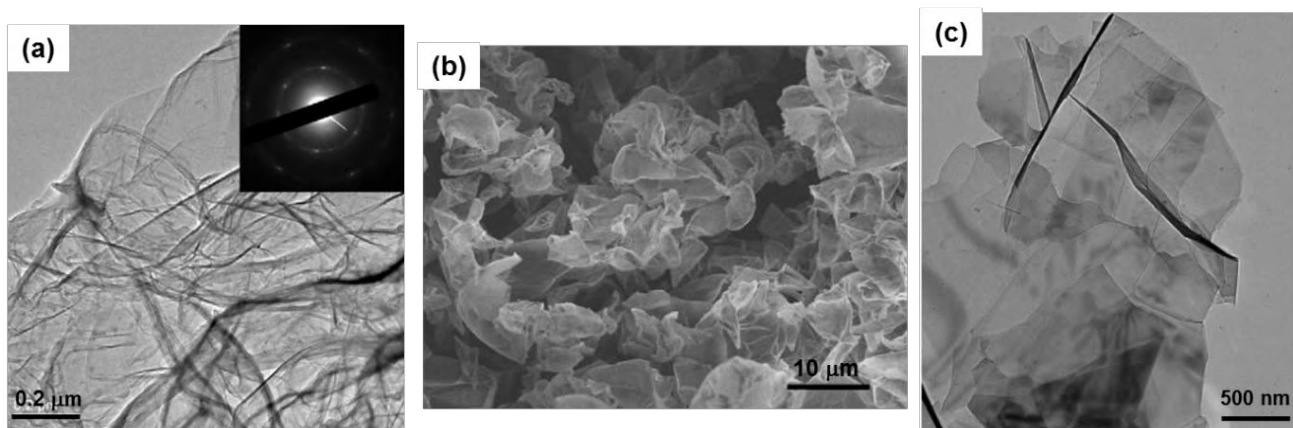
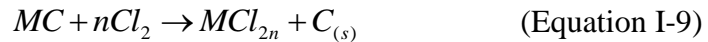


Figure I-9: Examples of graphene: (a) TEM image images of as-prepared microwave exfoliated graphene oxide and the corresponding electron diffraction pattern^[83], (b) SEM image of curved graphene sheets^[84], and (c) TEM image of flat graphene sheets prepared by a conventional chemical route. This TEM image clearly shows graphene sheets overlapped together with intergraphene spacing likely <1 nm.^[84]

Owing to the special way carbon atoms bond to each other within the graphene layer, graphene exhibit plenty of impressive properties which exceed other materials known today: light (only 0.77 mg with 1 m²), mechanically strong (> 100 times than steel), and high electron mobility (> 150,000 cm²/V.s).^[85] The most attractive feature of graphene as an electrode material for supercapacitors is that it has a high theoretical SSA value of 2670 m²/g, however in practice it still suffers from re-stacking. Graphene can be produced by various ways such as CVD^[86-88], electrophoretic deposition^[89,90], ink-jet printing^[91], whereas reduction of graphene oxide (GO) is the most cost-effective method to obtain graphene-based electrode materials (Figure I-9). Reduced graphene oxide (rGO) provides specific capacitance of 130 – 205 and 100 – 125 F/g in aqueous and organic electrolytes, respectively. Recently, rGO with large SSA (up to 3100 m²/g) derived by chemical activation of microwave exfoliated/reduced GO has been reported by Zhu et al^[66]. This rGO provides excellent performance with a specific capacitance of 200 F/g in neat EMI-TFSI ionic liquid electrolyte at 0.7 A/g. However, owing to its low packing density, graphene suffers from low volumetric capacitance.

3-D: Carbide-derived carbons (CDCs), templated carbons, and activated carbons (AC)

Carbide-derived carbons (CDCs) are produced by selective extraction of metals (M) from metal carbide (MC) precursors and transforming the carbide into pure carbon through different synthesis method (halogenation, hydrothermal treatment, vacuum decomposition, etc) [42]. The most common way for producing CDCs for supercapacitor application is through chlorination [41,92]. The reaction is:



During carbide chlorination, the original shape and volume of the carbide precursor are maintained; therefore it is also referred as *conformal transformation* process. [93,94] Carbons produced by this method are highly attractive as it allows fine control over the pore size and PSD by varying the carbide precursor, chlorination temperature, pressure, and other synthesis conditions (Figure I-10). CDCs possess high SSA ranging from 1000 – 3000 m²/g and tunable pore structures in microporous range with subnanometer accuracy, thus making them the best candidates for fundamental EDL studies (will be discussed in section I-3). In general, CDCs exhibit specific capacitance of 110 – 200 F/g in aqueous electrolytes, and 65 – 160 F/g in organic electrolytes. [95]

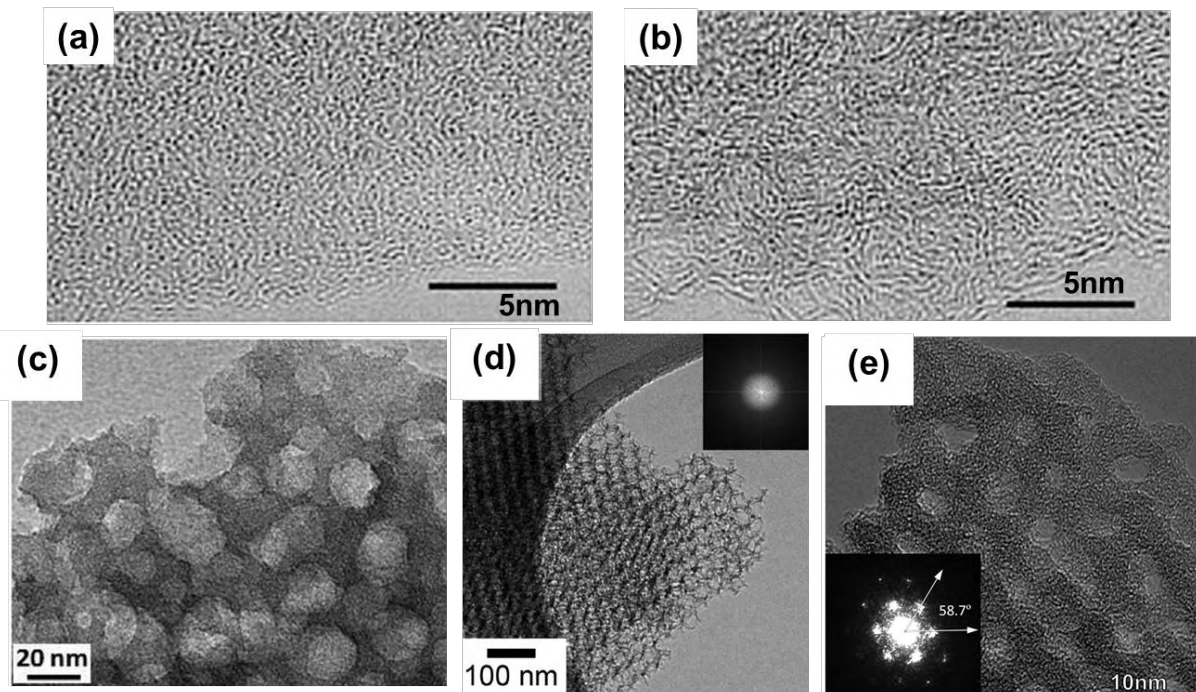


Figure I-10: Examples of CDCs: TEM micrographs of TiC–CDC synthesized at (a) 400 °C (b) 1000 °C. At 400 °C, the carbon produced is mostly amorphous. As the temperature increases to 800 °C and above, thin non-planar graphitic fringes are seen. Planarization of graphite fringes and increase in their length can be seen at higher temperatures [41]; TEM images of different template carbons (c-e) [96-98]

Templated carbons – the templating method provides an effective way to produce nanostructured carbons with well controlled narrow pore size distributions from micro- to macroporous range, ordered pore structures, and an interconnected pore network.^[99] Figure I-10 shows some examples of ordered porous carbon produced by template method.^[96-98] The templates can be roughly sorted into two types: *hard-templates* which are generally solid structure (e.g. silica), and *soft-templates* which are often organic surfactant-based (e.g. triblock copolymer). In hard-templated approach, allows exact replication of the template morphology hence offers a precise pore control, the template is generally first filled with carbon precursor, and followed by carbonization and removal of template, leaving a porous carbon structure. But the removal of template often involves toxic chemicals, such as HF. While soft-templated strategy is more cost-effective and environmental-friendly, though less precision in pore control. Specific capacitances of 120 – 350 and 60 – 140 F/g are found for these carbons in aqueous and organic electrolytes, respectively.^[100]

Activated carbons have been widely studied and are the most used electrode material for commercial supercapacitors owing to their large SSA ($> 1000 \text{ m}^2/\text{g}$) and pore volume ($>0.5 \text{ cm}^3/\text{g}$), relatively simple production method and low cost.^[1,40] They are produced by pyrolysis of carbon-rich precursors in an inert atmosphere (usually N_2) at 400 – 900 °C, followed by activation process using oxidizing agents such as CO_2 ^[35,101,102], steam^[101-103] or KOH ^[36,37,103], leading to opening of some closed pores and creating additional porosity. In general, the higher the activation temperature/activation time, the larger the porosity, however the broader the pore size distribution (PSD). Traditional activated carbons feature a broad pore size distribution ranging from micropore ($< 2 \text{ nm}$) to macropore ($> 50 \text{ nm}$) region, resulting in capacitance of 150 – 300 F/g and 80 – 120 F/g in aqueous and organic electrolytes, respectively^[1]. Among different activating agents, KOH is of great interest to supercapacitor applications since it generates large SSA (2000 – 3500 m^2/g) and pore volume (1 – 2.6 cm^3/g), and shows narrower and better tuned PSD though careful selection of carbon precursors and activation conditions. KOH activation can also be employed on other types of materials to increase SSA and improve capacitance.^[38,50,66] However, it should be noted that porosity creation often means increasing the amount of sp^3 -bonding resulting in reduction of carbon conductivity. Although recent developments in precursors and activation procedures showed improved control over PSD of activated carbons, templated carbons or carbide-derived carbons still present better tunability and narrower PSD.

2.2 Electrolytes

Electrolytes used in supercapacitors can be sorted into three categories: aqueous electrolytes, organic electrolytes, and room temperature ionic liquids. The two main criteria for electrolytes are (wide) electrochemical window and (high) ionic conductivity.

Aqueous electrolytes

Aqueous electrolytes possess high ionic conductivity (few hundreds of mS/cm) as compared to organic electrolytes or ionic liquids. However, the narrow stability window of water limits the cell voltage at < 1.3 V, giving the device poor energy density. Acid-based (e.g., H_2SO_4) or alkali-based (e.g., KOH) electrolytes are commonly used aqueous electrolytes.

Organic electrolytes

Organic electrolytes are made of salts dissolving in organic solvents. The ionic conductivity of organic electrolytes ranges from few to few tens of mS/cm. By shifting from aqueous to organic electrolytes, the electrochemical window was increased up to 2.7 V. Both properties are highly dependent on the nature of organic solvents (mainly viscosity). A detailed study of different salts and organic electrolytes was reported by Ue et al.^[104] Conventional organic electrolyte used in most of the commercial supercapacitors is composed of 1 – 1.5 M tetraethylammonium tetrafluoroborate (NEt_4BF_4) in acetonitrile (AN) with a conductivity of ~ 60 mS/cm at room temperature. The main concern of this electrolyte is the low flash point (~ 5 °C) of AN. However, current alternatives to AN, e.g., propylene carbonate (PC), often show poorer power performance due to their lower ionic conductivities.

Room temperature ionic liquids (RTILs)

Room temperature ionic liquids (RTILs), also referred as room temperature molten salts, have drawn much attention for energy storage applications during the past two decades thanks to their wide electrochemical window (~ 4 V, some ionic liquids can go up to 6 V)^[105-108]. Supercapacitors using pure ionic liquids as electrolytes usually exhibits potential windows more than 3 V, limited mainly by impurities or functional groups on the carbon surface. They are salts having low melting points thus exist as liquid state at room temperature, and they are considered as “green” electrolyte due to their non-volatility. However, RTILs suffers from their high viscosity (30 – 50 cP; some ILs even have viscosity values up to 600 cP at 25 °C)

hence relatively low ionic conductivity (0.1 – 18 mS/cm at 25 °C), which limits their practical use at elevated temperature ^[107]. Interestingly, Lin et al. have recently shown that the concern of ionic conductivity can be circumvented by selecting appropriate carbon nanostructures, such as exohedral surface materials ^[109]. Physical and chemical properties of different RTILs (to be used as electrolyte in electrochemical cells) have been summarized and discussed in detail in reference ^[110].

This thesis focuses mainly on organic electrolyte and ionic liquid-based electrolytes owing to their high energy density.

3. State-of-the-art of the EDL study: pore size vs electrolyte ion size

Traditional view of ion adsorption

Before mid-2000s, early efforts put in increasing the capacitance were focused on increasing specific surface area and porosity of the carbon materials. However, the SSA failed to show linear relationship with capacitance as predicted by equation.^[111,112] In search of other parameters that could improve capacitance, the relationship between electrolyte ion size and carbon pore size has also been investigated. Studies have suggested that electrolyte ions enter the pores with their entire solvation shells due to the high magnitude of solvation energy, and the maximum capacitance was expected to appear when the compact layers of ions residing on both adjacent pore walls. Taking into account the solvated ion size for organic electrolytes is larger than 1 nm^[113,114], the best electrode pore size was limited at about 2 – 5 nm (twice the solvated ions size)^[1,115], mainly in mesoporous range. Despite all efforts poured in tailoring pore size in small mesopore range, mainly achieved by template techniques, only small improvement has been achieved using mesoporous carbon. The capacitance is round 100-120 F/g and 150-200 F/g for organic and aqueous electrolytes, respectively.^[116-120] At the same time, high capacitance has also been reported in carbons containing large amount of micropores by different groups.^[121-123] Moreover, a study reported by Vix-Guterl et al^[121] has shown linear relationship between capacitance and microporous volume in the materials, leaving doubts in this EDL theory.

The rising of micropores: ion desolvation

Systematic studies of the *individual* effect of SSA, pore size, porosity, pore size distribution and conductivity on capacitive charge storage were difficult to be carried out due to poor control of traditional production methods over carbon pore characteristics. Therefore, the traditional belief in double layer structure in a charged porous carbon could not be studied and verified until a new category of carbon – carbide-derived carbons (CDCs) – has been developed.^[124] CDCs offer narrow PSD, and excellent pore size control with angstrom accuracy by changing the synthesis temperature.^[41] Among different CDCs, titanium carbide-derived carbons (TiC-CDCs) are very interesting for probing ion – pore size relationship because their pore sizes can be controlled in between 0.6 and 1.1 nm, in the same range as bare/solvated ion sizes (Figure I-11b^[125]). By using TiC-CDCs, Chmiola et al.^[126] have found a dramatic capacitance increase when pore size goes below solvated ion size (1

nm), as shown in Figure I-11a where capacitance was normalized by BET SSA to highlight the effect of pore size, contradicting the traditional EDL pictures. It was proposed that ions stripped off part of their solvation shells to squeeze in the confined micropores, leading to a reduction in distance between ion center and carbon surface, thus resulting in the capacitance increase. The capacitance increased from 100 to 140 F/g (55 to 80 F/cm³) while reducing the pore size from 1.1 to 0.68 nm, representing a gravimetric capacitance improvement of 40% over commercial carbons under the same testing condition (100 % for volumetric capacitance). The size effect has also been reported by other groups.^[121,123,127] These results have completely overturned the old belief in supercapacitor charging mechanisms, and changed the research directions in the capacitive storage domain.

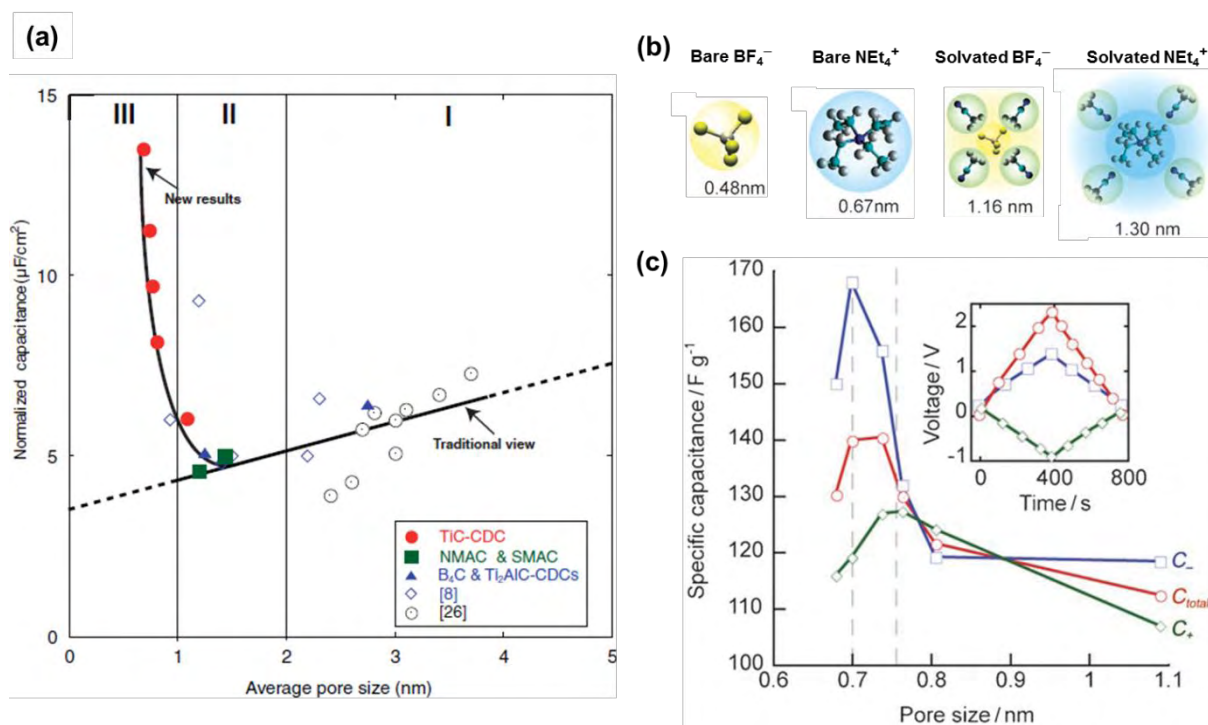


Figure I-11: CDCs with controlled and narrow PSD studies in 1.5 M NEt_4BF_4 solvated in acetonitrile: (a) Specific capacitance normalized by SBET for CDCs and in two other studies with identical organic electrolytes^[126], (b) bare and solvated electrolyte ion size calculated from reference^[128], (c) figure adapted from reference^[125], and specific capacitance of the cell and positive (C_{-}) and negative (C_{+}) electrodes as a function of pore size^[125].

Further study of the same system ($\text{NEt}_4\text{BF}_4/\text{AN}$) was conducted in a three-electrode cell configuration to investigate cation and anion behavior separately.^[125] Results confirm that both cations and anions are at least partially desolvated. Maximum capacitances for cation and anion appear at different pore sizes, suggesting different effective ion size; anion exhibits

higher capacitance than cation for all the pore size. (Figure I-11c). The authors attributed the difference in capacitance between anion and cation to different solvation energy, and suggesting that higher solvation energy leads to higher capacitance since part of the energy is stored in the reversible solvation/desolvation process.

Steric effect: ion sieving

The pore vs ion size relationship is further investigated using cavity microelectrode (CMEs) [129] by cyclic voltammetry and electrochemical impedance spectroscopy measurements [130-133]. From CV measurements (Figure I-12a), Lin et al have shown that despite the solvated ion sizes of NEt_4^+ and BF_4^- in acetonitrile (AN) are larger than 1 nm (Figure I-11b) [125], the CV shows nice rectangular profile in 1 nm-pore for both cation and anion adsorption (potential > OCV @ 0 V vs reference) while decreasing pore size from 1 down to 0.68 nm; whereas CV distortions are observed for pore size < 1 nm for cation adsorption (potential < OCV @ 0 V vs reference) suggesting a decrease of ion accessibility in the pores. The effective ion sizes for anion and cation are thus deduced to be < 0.68 nm and 0.76 – 1 nm, respectively.

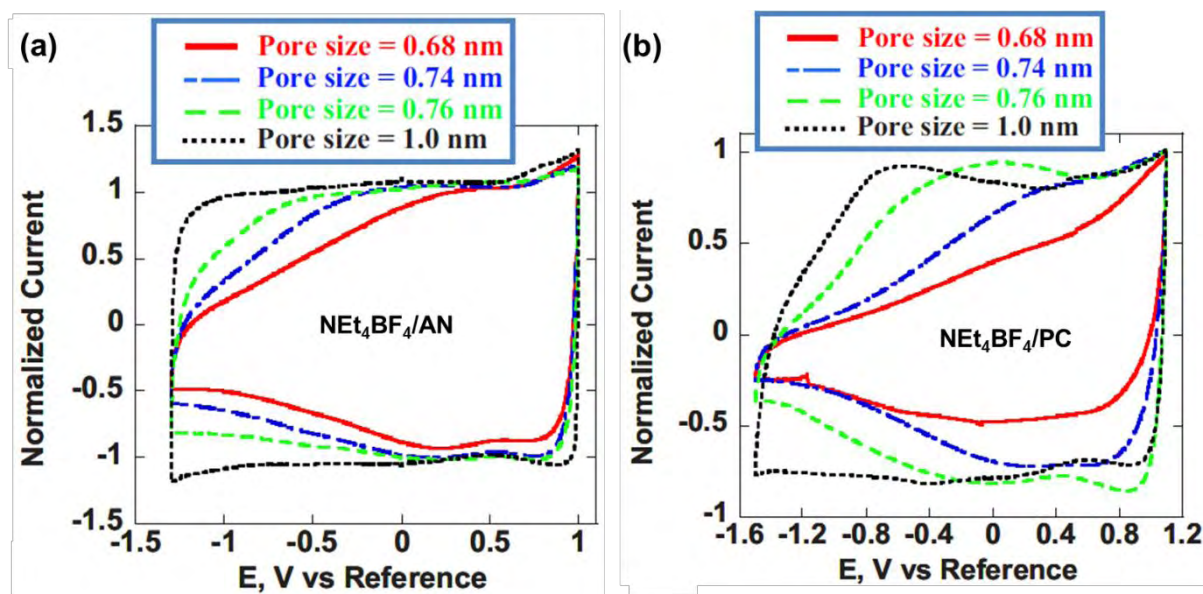


Figure I-12: Normalized CVs of CDC samples at scan rate of 100 mV/s in (a) 1.5 M $\text{NEt}_4\text{BF}_4/\text{AN}$ (OCV = 0 V vs ref) and (b) 1 M $\text{NEt}_4\text{BF}_4/\text{PC}$ (OCV = 0.3 ~ 0.5 V vs ref) [130]

The same trend has been observed when using propylene carbonate (PC) as solvent (Figure I-12b), and the effective ion sizes are found to be larger than that in acetonitrile: ~ 0.75 nm and > 1 nm for anion and cation, respectively, suggesting that effective size of the

same ion adsorbed in carbon pores is different depending on the nature of the solvent, and the ion-solvent interaction. These results confirm that ions move in and out the micropores without hindrance at light degree of desolvation (1 nm-pore); removal of the first few solvents is easy. The increase of confinement will increase the degree of desolvation until the energy of removing one more solvent becomes too high, and the minimum solvated ion size (effective ion size) is reached. Further decrease of pore size won't remove more solvent molecules but decrease the ion accessibility to the pore surface, resulting in deviated CVs from rectangular capacitive profile. A steric effect or ion sieving effect^[134] is thus observed. These results are also confirmed by using other ion/solvent pairs.^[132,133]

Instead of steric effect, some reports attributed the limited charge storage in small pore size to surface saturation effect.^[135,136] Segalini et al^[133] conducted experiments to clarify the origin of the current distortion in smaller pore size. A current increase was observed when adding EMI-BF₄ into 1.5 M NEt₄BF₄/AN (Figure I-13a). The added EMI-BF₄ have the same anion but cation with smaller effective ion size than NEt₄⁺, thus have access to smaller pores that were not reachable by larger solvated NEt₄⁺. Same trend has been observed when playing with effective anion size (Figure I-13b). These results have shown that the pore accessibility is not determined by charge saturation on the carbon surface but by steric effect.

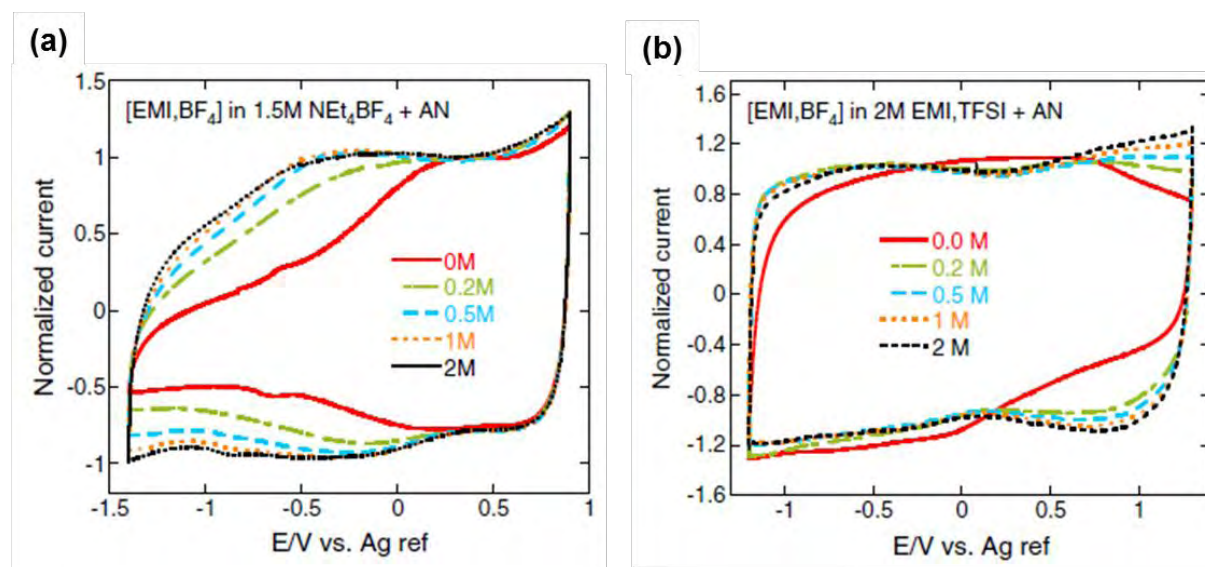


Figure I-13: Normalised CVs of TiC-CDC with 0.68 nm pores in 1.5 M NEt₄BF₄ in AN (a) and 2 M EMI-TFSI in AN (b) with addition of different amounts of EMI-BF₄

Solvent-free environment

After the breakthrough discovery of ion accessibility in the small micropores ^[126], the following question then becomes – what is the best pore size for efficient charge storage? In spite of the attempt in probing pore-ion size relationship, lots of uncertainties remain when studies were conducted with organic salts dissolved in solvent: To what extent can solvent been removed? Even if the pore size is close to ion size, is there any solvent residual in the pores? Do the solvent residuals participate in charge storage? Ionic liquid, as a solvent-free electrolyte, is thus a good candidate to help clarifying things one by one. Without the implication of solvent molecules, ionic liquid has a well identified ion size and thus makes the investigation of effect of ion-pore size relationship on capacitance simpler.

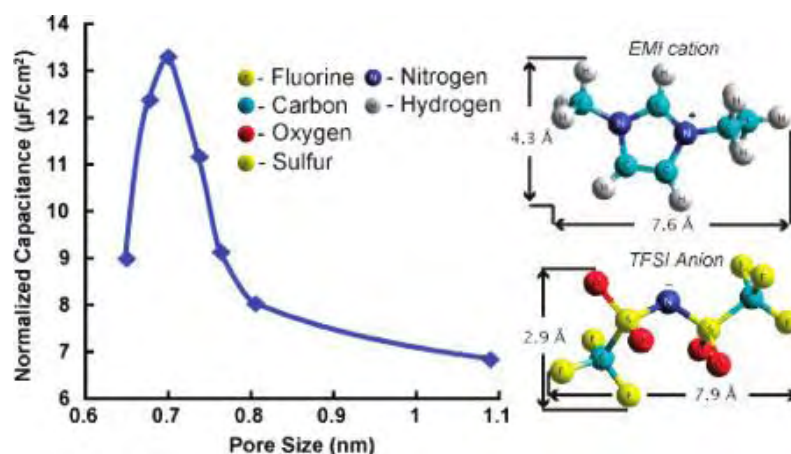


Figure I-14: Normalized capacitance change vs the pore size of the CDC samples prepared at different temperatures; normalized capacitance is obtained by dividing the specific capacitance by the SSA. HyperChem models of the structure of EMI and TFSI ions show a size correlation.^[137]

CDCs with different pore sizes measured in neat EMI-TFSI ionic liquid (Figure I-14) shows that maximum capacitance appears at pore size of ~ 0.7 nm, close to the longest dimension of both cation and anion.^[137] The optimized pore size offers high specific capacitance of 160 F/g (85 F/cm³), much greater than commercial activated carbon in ionic liquids (less than 100 F/g and 50 F/cm³). This confirms again the key contribution of micropores in the capacitive charge storage, and maximum capacitance arises when pore size is close to ion size.

From material design point of view, all these results highlighted the need to adapt the electrode pore size to the electrolyte ions size, which situates at the microporous range, for

maximizing the capacitance and thus the energy density. However, reports also suggest that if carbon contains only micropores, which have a long diffusion distance and high ion transport resistance, will result in large IR drop and small accessible surface area at high current charging hence poor rate performance.^[127] On the other hand, it has been proposed that the presence of mesopores, usually 2 – 8 nm, can accelerate the kinetic process of the ion transport in the electrodes and improve in power performance.^[14,138] In view of these, Wang et al have proposed an interesting approach^[139] in which they designed a carbon powder with *hierarchical* porous structures which combine macropores, mesopores and micropores (Figure I-15). In their design, macropores serve as ion-buffering reservoirs; mesopore walls provide good electrical conductivity and small ion diffusion distance; and micropores mainly contribute to charge accommodation. Following this report, new trend of electrode material design focuses on fabricating hierarchical micro-architecture in aim of increasing energy density with large amount of micropores and high SSA, and at the same time reducing the effective ion diffusion path.^[140-143] However, to efficiently design the electrode materials, fundamental research on ion dynamics in the electrode, especially in confined micropores, are necessary.

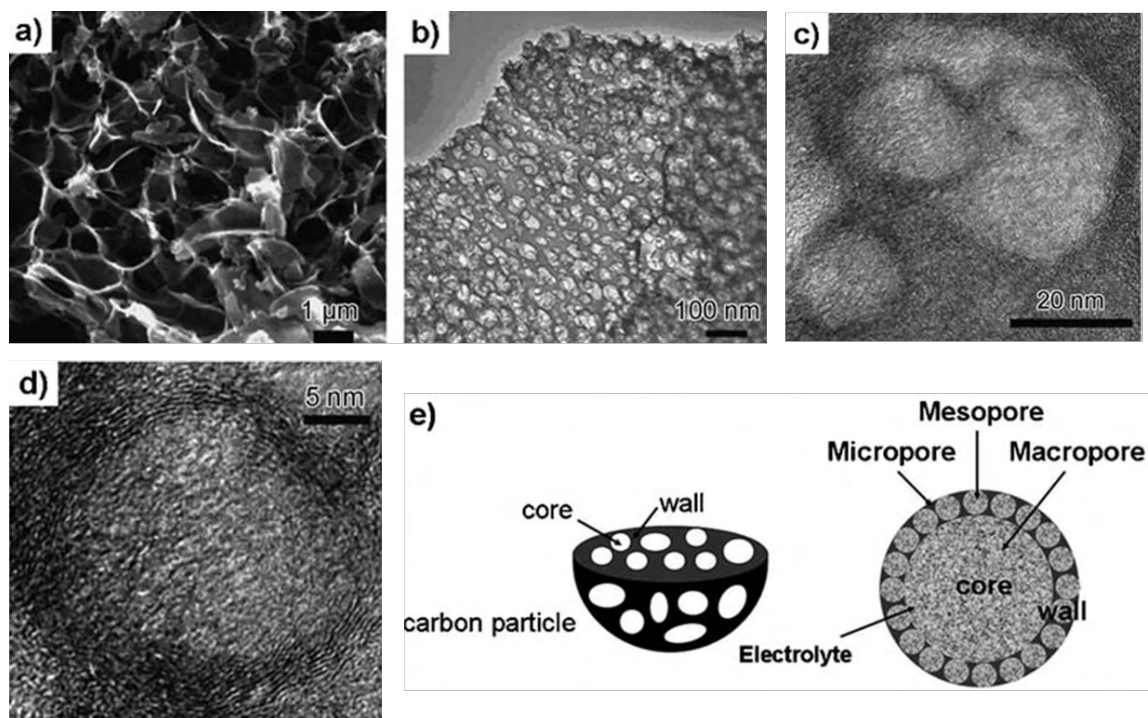


Figure I-15: (a) SEM image of the macroporous cores of the 3-dimensional (3D) hierarchical porous graphitic carbon (HPGC) material, (b) TEM image of the mesoporous walls, (c) TEM image showing the micropores, (d) high-resolution TEM (HRTEM) image of the localized graphitic mesopore walls, and (e) schematic representation of the 3D hierarchical porous texture.^[139]

If we look back to the capacitance equation (Equation I-2), the parameter – ϵ_r , dielectric constant – seems to receive less attention. In the traditional double layer theory, solvent molecules only act as continuum, and are often assumed to have no additional effect on the double layer during charging process by using constant permittivity. Whereas in reality, solvents largely populate in the double layer even in the case of partial desolvation, and the effective dielectric permittivity plays a certain role on the charging process. Although it has been suggested that the permittivity decreases when solvent molecules are adjacent to the charged electrode owing to the decreased ability to screen the charge ^[3,144], but up to now, individual contribution of solvent molecules and ions to charge storage, the details of how solvent molecules affect the double layer structure in such confined space, and the relationship between solvation energy, adsorption energy and charge storage are still poorly understood. Aside from these rather *thermodynamic* factors, realization of ion transport and instant molecular organization during charging/discharge is needed for achieving efficient charging. Fundamental understanding on the *kinetic* factors will efficiently help for better supercapacitors designs. Electrochemical techniques alone are insufficient to probe these issues, incorporation of simulation or other in-situ techniques are definitely required to reveal

4. State-of-the-art of the charging mechanism and ion transport: from modelling and in-situ techniques point of view

To obtain a clear picture of charging mechanism and dynamics in the confined space and the physics behind the capacitance increase, one needs *in-situ electrochemical methods* to track the electrolyte molecules in real time. To date, we lack the techniques to probe the relationship between the local degree of charge separation and the local structure of pores. Therefore, *computational simulations and modellings* are equally important for understanding what accounts for the anomalous increase of charge storage and how it happens. This section will summarize what we know now about charging the EDL in confined space from modelling and empirical points of view. Exohedral surface materials (e.g. onion-like carbons or nanotubes) are also gaining increasing attentions from fundamental point of view, however high energy density requires porous confinement. Therefore, this thesis work and the following discussion will focus on porous materials.

4.1 Theoretical Approaches

There was a clear lack of fundamental understanding of the double layer charging in the confined space of micropores as the traditional theories fail to explain the anomalous capacitance increase in the microporous carbon. This has triggered significant research efforts in computational simulations and modeling, aimed at developing new theories or improving the existing ones. Among different methods, Monte Carlo (MC) and molecular dynamics (MD) are the most favored molecular simulation techniques. MC simulations are based on statistical mechanics which obtains the thermodynamic properties of the system by averaging over a large number of sampling steps, and are thus limited to equilibrium properties. MD simulations solve the Newton's equation of motion for the system over a period of simulation time, and are able to predict both equilibrium and dynamic properties.

In the development of molecular modeling, the selection of electrolyte and electrode models is critical for the accuracy and reliability of the simulation results. Commonly used electrolyte includes primitive models, all-atom electrolyte models, united-atom models and coarse-grained models. *Primitive models* are often used in the early simulations of EDLCs since they are simplest models among the aforementioned ones by describing ions as hard spheres, electrodes as hard walls, and solvents are considered as a dielectric constant [145][146][147]. The accuracy of these models is restrained due to the lack of realistic structure.

All-atom electrolyte models include every single electrolyte atom, and are the most realistic models for studying EDL structure and polarizability ^[148]. However, all-atom electrolyte models are of limited use due to their high computational cost. *United-atom models* and *coarse-grained models* applied some simplification by grouping different atoms into single pseudo-atoms ^[148]. Coarse-grained models are highly attractive for simulating RTILs since they allow accurate prediction of IL physical properties, IL/electrode interaction and EDL structure as that of all-atom models ^[149], with greatly reduced simulation times (by 100 times) ^[148]. The electrode models can be roughly sorted into *constant and uniform surface charges* or *polarizable electrodes* where the electrode potential is hold constant and the local carbon charges are allowed to fluctuate. Besides these, different electrode structures (e.g. planar electrodes, slit-type pores, carbon nanotubes, etc.) could be given. In general, simplified carbon structure (e.g. planar electrode) often results in underestimated capacitance as compared to experimental values; hence it is important to include the carbon structural complexity and polarizability.^[150-153]

4.1.1 Solvent-free environment: room temperature ionic liquids (RTILs)

Planar electrodes

Due to their promising features for supercapacitor applications, RTILs have also attracted significant attention from modelling researchers. The molecular simulations of RTILs on planar electrodes during charging have revealed the EDL structures at the electrode-electrolyte interface and provided different pictures and factors which may involve in charging/discharging procedures.

It has been pointed out that one cannot apply Gouy–Chapman–Stern theory, which is based on diluted electrolytes, to RTILs.^[154] Due to the absence of solvent, short-range Coulomb correlations ^[155] are strong in these dense ionic systems ^[156,157]; hence it is important to take the strong electrostatic interaction between cations and anions into account when constructing the EDL structure of RTILs. Two EDL structures at the planar charged electrode, which took into account the natural constrain of maximum ion packing density and short-range ionic correlations, have been proposed by Fedorov and Kornyshev ^[158] (Figure I-16): *overscreening* where the electrode surface charge is overscreened by a monolayer of counter-ions and is corrected by an excess of co-ions in the second monolayer; and *crowding* where counter-ions extends across two monolayers leading to a co-ion excess in the third

monolayer. It predicts that ^[159] overscreening is pronounced at small voltages polarization and gradually replaced by the formation of a condensed layer of counter-ions, followed by complete lattice saturation at very high electrode polarization. These results suggest that the “over-compensation” leads to an oscillatory behavior of the charge density extending several layers from the electrode surface to bulk electrolyte until the electroneutrality is reached; hence the double layer in IL is *not* one layer thick.

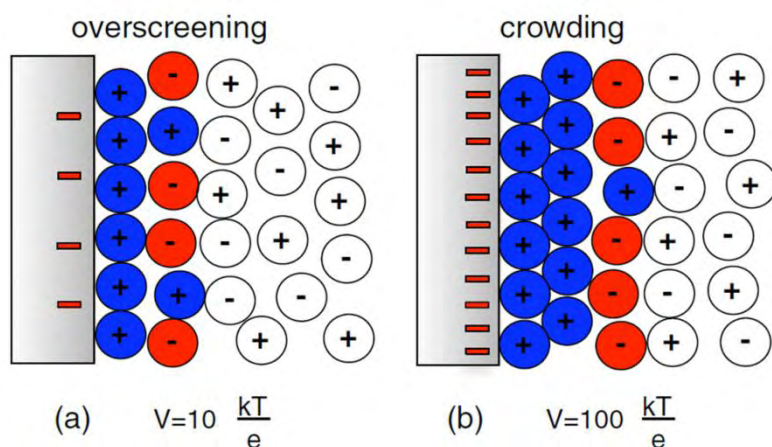


Figure I-16: Structure of the ionic-liquid double layer (in color) predicted from MD simulation of Ref ^[158]. (a) Overscreening is pronounced at a moderate voltage, $V = 10k_B T/e$ (0.26 V), (b) whereas crowding dominates overscreening at a high voltage, $V=100k_B T/e$ (2.6 V) Because of electrostriction, the diffuse double layer (colored ions) is more dense than the quasineutral bulk liquid (white ions) ^[159]

Several simulations highlighted the effect of *ion size*, *ion size asymmetry* (cation size different from anion size) and *ion shape asymmetry* on interfacial structure and capacitance ^[158-163]. On the other hand, by using all-atom models of BMI-PF₆ ionic liquid ^[164,165], simulations have shown that near uncharged graphite surface, the ionic liquid structure differs from its bulk structure, and shows a well-organized region extended ~ 2 nm from the electrode surface. The imidazolium rings in cations tend to lie flat, parallel to the graphite surface with a distance of 0.35 nm, while the alkyl chains stretch in the perpendicular direction. When the surface is charged negatively, more cations are adsorbed on the electrode but with the same ring-electrode distance, while anions are repelled toward the electrolyte bulk, resulting in an alternating cationic and anionic layer profile. At the positively charged surface, anions are adsorbed on the surface; the cation concentration in the adsorption layer decreases but still has a nonzero value. In addition, the tilt angle of the adsorbed rings increases, which is in accordance with the experimental observations ^[166,167]. These results

highlight that RTILs undergo a high level of *structural rearrangement* near charged surface.

Porous electrodes

Understanding the IL properties on planar electrodes is essential but not sufficient to understand the origin of the anomalous capacitance increase in confined micropores, therefore the pore-ion size relationship has also been investigated by the introduction of micropores in the modelling system. Qualitative agreements are found in different micropore models. Kondrat et al. ^[168,169] suggested performed grand canonical MC simulations of a restricted primitive model of ionic liquid in which image forces exponentially screen out the ion-ion interactions in the metallic **slit-like narrow pores** and ion-pore wall interactions. Packing of ions with the same sign becomes easier and is mainly restricted by steric factors. The authors termed this phenomenon as “*superionic*” state, which explains the anomalous capacitance increase when pore size decreases (Figure I-17). Simulation results showed that both total charge (per surface area) increase in a pore and total ion density increase along with the capacitance increase. The saturation of the total ion density in a pore (which means a complete filling of a pore is reached) is account for the peak in the capacitance vs voltage plot.

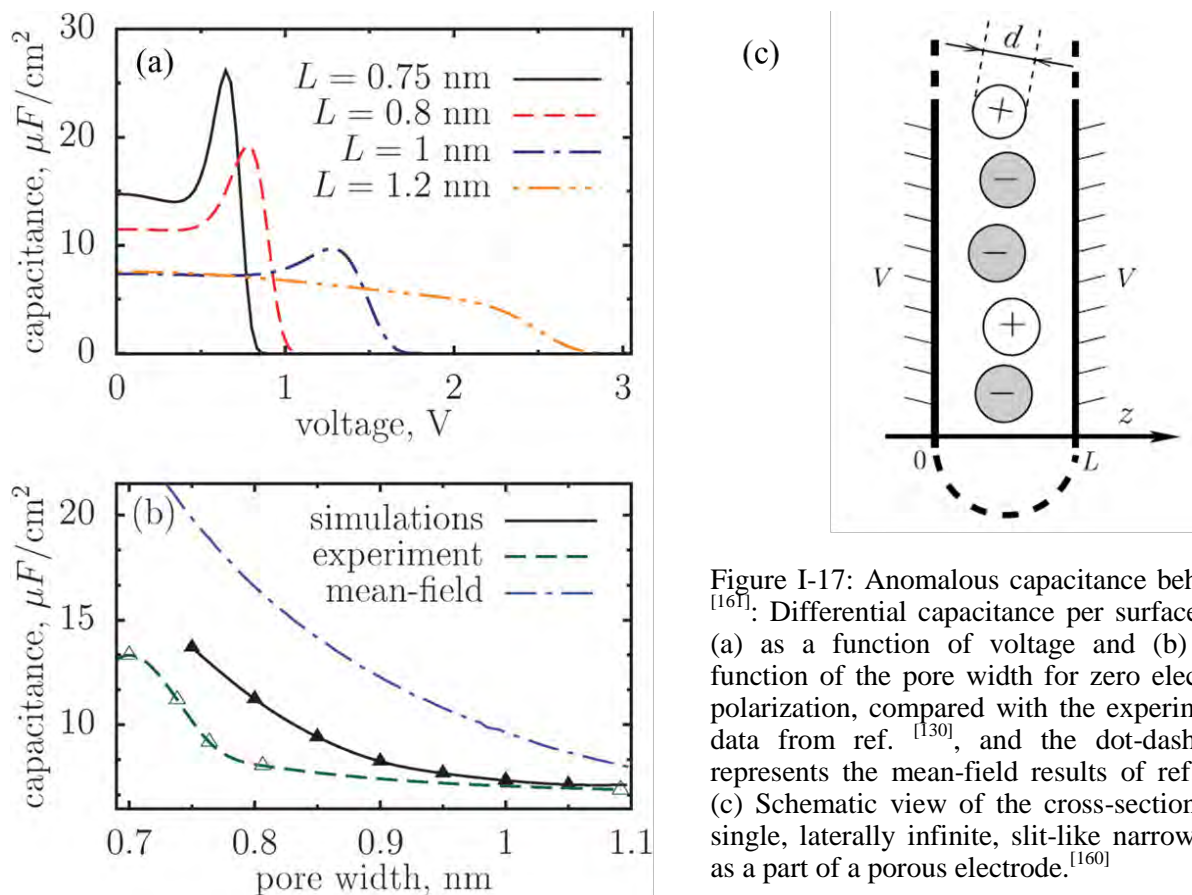


Figure I-17: Anomalous capacitance behavior ^[161]. Differential capacitance per surface area (a) as a function of voltage and (b) as a function of the pore width for zero electrode polarization, compared with the experimental data from ref. ^[130], and the dot-dash line represents the mean-field results of ref. ^[160]; (c) Schematic view of the cross-section of a single, laterally infinite, slit-like narrow pore as a part of a porous electrode. ^[160]

By using CNTs as porous electrodes, which differs from slit-type electrodes by addition of *curvature effect*, Shim et al. ^[151] have shown that capacitance increases when the CNT diameter goes from 2 down to 0.9 nm. Below 0.8 nm, the capacitance drops as the pores become too small to accommodate ions, which corresponds to the “ion sieving” observed experimentally ^[126,134,137]. However, concerns are raised due to a large disparity between the capacitances obtained from simulation ($0.5 - 1.5 \mu\text{F}/\text{cm}^2$) and experimental results ($7 - 13 \mu\text{F}/\text{cm}^2$) ^[137]. The authors attributed this to the lack of polarizability of electrode and electrolyte in the models.

Merlet et al ^[152] conducted an insightful MD simulations using coarse-grained model of BMI-PF₆ with **realistic microporous electrodes** (Figure I-18). The electrode model

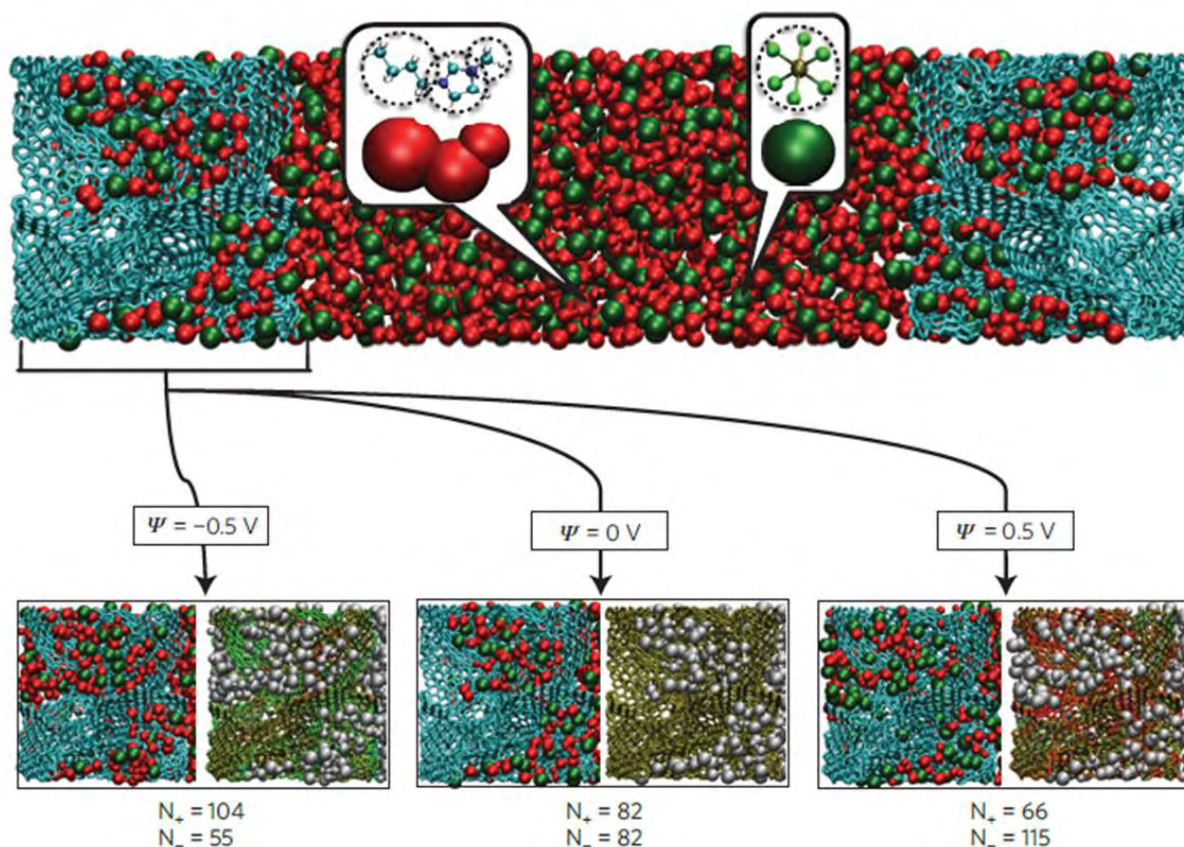


Figure I-18: The EDLC simulation cell. Upper panel: the simulation cell consists of a BMI-PF₆ ionic liquid electrolyte surrounded by two porous electrodes (CDC-1200) held at constant electrical potentials (blue: C atoms, red: the three sites of BMI⁺ and green: PF₆⁻ ions). Lower panel: structure of the electrode for various voltages. For each value, the same snapshot is shown twice: The ionic distribution is shown on the left. The degree of charging of the electrode atoms is shown on the right, where the carbon atoms are colored according to the charge q they carry (green: $q < 0$, red: $q > 0$ and yellow: $q = 0$). ^[152]

was derived from quenched molecular dynamics simulations by Palmer^[170] which was proved to mimic well the morphology of TiC-CDCs. The polarization of the electrode atoms by the electrolyte ions was also taken into account in the simulation. Capacitances of 87 and 125 F/g are obtained for CDC-1200 and CDC-950, respectively (correspond to CDC synthesized at temperature of 1200 and 950 °C). The results are in excellent agreement experimental data^[126,137]. It has been found that the electrodes are wetted by equal number of cations and anions even at null potential, which was also observed previously in other simulations using slit-type micropore electrodes^[169,171], implying that the charging is not a simple potential-driven mechanism. During charging, the total volume occupied by the ions in the electrodes remains almost constant, but ions in the electrode exchange with those in bulk and the ratio of cation to anion in the pores varies. Although the average coordination number drops from seven in the bulk to four inside the electrode, the Coulomb ordering effect that occurs in the bulk is also found to dominate the IL structure in the pores.

Comparison of the double layer structure adsorbed on CDC-1200 porous electrode and planar graphite electrode confirms that *local electrode structure* plays a role on capacitive charge storage. An overscreening was observed on planar electrode whereas in the pores of CDC-1200, there is only one adsorbed layer. Although there are three times more of counter-ions in the closest adsorbed layer on the graphite surface than on the CDC-1200 surface due to the overscreening effect, the second adsorbed layer of co-ions not only counterbalances the charge in the first layer and also drags the first adsorbed layer further toward the bulk hence leaves a larger distance between ions and electrode, resulting in a less efficient charge storage. This may be part of the reasons to explain the better capacitive performance in the confined micropores. Interestingly, the capacitance of CDC-950 exceeds that of CDC-1200 by 43 % even though they have similar PSD and average pore size (0.93nm and 0.95 nm), indicating that the local structures can affect capacitance.

4.1.2 Solvent-containing electrolytes

Acetonitrile-solvated RTILs have been studied in molecular simulations to investigate the influence of solvent and determine which system (between pure and solvated IL electrolytes) is better for EDLC designs. From the simulation performed on a **planar electrode** by Feng et al^[172-174], two competing phenomena have been found when adding acetonitrile molecules in neat IL: the capacitance may decrease as acetonitrile molecules screen the interaction between cation and anion thus reducing the overscreening effect;

whereas capacitance may increase as the dielectric constant of the solvent is higher than RTILs.

Recently, charging process of neat and acetonitrile solvated ionic liquid in a **realistic carbon electrode** has been studied by Merlet et al using MD simulations.^[175] The local structure and solvation environment have been investigated. For solvated ILs at null potential, wetting of the carbon electrode is already achieved by partial desolvation. When applying potential, counter-ions are dragged deeper in more confined sites (Figure I-19), and the solvation number decreases from 9 in the bulk down to 3 (in some cases even 1) depending on the degree of confinement around the ions. The more confined environment results in higher degree of desolvation, which is in good agreement with experimental observation.^[126] On the other hand, co-ions are expelled to less confined sites. These results first confirmed that the origin of the anomalous capacitance increase in microporous carbon is the electronic screening by the pore walls of the repulsive Coulombic interactions between ions of the same charge. It also highlights the role of local carbon structure.

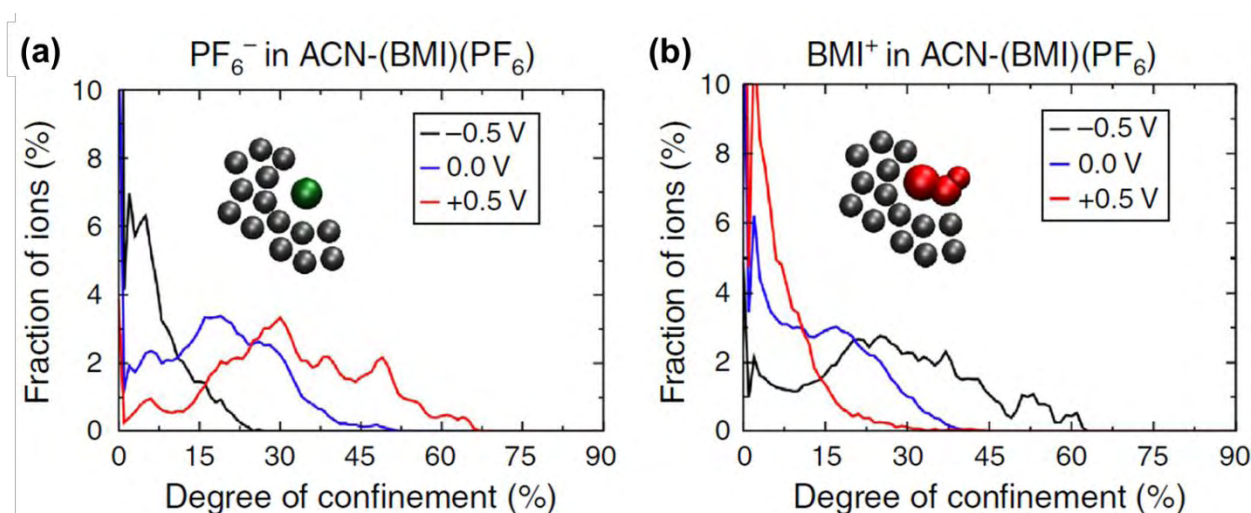


Figure I-19: Distribution of the DoC experienced by each (a) PF₆⁻ and (b) BMI⁺ for three different applied electrode potentials (-0.5, 0 and +0.5 V), in the case of the ACN-containing electrolyte.^[175]

Kaneko's group has carried out reverse MC simulations of the structure of PC in a slit-shaped micropores by using experimental synchrotron XRD data^[176,177]. Results have shown that PC and NEt₄⁺ molecules in the micropores are vertically aligned against the carbon walls leading to a more ordering and denser packing way than in the bulk. The degree of PC ordering is dependent on the pore size.

Dynamics

Due to the high computational cost, relatively few studies have focused on the dynamic effects on EDL charging. By applying a mean-field model to study ionic liquid in a **slit-like** metallic micropore, Kondrat and Kornyshev^[178] have shown that the charging of initially empty pores proceeds in a front-like way, while that of already filled pores is diffusive. The dynamics of charging in **realistic nanoporous carbon electrodes** have been investigated by Péan et al^[179]. Results show that the general tendency observed for the charging process is that the charge penetrates progressively from the electrode-electrolyte boundary toward the interior of the electrode in a *diffusive way*, in qualitative agreement as reported by Kondrat et al^[178]. Ion transport is found to be slower in pores with smaller pore size. The results also highlight that besides the pore size, the *connectivity* between the pores should play an important role in the charging process and influence its heterogeneous characteristic.

4.2 In-situ Experimental Approaches

Standard electrochemical experiments and other ex-situ measurements offer important insights but they do not give a realistic picture of a working device, hence it is important to develop in-situ electrochemical techniques to study the capacitive charge storage, which is also critical for investigating the charging dynamics of the electrode/electrolyte pairs. There are only few in-situ electrochemical techniques which are able to reveal the EDL structure or investigate the charging mechanism and ion transport at near electrode/electrolyte interface. This section will briefly sum up different in-situ techniques that have been involved in the investigation of EDLC charging mechanisms. Most of them are relatively new techniques and are still under development. Different from simulations, it is more difficult to investigate neat ionic liquids than solvent-containing systems due to technical limitations, generally arising from the high viscosity of ionic liquid. Technical improvement is definitely needed for each in-situ methods to reveal the real double layer charging scenarios at molecular/atomic scale.

Nuclear Magnetic Resonance Spectroscopy

Nuclear Magnetic Resonance (NMR) is an appealing technique for revealing the charging mechanism as it is able to probe local interaction between electrode and electrolyte and dynamics at the interfaces. Its *element selective* nature makes it extremely powerful as it can track specific species individually, thus allow separate observation of cations and anions in the system. Recent Ex-situ NMR measurements^[180] reported by Deschamps et al, where NMR spectra were collected on a dismantled supercapacitor after charging in different states, are combined with magic-angle spinning (MAS) techniques^[181] to improve spectral resolution. However, concerns are raised owing to the fast self-discharge in the EDLCs and solvent evaporation.

In-situ NMR technique for EDLC study was recently developed by Grey's group.^[182,183] Wang et al^[183] have reported that by using an optimized cell configuration, BF_4^- anions was successfully tracked during supercapacitors operation in real time by both potentiostatic (Figure I-20a and b) and potentiodynamic measurement (Figure I-20c to f).

In the ^{19}F NMR spectra, the peak at around -156.5 ppm corresponds to anions strongly adsorbed on the carbon surface in the micropores, whereas the intense peak observed between -148 and -150 ppm is assigned to weakly adsorbed anions which situate further from the carbon surface in the larger pores or between carbon particles. The position and the intensity of the peak of strongly adsorbed anions change with the charge stored the YP-50F activated carbon electrode. NMR spectra collected during cyclic voltammetry (Figure I-20c-f) qualitatively agree with those collected during chronoamperometry (Figure I-20a and b). In addition, quantitative information could be extracted from the spectra by deconvolution of the peaks. It has been found that when charging the electrode negatively, anions are expelled from the electrode micropores constantly, whereas during positive charging, anion population in the micropores keeps constant at low polarization and increases at higher polarization (cell potential > 0.75 V). This indicates that at low level of positive polarization, the charge storage is achieved by short-scale rearrangement or co-ion (cation) ejection. These results provide important insights into the charge storage mechanisms. However, cations and acetonitrile solvent molecules are not monitored in these reports. It is thus difficult to confirm that the charge storage is achieved by ion exchange (ion swapping), counter-ion adsorption or co-ion ejection, and also the role of solvent, leaving the charging pictures incomplete.

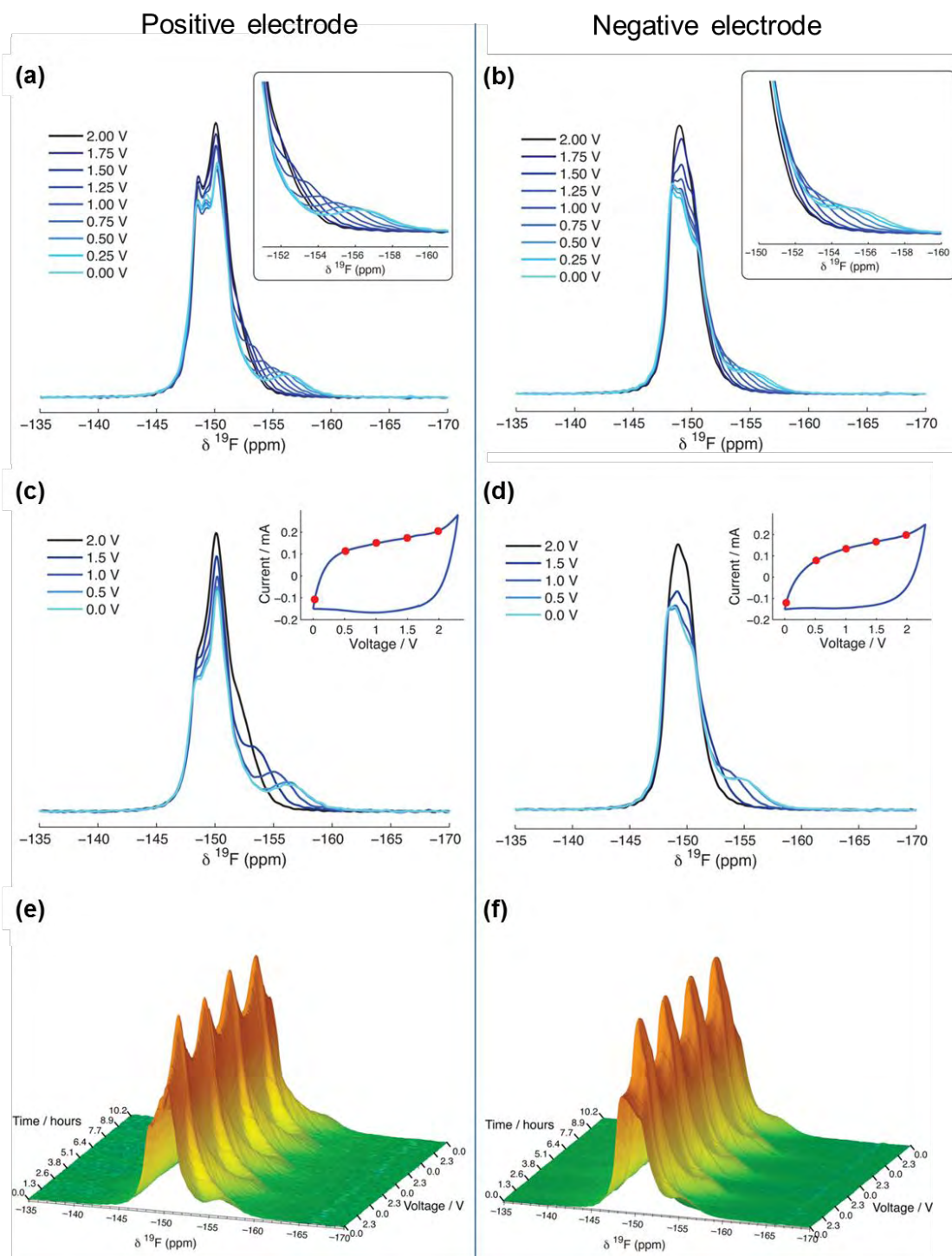


Figure I-20: ^{19}F NMR spectra collected at different potential step between 0 and 2 V (a, b) during cyclic voltammetry (c, d), and successive NMR spectra from four full cyclic voltammetric cycles (e, f). (a, c, e) are NMR spectra collected from positive electrode, and (b, d, f) from negative electrode [183]

Infrared Spectroscopy (IR)

In-situ infrared spectroscopy technique, which is able to couple the chemical changes with electrical inputs/outputs, has been developed very recently by Richey et al.^[184-186] The in-situ IR study conducted with EMI-TFSI electrolyte in CDC microporous carbon^[185] showed that the peak intensity corresponding to both ions residing at the exterior surface (not in the micropores) is found to decrease while polarizing the electrode, indicating that both ions enter the pores when charge is stored in the electrode regardless of charging sign. The authors attribute the observation to that ions are moving as aggregate into the pores owing to the strong cation-anion interaction. In addition, same trend (both ions entering the pores during charging) has been found in the measurements testing CDC electrode in EMI-TFSI solvated in PC, whereas the entrance of PC molecules into the micropores is IL concentration dependent. Further study using the same neat ionic liquid in nanoporous carbon nanofibers (NCNFs) and KOH-activated NCNFs^[186] with improved cell configuration and calibration method enabling quantitative data analysis provides interesting results (Figure I-21).

For the as-prepared NCNFs, anions drag cations together into the pores, resulting in both ion concentrations observed outside of the pores of nanofibers decrease (Figure I-21a-c). Larger amount of anion than cation is adsorbed in the pores when increasing polarization (from Figure I-21a to c). On the other hand, the KOH-activated NCNFs showed a significantly different behavior (Figure I-21d-f). The cations are expelled from the pores while anions are adsorbed in the pores during positively charging of the electrode. The difference between cation and anion affinity to the pores is attributed to the oxygen functionalities introduced during KOH activation process. These results suggest different charge storage mechanisms depending on the electrode pore structures and surface functional groups: NCNFs seemed to be purely adsorptive while KOH-activated NCNFs involve ion exchange. These results highlight the influence of surface chemistry and ionophilicity on charge storage behaviors. However, these results are questionable, especially in the case of NCNFs where both counter-ions and co-ions are adsorbed during charging. If the pores are wetted before charging, the purely adsorptive mechanism will result in > 10 % expansion of the pore volume, which is large and seems unfavorable from both mechanical and energy point of view.

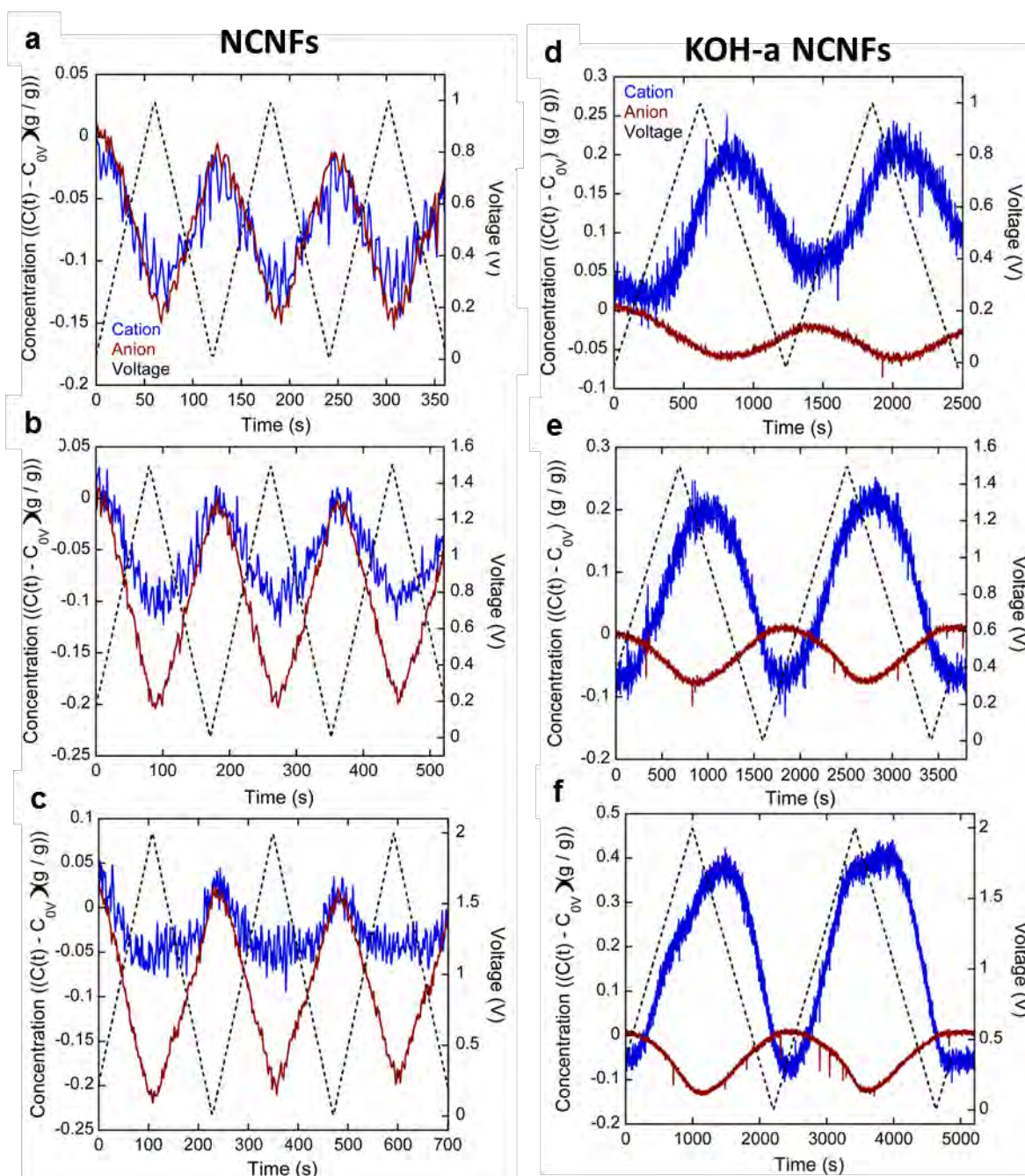


Figure I-21: In operando infrared spectroelectrochemical results: Initialized time-resolved concentration (concentration units g/g corresponds to g EMI⁺-TFSI⁻/g electrode) of the EMI⁺ cation and TFSI⁻ anion in as-prepared NCNFs (a-c) and KOH-activated NCNFs (d-f) during three CV cycles from (a, d) 0 to 1 V, (b, e) 0 to 1.5 V, and (c, f) 0 to 2 V.^[186]

In-situ Dilatometry

In-situ dilatometry technique has been used to investigate the volume change of different supercapacitor electrodes due to ion uptake during charging.^[187-189] Systematic study on the

effect of the pore size and exohedral electrode surface on the expansion behavior was directed by Hantel et al.^[190,191] In-situ dilatometry measurements with CDCs in NEt₄BF₄/AN showed that no matter the pore size (0.58 – 0.85 nm), the electrode expansion is no more than 3 %. The degree of expansion is related to effective ion size. Larger swelling observed in negatively charged electrode originates from the larger effective cation size.^[190]

Electrochemical Quartz Crystal Microbalance (EQCM)

Aside from the aforementioned in-situ techniques, electrochemical quartz crystal microbalance (EQCM), which measures the mass change arising from the compositional changes in the porous electrode during charging/discharge, has recently been involved in studying EDL adsorption/desorption mechanism and solvation situation by Aurbach's group.^[192-194] The heart of this thesis work is devoted into using EQCM to study the charging process and the phenomena involved. The principle of EQCM and state-of-the-art of the current EQCM study on capacitive charging will be described later in detail in chapter IV.

4.3 What do we know today about charging mechanism?

The breakthrough discovery of anomalous capacitance increase in confined micropores^[126] sparks a spate of research into fundamental charge storage mechanisms. To date, we know that micropores are important for capacitive charging while mesopores are also essential for fast ion transport. Ions are able to enter the pores smaller than their bulk solvated ion size by removing or deforming part of their solvation, and this is the origin of the anomalous capacitance increase. Molecular simulations and modellings provide different possible scenarios that could exist at the electrode/electrolyte interface during charging: overscreening^[154], overcrowding^[159], superionic state^[168,169], ion insertion^[152,171], ion swapping^[152,171], structural rearrangement^[164,165,176,195], de-coordination for pure IL^[152], solvent screening and pore wetting before charging^[152,169,171]. From both theoretical and empirical approaches, we know factors that may affect the EDL structures and the capacitance contain: ion structure, ion size asymmetry, cation-anion interaction, ion-solvent interaction^[130], electrode surface roughness^[196], electrode pore structures, and the surface chemistry.^[186]

However, ion transport and dynamics have not been well addressed until now. How the aforementioned factors affect the charging dynamics is critical for a better supercapacitor

design and thus clearly needs research attentions. This is also the reason why in-situ techniques are of great importance and require further developments to unveil the whole charging picture.

5. Objectives of the thesis

5.1 Study of carbon microstructure effect on capacitive storage

As mentioned previously, high performance supercapacitors require both micropores and mesopores, and microstructure play an important role on both energy and power performance. Therefore, the first part of the thesis will be dedicated into studying the effect of the carbon micro-architecture on the supercapacitor performance. Results will be presented in chapter III.

5.2 In-situ EQCM study on ion dynamics and charging mechanisms in confined carbon micropores

Regardless of the great efforts that have been put in the fundamental understanding from both theoretical and empirical sides, there is still a clear lack of knowledge of the charge storage mechanism and the ion transport dynamics in the confined space, thus hampering the performance improvement and the future design of supercapacitors. Therefore, this thesis work is devoted into using in-situ EQCM to study charging dynamics, adsorption mechanism, and also solvent effect in aim to answer the remaining fundamental questions that are unanswered by other in-situ techniques, also to verify the validities of the theories and models proposed by theoreticians. Results will be presented in chapter IV.

Another problem that hinders the analysis of current double layer studies is that it is difficult to compare the results derived from different techniques. Due to the intrinsic limitation of each technique, it turns out that each in-situ technique investigates different electrodes and electrolytes. For example, computational simulations are limited by existing realistic porous electrode (CDCs) or electrolyte (coarse-grained BMI-PF₆, EMI-TFSI) models, otherwise new models need to be created and validated; NMR measurements are limited by NMR active elements such as ¹¹B, ¹³C, ¹⁹F, etc. As highlighted by simulations and some ex-situ empirical studies show that pore structure, cation-anion interaction, and ion-solvent interaction will all contribute to the EDL structure and capacitance, comparing results using different components in different techniques may be somehow misleading. Therefore, in

chapter V, in-situ NMR and in-situ EQCM are coupled to study the same electrode/electrolyte system under the same electrochemical method to verify the results in different techniques. The combination of two in-situ techniques incorporate the advantages of both techniques, and is expected to provide a more complete scenario of the EDL charge storage.

6. Reference

- [1] P. Simon, Y. Gogotsi, *Nat. Mater.* **2008**, 7, 845.
- [2] T. Christen, M. W. Carlen, *J. Power Sources* **2000**, 91, 210.
- [3] B. E. Conway, *Electrochemical Supercapacitors: Scientific Fundamentals and Technological Applications*, Springer, **1999**.
- [4] F. Beguin, E. Frackowiak, Eds. , *Supercapacitors: Materials, Systems and Applications - Max Lu, Francois Beguin, Elzbieta Frackowiak*, Wiley-VCH, **2013**.
- [5] H. von Helmholtz, *Ann Phys Chem* **1853**, 89, 211.
- [6] H. I. Becker, *Low Voltage Electrolytic Capacitor*, **1957**, US2800616 A.
- [7] “Where There Is Charge, There Can Be Sparks!,” can be found under http://www.sciencebuddies.org/science-fair-projects/project_ideas/Elec_p049.shtml, **n.d.**
- [8] R. A. Rightmire, *Electrical Energy Storage Apparatus*, **1966**, US3288641 A.
- [9] D. L. Boos, *Electrolytic Capacitor Having Carbon Paste Electrodes*, **1970**, US3536963 A.
- [10] M. Endo, T. Takeda, Y. J. Kim, K. Koshiba, K. Ishii, *Carbon Sci.* **2001**, 1, 117.
- [11] “Supercapacitor Market by Materials & Products - 2020 | MarketsandMarkets,” can be found under <http://www.marketsandmarkets.com/Market-Reports/supercapacitor-market-37140453.html>
- [12] “Electric Double Layer Capacitors (Gold Capacitors) | Industrial Devices & Solutions | Panasonic,” can be found under <http://industrial.panasonic.com/ww/products/capacitors/edlc>
- [13] A. G. Pandolfo, A. F. Hollenkamp, *J. Power Sources* **2006**, 157, 11.
- [14] E. Frackowiak, *Phys. Chem. Chem. Phys.* **2007**, 9, 1774.
- [15] G. A. Snook, P. Kao, A. S. Best, *J. Power Sources* **2011**, 196, 1.
- [16] D. Cericola, R. Kötz, *Electrochimica Acta* **2012**, 72, 1.
- [17] G. Wang, L. Zhang, J. Zhang, *Chem Soc Rev* **2012**, 41, 797.
- [18] V. Augustyn, P. Simon, B. Dunn, *Energy Environ. Sci.* **2014**, 7, 1597.
- [19] K. Wang, H. Wu, Y. Meng, Z. Wei, *Small* **2014**, 10, 14.
- [20] H. von Helmholtz, *Ann. Phys.* **1879**, 243, 337.
- [21] L. G. Gouy, *Compt Rend* **1910**, 149, 654.

- [22] D. L. Chapman, *Philos. Mag. Ser. 6* **1913**, 25, 475.
- [23] O. Stern, *Z. Elektrochem. Lnd Angew. Phys. Chem.* **1924**, 30, 508.
- [24] J. R. Miller, P. Simon, *Science* **2008**, 321, 651.
- [25] “Maxwell Technologies Power Grid Solutions,” can be found under <http://www.maxwell.com/solutions/power-grid/default.aspx>
- [26] “Maxwell Technologies Ultracapacitors Deployed in Ireland Microgrid Energy Storage System,” can be found under <http://www.prnewswire.com/news-releases/maxwell-technologies-ultracapacitors-deployed-in-ireland-microgrid-energy-storage-system-300037291.html>
- [27] “Opening doors to space,” can be found under http://www.esa.int/Our_Activities/Telecommunications_Integrated_Applications/Opening_doors_to_space
- [28] “Transportation Solutions,” can be found under <http://www.maxwell.com/solutions/transportation>
- [29] “Nice: a fully electric bus with unlimited range,” can be found under <http://www.investincotedazur.com/en/info/news/nice-a-fully-electric-bus-with-unlimited-range/>
- [30] X. Navarro, “Paris tests a new hybrid bus that uses ultracapacitors,” can be found under <http://www.autoblog.com/2009/04/15/paris-tests-a-new-hybrid-bus-that-uses-ultracapacitors/>, **n.d.**
- [31] T. Hamilton, “Next Stop: Ultracapacitor Buses,” can be found under <http://www.technologyreview.com/news/415773/next-stop-ultracapacitor-buses/>, **2009**.
- [32] “Maxwell Technologies Wins ESNA Innovation Award for Philadelphia Electric Rail Project,” can be found under <http://www.prnewswire.com/news-releases/maxwell-technologies-wins-esna-innovation-award-for-philadelphia-electric-rail-project-277873761.html>
- [33] “Toyota details its triple-motor, super capacitor-powered Yaris Hybrid-R - Images,” can be found under <http://www.gizmag.com/toyota-details-yaris-hybrid-r/28827/pictures>,
- [34] “Guangzhou supercapacitor tram unveiled,” can be found under <http://www.railwaygazette.com/news/urban/single-view/view/guangzhou-supercapacitor-tram-unveiled.html>
- [35] O. Barbieri, M. Hahn, A. Herzog, R. Kötz, *Carbon* **2005**, 43, 1303.
- [36] D. Lozano-Castelló, D. Cazorla-Amorós, A. Linares-Solano, S. Shiraishi, H. Kurihara, A. Oya, *Carbon* **2003**, 41, 1765.
- [37] E. Raymundo-Piñero, K. Kierzek, J. Machnikowski, F. Béguin, *Carbon* **2006**, 44, 2498.
- [38] B. Xu, F. Wu, Y. Su, G. Cao, S. Chen, Z. Zhou, Y. Yang, *Electrochimica Acta* **2008**, 53, 7730.
- [39] Y. Zhai, Y. Dou, D. Zhao, P. F. Fulvio, R. T. Mayes, S. Dai, *Adv. Mater.* **2011**, 23, 4828.
- [40] M. Sevilla, R. Mokaya, *Energy Environ. Sci.* **2014**, 7, 1250.
- [41] R. Dash, J. Chmiola, G. Yushin, Y. Gogotsi, G. Laudisio, J. Singer, J. Fischer, S. Kucheyev, *Carbon* **2006**, 44, 2489.
- [42] V. Presser, M. Heon, Y. Gogotsi, *Adv. Funct. Mater.* **2011**, 21, 810.

- [43] C. R. Pérez, S.-H. Yeon, J. Ségalini, V. Presser, P.-L. Taberna, P. Simon, Y. Gogotsi, *Adv. Funct. Mater.* **2013**, *23*, 1081.
- [44] H. Wu, X. Wang, L. Jiang, C. Wu, Q. Zhao, X. Liu, B. Hu, L. Yi, *J. Power Sources* **2013**, *226*, 202.
- [45] E. Tee, I. Tallo, H. Kurig, T. Thomberg, A. Jänes, E. Lust, *Electrochimica Acta* **2015**, *161*, 364.
- [46] A. B. Fuertes, G. Lota, T. A. Centeno, E. Frackowiak, *Electrochimica Acta* **2005**, *50*, 2799.
- [47] A. Kajdos, A. Kvit, F. Jones, J. Jagiello, G. Yushin, *J. Am. Chem. Soc.* **2010**, *132*, 3252.
- [48] Y. Korenblit, A. Kajdos, W. C. West, M. C. Smart, E. J. Brandon, A. Kvit, J. Jagiello, G. Yushin, *Adv. Funct. Mater.* **2012**, *22*, 1655.
- [49] C. Portet, G. Yushin, Y. Gogotsi, *Carbon* **2007**, *45*, 2511.
- [50] Y. Gao, Y. S. Zhou, M. Qian, X. N. He, J. Redepenning, P. Goodman, H. M. Li, L. Jiang, Y. F. Lu, *Carbon* **2013**, *51*, 52.
- [51] J. K. McDonough, Y. Gogotsi, *Electrochem Soc Interface* **2013**, *22*, 61.
- [52] D. N. Futaba, K. Hata, T. Yamada, T. Hiraoka, Y. Hayamizu, Y. Kakudate, O. Tanaike, H. Hatori, M. Yumura, S. Iijima, *Nat. Mater.* **2006**, *5*, 987.
- [53] S. Dörfler, I. Felhösi, T. Marek, S. Thieme, H. Althues, L. Nyikos, S. Kaskel, *J. Power Sources* **2013**, *227*, 218.
- [54] M. Kaempgen, C. K. Chan, J. Ma, Y. Cui, G. Gruner, *Nano Lett.* **2009**, *9*, 1872.
- [55] M. Noked, S. Okashy, T. Zimrin, D. Aurbach, *Carbon* **2013**, *58*, 134.
- [56] M. F. De Volder, S. H. Tawfick, R. H. Baughman, A. J. Hart, *Science* **2013**, *339*, 535.
- [57] C.-M. Yang, Y.-J. Kim, M. Endo, H. Kanoh, M. Yudasaka, S. Iijima, K. Kaneko, *J. Am. Chem. Soc.* **2007**, *129*, 20.
- [58] H. J. Jung, Y.-J. Kim, J. H. Han, M. Yudasaka, S. Iijima, H. Kanoh, Y. A. Kim, K. Kaneko, C.-M. Yang, *J. Phys. Chem. C* **2013**, *117*, 25877.
- [59] K. Hung, C. Masarapu, T. Ko, B. Wei, *J. Power Sources* **2009**, *193*, 944.
- [60] C.-C. Hu, C.-C. Wang, *J. Power Sources* **2004**, *125*, 299.
- [61] H. Y. Jin, Z. H. Peng, W. M. Tang, H. L. W. Chan, *RSC Adv.* **2014**, *4*, 33022.
- [62] X. Li, X. Zang, Z. Li, X. Li, P. Li, P. Sun, X. Lee, R. Zhang, Z. Huang, K. Wang, D. Wu, F. Kang, H. Zhu, *Adv. Funct. Mater.* **2013**, n/a.
- [63] S. Shiraiishi, H. Kurihara, L. Shi, T. Nakayama, A. Oya, *J. Electrochem. Soc.* **2002**, *149*, A855.
- [64] V. T. Le, H. Kim, A. Ghosh, J. Kim, J. Chang, Q. A. Vu, D. T. Pham, J.-H. Lee, S.-W. Kim, Y. H. Lee, *ACS Nano* **2013**, *7*, 5940.
- [65] S. Pan, H. Lin, J. Deng, P. Chen, X. Chen, Z. Yang, H. Peng, *Adv. Energy Mater.* **2015**, *5*, n/a.
- [66] Y. Zhu, S. Murali, M. D. Stoller, K. J. Ganesh, W. Cai, P. J. Ferreira, A. Pirkle, R. M. Wallace, K. A. Cychoz, M. Thommes, D. Su, E. A. Stach, R. S. Ruoff, *Science* **2011**, *332*, 1537.

- [67] M. F. El-Kady, V. Strong, S. Dubin, R. B. Kaner, *Science* **2012**, 335, 1326.
- [68] P. Tamilarasan, S. Ramaprabhu, *J. Nanosci. Nanotechnol.* **2015**, 15, 1154.
- [69] W. Li, H.-Y. Lü, X.-L. Wu, H. Guan, Y.-Y. Wang, F. Wan, G. Wang, L.-Q. Yan, H.-M. Xie, R.-S. Wang, *RSC Adv* **2015**, 5, 12583.
- [70] F. Bonaccorso, L. Colombo, G. Yu, M. Stoller, V. Tozzini, A. C. Ferrari, R. S. Ruoff, V. Pellegrini, *Science* **2015**, 347, 1246501.
- [71] P. Simon, Y. Gogotsi, *Acc. Chem. Res.* **2013**, 46, 1094.
- [72] Y. Gao, Y. S. Zhou, J. B. Park, H. Wang, X. N. He, H. F. Luo, L. Jiang, Y. F. Lu, *Nanotechnology* **2011**, 22, 165604.
- [73] D. Pech, M. Brunet, H. Durou, P. Huang, V. Mochalin, Y. Gogotsi, P.-L. Taberna, P. Simon, *Nat. Nanotechnol.* **2010**, 5, 651.
- [74] I. Alexandrou, H. Wang, N. Sano, G. A. J. Amaratunga, *J. Chem. Phys.* **2004**, 120, 1055.
- [75] C. Emmenegger, P. Mauron, P. Sudan, P. Wenger, V. Hermann, R. Gallay, A. Züttel, *J. Power Sources* **2003**, 124, 321.
- [76] H. Zhang, G. Cao, Y. Yang, Z. Gu, *J. Electrochem. Soc.* **2008**, 155, K19.
- [77] C.-C. Hu, K.-H. Chang, M.-C. Lin, Y.-T. Wu, *Nano Lett.* **2006**, 6, 2690.
- [78] L. Hu, M. Pasta, F. L. Mantia, L. Cui, S. Jeong, H. D. Deshazer, J. W. Choi, S. M. Han, Y. Cui, *Nano Lett.* **2010**, 10, 708.
- [79] C. Choi, S. H. Kim, H. J. Sim, J. A. Lee, A. Y. Choi, Y. T. Kim, X. Lepró, G. M. Spinks, R. H. Baughman, S. J. Kim, *Sci. Rep.* **2015**, 5, 9387.
- [80] K. S. Novoselov, A. K. Geim, S. V. Morozov, D. Jiang, Y. Zhang, S. V. Dubonos, I. V. Grigorieva, A. A. Firsov, *Science* **2004**, 306, 666.
- [81] L. L. Zhang, R. Zhou, X. S. Zhao, *J. Mater. Chem.* **2010**, 20, 5983.
- [82] Y. Huang, J. Liang, Y. Chen, *Small* **2012**, 8, 1805.
- [83] Y. Zhu, S. Murali, M. D. Stoller, A. Velamakanni, R. D. Piner, R. S. Ruoff, *Carbon* **2010**, 48, 2118.
- [84] C. Liu, Z. Yu, D. Neff, A. Zhamu, B. Z. Jang, *Nano Lett.* **2010**, 10, 4863.
- [85] “Graphene - What Is It?,” can be found under <http://www.graphenea.com/pages/graphene>, **n.d.**
- [86] J. J. Wang, M. Y. Zhu, R. A. Outlaw, X. Zhao, D. M. Manos, B. C. Holloway, V. P. Mammana, *Appl. Phys. Lett.* **2004**, 85, 1265.
- [87] M. Zhu, J. Wang, B. C. Holloway, R. A. Outlaw, X. Zhao, K. Hou, V. Shutthanandan, D. M. Manos, *Carbon* **2007**, 45, 2229.
- [88] J. J. Yoo, K. Balakrishnan, J. Huang, V. Meunier, B. G. Sumpter, A. Srivastava, M. Conway, A. L. Mohana Reddy, J. Yu, R. Vajtai, P. M. Ajayan, *Nano Lett.* **2011**, 11, 1423.
- [89] M. Beidaghi, Y. Gogotsi, *Energy Environ. Sci.* **2014**, 7, 867.
- [90] S. J. An, Y. Zhu, S. H. Lee, M. D. Stoller, T. Emilsson, S. Park, A. Velamakanni, J. An, R. S. Ruoff, *J. Phys. Chem. Lett.* **2010**, 1, 1259.
- [91] L. T. Le, M. H. Ervin, H. Qiu, B. E. Fuchs, W. Y. Lee, *Electrochem. Commun.* **2011**, 13,

355.

- [92] Y. Korenblit, M. Rose, E. Kockrick, L. Borchardt, A. Kvit, S. Kaskel, G. Yushin, *ACS Nano* **2010**, *4*, 1337.
- [93] D. A. Ersoy, M. J. McNallan, Y. Gogotsi, *Mater. Res. Innov.* **2001**, *5*, 55.
- [94] L. Chen, G. Behlau, Y. Gogotsi, M. J. McNallan, in *27th Annu. Cocoa Beach Conf. Adv. Ceram. Compos. Ceram. Eng. Sci. Proc.* (Eds.: W.M. Kriven, H.-T. Lin), John Wiley & Sons, Inc., **2003**, pp. 57–62.
- [95] W. Gu, G. Yushin, *Wiley Interdiscip. Rev. Energy Environ.* **2014**, *3*, 424.
- [96] C. Matei Ghimbeu, L. Vidal, L. Delmotte, J.-M. Le Meins, C. Vix-Guterl, *Green Chem.* **2014**, *16*, 3079.
- [97] A. Vu, X. Li, J. Phillips, A. Han, W. H. Smyrl, P. Bühlmann, A. Stein, *Chem. Mater.* **2013**, *25*, 4137.
- [98] M. Karthik, E. Redondo, E. Goikolea, V. Roddatis, S. Doppiu, R. Mysyk, *J. Phys. Chem. C* **2014**, *118*, 27715.
- [99] X. S. Zhao, F. Su, Q. Yan, W. Guo, X. Y. Bao, L. Lv, Z. Zhou, *J. Mater. Chem.* **2006**, *16*, 637.
- [100] L. L. Zhang, X. S. Zhao, *Chem. Soc. Rev.* **2009**, *38*, 2520.
- [101] F. Rodríguez-Reinoso, M. Molina-Sabio, M. T. González, *Carbon* **1995**, *33*, 15.
- [102] G. San Miguel, G. D. Fowler, C. J. Sollars, *Carbon* **2003**, *41*, 1009.
- [103] F.-C. Wu, R.-L. Tseng, C.-C. Hu, C.-C. Wang, *J. Power Sources* **2005**, *144*, 302.
- [104] M. Ue, K. Ida, S. Mori, *J. Electrochem. Soc.* **1994**, *141*, 2989.
- [105] T. Welton, *Chem. Rev.* **1999**, *99*, 2071.
- [106] M. J. Earle, K. R. Seddon, *Pure Appl. Chem.* **2000**, *72*, 1391.
- [107] M. Armand, F. Endres, D. R. MacFarlane, H. Ohno, B. Scrosati, *Nat. Mater.* **2009**, *8*, 621.
- [108] D. R. MacFarlane, N. Tachikawa, M. Forsyth, J. M. Pringle, P. C. Howlett, G. D. Elliott, J. H. Davis, M. Watanabe, P. Simon, C. A. Angell, *Energy Environ. Sci.* **2013**.
- [109] R. Lin, P.-L. Taberna, S. Fantini, V. Presser, C. R. Pérez, F. Malbosc, N. L. Rupesinghe, K. B. K. Teo, Y. Gogotsi, P. Simon, *J. Phys. Chem. Lett.* **2011**, *2*, 2396.
- [110] M. Galiński, A. Lewandowski, I. Stepniak, *Electrochimica Acta* **2006**, *51*, 5567.
- [111] J. Gamby, P. L. Taberna, P. Simon, J. F. Fauvarque, M. Chesneau, *J. Power Sources* **2001**, *101*, 109.
- [112] D. Qu, *J. Power Sources* **2002**, *109*, 403.
- [113] Y. . Kim, Y. Horie, S. Ozaki, Y. Matsuzawa, H. Suezaki, C. Kim, N. Miyashita, M. Endo, *Carbon* **2004**, *42*, 1491.
- [114] Y. Marcus, *Ion Solvation*, Wiley, **1985**.
- [115] P. Simon, Y. Gogotsi, *Philos. Trans. R. Soc. Math. Phys. Eng. Sci.* **2010**, *368*, 3457.
- [116] J. A. Fernández, T. Morishita, M. Toyoda, M. Inagaki, F. Stoeckli, T. A. Centeno, *J. Power Sources* **2008**, *175*, 675.

- [117] S. Álvarez, M. C. Blanco-López, A. J. Miranda-Ordieres, A. B. Fuertes, T. A. Centeno, *Carbon* **2005**, *43*, 866.
- [118] H. Zhou, S. Zhu, M. Hibino, I. Honma, *J. Power Sources* **2003**, *122*, 219.
- [119] M. Sevilla, S. Álvarez, T. A. Centeno, A. B. Fuertes, F. Stoeckli, *Electrochimica Acta* **2007**, *52*, 3207.
- [120] W. Li, D. Chen, Z. Li, Y. Shi, Y. Wan, G. Wang, Z. Jiang, D. Zhao, *Carbon* **2007**, *45*, 1757.
- [121] C. Vix-Guterl, E. Frackowiak, K. Jurewicz, M. Friebe, J. Parmentier, F. Béguin, *Carbon* **2005**, *43*, 1293.
- [122] L. Eliad, G. Salitra, A. Soffer, D. Aurbach, *Langmuir* **2005**, *21*, 3198.
- [123] L. Eliad, E. Pollak, N. Levy, G. Salitra, A. Soffer, D. Aurbach, *Appl. Phys. A* **2006**, *82*, 607.
- [124] Y. Gogotsi, R. K. Dash, G. Yushin, T. Yildirim, G. Laudisio, J. E. Fischer, *J. Am. Chem. Soc.* **2005**, *127*, 16006.
- [125] J. Chmiola, C. Largeot, P.-L. Taberna, P. Simon, Y. Gogotsi, *Angew. Chem. Int. Ed.* **2008**, *47*, 3392.
- [126] J. Chmiola, G. Yushin, Y. Gogotsi, C. Portet, P. Simon, P. L. Taberna, *Science* **2006**, *313*, 1760.
- [127] J. Leis, M. Arulepp, A. Kuura, M. Lätt, E. Lust, *Carbon* **2006**, *44*, 2122.
- [128] Y.-J. Kim, Y. Masuzawa, S. Ozaki, M. Endo, M. S. Dresselhaus, *J. Electrochem. Soc.* **2004**, *151*, E199.
- [129] C. Cachet-Vivier, V. Vivier, C. S. Cha, J.-Y. Nedelec, L. T. Yu, *Electrochimica Acta* **2001**, *47*, 181.
- [130] R. Lin, P. L. Taberna, J. Chmiola, D. Guay, Y. Gogotsi, P. Simon, *J. Electrochem. Soc.* **2009**, *156*, A7.
- [131] J. Segalini, B. Daffos, P. L. Taberna, Y. Gogotsi, P. Simon, *Electrochimica Acta* **2010**, *55*, 7489.
- [132] R. Lin, P. Huang, J. Ségalini, C. Largeot, P. L. Taberna, J. Chmiola, Y. Gogotsi, P. Simon, *Electrochimica Acta* **2009**, *54*, 7025.
- [133] J. Segalini, E. Iwama, P.-L. Taberna, Y. Gogotsi, P. Simon, *Electrochem. Commun.* **2012**, *15*, 63.
- [134] G. Salitra, A. Soffer, L. Eliad, Y. Cohen, D. Aurbach, *J. Electrochem. Soc.* **2000**, *147*, 2486.
- [135] R. Mysyk, E. Raymundo-Piñero, F. Béguin, *Electrochem. Commun.* **2009**, *11*, 554.
- [136] G. Sun, W. Song, X. Liu, D. Long, W. Qiao, L. Ling, *Electrochimica Acta* **2011**, *56*, 9248.
- [137] C. Largeot, C. Portet, J. Chmiola, P.-L. Taberna, Y. Gogotsi, P. Simon, *J. Am. Chem. Soc.* **2008**, *130*, 2730.
- [138] J. Huang, B. G. Sumpter, V. Meunier, *Chem. - Eur. J.* **2008**, *14*, 6614.
- [139] D.-W. Wang, F. Li, M. Liu, G. Q. Lu, H.-M. Cheng, *Angew. Chem. Int. Ed.* **2008**, *47*, 373.

- [140] D.-D. Zhou, Y.-J. Du, Y.-F. Song, Y.-G. Wang, C.-X. Wang, Y.-Y. Xia, *J Mater Chem A* **2013**, *1*, 1192.
- [141] A. Stein, S. G. Rudisill, N. D. Petkovich, *Chem. Mater.* **2014**, *26*, 259.
- [142] Q. Wang, J. Yan, Y. Wang, T. Wei, M. Zhang, X. Jing, Z. Fan, *Carbon* **2014**, *67*, 119.
- [143] Y. Zhang, M. Ma, J. Yang, W. Huang, X. Dong, *RSC Adv.* **2014**, *4*, 8466.
- [144] J. Dzubiella, J.-P. Hansen, *J. Chem. Phys.* **2005**, *122*, 234706.
- [145] D. Boda, W. R. Fawcett, D. Henderson, S. Sokolowski, *J. Chem. Phys.* **2002**, *116*, 7170.
- [146] C. N. Patra, S. K. Ghosh, *J. Chem. Phys.* **2002**, *117*, 8938.
- [147] C. N. Patra, *J. Phys. Chem. B* **2010**, *114*, 10550.
- [148] Y. Wang, W. Jiang, T. Yan, G. A. Voth, *Acc. Chem. Res.* **2007**, *40*, 1193.
- [149] C. Merlet, M. Salanne, B. Rotenberg, *J. Phys. Chem. C* **2012**, *116*, 7687.
- [150] L. Yang, B. H. Fishbine, A. Migliori, L. R. Pratt, *J. Am. Chem. Soc.* **2009**, *131*, 12373.
- [151] Y. Shim, H. J. Kim, *ACS Nano* **2010**, *4*, 2345.
- [152] C. Merlet, B. Rotenberg, P. A. Madden, P.-L. Taberna, P. Simon, Y. Gogotsi, M. Salanne, *Nat. Mater.* **2012**, *11*, 306.
- [153] R. Burt, G. Birkett, X. S. Zhao, *Phys. Chem. Chem. Phys.* **2014**, *16*, 6519.
- [154] A. A. Kornyshev, *J. Phys. Chem. B* **2007**, *111*, 5545.
- [155] Y. Levin, *Rep. Prog. Phys.* **2002**, *65*, 1577.
- [156] M. Mezger, H. Schröder, H. Reichert, S. Schramm, J. S. Okasinski, S. Schöder, V. Honkimäki, M. Deutsch, B. M. Ocko, J. Ralston, M. Rohwerder, M. Stratmann, H. Dosch, *Science* **2008**, *322*, 424.
- [157] B. Skinner, M. S. Loth, B. I. Shklovskii, *Phys. Rev. Lett.* **2010**, *104*, 128302.
- [158] M. V. Fedorov, A. A. Kornyshev, *Electrochimica Acta* **2008**, *53*, 6835.
- [159] M. Z. Bazant, B. D. Storey, A. A. Kornyshev, *Phys. Rev. Lett.* **2011**, *106*.
- [160] S. K. Reed, O. J. Lanning, P. A. Madden, *J. Chem. Phys.* **2007**, *126*, 084704.
- [161] M. V. Fedorov, A. A. Kornyshev, *J. Phys. Chem. B* **2008**, *112*, 11868.
- [162] N. Georgi, A. A. Kornyshev, M. V. Fedorov, *J. Electroanal. Chem.* **2010**, *649*, 261.
- [163] M. V. Fedorov, N. Georgi, A. A. Kornyshev, *Electrochem. Commun.* **2010**, *12*, 296.
- [164] S. A. Kislenco, I. S. Samoylov, R. H. Amirov, *Phys. Chem. Chem. Phys.* **2009**, *11*, 5584.
- [165] S. Wang, S. Li, Z. Cao, T. Yan, *J. Phys. Chem. C* **2010**, *114*, 990.
- [166] S. Rivera-Rubero, S. Baldelli, *J. Phys. Chem. B* **2004**, *108*, 15133.
- [167] C. Aliaga, S. Baldelli, *J. Phys. Chem. B* **2006**, *110*, 18481.
- [168] S. Kondrat, A. Kornyshev, *J. Phys. Condens. Matter* **2011**, *23*, 022201.
- [169] S. Kondrat, N. Georgi, M. V. Fedorov, A. A. Kornyshev, *Phys. Chem. Chem. Phys.* **2011**, *13*, 11359.

- [170] J. C. Palmer, A. Llobet, S.-H. Yeon, J. E. Fischer, Y. Shi, Y. Gogotsi, K. E. Gubbins, *Carbon* **2010**, *48*, 1116.
- [171] P. Wu, J. Huang, V. Meunier, B. G. Sumpter, R. Qiao, *J. Phys. Chem. Lett.* **2012**, *3*, 1732.
- [172] G. Feng, J. Huang, B. G. Sumpter, V. Meunier, R. Qiao, *Phys. Chem. Chem. Phys.* **2010**, *12*, 5468.
- [173] G. Feng, J. Huang, B. G. Sumpter, V. Meunier, R. Qiao, *Phys. Chem. Chem. Phys.* **2011**, *13*, 14723.
- [174] G. Feng, R. Qiao, J. Huang, S. Dai, B. G. Sumpter, V. Meunier, *Phys Chem Chem Phys* **2011**, *13*, 1152.
- [175] C. Merlet, C. Péan, B. Rotenberg, P. A. Madden, B. Daffos, P.-L. Taberna, P. Simon, M. Salanne, *Nat. Commun.* **2013**, *4*, DOI 10.1038/ncomms3701.
- [176] A. Tanaka, T. Iiyama, T. Ohba, S. Ozeki, K. Urita, T. Fujimori, H. Kanoh, K. Kaneko, *J. Am. Chem. Soc.* **2010**, *132*, 2112.
- [177] M. Fukano, T. Fujimori, J. Ségalini, E. Iwama, P.-L. Taberna, T. Iiyama, T. Ohba, H. Kanoh, Y. Gogotsi, P. Simon, K. Kaneko, *J. Phys. Chem. C* **2013**, *117*, 5752.
- [178] S. Kondrat, A. Kornyshev, *J. Phys. Chem. C* **2013**, *117*, 12399.
- [179] C. Péan, C. Merlet, B. Rotenberg, P. A. Madden, P.-L. Taberna, B. Daffos, M. Salanne, P. Simon, *ACS Nano* **2014**, *8*, 1576.
- [180] M. Deschamps, E. Gilbert, P. Azais, E. Raymundo-Piñero, M. R. Ammar, P. Simon, D. Massiot, F. Béguin, *Nat. Mater.* **2013**, *12*, 351.
- [181] J. W. Hennel, J. Klinowski, in *New Tech. Solid-State NMR* (Ed.: J. Klinowski), Springer Berlin Heidelberg, **2005**, pp. 1–14.
- [182] H. Wang, T. K.-J. Köster, N. M. Trease, J. Ségalini, P.-L. Taberna, P. Simon, Y. Gogotsi, C. P. Grey, *J. Am. Chem. Soc.* **2011**, *133*, 19270.
- [183] H. Wang, A. C. Forse, J. M. Griffin, N. M. Trease, L. Trognko, P.-L. Taberna, P. Simon, C. P. Grey, *J. Am. Chem. Soc.* **2013**, *135*, 18968.
- [184] F. W. Richey, Y. A. Elabd, *J. Phys. Chem. Lett.* **2012**, *3*, 3297.
- [185] F. W. Richey, B. Dyatkin, Y. Gogotsi, Y. A. Elabd, *J. Am. Chem. Soc.* **2013**, *135*, 12818.
- [186] F. W. Richey, C. Tran, V. Kalra, Y. A. Elabd, *J. Phys. Chem. C* **2014**, *118*, 21846.
- [187] M. Hahn, O. Barbieri, F. P. Campana, R. Kötz, R. Gallay, *Appl. Phys. A* **2006**, *82*, 633.
- [188] M. Hahn, O. Barbieri, R. Gallay, R. Kötz, *Carbon* **2006**, *44*, 2523.
- [189] B. H. Ka, S. M. Oh, *J. Electrochem. Soc.* **2008**, *155*, A685.
- [190] M. M. Hantel, V. Presser, R. Kötz, Y. Gogotsi, *Electrochem. Commun.* **2011**, *13*, 1221.
- [191] M. M. Hantel, R. Nesper, A. Wokaun, R. Kötz, *Electrochimica Acta* **2014**, *134*, 459.
- [192] M. D. Levi, G. Salitra, N. Levy, D. Aurbach, J. Maier, *Nat. Mater.* **2009**, *8*, 872.
- [193] M. D. Levi, N. Levy, S. Sigalov, G. Salitra, D. Aurbach, J. Maier, *J. Am. Chem. Soc.* **2010**, *132*, 13220.
- [194] S. Sigalov, M. D. Levi, G. Salitra, D. Aurbach, J. Maier, *Electrochem. Commun.* **2010**, *12*, 1718.

- [195] C. Pinilla, M. G. Del Pópolo, J. Kohanoff, R. M. Lynden-Bell, *J. Phys. Chem. B* **2007**, *111*, 4877.
- [196] L. Xing, J. Vatamanu, G. D. Smith, D. Bedrov, *J. Phys. Chem. Lett.* **2012**, *3*, 1124.

***Chapter II: Materials Studied and
Experimental set-ups***

1. Introduction

This chapter is aim to describe the different commercially-available active materials and electrolytes tested in the thesis work, and different electrochemical methods and cell configurations used to characterize the materials of supercapacitors. The experimentals of the materials synthesized in the lab will be described later in the result chapters, and EQCM principle and set-up will introduced in chapter IV.

2. Commercial Activated Carbons

Two commercial activated carbons were used in this work: YP-17 and YP-50F. Both are derived from coconut shell and bought from Kuraray Chemical Co., Japan. Their characteristics will be discussed in this section. Other carbons used in this work which are synthesized in the labs will be discussed individually in each section later. All the porosity characteristics of the as-received commercial carbons are characterized from Ar sorption isotherm measured at 77 K with Micromeritics ASAP 2020 porosimetry analyser, and the pore size distributions (PSD) were calculated from the isotherm by using Quenched Solid Density Functional Theory (QSDFT) method ^[1] assuming a slit pore geometry.

YP-50F

The porosity characteristics of the YP-50F carbon were obtained from Ar sorption isotherm measured at 77 K (Figure II-1a), and the specific surface area estimated by using Brunauer-Emmett-Teller (BET) method ^{[2][3]} is 1732 m²/g. The pore size distributions (PSD) calculated from the isotherm by using QSDFT method is shown in Figure II-1b. The calculated average pore size is 0.9 nm, and the total pore volume is 0.75 cm³/g with 92 % of the pores smaller than 2 nm (micropores). Other characteristics provided by the supplier are also shown in Table II-1 ^[4].

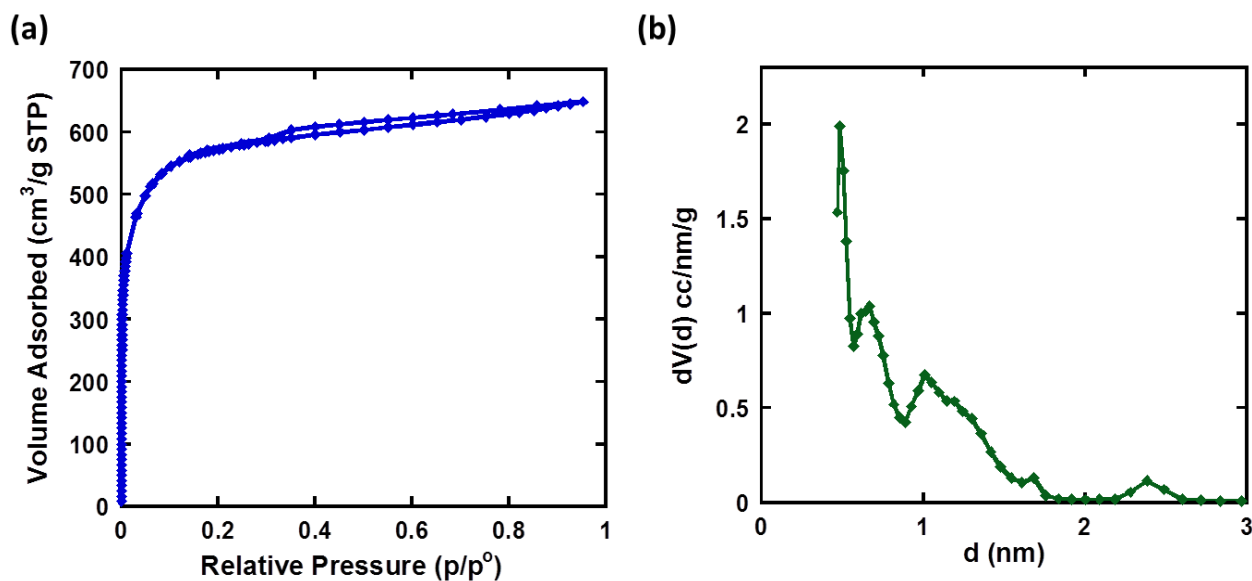


Figure II-1: Porosity Characteristics of the as-received YP-50F carbon: (a) Ar sorption isotherm collected at 77K and (b) pore size distribution calculated from QSDFT model.

Table II-1: Characteristics of YP-50F activated carbon

Surface area (m ² /g)	1500 - 1800
pH	7-10
Particle size (μm)	5-20
Ash content (wt%)	1 max
Moisture content (wt%)	3 max

YP-17

The porosity characteristics of the as-received YP-17 carbon were obtained from Ar sorption isotherm at 77 K (Figure II-2a). The PSD were calculated from the isotherm by using QSDFT is shown in Figure II-2b. The calculated average pore size is 1 nm and the BET SSA was estimated to be is 1602 m²/g.

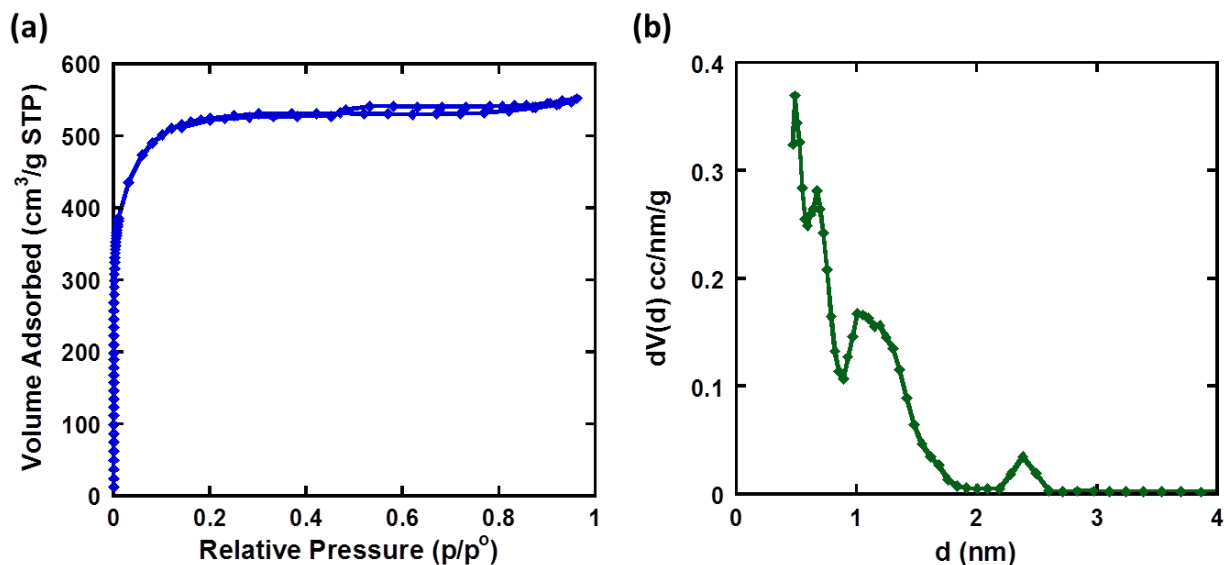


Figure II-2: Porosity Characteristics of the as-received YP-17 carbon: (a) Ar sorption isotherm and (b) pore size distribution calculated from QSDFT model

Other characteristics provided by the supplier are listed in Table II-2. It was also mentioned that for pores which are smaller than 3 nm, 40 vol % of which are less than 1 nm, 55 vol % are between 1 to 1.5 nm, and the remaining 5 vol % have the pore size larger than 1.5 nm.

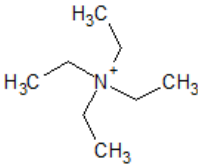

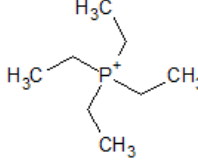
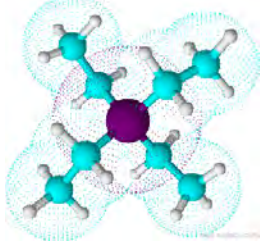
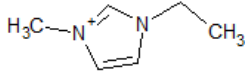
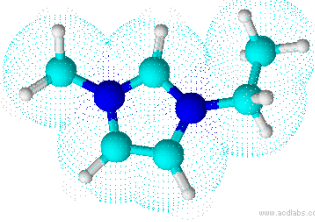
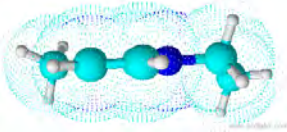
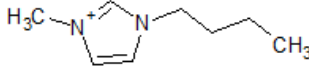
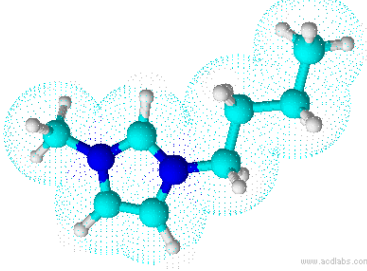
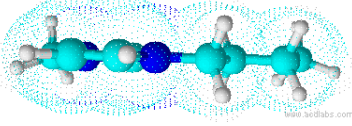
Table II-2: Characteristics of YP-17 activated carbon

BET Surface (m ² /g)	1709
Microporous volume (cm ³ /g), < 2 nm	0.690
Mesoporous volume (cm ³ /g), 2 – 5 nm	0.038
Mesoporous volume (cm ³ /g), 2 – 50 nm	0.080
Macroporous volume (cm ³ /g), > 50 nm	0.108
Total volume (cm ³ /g)	0.877
Ash content (%)	0.3
pH	5.7

3. Electrolytes

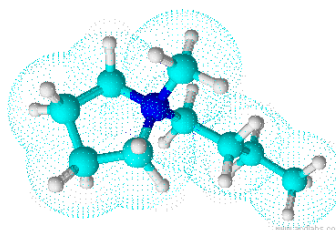
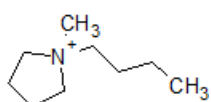
Different organic and ionic liquid-based solutions were used as electrolytes: tetraethylammonium tetrafluoroborate (NEt_4BF_4 , CAS #429-06-1) and tetraethylphosphonium tetrafluoroborate (PEt_4BF_4 , CAS #665-49-6) salts were purchased from Acros Organics and Tokyo Chemical Industries, respectively. Ionic liquids 1-ethyl-3-methylimidazolium bis(trifluoromethanesulfonyl)imide (EMI-TFSI, CAS #174899-82-2), 1-Butyl-3-methylimidazolium hexafluorophosphate (BMI- PF_6 , CAS #174501-64-5), N-butyl-N-methylpyrrolidinium, bis(fluorosulfonyl)imide (PYR14-FSI, CAS #1057745-51-3), and N-methyl-N-propylpiperidinium bis(fluorosulfonyl)imide (PIP_{13} -FSI) were bought or obtained from Solvionic. The acetonitrile (AN) (CAS #75-05-8, $\text{H}_2\text{O} < 10$ ppm) solvent was also obtained from Acros Organics. Table II-3, Table II-4, and Table II-5 present respectively the cations, anions and solvent molecules and their structures (drawn by using ChemSketch Freeware V.14.01). As an important part of this thesis work is to study the relationship between the ion size and pore size, the size of the molecules found in the literatures are also given in the tables. The detailed information of each electrolyte regarding applied voltage, viscosity, etc. will be further discussed individually in each part of results.

Table II-3: Structure and size of the cations studied in this work

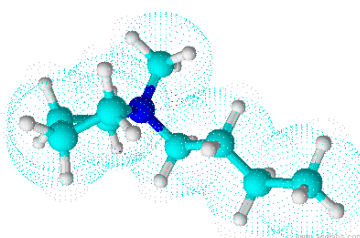
Cations	Structure	Size max/min length (nm)
NEt_4^+ tetraethylammonium 		0.85/0.75 ^[5]
PEt_4^+ tetraethylphosphonium 		---/0.72 ^[6]
EMI^+ 1-ethyl-3-methylimidazolium 	 <p style="text-align: center;">Side view</p> 	0.76 ^[7] /---
BMI^+ 1-Butyl-3-methylimidazolium 	 <p style="text-align: center;">Side view</p> 	---

PYR₁₄⁺

N-butyl-N-methylpyrrolidinium

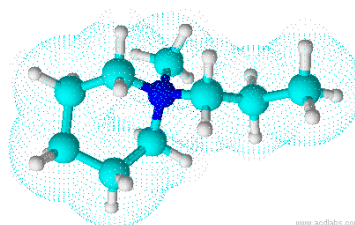
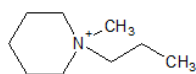


Side view



PIP₁₃⁺

N-methyl-N-propylpiperidinium



Side view

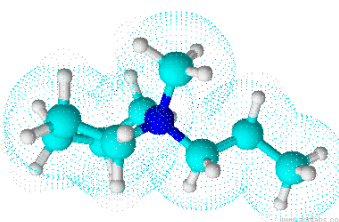


Table II-4: Structure and size of the anions studied in this work

Anions	Structure	Structure	Size max/min length (nm)
BF ₄ ⁻ tetrafluoroborate			0.51/0.50 ^[5]
PF ₆ ⁻ hexafluorophosphate			0.54/ ---

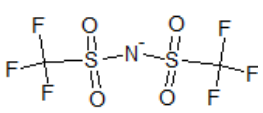
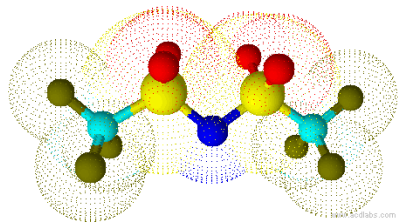
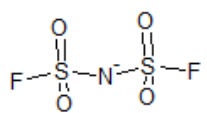
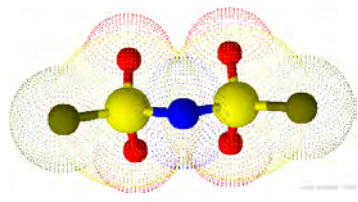
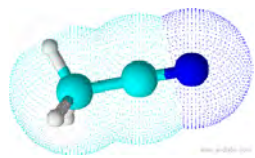
<p>TFSI bis(trifluoromethylsulfonyl)imide</p> 		<p>0.79^[7]/0.37^[5]</p>
<p>FSI bis(fluorosulfonyl)imide</p> 		<p>---</p>

Table II-5: Structure and size of the solvent molecule studied in this work

Solvent	Structure	Size max/min length (nm)
<p>AN Acetonitrile $\text{H}_3\text{C}-\text{C}\equiv\text{N}$</p>		<p>0.58/0.40^[5]</p>

4. Electrochemical Characterization of Supercapacitors

4.1 Electrochemical characterization techniques

In this section, different electrochemical characterization techniques used in this thesis work will be introduced. The information that can be extracted from these techniques will also be discussed. Since this thesis focuses on “double-layer” type of supercapacitors, different from standard electrochemical characterizations which focus on charge transfer (redox reaction), the discussion will focus on *capacitive* behavior.

4.1.1 Cyclic voltammetry (CV)

Cyclic voltammetry is one of the most used techniques for fast screening and characterizing an electrochemical system. The electrochemical cell is controlled *potentiodynamically*, cycled between two pre-selected potential values with a chosen sweep rate and the current response is recorded. This technique provides useful information such as stable electrochemical window, capacitance, and cyclability of the active materials or devices. Kinetics of the system can also be studied by varying the sweep rate.

Different equivalent circuit models of EDLCs and the corresponding CV profiles as shown in Figure II-3. An ideal double layer capacitor (C_{dl}) exhibits a perfect rectangular CV profile (Figure II-3a). However in reality, much more complex behaviors are involved in the double layer charging. Two simplified examples are given in Figure II-3b and c. Non-ideal polarizability which involves charge transfer across the electrode surface (represented as faradaic or leakage resistance, R_F , in parallel with double layer capacitance, as shown in Figure II-3b) gives a sloping CV curve. The slope of the CV ($\Delta I/\Delta E$) corresponds to the reciprocal of faradaic resistance ($1/R_F$). Also, resistances which come from the bulk electrolyte and contact between electrode films and current collectors, represented as a series resistance (R_s) in the equivalent circuit (Figure II-3c), deviates the CV curves from the ideal capacitive profile at the corner of the CV.

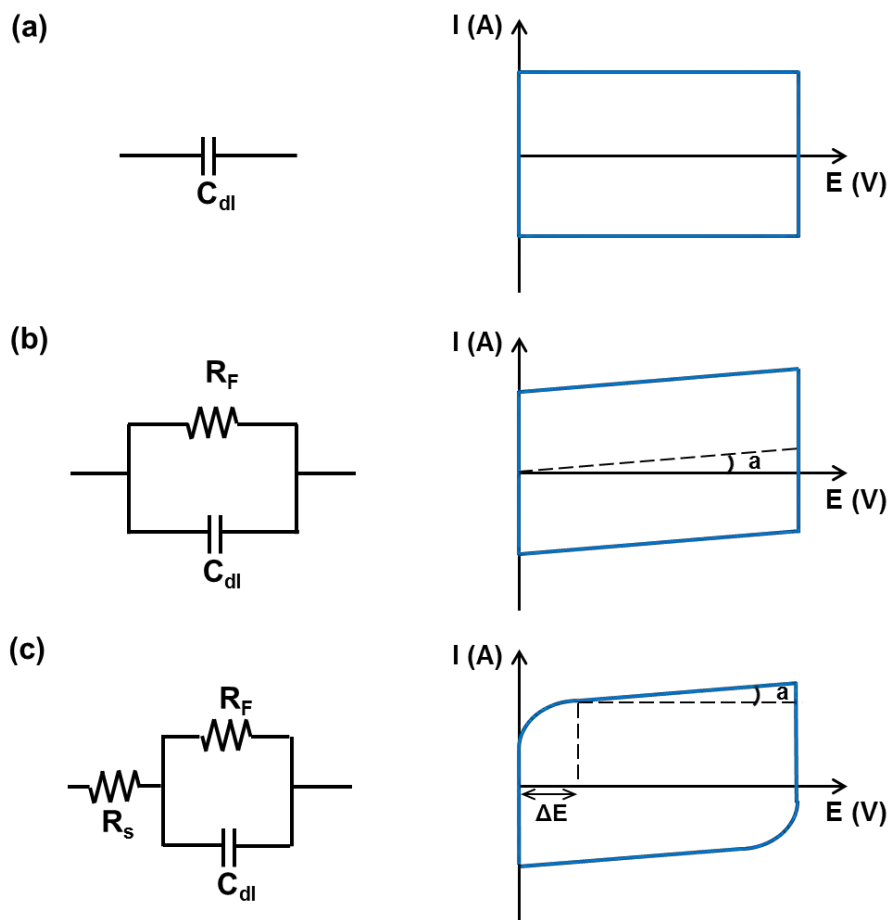


Figure II-3: Equivalent circuit models and corresponding cyclic voltammograms of (a) ideal double layer capacitor, (b) capacitor in parallel with leakage resistance, (c) and simplified supercapacitors model taking leakage resistance and equivalent series resistance into account

Capacitance of the electrode can be calculated from the cyclic voltammogram by the following equation:

$$C = \frac{I}{\left(\frac{dV}{dt}\right) \cdot m} \tag{Equation II-1}$$

where C is electrode capacitance in Farads per gram (F/g) in a non-symmetrical three-electrode cell, I is current in Ampere (A), dV/dt is scan rate used (V/s), m is the mass of active materials in gram (g). For two-electrode symmetrical cells, since the measured capacitance is the one of the cell (equivalent capacitance), the value must be multiplied by 2 to revert to single electrode capacitance, and an average electrode mass is used to go for gravimetric value.

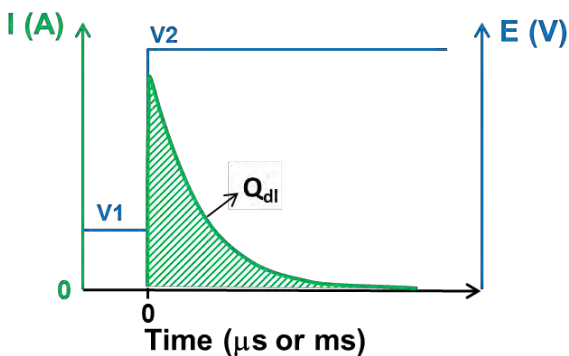
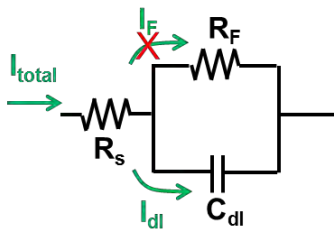
For a new electrode/electrolyte system, before conducting the designed electrochemical

measurements and collecting data, the electrochemical window of the system was first screened using cyclic voltammetry at low scan rate (e.g. 5 mV/s).

4.1.2 Chronoamperometry

The electrochemical behavior can also be studied *potentiostatically* by applying chronoamperometry: a sequence of potential steps are applied to the electrode, and the current transient response is recorded in each potential step. When applying a potential step to the electrode, a current transient is generated within a short time in response to the voltage pulse (Figure II-4). Since $\Delta Q = C \cdot \Delta V$, during the hold of the potential step ($\Delta V = 0$), the current transient becomes zero ($\Delta Q = 0 = I \cdot t$) after a certain period of time for a pure capacitive behavior (Figure II-4a). The total charge (ΔQ) flows in the electrode can be calculated through integration of current over time, and the capacitance (C) can be also obtained by dividing charge over voltage change ($\Delta V = V_2 - V_1$). If the measured system presents high leakage/faradaic current (I_F) due to electrolyte decomposition or other redox reactions at the electrode surface, the residual current will not be zero and is contributed from faradaic phenomena. For EDLC investigation, faradaic/leakage charge (Q_F) is unwanted, and should be separated from the charge stored at the supercapacitor double layer (Q_{dl}) (Figure II-4b).

(a) $I_F \approx 0$



(b) $I_F > 0$

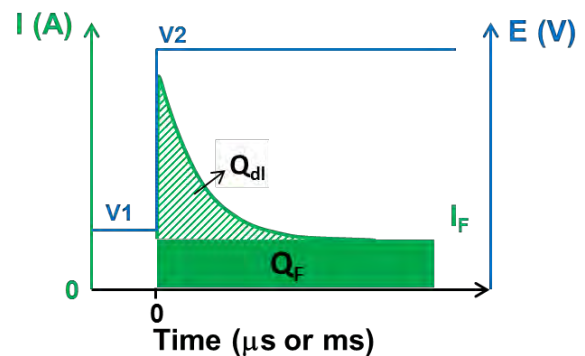
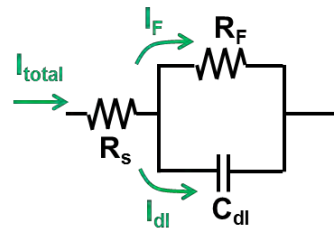


Figure II-4: simple equivalent circuit of a supercapacitor and the current transient of the electrode in response to a potential pulse from V_1 to V_2 : (a) without and (b) with leakage current in the system

4.1.3 Electrochemical Impedance Spectroscopy (EIS)

Electrochemical Impedance Spectroscopy (EIS) is an important method for characterizing supercapacitors. By investigating the alternating current (ac) response generated by an alternating voltage (av) addressed to the electrode over a wide range of frequency, EIS allows the capacitance of the electrode or cell to be determined as a function of frequency. Moreover, each physical/chemical phenomenon has its unique relaxation time (the time a perturbed system needed to return to its equilibrium) and its corresponding equivalent circuit. By sweeping a wide range of frequency, each physical/chemical process in the system could be separated, and the equivalent circuit of the electrochemical system could be modelled thus enabling the analysis of the device performance. Therefore, the equivalent series resistance (ESR, shown as R_s in the equivalent circuit in Figure II-4) in the supercapacitors can be *separately* evaluated. The ESR is an important parameter for device design since the power performance of the supercapacitors is often limited by the cell internal resistance.

EIS is conducted by applying a low-amplitude alternating voltage (5 mV) to the cell at its open circuit potential (fully discharged). The applied alternating voltage is expressed as:

$$V(\omega) = V_0 \sin(\omega t) \quad (\text{Equation II-2})$$

where V_0 is the (maximum) amplitude of the alternating voltage signal in Volt, ω is the angular frequency in radian per second, which is related to frequency (f , in Hertz) by the equation $\omega = 2\pi f$.

An alternating current (in Ampere) in response to the applied alternating voltage is measured and expressed as also as sinusoidal function with a peak value of I_0 :

$$I(\omega) = I_0 \sin(\omega t + \varphi) \quad (\text{Equation II-3})$$

Applying Euler's formula: $e^{ix} = \cos x + j \sin x$, Equation 1 and 2 can be presented in complex and thus facilitate the mathematical calculation later:

$$V(\omega) = V_0 \exp(j\omega t) \quad (\text{Equation II-4})$$

$$I(\omega) = I_0 \exp(j(\omega t + \varphi)) \quad (\text{Equation II-5})$$

The impedance is then defined as the ratio between potential complex and current complex:

$$Z(\omega) = \frac{V_0}{I_0} \exp(-j\varphi) \quad (\text{Equation II-6})$$

The complex impedance can also be represented as:

$$Z(\omega) = |Z| \exp(-j\varphi) = Z' + jZ'' \quad (\text{Equation II-7})$$

With the impedance modulus defined as

$$|Z(\omega)| = \frac{V_0}{I_0} = \sqrt{Z'^2 + Z''^2} \quad (\text{Equation II-8})$$

where Z' and Z'' are the real and imaginary parts of the complex impedance, respectively. The impedance of three commonly used ideal electrical elements – capacitors (Z_c), ohmic resistors (Z_R) and inductors (Z_L) – are described by equation II-9, 10, and 11, respectively.

$$Z_c = \frac{1}{j\omega C} \quad (\text{Equation II-9})$$

$$Z_R = R \quad (\text{Equation II-10})$$

$$Z_L = j\omega L \quad (\text{Equation II-11})$$

Where C, R and L are capacitance, resistance and inductance, respectively.

Nyquist plot (Z'' versus Z') is commonly used for EIS study. Figure II-5 shows the Nyquist plots corresponding to two simple equivalent circuit models mentioned in Figure II-3.

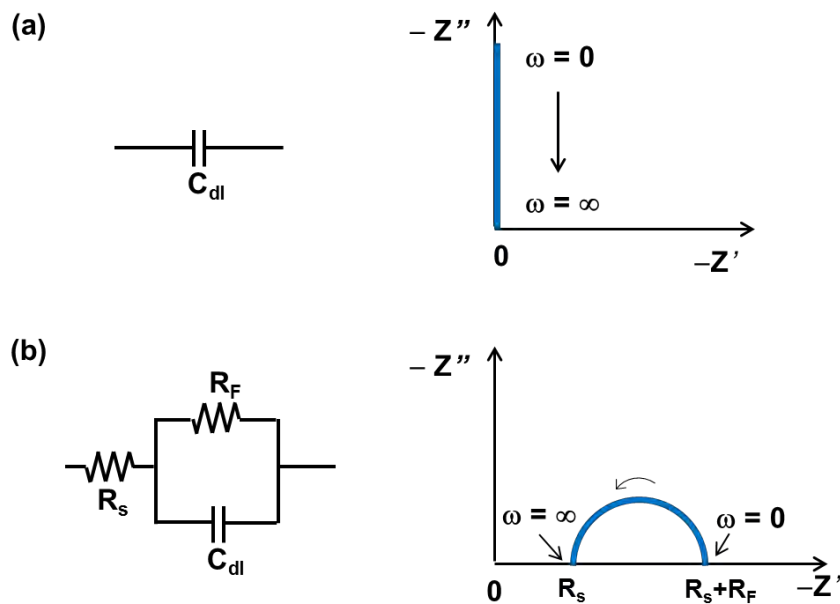


Figure II-5: Equivalent circuit and its corresponding Nyquist plot of (a) an ideal double-layer capacitor (C_{dl}), and (b) a more complex model also considering leakage resistance (R_F) and equivalent series resistance (R_s)

The equivalent model shown in Figure II-5b is still too simplified. Figure II-6 presents a common Nyquist plot obtained from a double-layer supercapacitor. Different characteristics can be seen: (1) at high frequency range, the supercapacitor behaves like pure resistance. The impedance curve intercepts with x-axis at R_s (as indicated in Figure II-6), corresponding to the series resistance of the cell. (2) A semi-circle loop (domain I) at high frequency can be observed. This loop originates from the current collector/carbon electrode interface, and can be removed by proper elaboration of current collector.^[8] (3) A line with a slope of 45° observed in the middle range of frequency (domain II) is related to the electrolyte penetration inside the porous electrode, which has been intensely studied by de Levie^{[9][10]}. (4) At low frequency, the impedance tends toward a pure capacitive behavior hence a vertical line is observed (Zone III).

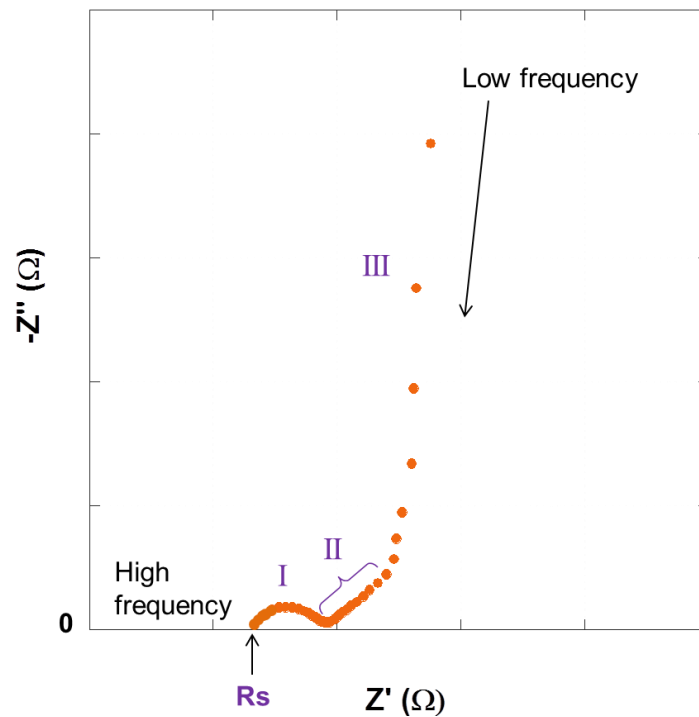


Figure II-6: Nyquist plot of a EDLC from low frequency to high frequency

The equivalent series resistance (ESR, in $\Omega \cdot \text{cm}^2$) of the supercapacitor can be obtained by:

$$ESR = R_s \cdot A \quad (\text{Equation II-12})$$

Where R_s is the impedance that intercepts with x-axis in Ω , and A is the surface area of the electrode in cm^2 .

Porous electrode: Transmission Line Model from De Levie

As one can easily imagine that for a porous carbon electrode, the time needed for inner surface to be charged is longer than that for outer surface since ions need to penetrate the pore. This non-uniform charging rate on the available electrode surface is revealed on the impedance, giving rise to the characteristic curve with slope of 45° in the medium frequency range (Figure II-6, zone II). This behavior of species mass transport in a pore has been investigated in detail by de Levie^{[9][10]} using the transmission line model as shown in Figure II-7. Therefore, this sloping region in the Nyquist plot gives information on the ionic resistance during penetration in the pore, which is highly related to the pore geometry.

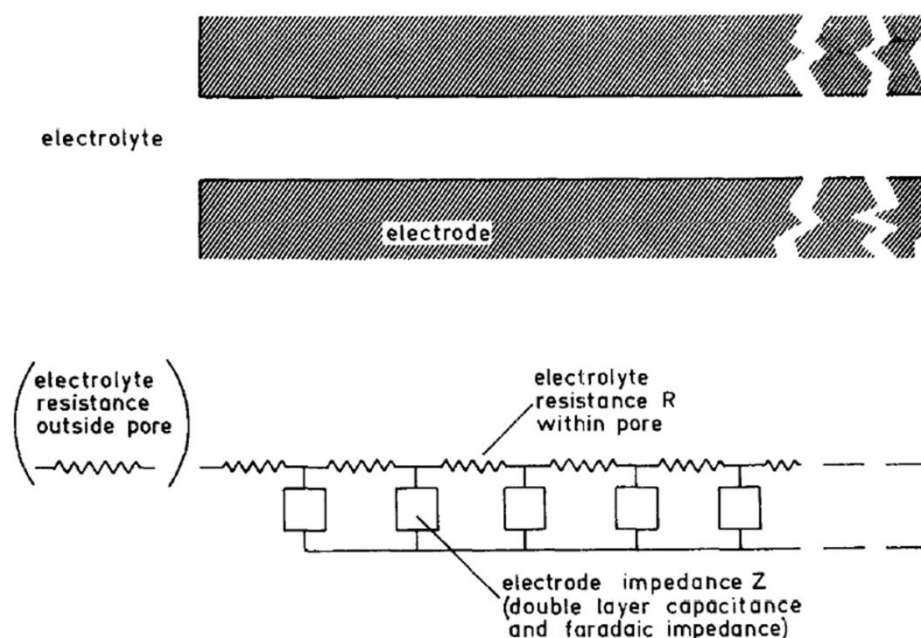


Figure II-7: Equivalent circuit in a pore suggested by de Levie^[10].

4.2 Set-ups

Two different cell configurations were used for studying electrochemical double layer. After cell assembly, the electrochemical measurements of these cells were conducted using a VMP3 potentiostat/galvanostat (Biologic, France).

4.2.1 Swagelok® Cells

The two-electrode or three-electrode Swagelok® stainless steel cell^[11], illustrated in

Figure II-8a, was assembled in a glove box under argon atmosphere of less than 1 ppm of oxygen and water content. The electrode films were laminated onto treated aluminum current collectors (Al CC), and two layers of 25 μ m-thick porous cellulose or other type of porous polymeric papers were used as separator. The stack (CC / electrode / separator / electrode / CC) was hold firmly between two stainless steel pistons. In the case of three-electrode Swagelok®, a silver wire (2 mm in diameter) was used as a quasi-reference electrode (Figure II-8b). For experiments conducting under various temperatures, a slight pressure was added on both sides of the pistons to ensure the contact between stacks will not be affected by thermal expansion of the cell.

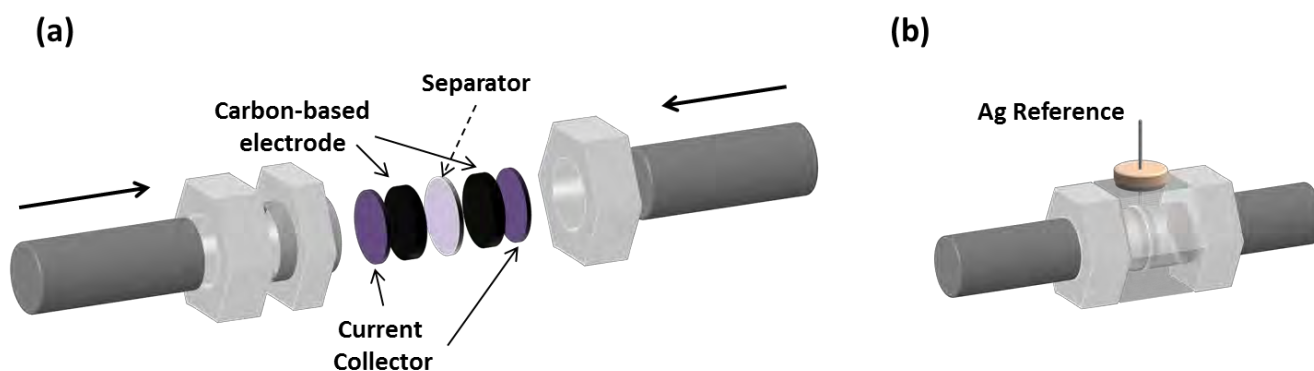


Figure II-8: Schemes of two-electrode (a) and three-electrode (b) Swagelok® cell

Current collectors

Aluminum current collectors were pre-treated in the following steps to improve the contact with the electrode film hence decrease the interface impedance: First, the aluminium foils were laminated to thickness of about 250 μ m, and immersed into 1M NaOH solution for 20 minutes at room temperature to remove the grease and native oxide on the Al surface. Then, the aluminum foils were rinsed with distilled water and placed into 80°C 1M HCl solution for 2 minutes in order to etch and create roughness on the Al surface. After etching, the Al current collectors were rinsed again by distilled water and blown dry.

To enhance the conductivity, the etched current collectors were then dip-coated at a withdrawal rate of 35cm/min. in a slurry consisting of a few percent of acetylene black powder suspended in a polymeric sol.^[8] Lastly, the collectors were subjected to a thermal treatment at 470°C in air for 4 hours to remove the polymeric sol. After thermal treatment, the Al current

collector surface was covered by the conducting acetylene black particles. The current collectors were then punched into the sizes corresponding to the sizes of the Swagelok.

Electrode films

The electrode films were prepared by mixing 95 wt.% active materials (CDCs, commercial activated carbons) with 5 wt.% of polytetrafluoroethylene binder (PTFE; 60 wt.% dispersion in water) in ethanol. The slurry was uniformly stirred on a watch glass until it formed a paste-like material, and then rolled into film using a glass tube and cut into circles. For a film with a carbon loading of 15 mg/cm², the thickness of the films ranged from 250 to 300 μm depending on the type of carbons.

Separators

Separator is used to prevent short circuit between two electrodes while allowing the transport of electrolyte ions during operation. There exist several types of separators and main requirements for separators in supercapacitors are listed as follow: (1) They need to be chemical and electrochemical stable in the system; (2) They should provide as low cell resistance as possible to avoid changing the cell performance, which means thin, high porosity and permeability allowing the electrolyte to penetrate; (3) They should be mechanically strong enough to withstand the pressure applied during cell assembly. In this set-up, two layer of 25 μm-thick porous cellulose (provided by Batscap) or Al₂O₃ (Separion®, average pore size of 240 nm, > 40 % porosity, Evonik Industries, Germany) were used as separators. Al₂O₃ separators were used for low temperature test.

4.2.2 Cavity Micro-Electrode (CME)

Cavity micro-electrode (CME) is a technique that allows investigating electrochemical kinetics of processes occurring at powder material electrode. The CME used in this work is provided by the French network “CNRS Microélectrode à cavité”. It consists of a thin platinum wire (60-150 μm in diameter) sealed in a glass tube as shown in Figure II-9a. The cavity was obtained either by laser ablation or controlled dissolution of the Pt-wire in a highly concentrated hot *aqua regia* solution (which was described in detail by Cachet-Vivier et al.^[12]) The platinum wire was connected to a copper rod current collector. The electrical contact between the Pt wire and the copper rod was reinforced by carbon graphite powder. The

diameter of the cavity is in between 20 and 150 μm , and the height-diameter (h/d) ratio, as indicated in Figure II-9a, was controlled between 0.4 and 1. If the h/d ratio was larger than 1, then establishing the contact between the platinum and the powder grains was difficult; if it was less than 0.4, the grains packed inside the cavity could escape easily during the tests.^[12]

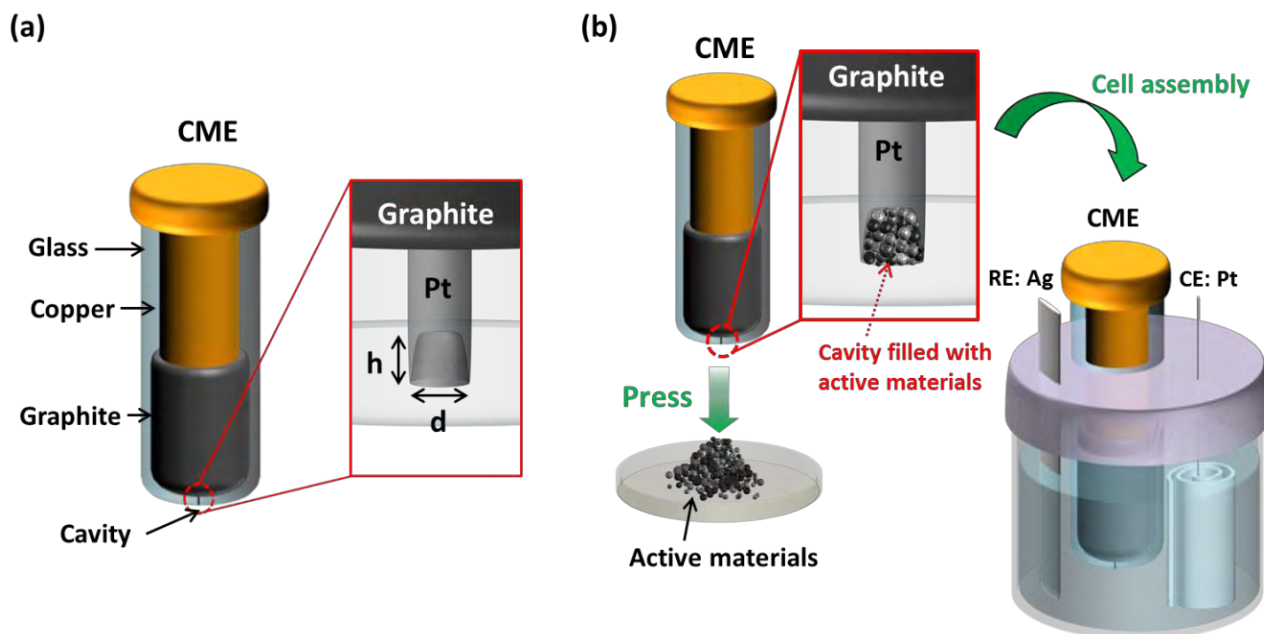


Figure II-9: Scheme of cavity micro-electrode (CME) (a) and CME electrochemical cell assembly and configuration (rolled-Pt as counter electrode and silver wire as reference) (b)

The electrochemical cell was assembled under glove box condition (oxygen and water content < 1 ppm) as follow (Figure II-9b): the powder was packed inside the cavity by simple pressing CME on the powder grains onto a glass substrate. The powder-packed CME was then used as the working electrode, and a laminated silver wire and a rolled platinum foil (with area of 1 cm^2) were used as reference and counter electrode, respectively.

Since the powder was hold physically inside the cavity by simple packing, the powder could detach from the cavity by shaking the cell, gas formation or volume change during electrochemical test. Therefore, all the CME tests were repeated at least twice, and the open-circuit voltage (OCV) was tracked between tests for the same sample to verify the reproducibility. Between different tests, the CME was cleaned by sonication in ethanol.

Cavity micro-electrode provides several advantages compared to conventional EDLC set-up (such as the $2\text{cm} \times 2\text{cm}$ electrode EDLC^[8]): First, it allows the study of electrochemical behavior at the active materials / electrolyte interface without influence of binders, separators, current collectors or other components in the conventional set-ups. Only

few micrograms of materials are needed, and the small size of electrochemical interface between the electrode grains and the electrolyte reduced hugely the ohmic drop, thus it allows recording voltammograms over a wide scan rate range between a few tens microvolts to several tens or even hundreds of volts per second, therefore makes CME a powerful technique to study electrochemical kinetics. Furthermore, the cell preparation and assembly are simple and fast, so it could be used for fast screening different materials. However, as the amount of material packed in the cavity is different between different experiments and the weight of material packed inside is too few to be measured, therefore CME cannot obtain quantitative information, e.g. specific capacitance (Farad *per gram*). Comparison between different CME experiments requires normalization with respect to a selected reference point, thus only qualitative information can be extracted. Figure II-10 shows an example of CVs collected using CME technique^[13]. Figure II-10a presents the CME raw data before normalization and Figure II-10b shows the comparison of CVs after normalization where all the current values in the CVs have been normalized to the current value measured at 1 V/Ref.

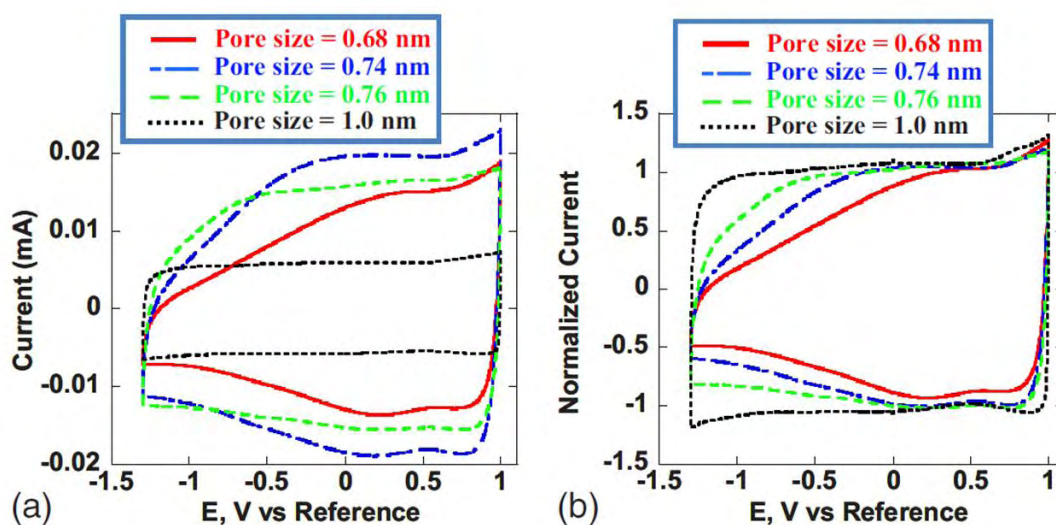


Figure II-10: (a) CVs of CDC samples in AN + 1.5 M NEt_4BF_4 electrolyte between -1.3 and $+1$ V/Ref at a scan rate of 100 mV and (b) normalized CVs of the same samples^[13]

5. Reference

- [1] A. V. Neimark, Y. Lin, P. I. Ravikovitch, M. Thommes, *Carbon* **2009**, *47*, 1617.
- [2] S. Brunauer, P. H. Emmett, E. Teller, *J. Am. Chem. Soc.* **1938**, *60*, 309.
- [3] K. S. Sing, *Adv. Colloid Interface Sci.* **1998**, *76*, 3.
- [4] “Kuraray, YP50F Specifications,” can be found under <http://www.kuraraychemical.com/products/sc/SCcarbon.htm>, **n.d.**
- [5] C. Decaux, C. Matei Ghimbeu, M. Dahbi, M. Anouti, D. Lemordant, F. Béguin, C. Vix-Guterl, E. Raymundo-Piñero, *J. Power Sources* **2014**, *263*, 130.
- [6] K. Matsumoto, U. Harinaga, R. Tanaka, A. Koyama, R. Hagiwara, K. Tsunashima, *Phys Chem Chem Phys* **2014**, *16*, 23616.
- [7] C. Largeot, C. Portet, J. Chmiola, P.-L. Taberna, Y. Gogotsi, P. Simon, *J. Am. Chem. Soc.* **2008**, *130*, 2730.
- [8] C. Portet, P. . Taberna, P. Simon, C. Laberty-Robert, *Electrochimica Acta* **2004**, *49*, 905.
- [9] R. de Levie, *Electrochimica Acta* **1963**, *8*, 751.
- [10] R. de Levie, *Electrochimica Acta* **1964**, *9*, 1231.
- [11] A. Blyr, C. Sigala, G. Amatucci, D. Guyomard, Y. Chabre, J.-M. Tarascon, *J. Electrochem. Soc.* **1998**, *145*, 194.
- [12] C. Cachet-Vivier, V. Vivier, C. S. Cha, J.-Y. Nedelec, L. T. Yu, *Electrochimica Acta* **2001**, *47*, 181.
- [13] R. Lin, P. L. Taberna, J. Chmiola, D. Guay, Y. Gogotsi, P. Simon, *J. Electrochem. Soc.* **2009**, *156*, A7.

Chapter III:

Study of carbon microstructure effect on capacitive storage

1. Introduction

As discussed in chapter I, it is important to adapt the electrode pore size to ion size but at the same time take the ion transport into account, which, in other words, means a 3-D interconnected porous structure containing both micro- and mesoporous material is needed as electrode materials. On the other hand, supercapacitors not only attract attention for high power applications, but also for application operated in wide temperature range (especially under low temperature condition, where batteries suffer from bad performance). As a result, a lot of efforts have been made for developing wide voltage electrolytes with large temperature range.

Our group has recently reported a novel ionic liquid electrolyte composed of (1:1 by weight or molar ratio) N-methyl-N-propylpiperidinium bis(fluorosulfonyl)imide (PIP₁₃-FSI) and N-butyl-N-methylpyrrolidinium bis(fluorosulfonyl)imide (PYR₁₄-FSI).^[1] The liquid state of this ionic liquid eutectic mixture is maintained several tens of degrees lower compared to the individual constituting ILs. Most importantly, the wide electrochemical stability window is preserved in the mixtures, which contributes to the goal of increasing energy density, as $E = \frac{1}{2} CV^2$, where C is capacitance and V is voltage. This electrolyte mixture has been investigated in our previous work with exohedral carbons such as onion-like carbon (OLC) or carbon nanotubes (CNTs). Excellent capacitive behavior has been observed (Figure III-1)^[1] in an

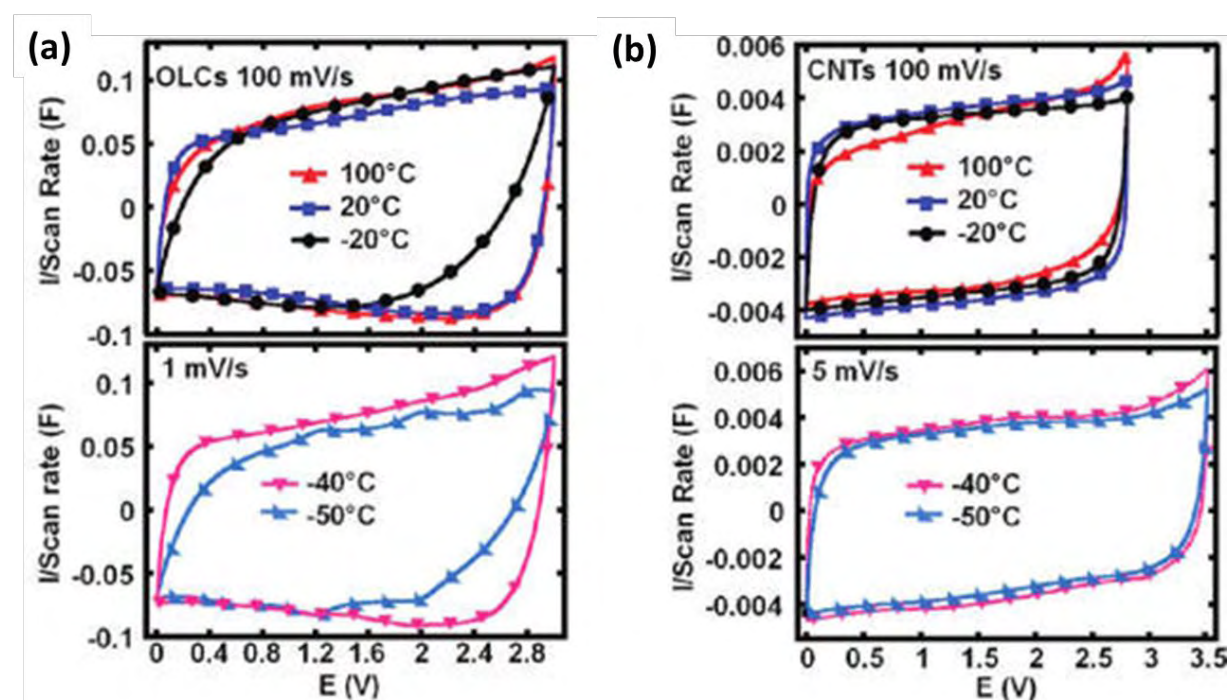


Figure III-1: CVs at temperatures from -40 to 100°C for OLCs recorded at 100 and 1 mV/s (a); CVs at temperatures from 50 to 100°C at 5 and 100 mV/s for CNTs (b)^[1]

extended operating temperature range of $-50\text{ }^{\circ}\text{C}$ to $100\text{ }^{\circ}\text{C}$ with high rate performance (60 % of capacitance retention at 20 V/s for $T \geq 20\text{ }^{\circ}\text{C}$, and 75 % of capacitance retention at 20 mV/s for $T = -50\text{ }^{\circ}\text{C}$) thanks to the highly accessible open carbon structure.

This work gives important insights into improving the material design of supercapacitors in different aspects. First, the selected two ionic liquids have the same electrochemically stable anion (FSI), same molecular weight, and same number of atoms of the same nature, and the only difference is their cation molecular structure, based on a five-member or six-member heterocycle, respectively. The similarities of the ionic liquids give the mixture high miscibility, and keep the chemical nature and interaction between cations and anions in the mixture close to those of its constituents. The slight difference in their cation molecular structure increases the disorder in the electrolyte hence inhibiting the formation of lattice and decreasing dramatically the melting point of the mixture. Therefore, the resulting mixture preserves the wide electrochemical window in a broad operating temperature range. This provides an inspiring concept for producing new electrolytes with large potential window (hence energy) in a wide temperature range by adapting the carbon structure to the electrolyte viscosity. Second, the good capacitive behavior and high capacitance retention in these systems at extreme temperature of $-50\text{ }^{\circ}\text{C}$ clearly lifted the long-hold restrictions of the use of ionic liquid in energy storage applications above room temperature. However, the main disadvantage of these exohedral carbons is their low specific surface area ($500\text{ m}^2/\text{g}$) as compared to other porous carbon materials ($1000\text{-}2000\text{ m}^2/\text{g}$), leading to low specific capacitance ($\sim 30\text{ F/g}$; 4 mF/cm^2). This highlights the importance of increasing specific surface area (SSA), more precisely *ion accessible surface area*, in the electrode materials.

Conventional supercapacitor electrode materials such as nanoporous activated or carbide-derived carbons that possess a high SSA and excellent performance in organic electrolytes exhibit poor capacitive performance with IL electrolytes at room temperature or below^[1-3] due to low ion mobility in the porous networks. Pore structure that contains both micropore and mesopores (usually $2\text{-}8\text{ }\mu\text{m}$) may enhance the ion transport kinetics in the materials. The aim of this chapter is to build high performance supercapacitors that allow operation under wide temperature range. $(\text{PIP}_{13}\text{FSI})_{0.5}(\text{PYR}_{14}\text{FSI})_{0.5}$ ionic liquid mixture was chosen in this study owing to its wide temperature range of liquid state. Carbons with different microstructures thus ion accessibility were investigated in order to optimize the carbon/electrolyte interface and to increase the magnitude and quality of charge storage, thereby further improving the energy density in an extended operating temperature range.

2. Characteristics of ionic liquid-mixture ((PIP₁₃FSI)_{0.5}(PYR₁₄FSI)_{0.5})

Ionic liquids PIP₁₃FSI and PYR₁₄FSI were purchased from Solvionic, and the mixture was obtained by simply mixing same weight of PIP₁₃FSI and PYR₁₄FSI in the glove box. The characteristics of PIP₁₃FSI, PYR₁₄FSI and their 1:1 mixture are presented in Figure III-2.^[1] As previously reported^[1], a proper combination of cations with the same anion prevents the molecules from ordered arrangement and crystallization. The liquid state of the IL mixture can therefore be maintained few tens of degrees lower than both of its constituents. The conductivity of both ILs and their mixture are shown in Figure III-2b. For PIP₁₃FSI and PYR₁₄FSI ionic liquids, their conductivities drop significantly when temperature goes below their melting points of 6 and -18°C, respectively. Whereas for the 1:1 mixture, conductivity values of 28.9 mS/cm and 4.9 mS/cm were found at 100 and 20°C, respectively, and the temperature dependence follows Arrhenius behaviour down to -70°C. This extended temperature of ionic conductivity allows the IL mixture to be operated at low temperature as low as -50°C with exohedral carbons.^[1]

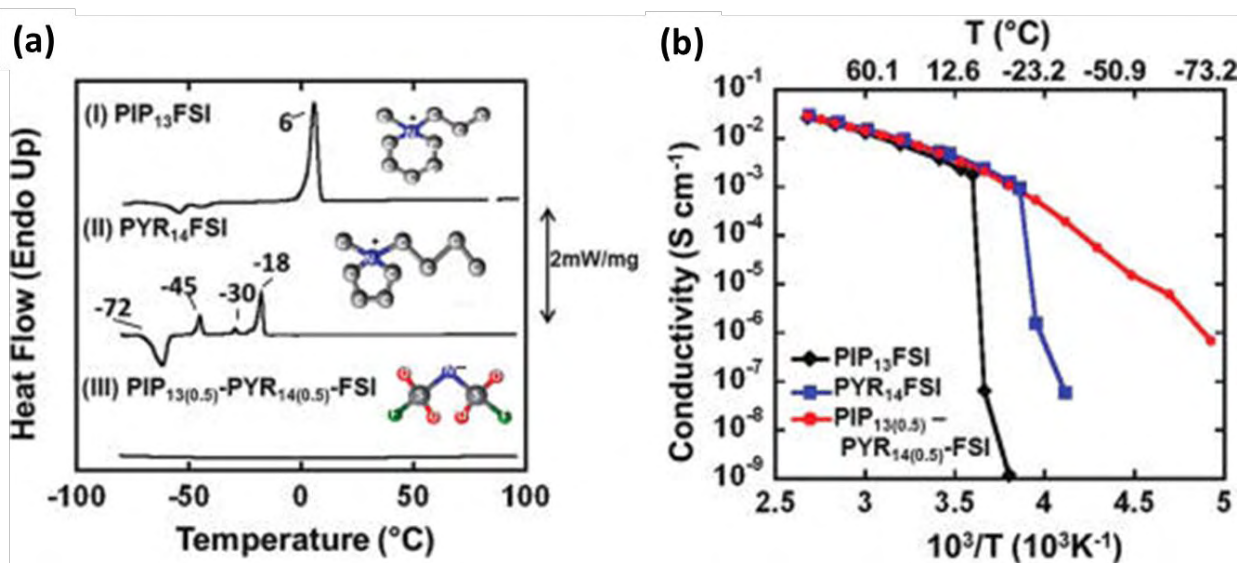


Figure III-2: Characteristics of the ILs: DSC profiles of (I) PIP₁₃FSI, (II) PYR₁₄FSI and (III) (PIP₁₃FSI)_{0.5}(PYR₁₄FSI)_{0.5} mixture, and their chemical structures (a); Change of the conductivity versus the inverse temperature for PIP₁₃FSI, PYR₁₄FSI and (PIP₁₃FSI)_{0.5}(PYR₁₄FSI)_{0.5} IL mixture (b)^[1]

3. Hierarchy silicon carbide-derived carbon (SiC-CDC) in organic electrolyte and IL mixture

Among different carbon-based materials, microporous carbide-derived carbon (CDC) family is highly attractive thanks to their tunable structure leading to high capacitance.^[4-7] As mentioned in chapter I, CDCs are prepared from chlorination of metal carbides; depending on the choice of precursor material and synthesis conditions, the resulting microstructure can be nicely controlled with a narrow pore size distribution, while retaining the original carbide shape and volume (a conformal transformation).^[2] An original route for the synthesis of ordered mesoporous carbides has been developed recently by Favier et al using a magnesio-thermal reaction on silica-carbon mesoporous composites.^[8,9]

This section investigates the electrochemical performance of such ordered micro/mesoporous silicon carbide – CDC (SiC-CDC) materials first in a conventional organic electrolyte (tetraethylammonium tetrafluoroborate (NEt_4BF_4) in acetonitrile (AN)), and further in the IL eutectic mixture. The synthesis of silicon carbide and part of the material characterizations were conducted in Professor Frédéric Favier's group in Montpellier, France. The chlorination of the as-prepared silicon carbide powder was implemented in Professor Yury Gogotsi's group (Drexel University, USA).

Ordered micro/mesoporous silicon carbide-derived carbon (SiC-CDC)

SiC-CDC synthesis

Mesoporous carbon-silica composites were prepared with slight modifications on the synthetic route described by Liu et al.^[10] A triblock copolymer P123 (Aldrich) was chosen as soft template. In a typical procedure, under vigorous stirring, 1 g of 0.2 M HCl was added to 9.6 g of 20 wt% P123 alcoholic solutions. After stirring at 40 °C for 4 h, a clear solution was obtained. Subsequently, 2.5 g of 20 wt% resol alcoholic solution and 2.08 g tetraethoxysilane (TEOs, 98% Alfa Aesar) were added. The mixture was continuously stirred for 2 h and painted afterwards onto a glass plate. The resulting film was kept at ambient temperature overnight to evaporate residual ethanol before being polymerized at 100 °C for 24 h. The as-made film was scraped and ground into fine powder before being carbonized in a tubular furnace at 800 °C for 3 h under N_2 flow. C/Si molar ratio was measured at 1.04:1 by residual silica content after burning SiC precursors at 550 °C for 2 h. By tuning the molar ratio between silica and carbon

precursors, as illustrated in Figure III-3a), the pore size could be finely tuned between 2.5 to 11 nm (Figure III-3b and c).^[9] Chlorination of this ordered silicon carbide creates micropores while maintaining the mother mesoporous structure, resulting in a hierarchical micro/mesoporous network in the material.

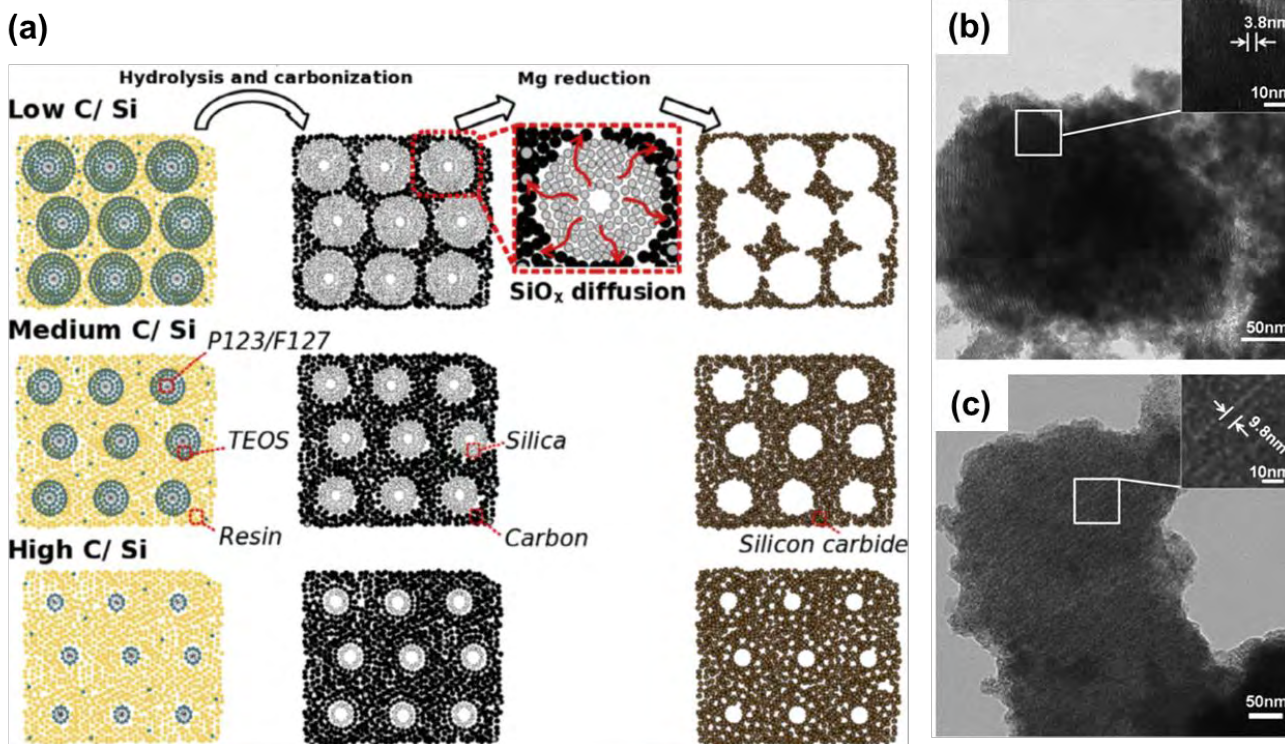


Figure III-3: SiC growth mechanism starting from various CS composite precursors (a) The pore size of the final SiC depends on the liquid polymer/TEOS ratio thanks to the size of the silica shell around the P123/F127 micelles. During the magnesio-thermal reduction, SiO₂ dissolves through SiO_x diffusion through the carbon matrix for pore opening in the final SiCs. TEM images of mesoporous silicon carbide using triblock copolymers P123 (b) and F127 (c) as structuring agent, respectively. (From reference [9])

The mesoporous silicon carbide was synthesized by using Mg as reducing agent at moderate temperatures as described in reference [8]. After sealing a carbon/SiO₂ composite mixed with Mg powder (10% Mg molar excess over SiO₂) under Ar in a 316L stainless tube, the magnesio-thermal reduction was performed at 800 °C for 24 h at a heating rate of 1 °C/min. SiC product was purified using 1 M HCl and 1 M HNO₃ aqueous solutions in sequence.

CDC powders were produced by chlorination of the SiC precursor, as previously described.^[2] The precursor was placed in a horizontal tube furnace and heated to 800 °C in Ar,

followed by Cl_2 flow ($10\text{--}15\text{ cm}^3/\text{min}$) for 3 h. After flushing residual Cl_2 with argon and lowering the temperature to $600\text{ }^\circ\text{C}$, the sample was annealed for 2 h using H_2 .

SiC-CDC Characterization

As mentioned in reference [9], XRD measurements conducted on the as-prepared SiC (Figure III-4a) shows the evidence for carbide formation. The SAXS reflection of the SiC (Figure III-4b)

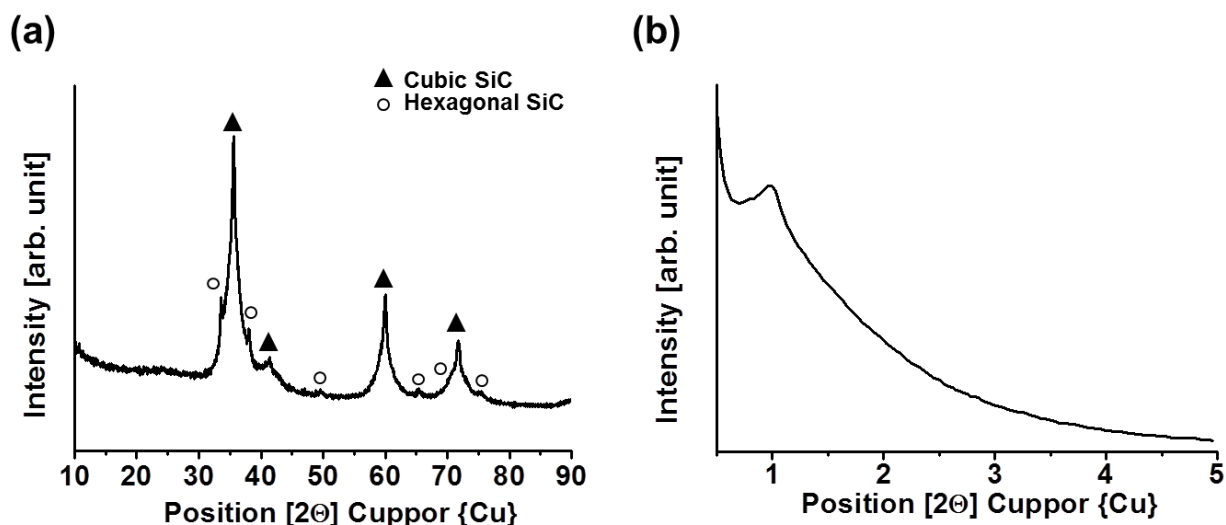


Figure III-4: XRD (a) and SAXS (b) patterns of the as-prepared silicon carbide powders (XRD and SAXS measurements were performed on a Philips X's Pert diffractometer using $\text{Cu K}\alpha$ radiation ($\lambda = 1.5405\text{ \AA}$))

TEM image (obtained using a JEOL 1200 EX2 TEM operating at 100 kV), Ar gas adsorption/desorption isotherm at 87K (Micromeritics ASAP 2020 porosimeter) and the pore size distribution obtained from Quenched Solid Density Functional Theory (QSDFT) method (Figure III-5) show that the mesoporous structure of the silicon carbide was retained after chlorination, with a significant fraction ($\sim 70\%$) of the pores having sizes greater than 2 nm. Additionally, the SiC-CDC contains narrowly distributed micropores as a peak at 1 nm is observed in Figure III-5b (inset). The specific surface areas of SiC-CDC calculated from Brunauer-Emmett-Teller (BET) and Density Functional Theory (DFT) method are $1619\text{ m}^2/\text{g}$ and $1335\text{ m}^2/\text{g}$, respectively.

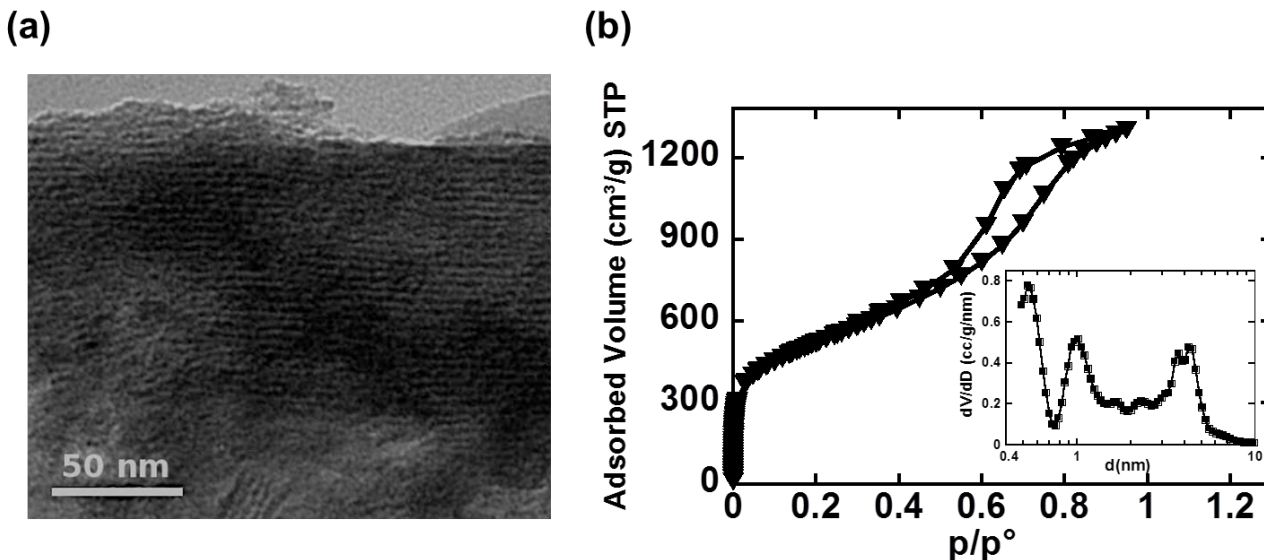


Figure III-5: TEM image of SiC-CDC (a) and gas adsorption/desorption analysis of SiC-CDC (BET SSA $\sim 1619 \text{ m}^2/\text{g}$) (Inset) Pore size distribution of the SiC-CDC powder derived from QSDFT (b)

3.1 Electrochemical characterization of SiC-CDC in conventional organic electrolyte ($\text{NEt}_4\text{BF}_4/\text{AN}$)

Electrochemical Cell Preparation and Assembly

SiC-CDC electrode films were prepared by mixing 95 wt% of SiC-CDC powder with 5 wt% of PTFE as described in Chapter II. The electrode films were laminated onto treated aluminum current collectors, and two layers of 25 μm -thick porous cellulose were used as separator. The symmetric cells were tested with two-electrode Swagelok® configuration in conventional organic electrolyte (1.5 M tetraethylammonium tetrafluoroborate/acetonitrile). Electrode film thickness was about 210 μm and the SiC-CDC loading was $7.3 \text{ mg}/\text{cm}^2$, close to that of commercial electrodes (100-200 μm or about $10 \text{ mg}/\text{cm}^2$),^[11] leading to an apparent electrode density of $0.35 \text{ g}/\text{cm}^3$.

CVs & EIS

Figure III-6a shows cyclic voltammograms of the SiC-CDC at various scan rates from 20 to 300 mV/s in 1.5 M NEt_4BF_4 in AN electrolyte. All the CVs exhibit a rectangular shape, which is characteristic of a pure capacitive behavior. When the potential scan rate was increased, the rectangular profile was nicely preserved up to 300 mV/s, although a slight distortion appeared when the potential was switched back. The perfect symmetry in the

distortion evidences an ohmic origin, which is originated from the ohmic drop in the bulk electrolyte. The specific capacitance of the prepared porous carbon is 80 F/g. This value is certainly not among the highest reported in the literature for porous carbons in organic electrolyte^[12]; however, taking into account the carbon weight loading of 7.3 mg/cm², it corresponds to a areal capacitance of more than 0.5 F/cm² per electrode, which compares favorably with most values reported in the literature^[13-16] at the same scan rate (will verify again). The specific capacitance per cm² of the electrode is representative to the energy that could be stored in a real device.^[11]

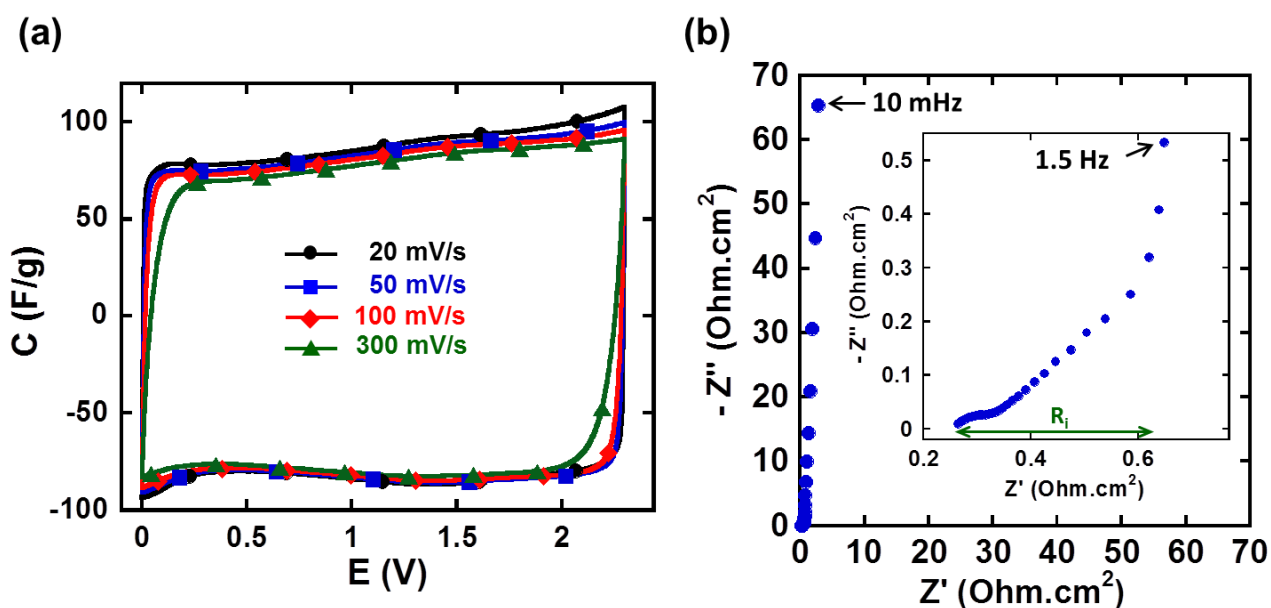


Figure III-6: Electrochemical characterization of Si-CDC in 1.5M NEt₄BF₄/Acetonitrile: CVs at different scan rates (a) and the corresponding EIS Nyquist plot (b). Inset in (b) shows data at high-frequency range (R_i = ionic resistance)

The EIS Nyquist plot of the cell (Figure III-6b) shows a typical capacitive behavior of a porous blocking electrode^[17] as well as an extremely low resistance: an equivalent series resistance (ESR) of 0.25 $\Omega \cdot \text{cm}^2$ and an ionic resistance of the electrolyte inside the porous carbon electrode of 0.35 $\Omega \cdot \text{cm}^2$. Both ESR and ionic resistance obtained are smaller than those found in the literature for other carbon-based materials (activated carbon^[17-20], other CDCs^[21], CNT^[13], CNF^[22], carbon onion^[13], graphene^[23]) in the same electrolyte under similar testing conditions. While micropores provide a good charge storage capability, a high power is anticipated from the low intrinsic resistance of SiC-CDC and high ion accessibility through the mesopores.

Figure III-7a shows CVs at high scan rates from 20 to 3,000 mV/s and Figure III-7b shows the gravimetric capacitance (derived from the slope of the Q-V curve during cell discharge) and the areal specific capacitance (obtained by dividing the electrode capacitance by the geometric area of the cell) as a function of the potential scan rate. The capacitive CV shape was preserved up to 1 V/s, with a gravimetric capacitance of 75 F/g, corresponding to > 90% of capacitance retention; this already evidences the high power performance of the material.

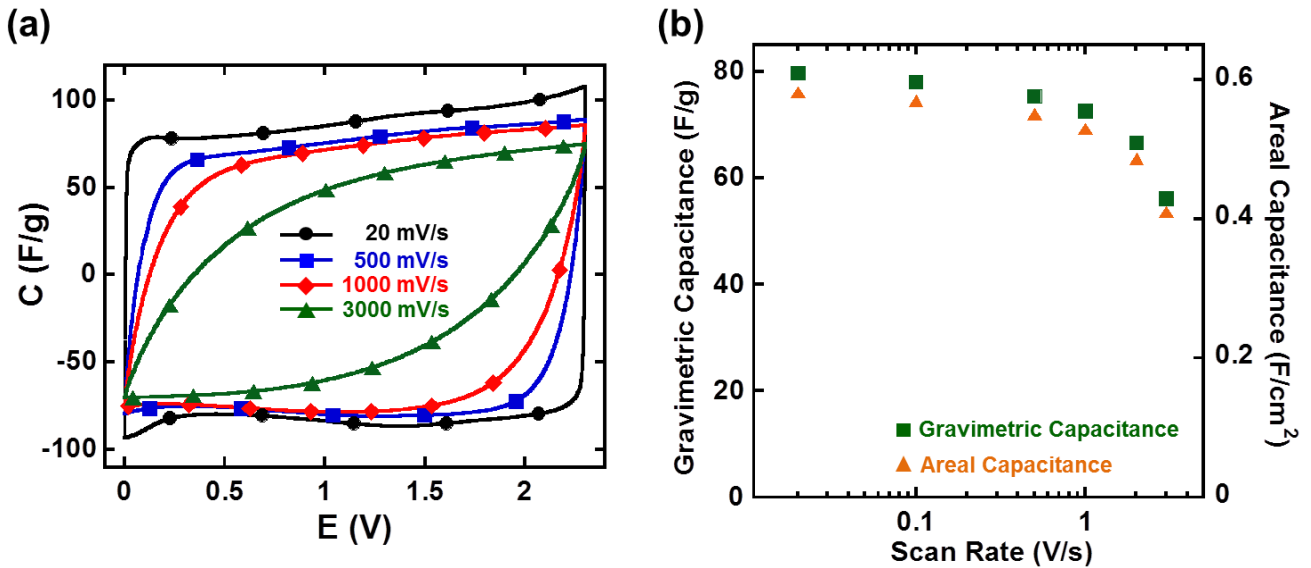


Figure III-7: Power performance investigation of SiC-CDC: CVs at high scan rates up to 3V/s (a) and capacitance vs scan rate (b)

Complex Capacitance Model (C' & C'' vs f)

The frequency behavior of the cell was analyzed using a complex capacitance model^[17], based on the modeling of the capacitance in real part $C'(\omega)$ and imaginary part $C''(\omega)$. In this model, the real part $C'(\omega)$ and imaginary part $C''(\omega)$ of the capacitance are both function of the frequency and can be extracted from the EIS data by the following equations:

$$C'(\omega) = \frac{-Z''(\omega)}{\omega|Z(\omega)|^2} \quad \text{and} \quad C''(\omega) = \frac{Z'(\omega)}{\omega|Z(\omega)|^2}$$

Where ω is the pulsation ($\omega = 2\pi \times \text{frequency}$), $Z(\omega)$ is the complex impedance, $Z'(\omega)$ and $Z''(\omega)$ are the real and imaginary part of the complex impedance, respectively.

Figure III-8a shows the change of the real part of the capacitance $C'(\omega)$ with frequency. The graph shows a transition from purely resistive behavior at high frequency (phase angle close to 0) to purely capacitive behavior at low frequency (phase angle of -87°). The whole

capacitance of the electrode is reached at around 0.2 Hz where the capacitance tends to be constant below this value; the capacitance value for a phase angle of -45° obtained at 1 Hz is 0.25 F/cm^2 . This corresponds to half of the total (low frequency) capacitance of the electrode.^[17] The change of C' vs. frequency first evidences the high power capability of the porous SiC-CDC, since the transition frequency is high, at 1 Hz. Higher power can be reached using thin-films in micro-devices for instance, or exohedral carbons with accessible but limited surface area. However, it is achieved at the expense of the energy density. As such, the areal capacitance (F/cm^2) of such devices or electrodes is low, from $\mu\text{F/cm}^2$ to few mF/cm^2 .^[15,24-26] In contrast, thanks to the hierarchical porous structure of the prepared SiC-CDC, an attractive areal capacitance of 0.5 F/cm^2 was obtained, demonstrating a higher energy density while maintaining high power performance.

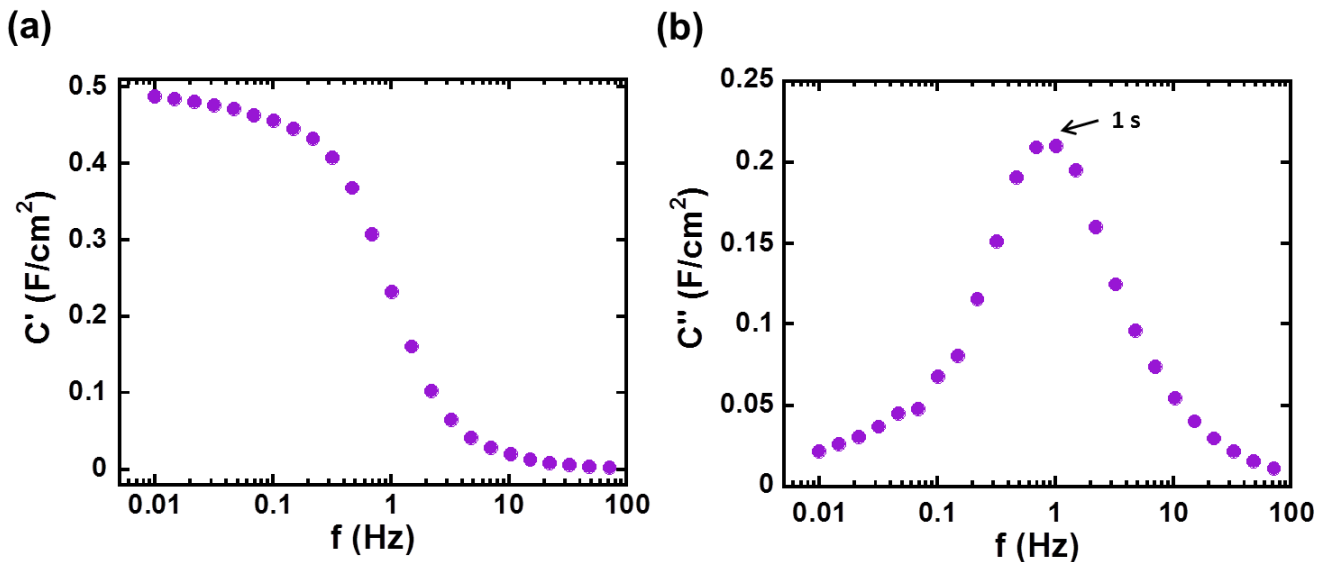


Figure III-8: Complex capacitance: Real capacitance, C' (a) and imaginary capacitance, C'' (b) vs the logarithm of frequency

Figure III-8b shows the imaginary part of the capacitance, $C''(\omega)$, versus frequency. The relaxation time τ_0 in this system is 1 second, which can be calculated from $\tau_0 = 1/f_0$, where f_0 is the frequency corresponding to the maximum of the curve of C'' vs. f . This time constant corresponds to the minimum time needed to discharge the supercapacitor while still maintaining an energy efficiency more than 50 %. These micro/mesoporous carbons thus show high power performance with high specific capacitance. These primary electrochemical characterizations in conventional organic electrolyte suggest that the magnesio-thermal reduction of SiC is an efficient way for producing carbon for high power applications.

3.2 Electrochemical characterization of SiC-CDC in IL eutectic mixture

The high power performance of micro/mesoporous SiC-CDC in $\text{NEt}_4\text{BF}_4/\text{AN}$ electrolyte indicates an improved ion accessibility in this hierarchical porous carbon thanks to the high content of mesopores; we therefore suggest that it might be a potential electrode candidate in IL eutectic mixture at low temperature with improved capacitance (hence energy density) as compared to the exohedral carbon (OLCs and CNTs). Commercial activated carbon (YP-50F) was tested under the same condition in this section for comparison. Although YP-50F exhibits higher specific capacitance (100 F/g) than that of SiC-CDC in 1.5 M $\text{NEt}_4\text{BF}_4/\text{AN}$ at ambient temperature, its structure contains mainly micropores (92 % of pores smaller than 2 nm) without hierarchical structure, hence it shows poorer power characteristics in $\text{NEt}_4\text{BF}_4/\text{AN}$ electrolyte. The pore characteristics of these two carbon materials are summarized in Table III-1. The comparison between the prepared SiC-CDC (hierarchical micro/mesoporous network) and YP-50F (microporous structure) in the much more viscous ionic liquid mixture, especially at low temperature, may highlight the effect of carbon microstructure on ion accessibility.

Table III-1: Characteristics of SiC-CDC and YP-50F

	SiC-CDC	YP-50F
BET SSA (m^2/g)	1619	1732
Total pore volume (cc/g)	1.59	0.75
Percentage of pore < 1 nm (%)	17.5	66
Percentage of pore of 1–2 nm (%)	13.5	26
Percentage of pore > 2 nm (%)	69	8
Peak pore size/mean pore size (nm)	1 and 3-4	0.9

Electrochemical Cell Preparation and Assembly

The SiC-CDC electrode films was prepared as mentioned in previous section, and tested with two-electrode Swagelok® configuration in $(\text{PIP}_{13}\text{FSI})_{0.5}(\text{PYR}_{14}\text{FSI})_{0.5}$ ionic liquid mixture. Platinum discs were used as current collectors and two layers of 25 μm -thick porous Al_2O_3 were used as separator. SiC-CDC loading is $6.2 \text{ mg}/\text{cm}^2$, close to that in previous test. YP-50F activated carbon was also prepared with similar weight loading and tested under the

same condition for comparison. Swagelok® cells were kept under light pressure during the measurement to buffer thermal expansion/contraction of the stainless steel pistons. Temperature control was achieved using a Votsch climatic chamber (Germany) with the temperature being additionally checked by a thermocouple.

Room Temperature

Figure III-9 shows the cyclic voltammograms and EIS Nyquist plots of SiC-CDC and YP-50F in IL mixture at room temperature (20°C) at 20mV/s. Both CVs of SiC-CDC and YP-50F present rectangular profiles, confirming nice capacitive characteristics of both

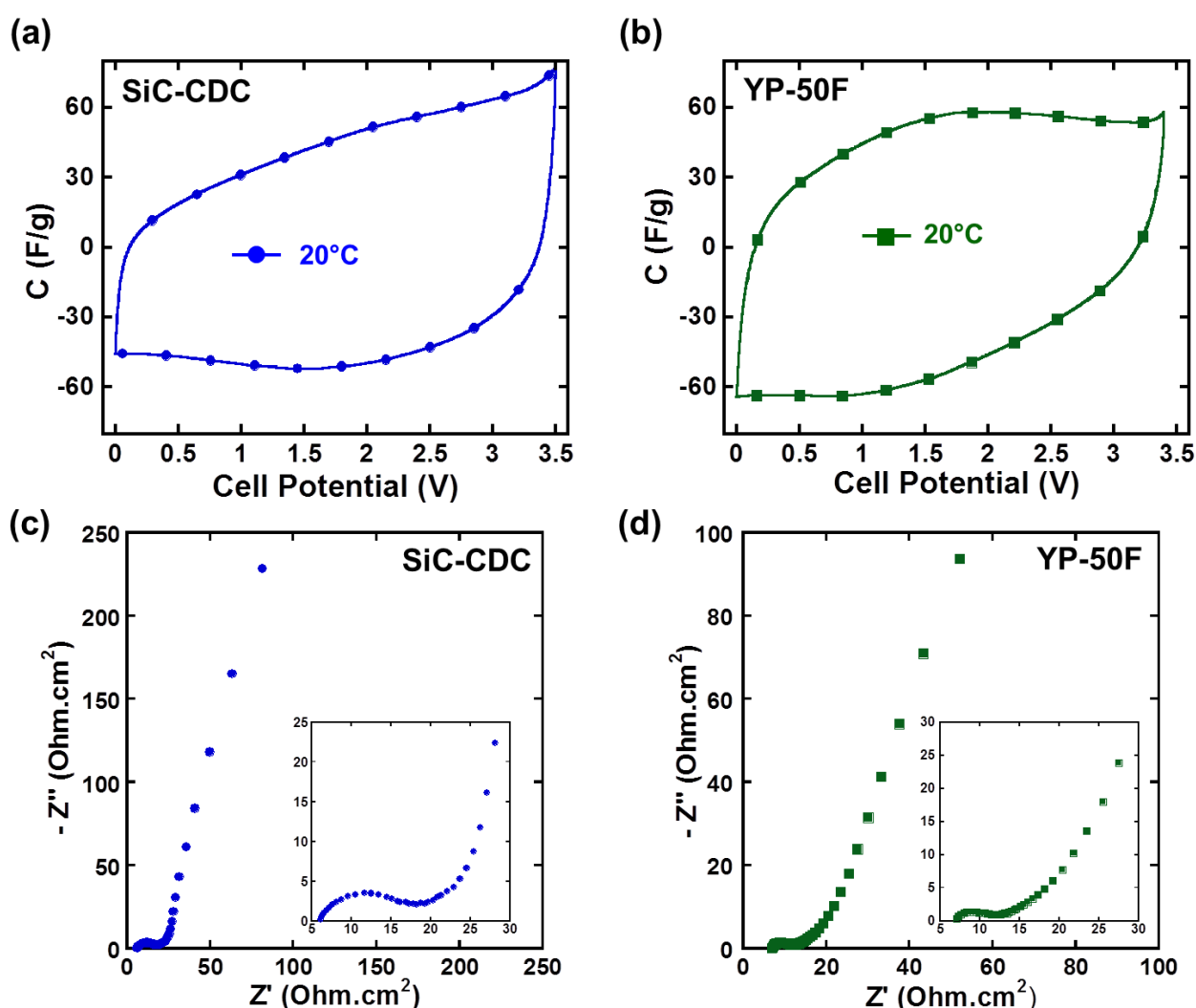


Figure III-9: Electrochemical characterization of SiC-CDC (a, c) and activated carbon YP-50F (b,d) in (PIP13FSI)0.5(PYR14FSI)0.5 ionic liquid mixture - cyclic voltammograms at 20mV/s (a, b) and EIS Nyquist plots (c, d)

materials. A wide electrochemical window of 3.5 V was achieved for both materials. The specific capacitance (calculated from the slope of the Q-V curve during cell discharge at 5mV/s rate) of SiC-CDC and YP-50F are 55 and 74 F/g, respectively. YP-50F exhibits higher capacitance due to its higher content of micropores, which are also responsible for the large distortion in the CVs.

The ESR of YP-50F ($7.1 \Omega \cdot \text{cm}^2$) in IL mixture was slightly higher than that of SiC-CDC ($6 \Omega \cdot \text{cm}^2$). The moderate capacitances and the relatively high ESRs of both carbon samples are attributed to the high viscosity (4.9 mS/cm)^[1] and low mobility of ionic liquid electrolyte at room temperature as compared to that in 1.5 M $\text{NEt}_4\text{BF}_4/\text{AN}$ (with a conductivity of 60 mS/cm).

Elevated Temperature ($20 \leq T \leq 60 \text{ }^\circ\text{C}$)

Figure III-10 shows CVs (plotted in the same scale) of SiC-CDC and YP-50F at elevated temperature ($20 \leq T \leq 60 \text{ }^\circ\text{C}$) with scan speed of 20 mV/s up to 3V. All the CVs preserve the capacitive characteristics at both scan samples. SiC-CDC held similar electrochemical behaviors between 20 to 60 °C, while YP-50F shows higher capacitance than SiC-CDC among all the elevated temperature.

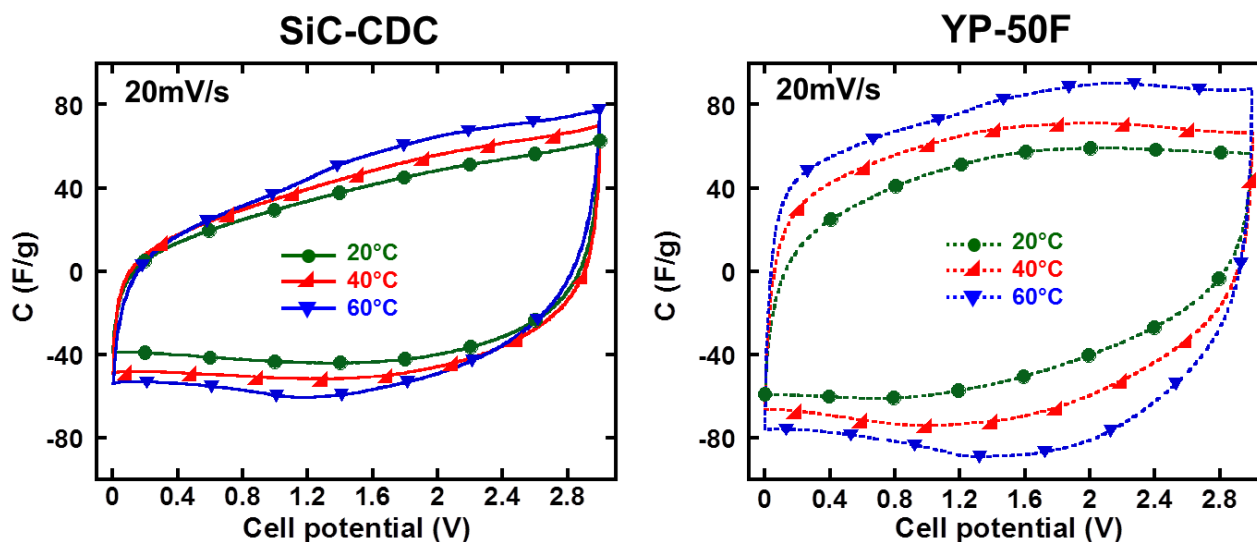


Figure III-10: Electrochemical characterization of SiC-CDC and activated carbon YP-50F in IL mixture at high temperature ($20 \leq T \leq 60 \text{ }^\circ\text{C}$) – CVs at scan rate of 20 mV/s

Temperature shows stronger influence on capacitance for YP-50F samples than SiC-CDC samples. The increase of capacitance with temperature is attributed to the increase ion mobility with temperature. The maximum applicable potential window is related to temperature - the higher the temperature, the higher the material activity, hence the narrower the window. The maximum windows of SiC-CDC and YP-50F at 20 mV/s at 60 °C were 3.5 and 3.3 V, respectively.

Sub-zero Temperatures (-20 & -40 °C)

The electrochemical characterization of both SiC-CDC and YP-50F at -20 & -40 °C are shown in Figure III-11. The CVs (Figure III-11a and b; plotted in the same scale) at 5 mV/s up to 3.5 V show that the two carbon samples behave differently when temperature decreases. The capacitance of YP-50F reduced significantly to 25 and 11 F/g at -20 and -40 °C, respectively, which correspond to 34 % and 15 % of the capacitance at room temperature with the same scan rate. While for SiC-CDC carbon, at low temperature of -40 °C, it kept 70 % of its capacitance when operating at room temperature.

EIS measurements (Figure III-11c and d) still show capacitive characteristics for both materials at -40 °C. The extra semi-circles at high frequency range might be attributed to the onset of the gelation or increased immobility of the electrolyte ions in the narrow porous structure. In addition, YP-50F carbons presented a higher resistance than that of SiC-CDC at low frequency tail. Both CV and EIS indicate that at low temperature, ions have lower mobility and less accessibility inside a pure microporous material (YP-50F) than in the material containing hierarchical network (SiC-CDC).

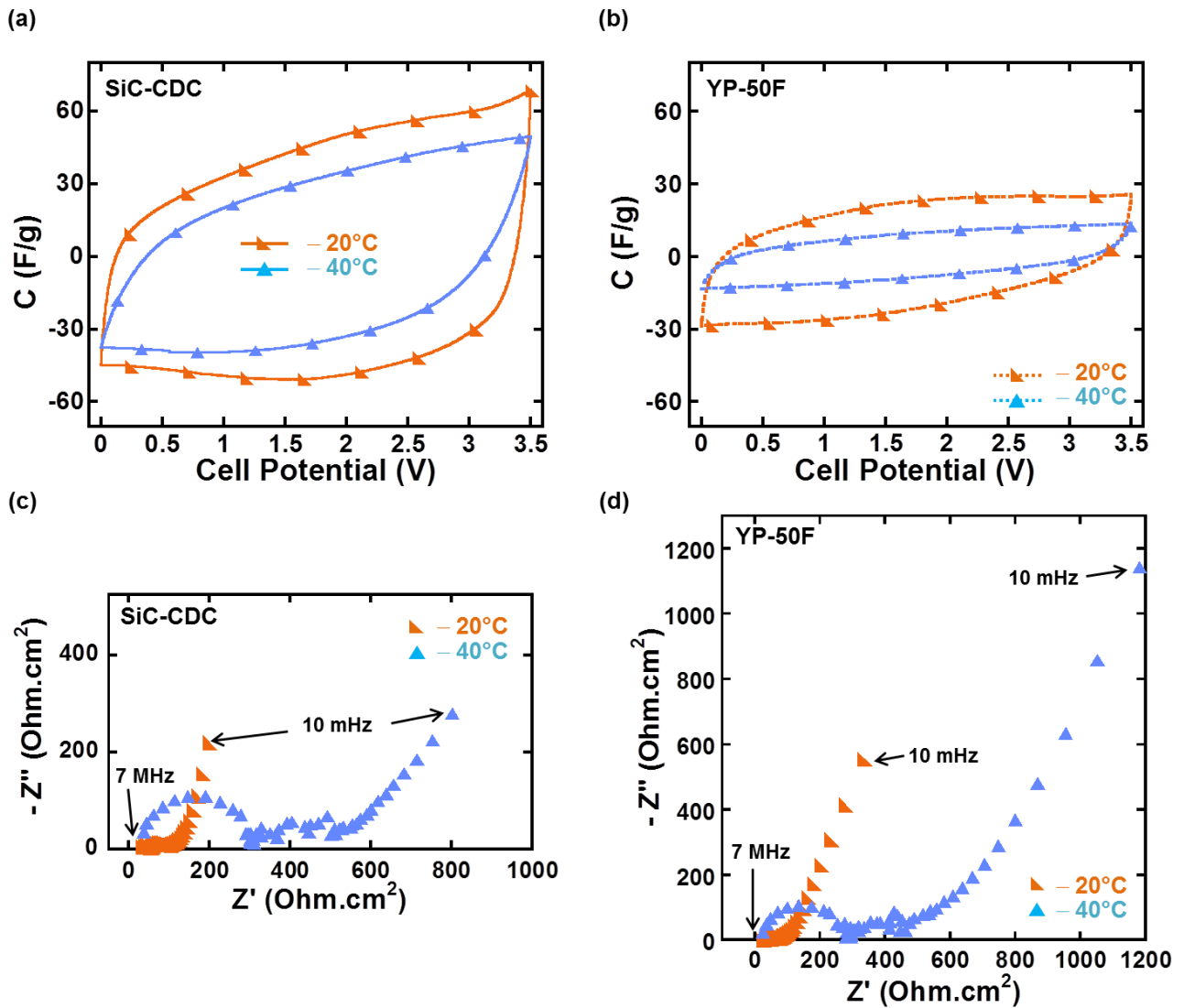


Figure III-11: Electrochemical characterization of SiC-CDC (a, c) and YP-50F (b,d) in (PIP13FSI)_{0.5}(PYR14FSI)_{0.5} ionic liquid mixture at low temperature - cyclic voltammograms at 5mV/s (a, b) and EIS Nyquist plots (c, d)

Temperature Dependence and Power Performance

Figure III-12 compares the electrochemical behaviors of SiC-CDC and YP-50F in terms of temperature and scan rate: CVs collected at 20 and 60 °C with scan rates of 20 and 100 mV/s, and at -20 and -40 °C with scan rates of 5 and 20 mV/s. In both carbon samples, the higher the temperature, the higher the ionic mobility in the pores, thus the higher the capacitance; on the other hand, the higher the scan rate, the less time allowed for ion to respond to the applied polarization, the lower the capacitance. The temperature dependence and power dependence are compared individually in Figure III-13 and Figure III-14.

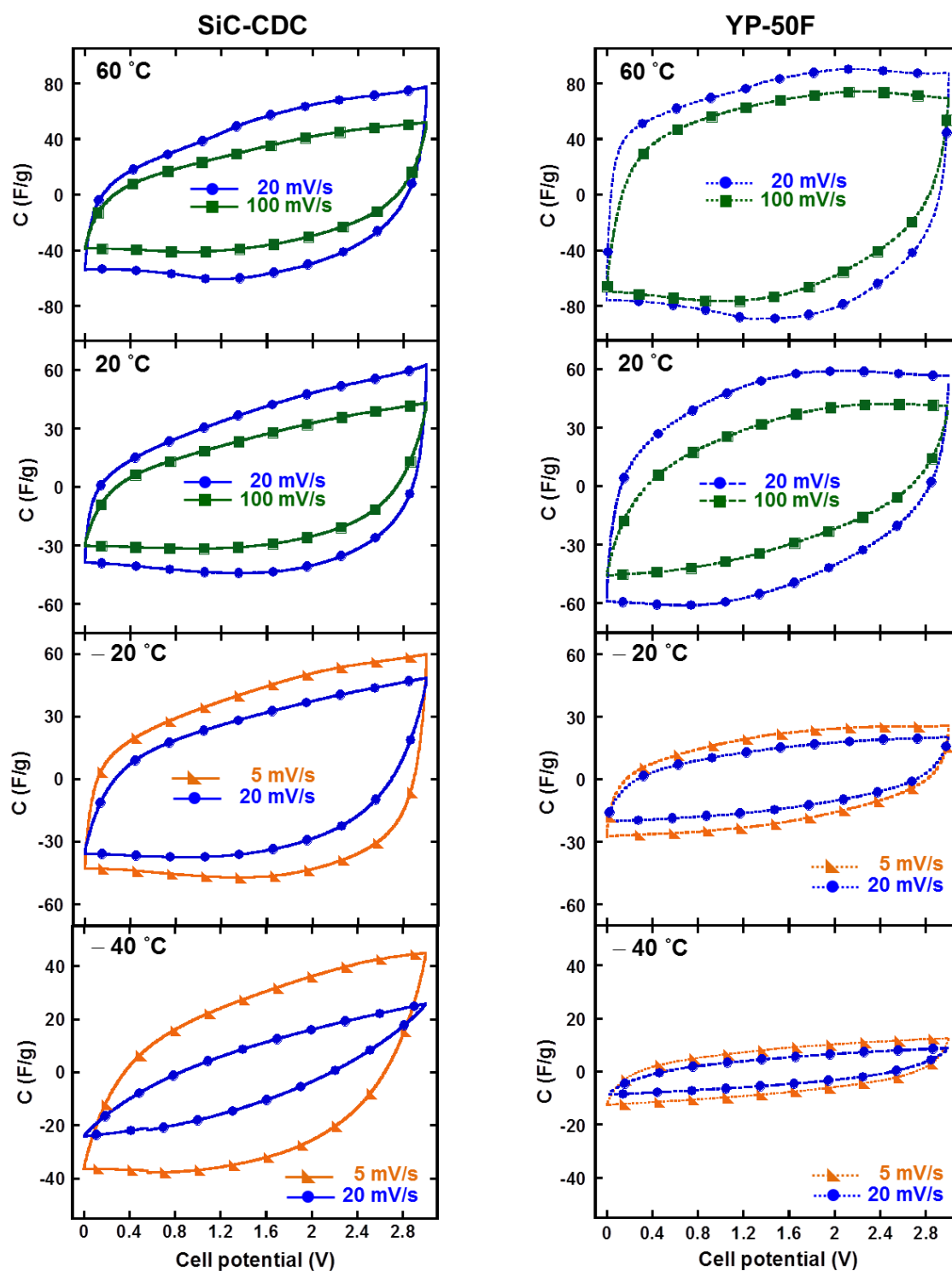


Figure III-12: CVs of SiC-CDC and activated carbon YP-50F in IL mixture at 20 and 60 °C with scan rates of 20 and 100 mV/s, and at -20 and -40 °C with scan rates of 5 and 20 mV/s.

The temperature dependence of the specific capacitance at moderate scan rate of 20 mV/s was plotted and shown in Figure III-13. At elevated temperature ($T \geq 20$ °C), where the ions own high mobility, YP-50F presents much higher capacitance than that of SiC-CDC

since it contains large amount of micropores. However, when the temperature decreases, the ion mobility is highly limited in such narrow microporous network, therefore the capacitance drops significantly with temperature. At 0 °C, the capacitance of YP-50F already becomes smaller than that of SiC-CDC. Whereas for SiC-CDC, the capacitance does not change a lot between -20 and 60 °C, indicating that good ion accessibility is achieved in the SiC-CDC hierarchical porous structure within this temperature range.

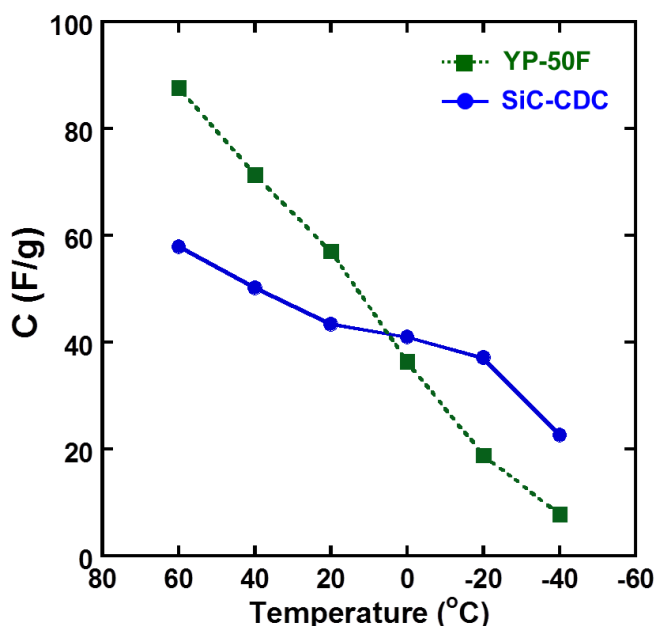


Figure III-13: Temperature dependence of specific capacitance (calculated from Q-V slope during discharge at 20 mV/s). SiC-CDC shows better capacitive behavior than YP-50F at low temperature.

The capacitance versus scan rate at 20, 0, -20, and -40 °C are shown in Figure III-14. SiC-CDC shows better capacitance retention than that of microporous activated carbon as scan rate increased. It also shows higher capacitance than exohedral carbons even at low temperature of -40 °C. These results evidence that the prepared SiC-CDC allows the operation in IL mixture at low temperature down to -40°C thanks to its ordered mesopores which serve as ion reservoirs and transport channels, and the capacitance was improved as compared to the exohedral carbons (20 to 30 F/g, highlighted in red dashed line in the Figure) owing to the presence of micropores.

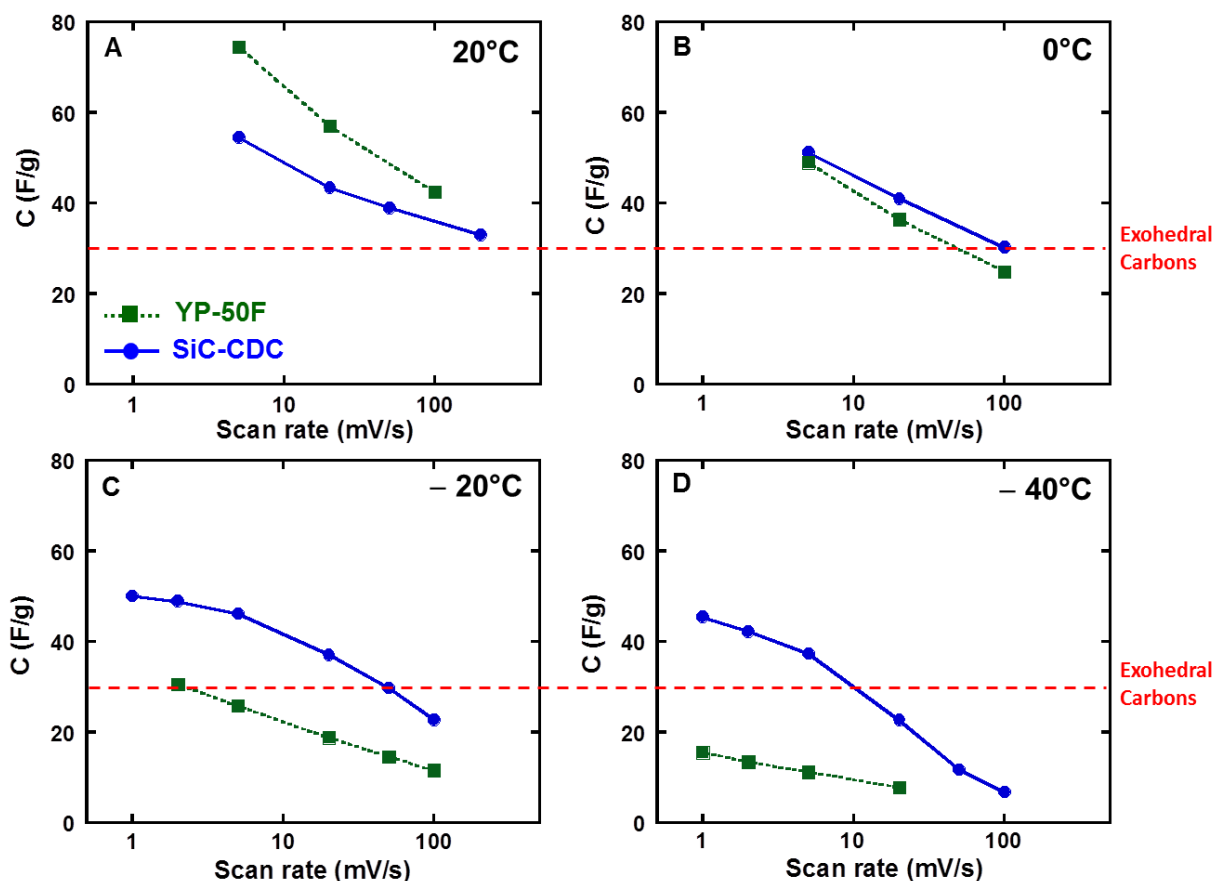


Figure III-14: Power performance of SiC-CDC and YP-50F at 20, 0, -20, and -40 °C. Capacitance was calculated from the Q-V slope during discharge at different scan rates. Capacitance of exohedral carbon (~30 F/g) used in the same ILs mixture was also highlighted in red dashed line as reference.

In this section, the hierarchical meso/microporous SiC-CDC was compared with microporous YP-50F and previously reported exohedral carbons^[1]. The mesopores offer a wider pathway for ion transport, thus greatly improve the supercapacitor performance at low temperature as compared to the commercial activated carbon which only contains micropores. Additionally, capacitance is improved as compared to the exohedral carbons due to the higher SSA and introduction of endohedral surface. These results highlight again the importance of selecting appropriate carbon nanostructures to match the nature of the electrolyte.

4. Activated Graphene (a-MEGO) in IL mixture

In previous section, the use of ordered micro/mesoporous SiC-CDC in ILs mixture has shown good capacitive behavior with improved capacitance at low temperature with regards to both exohedral carbons with a totally open surface and commercial activated carbon containing only micropores. This proves that both micropores and mesopores are important for energy storage in supercapacitors. However, due to the high amount of mesopore (~70%) in the SiC-CDC, an important part of the pore volume in the material does not contribute to charge storage; hence the capacitance only improves by a factor of two as compared to OLCs and CNTs in ILs mixture. A porous carbon possessing high accessible SSA, optimized ratio between micropores and mesopores, and ion accessible pore architecture is thus needed.

Graphene, as mentioned in Chapter I, its well-known high theoretical SSA (2630 m²/g) and high electrical conductivity make it an interesting candidate as supercapacitor electrode material. Ruoff's group has recently reported on the activation of microwave exfoliated graphite oxide ('MEGO') using potassium hydroxide.^[27] This carbon ('a-MEGO') shows unique structure and properties, such as high SSA (up to 3100 m²/g) and high accessible surface area, low O and H content, and is composed mostly of *sp*² bonded carbon, therefore we reasoned that it might yield to important increase in specific capacitance, compared to OLCs or CNTs, with the (PIP₁₃-FSI)_{0.5}(PYR₁₄-FSI)_{0.5} ionic liquid electrolyte.

Synthesis and Characterization of Activated graphene (a-MEGO)

The synthesis procedure for a-MEGO, as well as its characterization, has been conducted by Professor Rodney Ruoff's group (University of Texas at Austin, USA) and described in detail in reference 27. MEGO was prepared from graphite oxide (GO) by microwave irradiation,^[28] then dispersed and soaked in aqueous KOH solution for 20 h. The solid cake obtained after vacuum filtration of the excess KOH was then dried. The dry MEGO/KOH mixture was heated at 800 °C for 1 hour in a horizontal tube furnace with an argon flow of 150 sccm at atmospheric pressure. The sample was then washed with de-ionized water, and dried at 65 °C in ambient air for 2 hours. Annealing of activated graphene was done in a custom made vacuum furnace (Solar Atmospheres, USA) at 1100 °C, with the heating ramp 10 °C/min, and a vacuum ~10⁻⁶ Torr for 10 minutes.

Schematic showing the microwave exfoliation/reduction of GO and the following

chemical activation of MEGO with KOH, and SEM and TEM images of the prepared a-MEGO are reported in reference 27 and reproduced in Figure III-15. This graphene material showed a continuous, three dimensional pore structure comprised of highly curved single-layer sheets of n-membered rings of carbon, with n varying between 5 and 8.

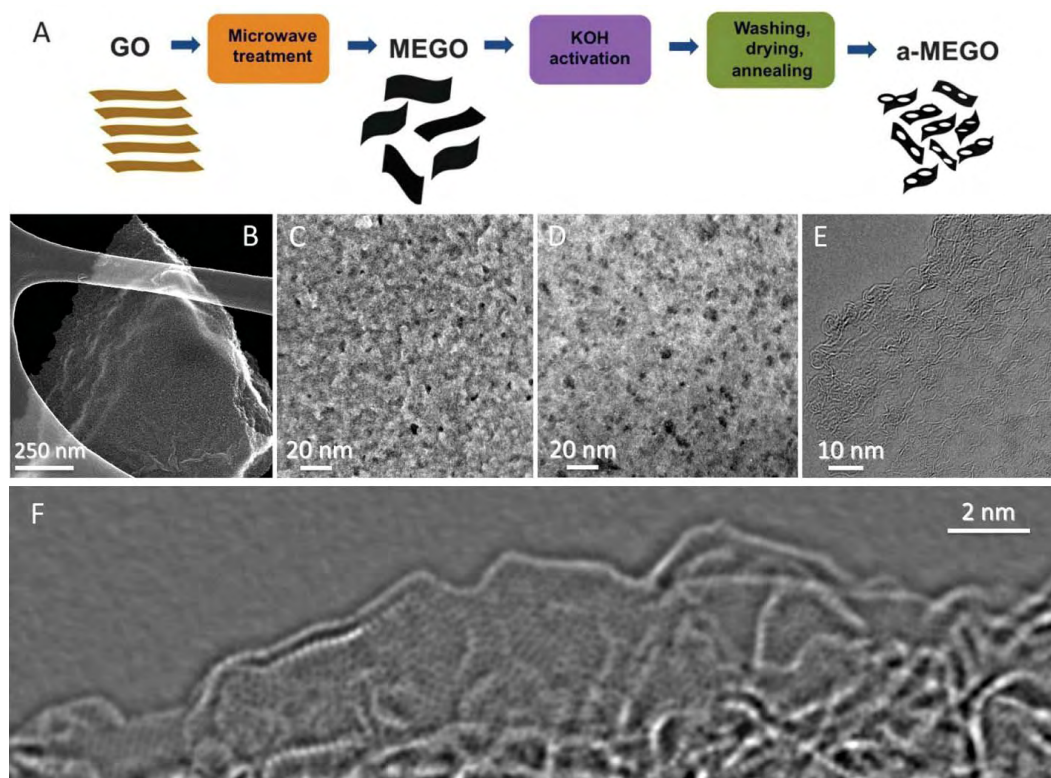


Figure III-15: Schematic showing the microwave exfoliation/reduction of GO and the following chemical activation of MEGO with KOH that creates pores while retaining high electrical conductivity (A). Low magnification SEM image of a 3D a-MEGO piece (B). High-resolution SEM image of a different sample region that demonstrates the porous morphology (C). ADF-STEM image of the same area as (C), acquired simultaneously. As seen, a-MEGO contains micro- and mesopores with a distribution of sizes between ~ 1 and ~ 10 nm (D). High-resolution phase contrast electron micrograph of the thin edge of an a-MEGO chunk, taken at 80 kV. There is a variation in focus across the image because of the sloped nature of the sample and changes in sample thickness. The image shows the presence of a dense network of nanometer scale pores surrounded by highly curved, predominantly single-layer carbon (E). Exit wave reconstructed HR-TEM image from the edge of a-MEGO (F). The in-plane carbon atoms are clearly resolved, and a variety of n-membered carbon rings can be seen. Substantial curvature of the single-carbon sheets is visible, with the in-plane crystallinity being preserved. (From reference ^[27])

Nitrogen gas sorption was performed at 77 K using a Quadrasorb Pore Size and Surface Area Analyzer (Quantachrome Instruments, USA). Prior to analysis, samples were outgassed at 200 °C in vacuum at about 10^{-2} Torr for 24 hours. BET surface area was calculated in the range of 0.05-0.3 P/P₀. Pore size distributions were determined using the quenched solid density functional theory (QSDFT) model, assuming a slit pore geometry, which was part of the QuadraWin software package (Quantachrome Instruments, USA).

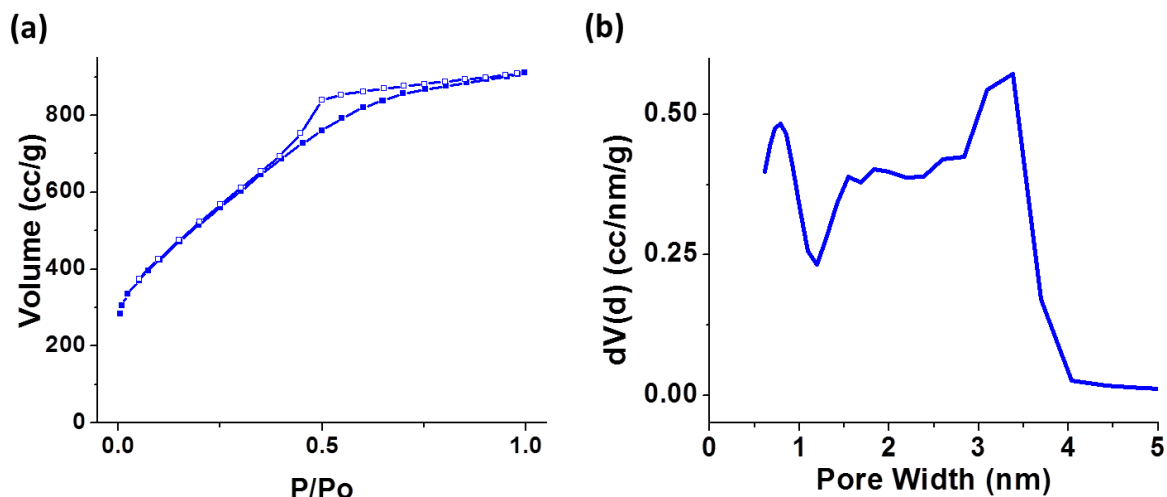


Figure III-16: Nitrogen sorption isotherms (a) and corresponding pore size distributions calculated by QSDFT model (b) for activated graphene (BET SSA 1901 m²/g)

Single-layer graphene has a theoretical specific surface area of 2630 m²/g, however in practice the BET SSA is generally much lower because of multi-layer sheets and agglomeration. We approach the theoretical value of a single sheet of graphene, with as-activated a-MEGO having a high surface area of 1901 m²/g and all pores less than 5 nm (Figure III-16a). The a-MEGO has a desirable PSD for supercapacitors, as it has both micropores that give it a high SSA, in the range of values typical for activated carbons, and mesopores that facilitate ion mobility during charging and discharging.

4.1 Electrochemical characterization of activated graphene in IL mixture

Electrochemical Cell Preparation and Assembly

Two-electrode Swagelok® nylon cells with stainless steel pistons were used for quantitative electrochemical characterizations of as-activated MEGO (a-MEGO) powder. Cells were assembled in the eutectic mixture of ILs under glove-box conditions. Pt disks were used as current collectors to decrease the contact resistance at the as-activated a-MEGO/piston interface. For the as-activated a-MEGO, electrode films (disks) of 1.1 cm², 1.65 mg and 55 μm thick were made of 95% of the carbon powder and 5% of PTFE (Dupont de Nemours) binder as described in Zhu *et al.*^[27] Electrodes and two layers of Al₂O₃ separators were wetted with the electrolyte prior to being placed between the electrodes. Swagelok® cells were kept under light pressure during the measurement to buffer thermal expansion/contraction of the stainless steel pistons. Temperature control was achieved using a Votsch climatic chamber (Germany) with the temperature being additionally checked by a thermocouple. After heating to a certain temperature, the system was kept isothermal for a period of no less than 5 hours prior to electrochemical measurements to ensure system equilibration. For low temperature experiments, this dwell time was increased to an overnight period (> 6 hours).

Room Temperature

Figure III-17a shows the CV of as-activated a-MEGO electrodes in the IL mixture scanned at 20 mV/s at room temperature. The characteristic rectangular CV profile confirms the feasibility of using the eutectic IL mixture with as-activated a-MEGO. A maximum operating voltage of 3.7 V (same as for the OLCs) was obtained at room temperature with a capacitance of ~160 F/g, which is a 5-fold increase compared to OLCs and CNTs (~30 F/g)^[1] and 3-fold increase to SiC-CDC. This huge increase can be firstly attributed to the highly accessible SSA of the as-activated a-MEGO electrodes. Moreover, the open inter-layer porosity of the as-activated a-MEGO electrodes allows electrolyte ions access to the subnanometer pores in a-MEGO sheets without much limitation in ion transfer, as may occur when using conventional activated carbons with a tortuous pore network and narrow bottlenecks between pores.^[1]

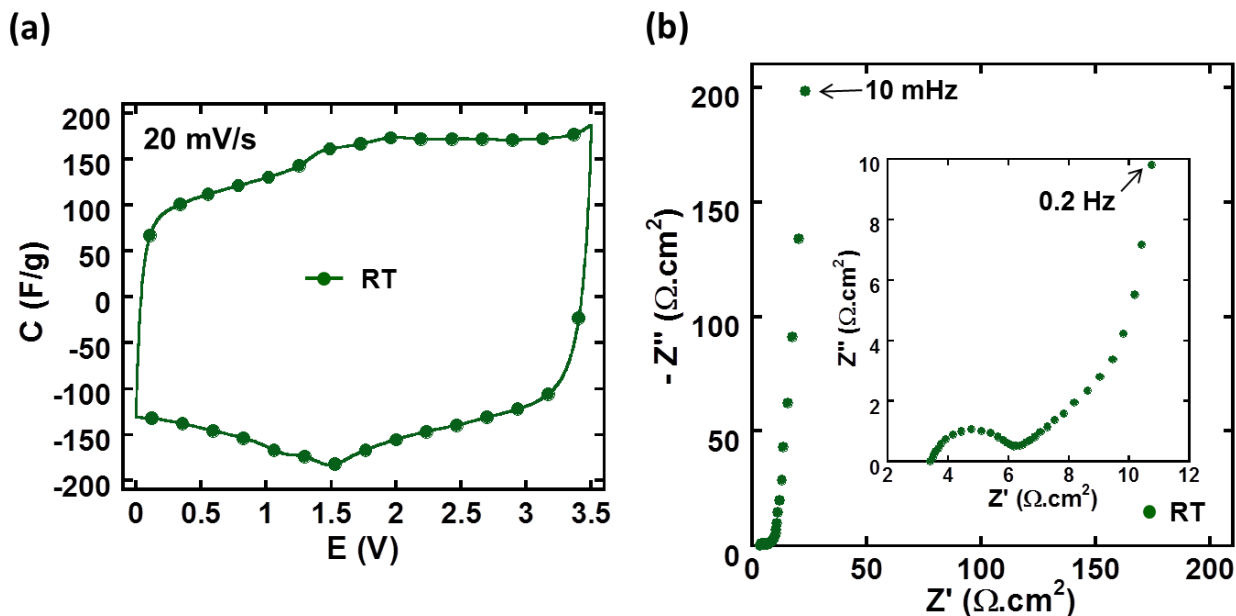


Figure III-17: Room temperature electrochemical characterization of a-MEGO electrodes in $(\text{PIP}_{13}\text{-FSI})_{0.5}(\text{PYR}_{14}\text{-FSI})_{0.5}$ electrolyte: CVs collected at 20 mV/s with the electrochemical window of 3.5 V and showing capacitance of 150 F/g (a) and the corresponding EIS Nyquist plot (b). Inset in (b) shows the high-frequency range.

Figure III-17b shows the EIS plot for the activated graphene electrodes assembled in the ionic liquid mixture. The vertical increase of the imaginary part of the impedance at low frequency provides evidence of the capacitive storage achieved with a-MEGO. A fairly low ESR of $3.4 \Omega \cdot \text{cm}^2$ was measured at room temperature ($10 \Omega \cdot \text{cm}^2$ ESR was measured for CNT electrodes^[1], and $6 \Omega \cdot \text{cm}^2$ for SiC-CDC), mainly due to the high electrical conductivity of the a-MEGO electrode (500 S/cm) compared to commercial activated carbons ($0.1 - 1 \text{ S/cm}$).^[29] Thanks to the 2-dimensional nature, both sides of the atom-thick pore walls of a-MEGO (graphene layers) can be used in charge storage, once the electrolyte gains access to these surfaces, a tremendous amount of charge could be stored as observed in the 5-fold increase in capacitance using a-MEGO.

Elevated Temperature ($20 \leq T \leq 80 \text{ }^\circ\text{C}$)

Figure III-18a shows CVs recorded at 100 mV/s to their respective maximum voltages at different temperatures. There is a gradual increase of capacitance with increasing temperature that can be explained by the higher ionic conductivity (ion mobility) of the electrolyte at elevated temperatures, which is also reflected in the more rectangular shape of the CVs with

increasing temperature, as observed in previous section. Electrochemical impedance measurements further confirm the decrease in ionic resistance as shown in Figure III-18b, and the ESR value decreases from 3.4 to $1.3 \Omega \cdot \text{cm}^2$ while increasing the temperature from 20°C to 80°C . The capacitance increases from 160 to 180 F/g as temperature increases from RT to 80°C .

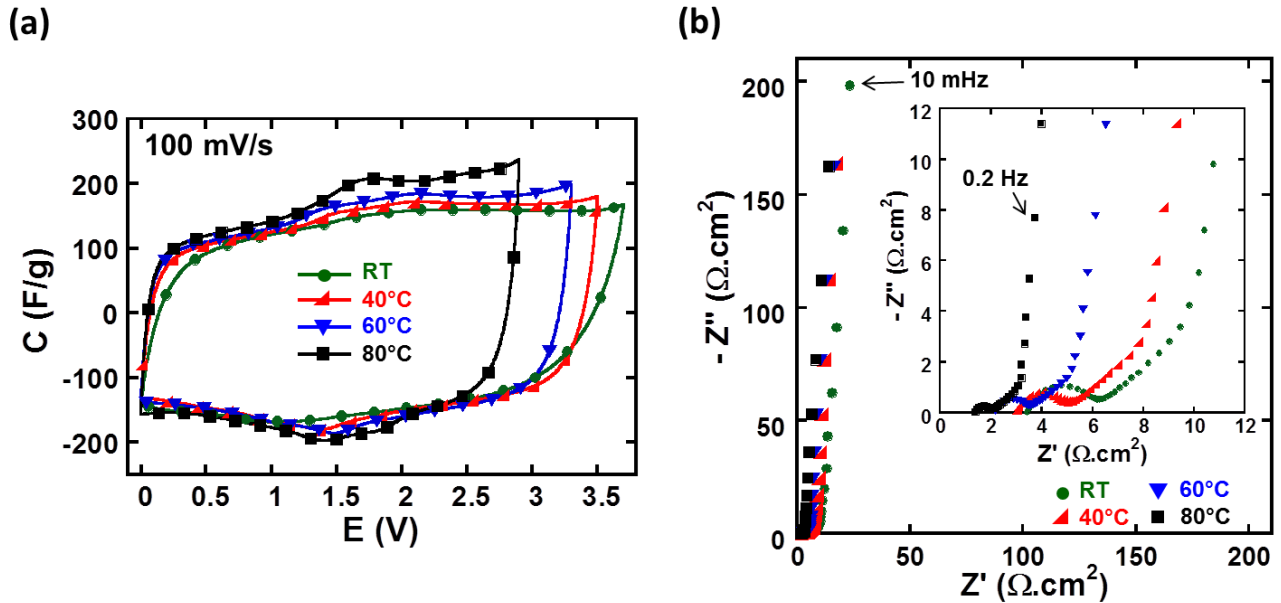


Figure III-18: Electrochemical characterization of a-MEGO electrodes in $(\text{PIP}_{13}\text{FSI})_{0.5}(\text{PYR}_{14}\text{-FSI})_{0.5}$ electrolyte at room and elevated temperatures: CVs collected at 100 mV/s (a), corresponding EIS Nyquist plots (b)

The electrochemical window decreases as the temperature increases, and is limited to 2.9 V at 80°C . This may be related with the catalytic nature of the platinum current collectors used in the tests. Further experiments were conducted by placing a spacer and ionic liquids in between two *platinum* or two *gold* current collectors, without a-MEGO electrodes, in same Swagelok® cell configuration as that of a-MEGO. CVs collected using different current collectors at room temperature and 80°C were presented in Figure III-19. The results showed that higher electrochemical activity at platinum current collectors is observed at elevated temperature due to its catalytic nature. This explains the reasons why the operating voltage is limited to smaller value at elevated temperature.

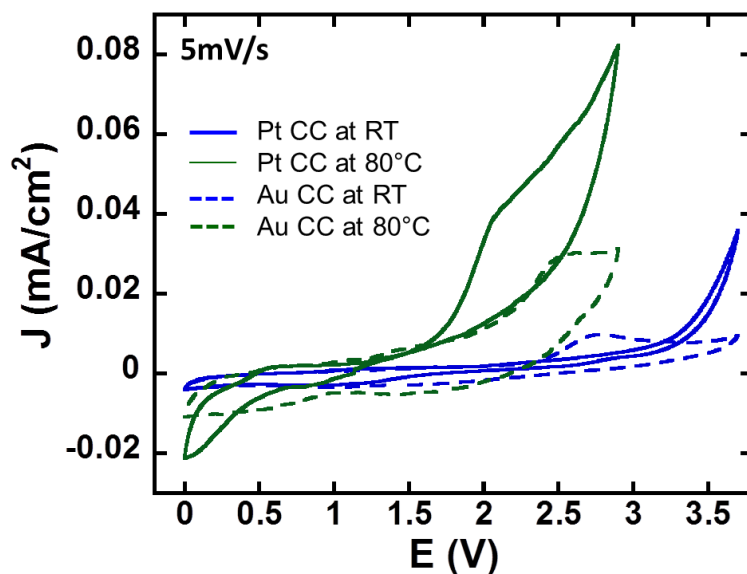


Figure III-19: Electrochemical activity of platinum and gold current collectors in $(\text{PIP}_{13}\text{FSI})_{0.5}(\text{PYR}_{14}\text{-FSI})_{0.5}$ at room temperature and $80\text{ }^{\circ}\text{C}$

Sub-zero temperatures (-40 and -50 °C)

Figure III-20a shows the CVs recorded at sub-zero temperatures of -40 and $-50\text{ }^{\circ}\text{C}$. About 70% of the capacitance is still retained at 1 mV/s (which is a reasonable scan rate taking into account the reduced ion mobility for such low temperatures) and the CVs show good capacitive behavior at $-40\text{ }^{\circ}\text{C}$ with high capacitance values of 100 to 120 F/g obtained when charged to 3 V. Such retention of capacitance over this wide operating temperature range (from $-50\text{ }^{\circ}\text{C}$ to $80\text{ }^{\circ}\text{C}$) with capacitance always above 100 F/g is, to our knowledge, has never been reported before in the literature.^[30-37] EIS measurements (Figure III-20b) still show a capacitive behavior, despite the presence of an expected extra semi-circle at high frequency, attributed to the onset of gelation and related decreased mobility of the electrolyte ions within the pores of a-MEGO at such low temperatures.^[38-40] The capacitive behavior of a-MEGO decreases at $-50\text{ }^{\circ}\text{C}$ which is evident by a less rectangular CV than that seen in the CNTs.

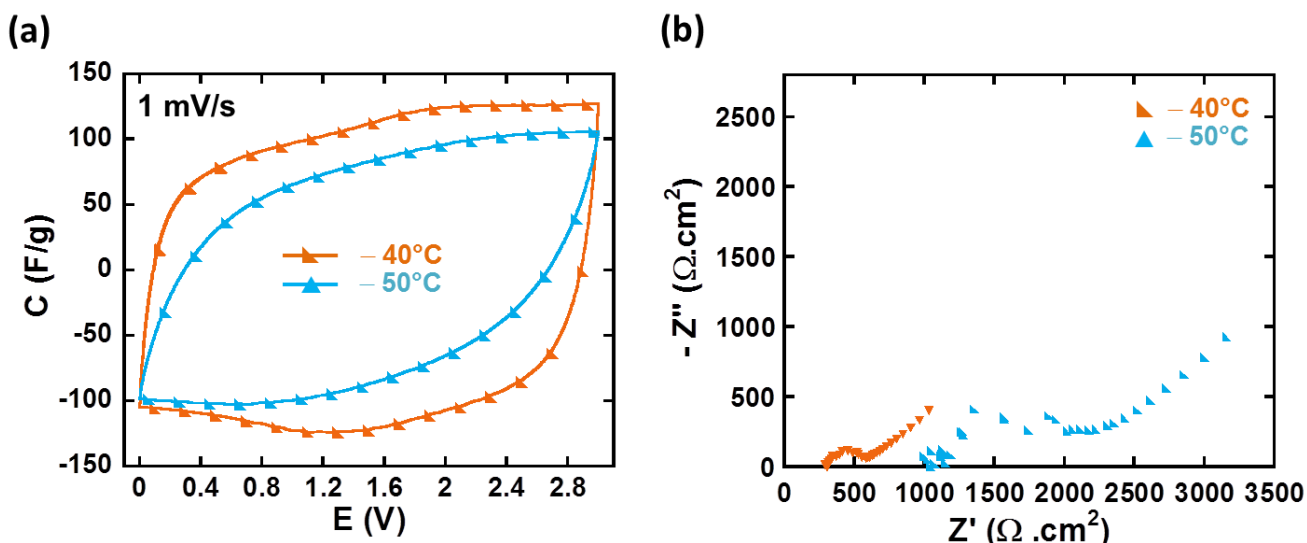


Figure III-20: Electrochemical characterization of a-MEGO electrodes in $(\text{PIP}_{13}\text{FSI})_{0.5}(\text{PYR}_{14}\text{-FSI})_{0.5}$ electrolyte at low temperatures (-40 and -50 C): CVs collected at 1 mV/s (a) and the corresponding EIS Nyquist plot (b).

4.2 Removal of surface functional group by vacuum annealing

While the a-MEGO electrodes show outstanding capacitance of ~ 160 F/g (see Figure III-17a), the presence of bumps in the CV at about 1.5 V could be due to electrochemically active oxygen-containing functional groups, such as carboxylic acid or hydroxyl groups on their surface. Such bumps were also observed when a-MEGO electrodes were tested in EMI-TFSI electrolyte.^[27] Although they are suitable for improving the capacitance, such surface groups are known to be unstable during cycling, thus limiting the cycle life of the cells.^[41] Therefore, we further conducted annealing on the a-MEGO powder under vacuum to try to eliminate functional groups that may be present on its surface. Apart from the point that the functional groups are generally unwanted for *double-layer* type of supercapacitors, from fundamental point of view, it can be interesting to determine the active oxygen sites by active surface area (ASA) quantification technique as proposed by Vix-Guterl et al^[42], and to further study the relationships between surface chemistry, interfacial properties and capacitive charging.

Vacuum Annealing

The a-MEGO was annealed at 1100 °C in vacuum at an attempt to remove the oxygen containing surface functional groups. At this temperature with appropriate exposure time, one

might expect that oxygen containing groups would be removed while the structure of the a-MEGO might be preserved.

The nitrogen sorption isotherms and pore size distributions of the as-activated and vacuum annealed a-MEGO are shown in Figure III-21. From Figure III-21b, after annealing, the BET SSA is $1586 \text{ m}^2/\text{g}$, and the peak in the PSD around 3.25 nm is smaller than for the as-activated a-MEGO. The microporous region ($< 2 \text{ nm}$) was unchanged after annealing, indicating the initial pore structure in graphene sheets has been largely preserved. Comparing the pore structure of vacuum annealed a-MEGO to the as-activated a-MEGO material, the pore size distribution of the vacuum annealed a-MEGO tends to a smaller average pore size and has a smaller specific surface area than those of as-activated a-MEGO. Both materials have all pores less than 10 nm . Other materials for supercapacitors, such as CDC and activated carbon, have similar surface areas to vacuum annealed a-MEGO, but tend to have an intricate network of pores that limits ion transport rates and prevents fast charging and discharging when viscous IL electrolytes are used.^[1,3]

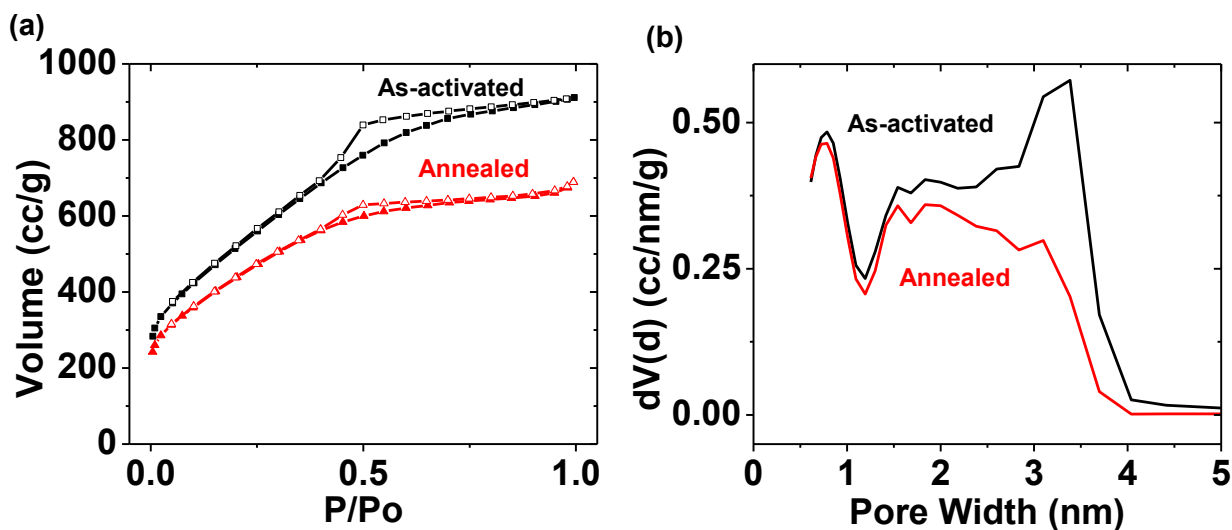


Figure III-21: Nitrogen sorption isotherms (a) and corresponding pore size distributions (b) for as-activated (BET SSA $1900 \text{ m}^2/\text{g}$) and vacuum annealed a-MEGO (BET SSA $1590 \text{ m}^2/\text{g}$). After annealing, there is a decrease in the volume of small mesopores around 3 nm , while the micropores within graphene sheets are preserved. Closed symbols in (a) represent the adsorption branch while open symbols represent the desorption branch.

The disorder and graphitic nature of the structure before and after annealing was analyzed using Raman spectroscopy, recorded with an Invia confocal Raman spectrometer (Renishaw, UK) using a laser with an excitation wavelength of 514.5 nm and having a spot size

of 2 μm (Figure III-22). There is very little difference in the two spectra, thus evidencing that the annealing process did not change the graphene layer structure. The main difference lies in the full width at half maximum (FWHM) of the disorder-induced (D) band, which narrows after annealing from 160 to 140 cm^{-1} , proving healing of some defects. The main goal of annealing the activated graphene was to remove oxygen groups on the surface without affecting a-MEGO structure, which seems to be successful from the Raman spectra as the difference before and after annealing is subtle. Here again, the determination of the ASA of the a-MEGO could be interesting for quantifying the effect of annealing treatment.

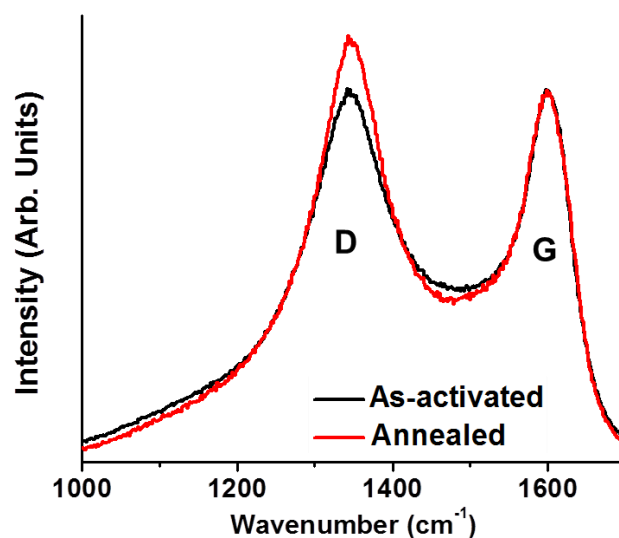


Figure III-22: Raman spectra of as-activated and annealed graphene in the carbon spectral range showing the bands corresponding to disordered structures (D) around 1350 cm^{-1} and in-plane vibrations of graphite (G) around 1600 cm^{-1} . Note that there is no significant change of the structure as a result of annealing.

Annealed a-MEGO Electrochemical Cell Preparation and Assembly

A three-electrode Swagelok® nylon cell was used to characterize vacuum annealed a-MEGO powders. The cell assembly was similar as described in previous section. A silver wire was used as a quasi-reference electrode, platinum discs as current collectors, YP17 activated carbon as counter electrode, and the annealed a-MEGO powders were tested directly without film processing.

Cavity microelectrode (CME) was also used for investigating the difference between the a-MEGO before and after annealing. The CME configuration is illustrated in Figure III-23 and described in detail in Chapter II. A cavity with diameter of 50 μm was created by laser

ablation on the tip of the electrode. The a-MEGO powders were packed inside the cavity by simply pressing CME on the powder grains onto a glass substrate (as shown in Figure III-23b). The powder-packed CME was then used as the working electrode, and a laminated silver wire and a rolled platinum foil (with area of 1 cm^2) were used as reference and counter electrode, respectively. The main advantage of utilizing CME is that this technique allows the study of electrochemical behavior at the active materials / electrolyte interface without influence of binders, separators, current collectors or other components in the conventional set-ups^[43,44], hence making it an interesting technique, in our case especially, to study the electrochemical signals which come *purely* from the active material, and to compare the electrochemical signatures between the two samples.

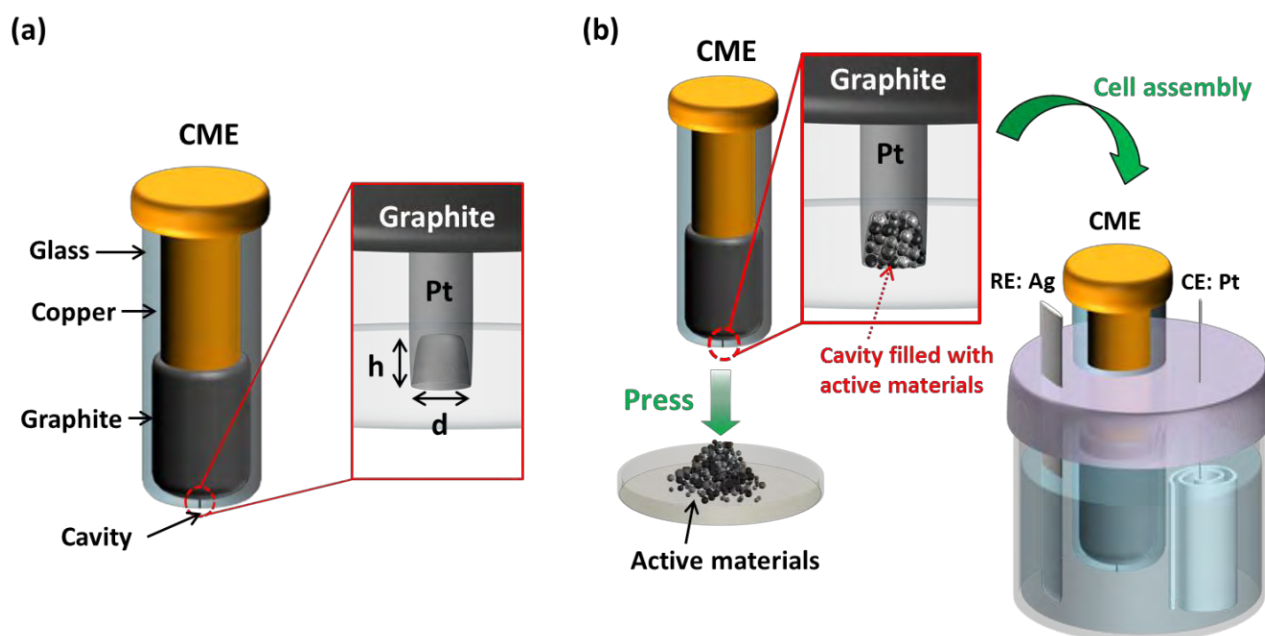


Figure III-23: Scheme of cavity micro-electrode (CME) (a) and CME electrochemical cell assembly and configuration (rolled-Pt as counter electrode and silver wire as reference) (b)

Electrochemical signatures: As-activated vs annealed a-MEGO

Annealed and as-activated a-MEGO powders were tested in the eutectic IL mixture at room temperature using cavity microelectrode to obtain information on any difference in electrochemical response as a result of vacuum annealing. The CVs collected from both samples at room temperature are shown in Figure III-24a, scanned within a potential window of -1.7 to $+1.3$ V/Ref. Bumps observed at ~ -0.3 V/Ref in the positive scan and at ~ -0.8 V/Ref in the negative scan are pronounced for the as-activated a-MEGO powder and clearly decreased after annealing.

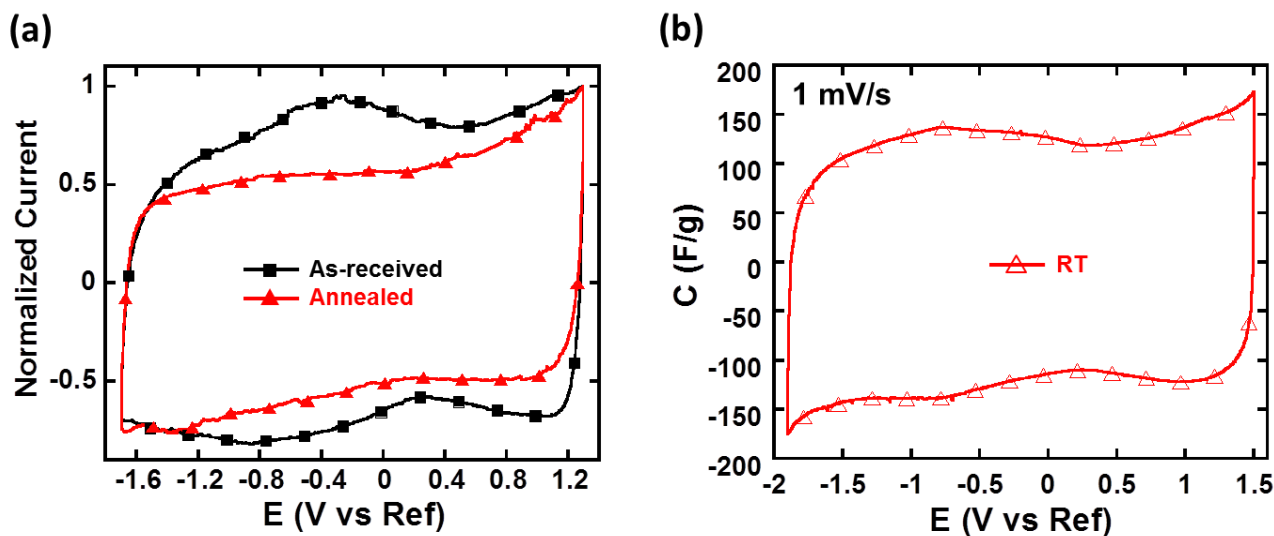


Figure III-24: Cyclic voltammograms of annealed and as-activated a-MEGO electrodes in $(\text{PIP}_{13}\text{-FSI})_{0.5}(\text{PYR}_{14}\text{-FSI})_{0.5}$ electrolyte: CVs collected at 500 mV/s at room temperature using CME (a); CV collected at 1 mV/s using a Swagelok® cell (b).

Annealed a-MEGO powders were then characterized in Swagelok® cells, using a 3-electrode configuration. Figure III-24b shows the CV of annealed a-MEGO powders at 1 mV/s at room temperature. Note that in these experiments, raw powders were tested without any binder (to echo the testing condition in CME) so that the ohmic drop was not optimized in the cell which is why a low scan rate was used. The specific capacitances at different scan rates are also measured and shown in Table III-2. Annealed a-MEGO powders reached a capacitance of 130 F/g, which is ~20% less than the capacitance obtained for the as-activated samples, as expected from a lower SSA of the annealed material. The other point to be taken into account is the processing of the electrode, which could have some effect on capacitance values measured.

Another notice is that since we would like to verify the bump is removed after annealing by comparing CVs of annealed and as-activated MEGO, hence we have to make sure the bump is not attributed to the oxidation or reduction of electrolyte and fix the same potential window for comparison of two samples, we limited the electrochemical window well below the oxidation/reduction potential limits of the electrode/electrolyte system (3V). However, in Figure III-24b, the full potential window for annealed a-MEGO was extracted (3.5V). Therefore, a difference in the potential window between Figure III-24a and b could be found.

Table III-2: Capacitance of annealed a-MEGO electrodes in (PIP₁₃-FSI)_{0.5}(PYR₁₄-FSI)_{0.5} electrolyte at room temperature.

Scan Rate (mV/s)	Charging/discharging capacitance (F/g)
20	100
5	110
1	130

5. Conclusions

In this chapter, carbons with different microstructures have been tested in (PIP₁₃FSI)_{0.5}(PYR₁₄FSI)_{0.5} ILs mixture, which possesses a wide stable electrochemical window over extended operating temperature range, to study the relationship between carbon architecture and capacitance, and ion accessibility (by varying temperature and scan rate). Two carbons containing both mesopores and micropores have been investigated: SiC-CDC prepared by chlorination of ordered mesoporous SiC which is derived from magnesio-thermal reduction of templated carbon-silica precursors, and KOH-activated microwave exfoliated graphite oxide (a-MEGO).

SiC-CDC, with hierarchical micro/mesoporous structure, was first tested in conventional organic electrolyte (1.5 M NEt₄BF₄/AN), showed outstanding rate capability (90% of capacity retention at 1 V/s and time constant of 1 second) with high specific areal capacitance (0.5 F/cm² of electrode).^[48] This hierarchical porous carbon was further tested in ILs mixture and compared with microporous activated carbon (YP-50F). SiC-CDC showed good capacitive behavior down to -40 °C and much better capacitance retention at subzero temperature than the microporous YP-50F. However, the large amount of mesopores (~70%) in this material gives it a respectable capacitance (80 F/g in 1.5 M NEt₄BF₄/AN; 55 F/g in ILs mixture at 20 °C).

The as activated a-MEGO presented an exceptionally high capacitance (up to 180 F/g) and wide electrochemical window (up to 3.7 V) over a wide temperature range from -50 °C to 80 °C in ILs mixture.^[49] Annealing the a-MEGO yields better electrochemical stability, but the specific capacitance somewhat decreases due to decreased mesoporosity and associated accessible SSA after annealing. This is 5 times higher capacitance compared to exohedral

nanostructured carbon (nanotubes and onions) electrodes and 3 times higher than SiC-CDC electrode, in the same eutectic mixture of ionic liquids. The high SSA, high electric conductivity and uniformly situated mesopores (2 to 4 nm), compared with the mesopores of SiC-CDC whose peak ranged from 2 to 10 nm, allow the KOH-activated MEGO to store the charge much more efficiently than SiC-CDC. These findings have largely overcast the temperature range offered by conventional organic electrolytes of 110 °C (from -30 °C to 80 °C) and would greatly contribute to the advances in electrical storage based on ILs, pushing the limits of energy storage to greater heights.

These studies have not only affirmed our previous findings on the need to design carbon structure for optimizing carbon/electrolyte interface, but also showed that ionic liquids are no longer confined to the category of “above room temperature” applications. Even more, they have proved their extended threshold for extreme climatic conditions, which clearly proved the robustness of ILs as electrolytes for electrical storage. Herein, the research pathway has been paved towards optimizing the carbon accessible surface area (e.g., by using activated graphene^[27], de-bundled single-walled nanotubes^[45], or mesoporous templated carbons^{[46][47]}) together with designing the IL-based electrolyte. Control of the electrolyte composition and its molecular/ionic structure is required for achieving better compatibilities with various carbon structures and surpassing the current capacitance and energy density limits of supercapacitors. On the other hand, fundamental understanding of the EDL charging mechanism is necessary and will efficiently help for better supercapacitors designs. In the next chapter, the study of charge storage mechanisms and ion dynamics using in-situ electrochemical quartz crystal microbalance (EQCM) will be presented.

6. Reference

- [1] R. Lin, P.-L. Taberna, S. Fantini, V. Presser, C. R. Pérez, F. Malbosc, N. L. Rupesinghe, K. B. K. Teo, Y. Gogotsi, P. Simon, *J. Phys. Chem. Lett.* **2011**, *2*, 2396.
- [2] V. Presser, M. Heon, Y. Gogotsi, *Adv. Funct. Mater.* **2011**, *21*, 810.
- [3] C. Largeot, C. Portet, J. Chmiola, P.-L. Taberna, Y. Gogotsi, P. Simon, *J. Am. Chem. Soc.* **2008**, *130*, 2730.
- [4] J. Chmiola, G. Yushin, Y. Gogotsi, C. Portet, P. Simon, P. L. Taberna, *Science* **2006**, *313*, 1760.
- [5] C. R. Pérez, S.-H. Yeon, J. Ségalini, V. Presser, P.-L. Taberna, P. Simon, Y. Gogotsi, *Adv. Funct. Mater.* **2013**, *23*, 1081.
- [6] M. Arulepp, J. Leis, M. Lätt, F. Miller, K. Rumma, E. Lust, A. F. Burke, *J. Power Sources* **2006**, *162*, 1460.
- [7] W. Gu, G. Yushin, *Wiley Interdiscip. Rev. Energy Environ.* **2014**, *3*, 424.
- [8] P.-C. Gao, Y. Lei, A. F. C. Pérez, K. Rajoua, D. Zitoun, F. Favier, *J. Mater. Chem.* **2011**, *21*, 15798.
- [9] P.-C. Gao, P. Simon, F. Favier, *Microporous Mesoporous Mater.* **2013**, *180*, 172.
- [10] R. Liu, Y. Shi, Y. Wan, Y. Meng, F. Zhang, D. Gu, Z. Chen, B. Tu, D. Zhao, *J. Am. Chem. Soc.* **2006**, *128*, 11652.
- [11] Y. Gogotsi, P. Simon, *Science* **2011**, *334*, 917.
- [12] L. Wei, M. Sevilla, A. B. Fuertes, R. Mokaya, G. Yushin, *Adv. Energy Mater.* **2011**, *1*, 356.
- [13] C. Portet, G. Yushin, Y. Gogotsi, *Carbon* **2007**, *45*, 2511.
- [14] S. Dörfler, I. Felhösi, T. Marek, S. Thieme, H. Althues, L. Nyikos, S. Kaskel, *J. Power Sources* **2013**, *227*, 218.
- [15] D. Pech, M. Brunet, H. Durou, P. Huang, V. Mochalin, Y. Gogotsi, P.-L. Taberna, P. Simon, *Nat. Nanotechnol.* **2010**, *5*, 651.
- [16] H. Wu, X. Wang, L. Jiang, C. Wu, Q. Zhao, X. Liu, B. Hu, L. Yi, *J. Power Sources* **2013**, *226*, 202.
- [17] P. L. Taberna, P. Simon, J. F. Fauvarque, *J. Electrochem. Soc.* **2003**, *150*, A292.
- [18] N. Jäckel, D. Weingarh, M. Zeiger, M. Aslan, I. Grobelsek, V. Presser, *J. Power Sources* **2014**, *272*, 1122.
- [19] D. Weingarh, D. Cericola, F. C. F. Mornaghini, T. Hucke, R. Kötz, *J. Power Sources* **2014**, *266*, 475.
- [20] N. Liu, J. Shen, D. Liu, *Microporous Mesoporous Mater.* **2013**, *167*, 176.
- [21] R. Lin, P. Huang, J. Ségalini, C. Largeot, P. L. Taberna, J. Chmiola, Y. Gogotsi, P. Simon, *Electrochimica Acta* **2009**, *54*, 7025.
- [22] B.-H. Kim, K. S. Yang, *J. Electroanal. Chem.* **2014**, *714-715*, 92.
- [23] Y. Zhu, S. Murali, M. D. Stoller, K. J. Ganesh, W. Cai, P. J. Ferreira, A. Pirkle, R. M. Wallace, K. A. Cychosz, M. Thommes, D. Su, E. A. Stach, R. S. Ruoff, *Science* **2011**, *332*, 1537.
- [24] W. Gu, N. Peters, G. Yushin, *Carbon* **2013**, *53*, 292.
- [25] M. Kaempgen, C. K. Chan, J. Ma, Y. Cui, G. Gruner, *Nano Lett.* **2009**, *9*, 1872.
- [26] C.-M. Yang, Y.-J. Kim, M. Endo, H. Kanoh, M. Yudasaka, S. Iijima, K. Kaneko, *J. Am. Chem. Soc.* **2007**, *129*, 20.
- [27] Y. Zhu, S. Murali, M. D. Stoller, K. J. Ganesh, W. Cai, P. J. Ferreira, A. Pirkle, R. M. Wallace, K. A. Cychosz, M. Thommes, D. Su, E. A. Stach, R. S. Ruoff, *Science* **2011**, *332*, 1537.
- [28] Y. Zhu, S. Murali, M. D. Stoller, A. Velamakanni, R. D. Piner, R. S. Ruoff, *Carbon* **2010**, *48*, 2118.
- [29] L. L. Zhang, R. Zhou, X. S. Zhao, *J. Mater. Chem.* **2010**, *20*, 5983.
- [30] R. Kötz, M. Hahn, R. Gallay, *J. Power Sources* **2006**, *154*, 550.
- [31] H. Kurig, A. Jänes, E. Lust, *J. Electrochem. Soc.* **2010**, *157*, A272.
- [32] V. Ruiz, T. Huynh, S. R. Sivakumar, A. G. Pandolfo, *RSC Adv.* **2012**, *2*, 5591.
- [33] E. Iwama, P. L. Taberna, P. Azais, L. Brégeon, P. Simon, *J. Power Sources* **2012**, *219*, 235.
- [34] C. Largeot, P. L. Taberna, Y. Gogotsi, P. Simon, *Electrochem. Solid-State Lett.* **2011**, *14*,

A174.

- [35] E. Brandon, M. Smart, W. West, *NASA Techncl Rep. Serv.* **2010**.
- [36] R. Vellacheri, A. Al-Haddad, H. Zhao, W. Wang, C. Wang, Y. Lei, *Nano Energy* **2014**, *8*, 231.
- [37] R. Väli, A. Laheäär, A. Jänes, E. Lust, *Electrochimica Acta* **2014**, *121*, 294.
- [38] J. Reiter, J. Vondrák, J. Michálek, Z. Mička, *Electrochimica Acta* **2006**, *52*, 1398.
- [39] E. J. Brandon, W. C. West, M. C. Smart, L. D. Whitcanack, G. A. Plett, *J. Power Sources* **2007**, *170*, 225.
- [40] A.-K. Hjelm, T. Eriksson, G. Lindbergh, *Electrochimica Acta* **2002**, *48*, 171.
- [41] A. G. Pandolfo, A. F. Hollenkamp, *J. Power Sources* **2006**, *157*, 11.
- [42] C. Vix-Guterl, M. Couzi, J. Dentzer, M. Trinqucoste, P. Delhaes, *J. Phys. Chem. B* **2004**, *108*, 19361.
- [43] R. Lin, P. L. Taberna, J. Chmiola, D. Guay, Y. Gogotsi, P. Simon, *J. Electrochem. Soc.* **2009**, *156*, A7.
- [44] C. Cachet-Vivier, V. Vivier, C. S. Cha, J.-Y. Nedelec, L. T. Yu, *Electrochimica Acta* **2001**, *47*, 181.
- [45] A. Izadi-Najafabadi, S. Yasuda, K. Kobashi, T. Yamada, D. N. Futaba, H. Hatori, M. Yumura, S. Iijima, K. Hata, *Adv. Mater.* **2010**, *22*, E235.
- [46] F. Beguin, E. Frackowiak, *Carbon Materials for Electrochemical Energy Storage Systems*, **n.d.**
- [47] C. Matei Ghimbeu, L. Vidal, L. Delmotte, J.-M. Le Meins, C. Vix-Guterl, *Green Chem.* **2014**, *16*, 3079.
- [48] W.-Y. Tsai, P.-C. Gao, B. Daffos, P.-L. Taberna, C. R. Perez, Y. Gogotsi, F. Favier, P. Simon, *Electrochem. Commun.* **2013**, *34*, 109.
- [49] W.-Y. Tsai, R. Lin, S. Murali, L. Li Zhang, J. K. McDonough, R. S. Ruoff, P.-L. Taberna, Y. Gogotsi, P. Simon, *Nano Energy* **2013**, *2*, 403.

Chapter IV:
In-situ EQCM Study on Ion Dynamics in
Confined Carbon Micropores

1. Introduction

Aside from searching for new electrolytes and electrode materials to increase the energy density, improving the electrode/electrolyte interface and electrode microstructure to enhance the power performance, fundamental understanding of the charge storage mechanism and ion dynamics during charging/discharge process at the molecular scale is of great importance for designing the next generation supercapacitors. As mentioned in chapter I, the traditional picture regarding charge storage in the porous carbon believes in that maximum capacitance appears when the compact layers of solvated counter-ions (ions having charge opposite to that of polarized carbon electrode) resides on both adjacent pore walls, which means the best electrode pore size should be twice the solvated ions size. It was overturned when a breakthrough discovery has been reported in 2006 using carbide-derived carbons (CDCs) with controlled and narrow pore size distribution.^[1] An anomalous capacitance increase was found when the pore size decreased down to less than 1 nm which corresponds to the solvated ion size. It has been proposed that the ions are partially desolvated to be able to squeeze in the micropores.

Since then, numerous works have been devoted to understanding the origin of the physics of ion adsorption and ionic transport in confined nanoporous carbon.^[2-13] However, owing to the lack of in-situ technique for studying the electrode/electrolyte interface during charging and discharging, lots of questions regarding how charge is stored at the molecular scale in confined environment remain unsolved: does *one* net charge stored on the electrode correspond to *one* single counter-ion adsorption (thus giving a charge storage efficiency of 100 %)? Since there is a strong interaction between cation and anion in neat ionic liquid, do co-ions (ions carrying charge same as that of polarized carbon electrode) affect counter-ions adsorption? In solvent-containing electrolyte systems, how do solvents affect the charge storage? Do solvents screen the charge of the ions leading to a less efficient charge storage?

As mentioned in chapter I, among the few in-situ electrochemical techniques (e.g. in-situ nuclear magnetic resonance spectroscopy or in-situ infrared spectroscopy), electrochemical quartz crystal microbalance (EQCM), which measures the mass change arising from the compositional changes in the porous electrode during charging/discharge, has recently been involved in investigating the EDL charging mechanism. The first demonstration of applying EQCM in the study of adsorption/desorption mechanism was initiated by Aurbach's group^[14]. In this work, different porous and non-porous carbons have been deposited on the quartz of

EQCM and tested in different aqueous electrolytes. Other factors (amount of carbon deposit, scan rate of cyclic voltammetry, etc) have also been studied. The results have proved the validity of using EQCM as an electrogravimetric probe to study the concentration and compositional changes in porous carbon during its charging and discharging. Further study using a commercial activated carbon in organic electrolytes was conducted by the same group [15]. By varying the cation size of the salts (from small Li^+ to bulky quaternary ammonium cations), ion-sieving effect was observed, and the carbon perm-selective behavior was discussed. Depending on the degree of carbon polarization, different charging phenomena of $\text{NEt}_4\text{BF}_4/\text{PC}$ in porous carbon have been observed/proposed by EQCM (Figure IV-1): ion-mixing at low polarization (zone I), ion adsorption without their solvation shell (zone II), and pore expansion (Figure III). Furthermore, the cation solvation numbers can be calculated from EQCM data: the lithium solvation number was found to be 3 PC molecules, smaller than its bulk solvation number. Ion partial desolvation has been observed in a *quantitative* manner.

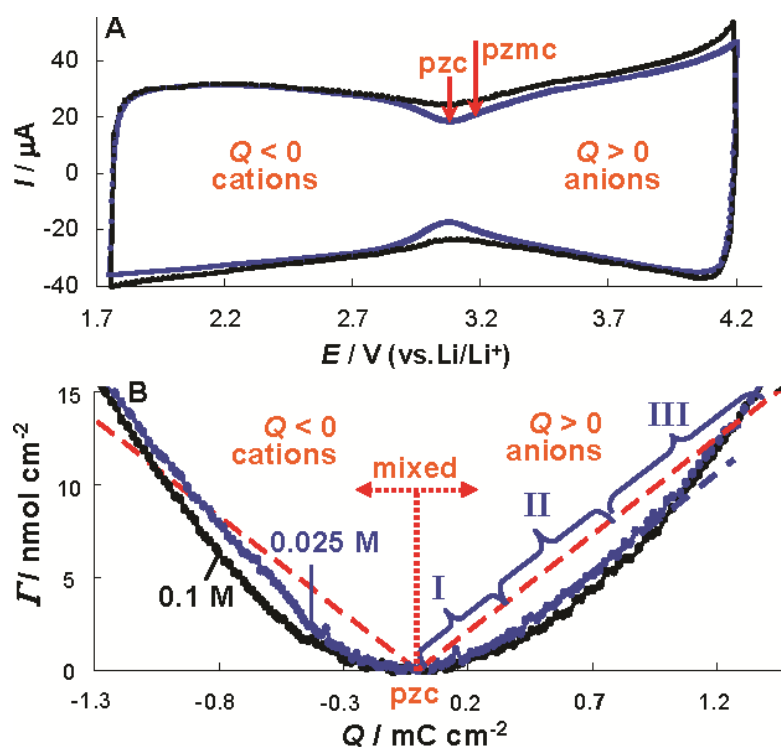


Figure IV-1: CVs of a carbon-coated quartz crystal electrode in 0.1 and 0.025 M TEABF_4/PC solutions (A), and the related treated EQCM responses, Γ vs Q (B). Three domains with the characteristic different Γ/Q slopes for the 0.025 M solution are indicated. The slope within domain II (the broken blue line) is equal to the theoretical slope of the broken red straight line calculated from the Faraday law. [15]

These results have clearly shown that EQCM allows direct monitoring the ion fluxes during charging/discharging of the carbon porous electrode, thus making it a promising in-situ electrochemical technique for studying the charging mechanism and ion transport in the electric double layer. The adsorption/desorption mechanism and solvation environment have then been intensely studied by the same group using EQCM technique since their pioneer work ^[16-18], however, most of the studies are performed with commercial activated carbons in aqueous or organic electrolytes with the presence of solvents. Because of the large pore size distribution of the porous carbon used, it was difficult to link pore size to local solvation number and molecular information during charging/discharging. The charging mechanism and dynamics in a solvent-free environment has not been investigated, either. In view of this, we are thus interested in using the powerful electrogravimetric EQCM to study carbon-derived carbides *with controlled, narrow pore size distribution in neat and solvated* ionic liquids.

Previous studies using carbide-derived carbons with different pore sizes in neat 1-Ethyl-3-methylimidazolium bis(trifluoromethanesulfonyl)imide (EMI-TFSI) ionic liquid electrolyte showed that the maximum capacitance was achieved when the carbon pore size was close to that of the adsorbing ions of the electrolyte (Figure IV-2).^[19] Further study extended the experiments on CDCs in 2M EMI-TFSI dissolved in acetonitrile (AN) to understand the solvation effect onto the ion adsorption in porous carbons.^[20] It was found that cation and anion adsorption showed different electrochemical signature when decreasing the carbon pore size below 1 nm: the capacitive behavior was kept for pore size between 0.74 nm ~ 1 nm during EMI⁺ cation adsorption (Figure IV-3a) while severe asymmetrical distortion of CVs was observed for pore size smaller than 0.8 nm for TFSI⁻ anion adsorption (Figure IV-3b). From Figure IV-3 and considering that the calculated ion sizes in longest dimension are 0.76 and 0.79 nm for EMI⁺ cation and TFSI⁻ anion, desolvation was observed for both anion and cation adsorption, and the effective sizes of adsorbed ions were found to decrease in the order: TFSI⁻ in AN > EMI⁺ in AN > EMI⁺ \cong TFSI⁻. Furthermore, it has also been found that TFSI⁻ anion adsorption in the pores was a diffusion-controlled process because of the lack of accessibility due to size effect.

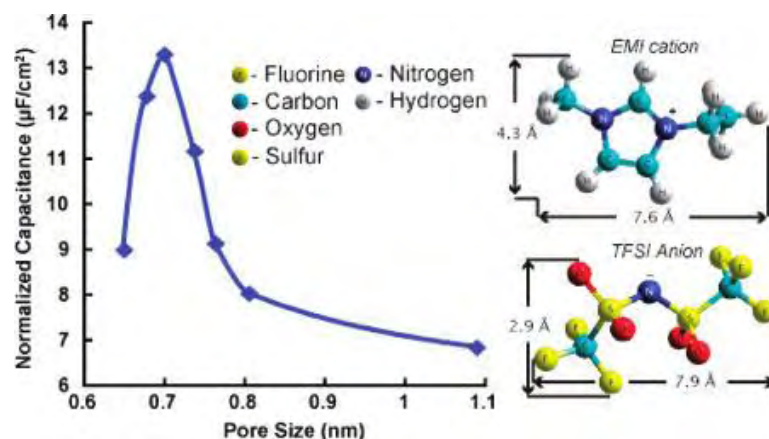


Figure IV-2: Normalized capacitance change vs the pore size of the CDC samples prepared at different temperatures; normalized capacitance is obtained by dividing the specific capacitance by the SSA. HyperChem models of the structure of EMI and TFSI ions show a size correlation.^[19]

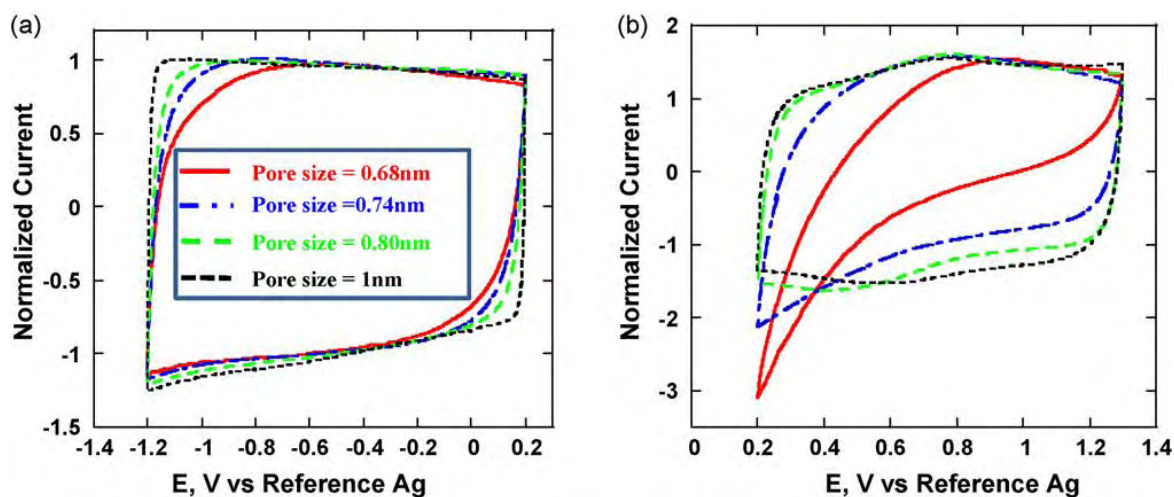
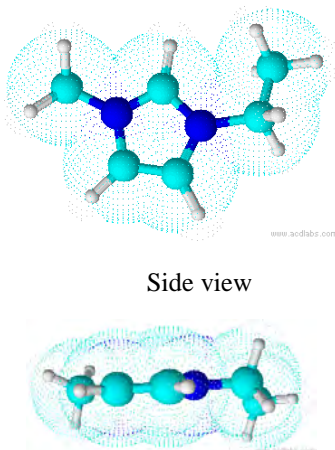
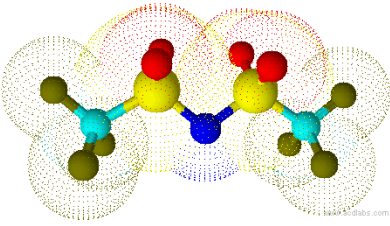
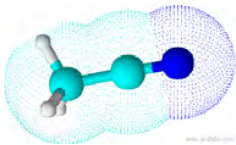


Figure IV-3: Normalized CVs of CDC samples in AN+2M EMITFSI electrolyte (b) between OCV and -1.2 V/Ref at a scan rate of 100 mV/s (b) and between OCV and $+1.3$ V/Ref of the CDC samples^[20]

Table IV-1 summarizes the structures of EMI^+ cation and TFSI^- anion, the sizes of their longest and shortest dimension, and effective ion size in acetonitrile in confined CDC nanopore^[20]. When “ion size” is mentioned in this chapter, it refers to the ions’ longest dimension (0.76 nm for EMI^+ cation, and 0.79 nm for TFSI^- anion). The structure and the size of acetonitrile were also listed in Table IV-1.

Table IV-1: Structure and size of the EMI⁺ cation, TFSI⁻ anion and acetonitrile (AN) solvent

Ions	Structure*	Size max/min length (nm) ^[19,21]	Effective ion size in AN (nm) ^[20]
EMI ⁺	 <p>Side view</p>	0.76/---	~ 0.7
TFSI ⁻		0.79/0.37	> 0.75
AN		0.58/0.40	---

*Molecular structures were drawn by using ChemSketch Freeware

Here, to further obtain the detail picture of the fundamental charging mechanism in confined environment, in-situ EQCM was used to study the same electrolytes at room temperature. In this chapter, neat EMI-TFSI ionic liquid and 2M EMI-TFSI dissolved in acetonitrile (AN) and microporous CDCs with large (1 nm) and small (0.65 nm) pore sizes have been used to study both the influence of the presence of solvent and the impact of the carbon pore size.

Carbide-derived carbons (CDCs)

The two titanium carbide derived carbons (TiC-CDCs) used in this study were purchased from YCarbon Inc (USA). The as-received CDC carbons are characterized from Ar sorption isotherm measured at 77 K with Micromeritics ASAP 2020 porosimetry analyser, and the pore size distributions (PSD) were calculated from the isotherm by using Quenched Solid Density Functional Theory (QSDFT) method assuming a slit pore geometry.

CDC-0.65nm

The CDC-0.65nm was obtained at chlorination temperature of 400 °C. The Ar sorption isotherm (77K) and PSD obtained from QSDFT methods of the as-received CDC-0.65nm were shown in Figure IV-4. The calculated BET SSA is 1023 m²/g, and the average pore size is 0.65 nm.

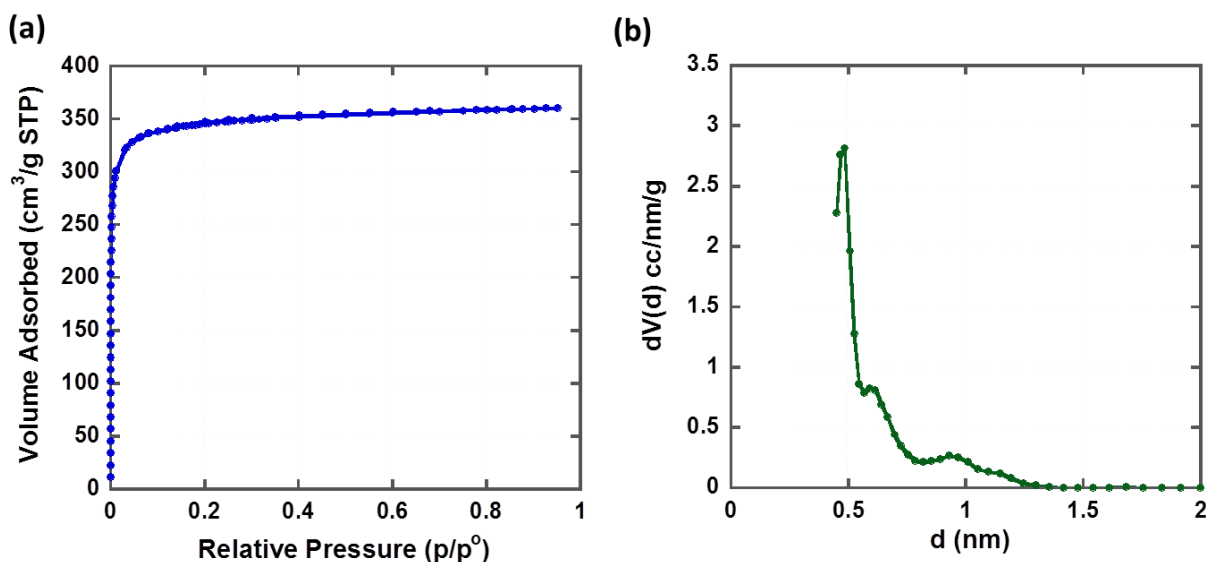


Figure IV-4: Porosity Characteristics of the as-received CDC-0.65nm carbon: (a) Ar sorption isotherm collected at 77K and (b) pore size distribution calculated from QSDFT model

CDC-1nm

The CDC-1nm was obtained at chlorination temperature of 1100 °C. Figure IV-5 shows the Ar sorption isotherm measured at 77K and PSD obtained from QSDFT methods of the as-received CDC-1nm carbon samples. The average pore size and the calculated BET SSA are 1 nm and 1542 m²/g, respectively. The presence of mesopores is due to the high chlorination temperature (> 1000 °C), as reported by Dash et al ^[22].

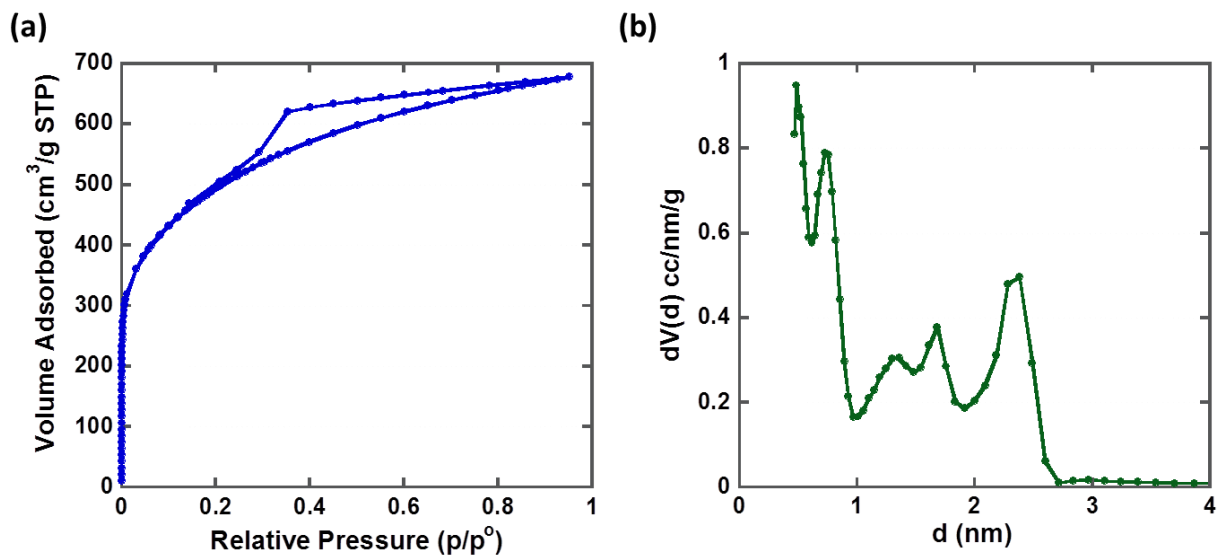


Figure IV-5: Porosity Characteristics of the as-received CDC-1nm carbon: (a) Ar sorption isotherm collected at 77K and (b) pore size distribution calculated from QSDFT model

2. Electrochemical quartz crystal microbalance (EQCM)

2.1 EQCM Principle

Electrochemical Quartz Crystal Microbalance (EQCM) is an experimental set-up allowing the measurement of an electrode mass variation while electrochemical reactions proceed. The EQCM technique has been widely used for electrodeposition studies since it helps elucidating the electrochemical mechanisms. The bottom line of the technique is the tracking of the resonance frequency of the quartz upon mass uptake.

Resonance Frequency - Sauerbrey Equation

The quartz crystal is piezoelectric^[23-26]; it is composed of a thin quartz crystal (usually an AT-cut quartz, with thickness of few hundreds of micrometers, because of its higher thermal stability) sandwiched by two metal electrodes in between where an alternating electric field is applied, causing vibrational motion of the crystal that creates a transverse acoustic wave which propagates across the thickness of the quartz crystal, and is reflected back into the crystal at the surface (Figure IV-6). Therefore, a standing wave condition can be fulfilled when the acoustic wavelength is equal to $2 t_q$. The corresponding resonance frequency, f_o , is given below^[24]:

$$f_o = \frac{v_{tr}}{2t_q} = \frac{\sqrt{\mu_q / \rho_q}}{2t_q} \quad (\text{Equation IV-1})$$

Where v_{tr} is the transverse velocity in AT-cut quartz (3.34×10^4 m/s), t_q is the thickness of the quartz crystal, ρ_q is the density of quartz (2.648 g/cm^3), μ_q is the shear modulus of quartz ($2.947 \times 10^{11} \text{ g /cm.s}^2$). According to Equation IV-1, the fundamental resonance frequency (f_o) is dependent on the thickness of the quartz (t_q).

Since it has been reported by Sauerbrey^[27] that this resonance frequency is sensitive to the mass changes of the crystal, by using one side of EQCM as a working electrode in an electrochemical cell while simultaneously measuring the mass changes, it is able to monitor electrochemical processes that take place at the electrode surface, such as electrodeposition or electrosorption, in real time. (EQCM and QCM are names used to distinguish between electrochemical and non-electrochemical applications of QCM).

Actually, when a uniform layer of foreign material is added onto the quartz crystal, the acoustic wave can go across crystal/foreign material interface and propagate through the foreign layer (assuming that the displacement and shear stress are continuous across the

interface). Assuming that the foreign material has *the same acoustic properties* as quartz crystal, then the foreign layer can be simply treated as a thickness increment of the quartz (shown in Figure IV-6) ^[24].

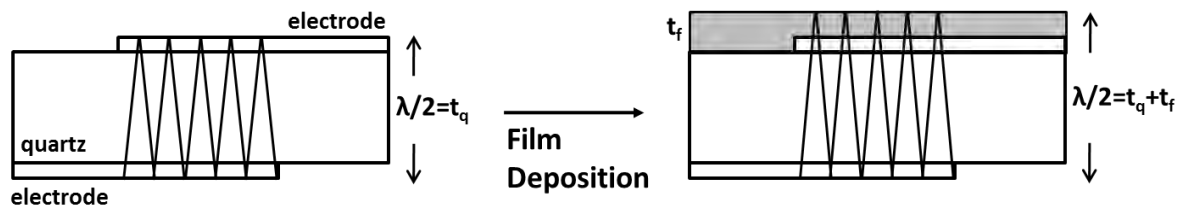


Figure IV-6: Schematic of the transverse shear wave in quartz crystal (re-plotted from reference ^[24])

The thickness change leads to a frequency change, and the relation is given as following equation:

$$\frac{\Delta f}{f_o} = -\frac{\Delta t}{t_q} = \frac{-2f_o \cdot \Delta t}{v_{tr}} \quad (\text{Equation IV-2})$$

Where the Δt and Δf are the fractional changes in thickness and frequency respectively. Applying that $\Delta t = \Delta m / \rho_q \cdot A$ based on previous assumption, and appropriate substitution of Equation IV-1 and Equation IV-2 gives the Sauerbrey Equation (Equation IV-3) ^[24,27]:

$$\Delta m = -\frac{A\sqrt{\rho_q \mu_q}}{2f_o^2} \cdot \Delta f = -C_f \cdot \Delta f \quad (\text{Equation IV-3})$$

Where Δm is the mass change, A the piezoelectrically active area, and C_f is the sensitivity factor (ng/Hz) of the crystal (referred to as the “calibration constant” when it is determined through the calibration procedure which will be discussed later in the chapter) Studies have shown that this sensitivity factor of the crystal is approximately Gaussian: the maximum mass sensitivity is in the center of the quartz crystal and it tapers off towards the edge. Therefore, the larger the quartz surface, the more stable the signal ^[28-30].

The Sauerbrey relationship is the key equation to convert the frequency change to mass changes during electrochemical process. However, it should be noted that Sauerbrey equation is valid under the assumption that the deposited layer is an ideal rigid film, and the mass loading should not exceed 2% of the mass of the crystal since the relative “non-ideal” contribution of the foreign layer to the overall composite resonator increases.

Electrical Equivalent Circuit

A convenient way for studying the electroacoustical/electromechanical behavior of the QCM is through its electrical equivalent circuit. The Butterworth-Van Dyke (BVD) equivalent circuit is a typical model used to describe an *unperturbed* (without mass or liquid loading) quartz resonator, as shown in Figure IV-7: here in the series branch, L_1 represents the inertial component related to the displaced mass during oscillation (analogous to a purely mechanical model of a mass attached to a spring of compliance), C_1 represents the energy stored during oscillation (elasticity of the quartz and surrounding medium), and R_1 represents the energy dissipated during oscillation (damping coming from viscosity and the mounting of the quartz). This series branch is commonly referred as the *motional branch* since it is the segment which defines the electromechanical characteristics (vibrational motion) of the quartz resonator. C_o , parallel branch, arises from the electrical capacitance of the quartz sandwiched between the electrodes on both faces of the quartz.

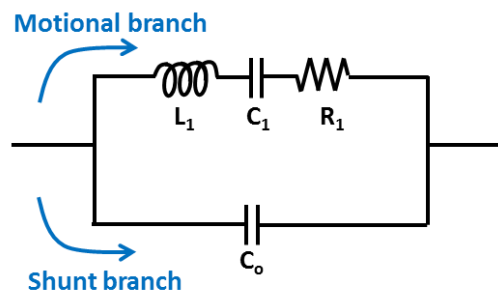


Figure IV-7: Butterworth-Van Dyke (BVD) equivalent circuit for an unperturbed quartz crystal microbalance (re-plotted from reference ^[24])

Since the piezoelectric quartz resonator couples the *mechanical* displacement and *electrical* potential, the mechanical interaction between the quartz crystal and contacting media (e.g. foreign deposit layer or immersing in a liquid) will influence the electrical characteristics of the QCM, particularly the quality factor. Therefore, when a thin film is deposited on the quartz crystal and the quartz resonator is immersed in a liquid media (which is the case for electrochemical studies), not only the mass loading of the deposit film, but also the liquid density (ρ_L) and dynamic viscosity (η_L) will affect the resonance frequency value. In general, immersing the QCM in a liquid results in a decrease in frequency arise from the additional mass of vibrating liquid (represent as L_L in the equivalent circuit in Figure IV-8) ^[31-34], which

is dependent upon the viscosity and density of the liquid as described by Kanazawa's equation [31]:

$$\Delta f = -f_q^{3/2} \sqrt{\frac{\rho_L \cdot \eta_L}{\pi \cdot \rho_q \cdot \mu_q}} \quad (\text{Equation IV-4})$$

Where f_q is the resonance frequency of unloaded crystal in Hz, ρ_q is density of quartz ($2.648 \times 10^3 \text{ kg/m}^3$), μ_q is shear modulus of quartz ($2.974 \times 10^{10} \text{ Pa}$), ρ_L is density of the liquid in kg/m^3 , and η_L is viscosity of the liquid in Pa.s.

The immersion of QCM in a liquid medium also results in an increase in motional resistance caused by the power dissipation of the shear wave that radiates into the liquid (damping of the resonance). The increase in motional resistance and the mean decay length of the shear wave into the liquid (at the interface) is defined by Equation IV-5 and Equation IV-6:

$$\Delta R = \Delta f \frac{2\pi \cdot (\rho_q \cdot \mu_q)^{3/2}}{f^3 \cdot 32 \cdot A_r \cdot (\rho_q \cdot e_{26})^2} \quad (\text{Equation IV-5})$$

$$L_D = \sqrt{\frac{2\eta_L}{\rho_L \cdot \omega_s}} \quad (\text{Equation IV-6})$$

Where ΔR (shown as R_L in the modified BVD equivalent circuit Figure IV-8) is the change in series resistance due to the quartz immersion in the liquid in Ω , A_r is the active area of the quartz (for Maxtek 1-inch quartz is $3.419 \cdot 10^5 \text{ m}^2$), e_{26} is the piezoelectric constant for an AT-cut quartz ($0.095 \text{ kg/sec}^2/\text{V}$), L_D is the decay length in m, and $\omega_s = \text{Angular frequency at series resonance}$ ($2\pi f$). As indicated by Equation IV-4 to 6, when immersing a quartz resonator in a liquid, the higher the liquid viscosity, the higher the mass loading on the quartz, the higher the series resistance, and the higher the decay length.

Furthermore, if the deposit layer is a viscoelastic polymer film, then except for the parameters just mentioned, the density (ρ_f), viscosity (η_f), and elasticity (μ_f) of the film material will also affect the resonance frequency. Figure IV-8 depicts a modified BVD model of a quartz resonator coated with a viscoelastic polymer film and immersed in a liquid. Besides from above mentioned factors, the microscopic surface roughness of the electrode also plays a role when immersing in the liquid since the liquid that trapped in the surface cavities will lead to an

additional mass component.

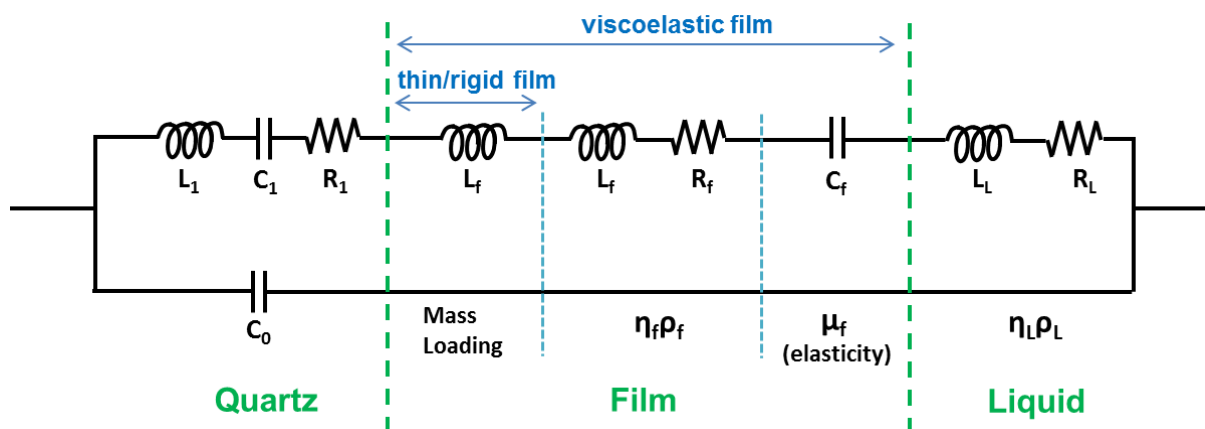


Figure IV-8: Modified Butterworth-Van Dyke (BVD) equivalent circuit for a quartz crystal coated with viscoelastic polymer film and immersed in a liquid (re-plotted from reference ^[24])

Validation of the Sauerbrey Equation

Owing to the complex electroacoustic behavior of a film-coated quartz resonator immersed in a liquid, it is important to validate the use of Sauerbrey equation (Equation IV-3) by verifying the frequency change only originates from *gravimetric* nature rather than other causes. In our case, the concept is rather simple: carbon electrode is deposited on the quartz prior to its immersion in the electrolytes; during electrochemical measurements, the only incident involved is the electrolytic ions entering or leaving the porous electrode hence resulting in a mass change observed by EQCM. Other unwanted events in the supercapacitors, such as redox reaction or electrode film swelling, will either generate local stress/strain or change in the local acoustic properties hence giving rise to a change in motional resistance which is linked to the quality factor of the QCM. In this study, an EQCM (Maxtek, USA) allows tracking of the QCM motional resistance in real time together with the resonance frequency, which offers important information on the validation of the Sauerbrey equation during electrochemical incidents.

2.2 EQCM set-up

Figure IV-9 depicts a simple schematic for a typical EQCM apparatus^[24,35]: Generally, a computer interfaces to both electrochemical instrumentation and the frequency instrumentation, and it simultaneously conducts the electrochemical tests and measures the frequency response. Comparison of both data provides information about film deposition and dissolution, surface morphology changes, and mass changes in thin films caused by redox or other chemical processes.

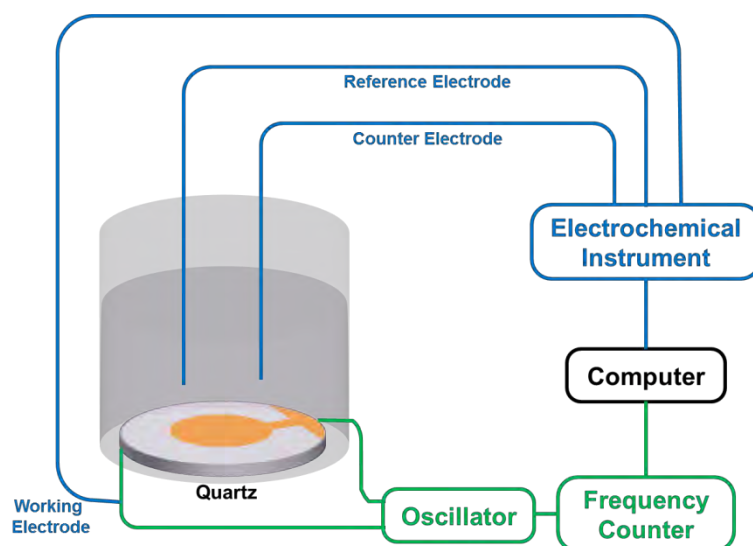


Figure IV-9: Schematic of EQCM apparatus (re-plotted from reference^[24])

In this work, Maxtek 1-inch-diameter AT-cut quartz crystals were used for all the EQCM measurements. The large surface of these quartz crystals (1-inch diameter) allows enough distance between the active area of the crystal and the mounting area, which improves the overall stability of the quartz by reducing the frequency changes due to the mounting stress^[28-30]. Sauerbrey equation (Equation IV-3) shows that the higher the fundamental quartz resonance frequency (f_0), the higher the sensitivity of the microbalance hence the smaller the detectable mass. Nevertheless, a fundamental frequency of 5 MHz was chosen for our study since a carbon electrode layer is deposited on the quartz as working electrode of supercapacitor, which disturbs the quartz resonance and make it difficult to obtain stable and neat frequency signal. Therefore, quartz crystals with higher fundamental quartz frequency are too sensitive for our application. Another advantage of choosing lower fundamental frequency is that the quartz is thicker (333 μm) as compared to quartz with higher fundamental frequency (e.g. 185 μm for 9 MHz) hence less fragile and larger active area is

allowed.

Both sides of the quartz crystal were patterned with polished gold electrodes (as shown in Figure IV-10a^[33]), and titanium was chosen as adhesion layer between gold and quartz crystal due to its electrochemical stability in our system. The diameters of front electrode which is in contact the electrolyte and rear electrode are 1/2 and 1/4 inch, respectively. The electrochemical active area is the area of front electrode (1.37 cm^2), and the measured current and mass change shown in this chapter are normalized by this area.

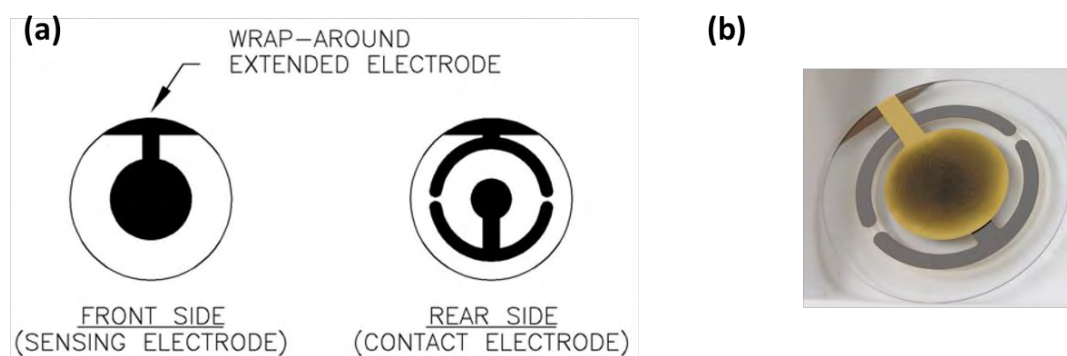


Figure IV-10: Maxtek quartz crystal: (a) crystal electrode patterns and (b) quartz crystal with carbon deposition (CDC-0.65nm)

As mentioned previously, to be able to apply Sauerbrey equation (Equation IV-3) for converting frequency change into mass change, the carbon deposition has to be uniform, rigid and thin. Therefore, the amount of carbon deposited on the quartz crystal cannot be too high, but at the same time sufficient to acquire reliable electrochemical data. The optimized mass loading of the carbon deposition on the quartz is around $20 - 60 \mu\text{g}/\text{cm}^2$. Figure IV-10b shows an example of a carbon-coated quartz crystal. Moreover, as mentioned in previous section, the motional resistance of the quartz represents the energy dissipated during oscillation and is related to the electroacoustic properties of the QCM and the contacting medium is also tracked in different stages of the experiments, and will be discussed later in section IV-3.1.

The EQCM three-electrode cell was prepared as follow: Slurry composed of 80 - 90 wt % of active electrode materials and 10 - 20 % of polyvinylidene fluoride (Arkema, CAS #24937-79-9) in N-Methyl-2-pyrrolidone (Sigma-Aldrich, CAS #872-50-4) was prepared and dripped on the quartz. The carbon-coated quartz was then dried in 60°C oven overnight, and mounted in a Teflon quartz holder. The electrochemical cell was assembled in a glove box under argon atmosphere (oxygen and water content $< 1 \text{ ppm}$) at room temperature by using

the carbon-coated quartz as working electrode, platinum-coated titanium mesh as counter electrode and a silver wire as a quasi-reference electrode, as shown in Figure IV-11. Maxtek RQCM system combined with Metrohm Autolab Potentiostats / Galvanostats (Autolab PGSTAT101) was used for simultaneous EQCM and electrochemical measurements. After the cell was assembled, prior to electrochemical measurements, cyclic voltammetry at 10 mV/s was launched for few cycles until stable EQCM signals were obtained.

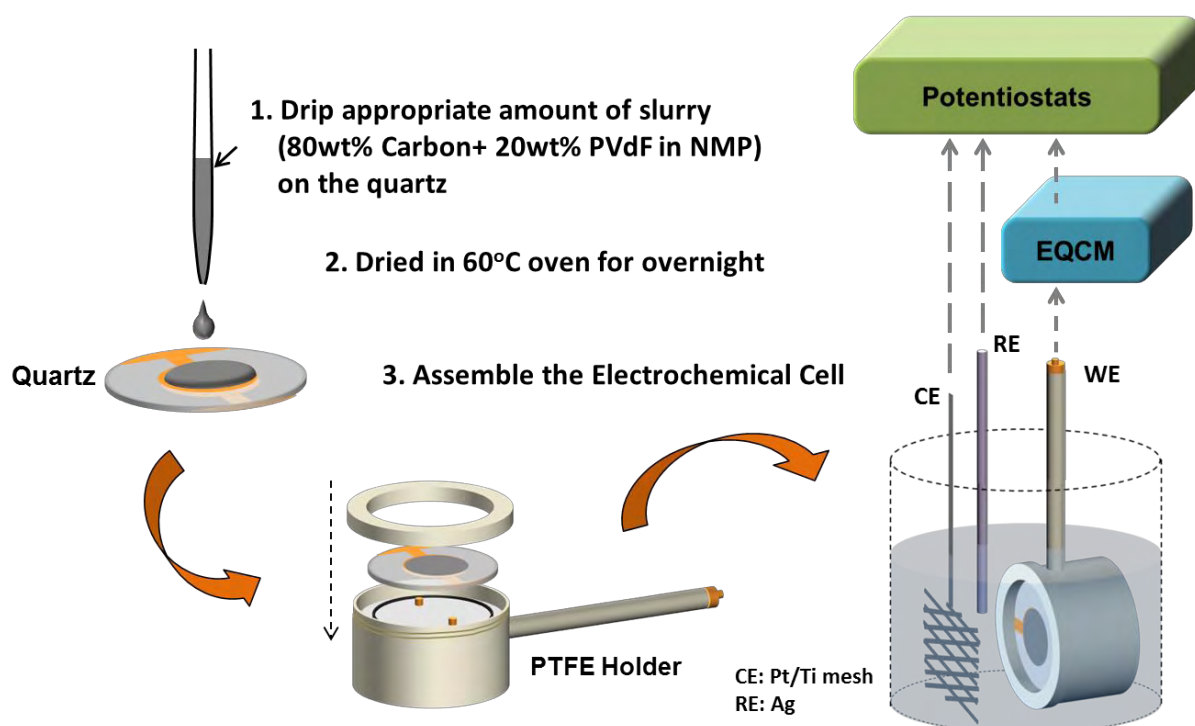


Figure IV-11: Schematic of EQCM set-up

2.3 Calibration (sensitivity constant, C_f)

To apply Sauerbrey equation for converting the shift of the quartz resonance frequency (Δf) into mass change (Δm) on the quartz electrode, the calibration constant (sensitivity factor, C_f) is needed. The sensitivity factor, C_f , was obtained by carrying out a silver electroplating under constant current (chronopotentiometry @ $-0.18\text{mA}/\text{cm}^2$) on a bare quartz soaked in electrolytic solution containing 0.01 M silver nitrate and 0.1 M tetraethylammonium tetrafluoroborate in acetonitrile. The frequency response recorded by EQCM during silver electroplating was shown in Figure IV-12.

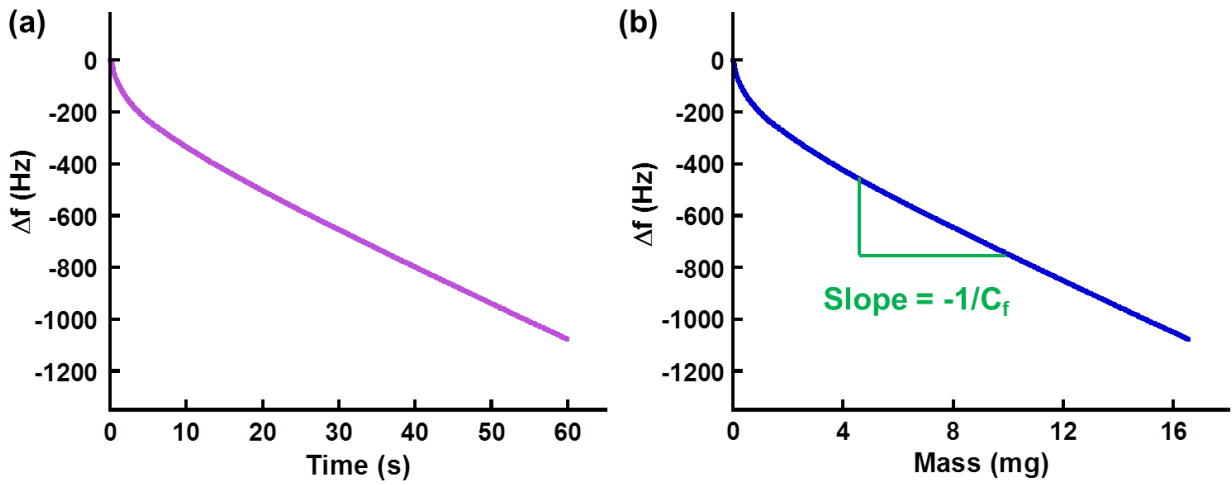


Figure IV-12: EQCM calibration by conducting silver electroplating under constant current: (a) frequency change versus time, and (b) frequency change versus mass change

The mass of silver deposit (m) was calculated by applying Faraday's law (Equation IV-7), assuming a 100% faradic efficiency:

$$m = \frac{Q \cdot M_w}{n \cdot F} = \frac{I \cdot t \cdot M_w}{n \cdot F} \quad (\text{Equation IV-7})$$

Where Q is the charge stored on the electrode in Coulomb, I is the current in Ampere, t is the time in seconds, M_w is the molecular weight of silver (107.9 g/mol), F is the Faraday Constant (96485 C/mol), and n is the valence number of the ion (in this case it is one for silver ion). Figure IV-12a then can be re-plotted into frequency change versus mass change (Figure IV-12b). The calibration constant C_f was then determined from the slope of Δf versus Δm curve. The value of the calibration constant used in this work is 13.8 ng/Hz/cm².

2.4 Theoretical mass change, apparent molecular weight, and solvation number

Theoretical Mass Change (Δm_{Theo})

From cyclic voltammogram, the charge stored on the electrode can be calculated by integration of the current versus time. If we consider that one electrical charge stored on the electrode corresponds to one counter-ion adsorption (assuming 100 % efficiency), the *theoretical mass change* (Δm_{Theo}), caused by this amount of ion adsorption, could be obtained

by applying Faraday's Law (Equation IV-8):

$$\Delta m_{Theo} = \frac{Q \cdot M_w}{n \cdot F} = \frac{I \cdot t \cdot M_w}{n \cdot F} \quad (\text{Equation IV-8})$$

Where Q is the charge passed through the electrode in Coulomb, I is the current in Ampere, t is the time in seconds, M_w is the molecular weight of EMI^+ (111 g/mol) or TFSI^- (280 g/mol), F is the Faraday Constant (96485 C/mol), and n is the valence number of the ion, which is one for both cation and anion in this case. Both mass change and charge change are normalized by the electrochemical active area of the quartz (1.27cm^2).

Apparent Molecular Weight (M_w')

As EQCM measures the mass change during electrochemical tests and the amount of electronic charge stored can be calculated from current, further plotting mass change (Δm) versus charge (ΔQ), one can obtain more quantitative information from EQCM: the *apparent molecular weight* (M_w') of the species that interact with the electrode during electrochemical measurements could be calculated from the slope of the experimental Δm - ΔQ curve by the following equation (derived from Faraday's Law):

$$\frac{M_w'}{nF} = \frac{m}{Q} \quad (\text{Equation IV-9})$$

Acetonitrile Solvation Number (n)

As the apparent molecular weight of the species that interact with the electrode during electrochemical measurements can be determined, the acetonitrile solvation number can thus be calculated by the following equation:

$$n = \frac{M_w' - M_{w(\text{bare ion})}}{M_{w(\text{AN})}} \quad (\text{Equation IV-10})$$

where $M_{w(\text{bare ion})}$ and $M_{w(\text{AN})}$ are the molecular weight of ions and acetonitrile, respectively.

3. In-situ EQCM study of charge mechanism and the solvation effect at the electrode/electrolyte interface

3.1 Different experimental parameters

In this chapter, CDC-1nm and CDC-0.65nm will be studied with neat and solvated ionic liquid (EMI-TFSI) under potentiodynamic condition (cyclic voltammetry at 10 mV/s) with simultaneous quartz resonance frequency record. Before discussing EQCM results, there are few points need to be clarified. The *potential of zero charge (PZC)* is close to the open-circuit voltage (OCV) in each experiment conducted in this chapter (± 50 mV). In each experiment, the system was studied with three different potential ranges: individually above and below its open-circuit voltage (OCV), and the full electrochemical window range. Cycling the carbon electrode only above or only below OCV means the electrode is polarized in only one direction at one time; whereas charging the electrode in the full window, the electrode undergoes alternatively positive and negative polarization. Figure IV-13 compares the CVs and EQCM frequency responses between separate and full potential window. Both electrochemical and frequency responses showed exactly the same behavior, indicating that, under the applied scan speed, there is no difference in charging mechanisms between polarization held in the same direction or alternating direction. For simplicity's sake, only *separate polarizations* above and below OCV will be shown and discussed in this chapter.

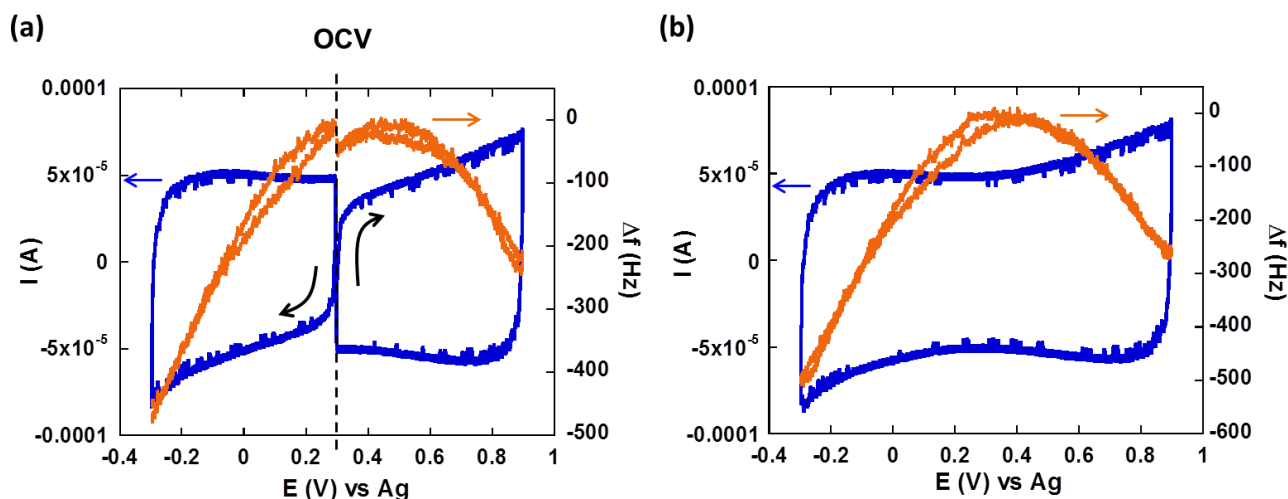


Figure IV-13: CVs and simultaneous frequency record from EQCM conducted (a) individually above and below its open-circuit voltage, and (b) with full potential window

Except for the fundamental reason mentioned previously in section IV-2.1 (validation of Sauerbrey equation), the motional resistance is important also for technical reason: high motional resistance results in the broadening of the resonance frequency peak, hence making it difficult for the EQCM apparatus to read accurate frequency value so increasing the noise. The motional resistance of an as-received Maxtek polished quartz (measured under air) is generally between 5 to 15 Ω , and it was controlled to be less than 100 Ω (measured under air) for a carbon deposited quartz. Beyond this value, no consistent measurement is achievable.

The *motional resistance* was further tracked and investigated after immersion in the liquid electrolytes (neat and acetonitrile (AN)-solvated EMI-TFSI). Here, as the 2M EMI-TFSI/AN may not be an ideal solution, motional resistances were estimated (calculation made from Equation IV-5) for two extremes: pure salt (EMI-TFSI in this case) and pure solvent. According to Equation IV-5, when immersing a *non-coated* quartz resonator in the liquid, the motional resistance increases are calculated to be ~ 2200 and ~ 592 Ω for neat EMI-TFSI ionic liquid and pure AN, respectively. Therefore, the motional resistance of a non-coated quartz immersed in the high concentration 2M EMI-TFSI/AN is expected to be in between these two values. The motional resistance of CDC carbon-coated quartz measured in both electrolytes situate in the range of 1700 – 2500 Ω , which is a reasonable value if taking into account the carbon deposit layer.

In all the results shown in this chapter, the motional resistance during supercapacitor charging/discharging is stable and only exhibits a change less than 50 Ω during cycling. An example, using CDC-1nm tested in the viscous neat EMI-TFSI, is shown in Figure IV-14 where resonance frequency changes with potential polarization and the motional resistance is kept almost constant during cycling. This indicates that the carbon electrode is stable on the quartz in the electrolyte and the frequency change is originated from gravimetric events (ion adsorption/desorption), hence the use of Sauerbrey equation to convert frequency change into mass change is valid.

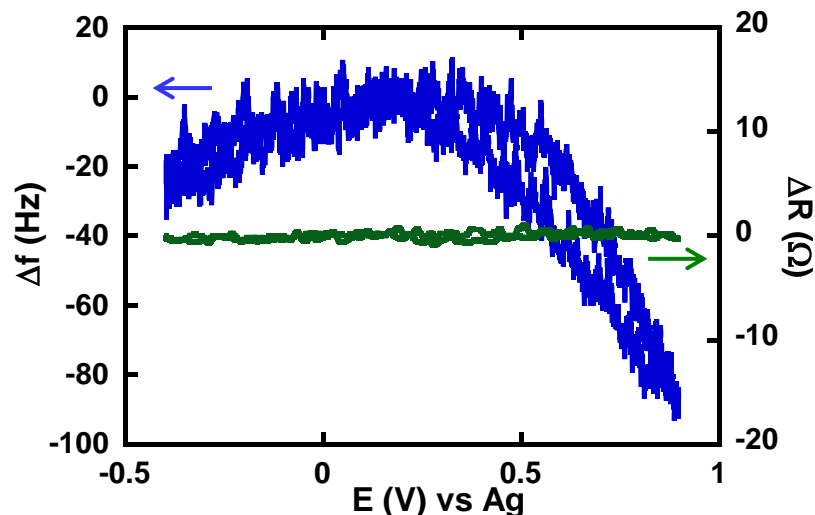


Figure IV-14: Change of resonance frequency (Δf) and motional resistance (ΔR) during one cycle versus potential after stabilization for CDC-1nm in neat EMI-TFSI

3.2 Neat EMI-TFSI

3.2.1 CDC-1nm

The Cyclic voltammograms (CVs) and EQCM results of CDC-1nm tested at room temperature in neat EMI-TFSI is presented in Figure IV-15. For studying the individual contribution anion and cation, results were collected in two different potential ranges in each experiment in this chapter: starting from the open-circuit voltage (OCV) vs silver quasi-reference indicated with purple dots in the figure, the potential was scanned negatively down to negative potential values (Figure IV-15a) or up to positive potential values (Figure IV-15b). CVs are presented in dashed line and frequency responses are presented in solid line, and the different colors indicate the ion charging (orange curves) and discharge (blue curves). According to Sauerbrey's equation (Equation IV-3), the frequency response (Δf) decreases when the electrode mass (Δm) increases. For visual convenience, negative frequency responses ($-\Delta f$), proportional to Δm , are shown in the Figure. In all the following tests, the electrochemical potential windows were found to be smaller than those of previously reported using conventional CDC film electrodes (3V for neat EMI-TFSI and 2.5V for 2M EMI-TFSI/AN).^[20] It is mainly due to the small amount of carbon deposited on the quartz (20 - 45 $\mu\text{g}/\text{cm}^2$) as compare to the carbon loading of conventional supercapacitors (about 10 mg/cm^2), thus exalting the electrochemical activity of the electrolyte on the Au electrode at highly positive or negative potentials..

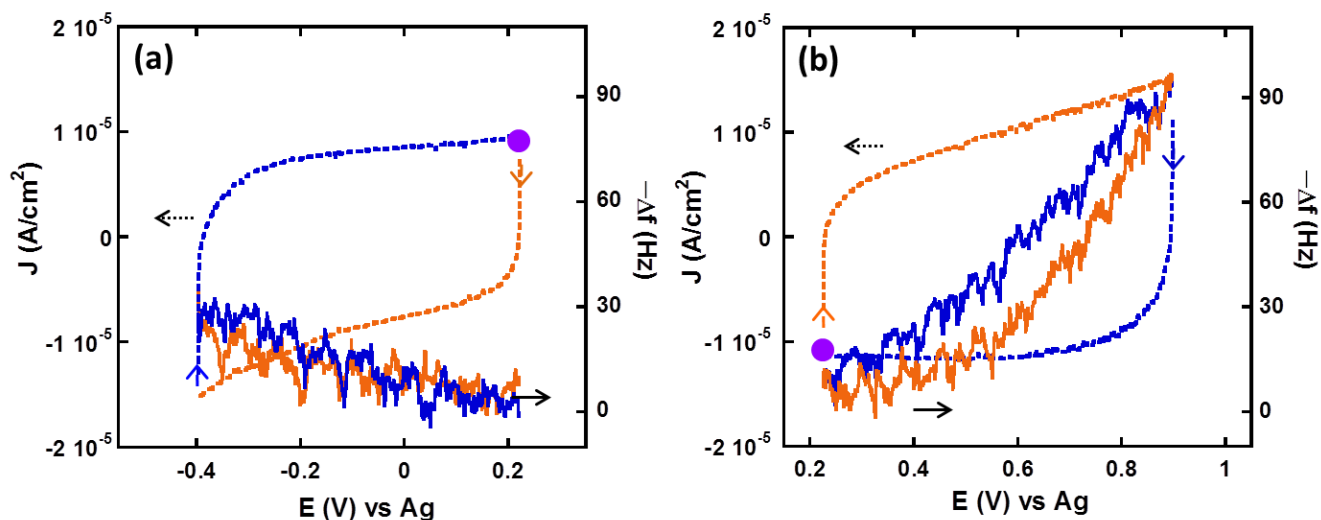


Figure IV-15: CV and EQCM frequency response of CDC-1nm in neat EMI-TFSI (a) below OCV and (b) above OCV. Purple dot is where the cycle starts. Orange and blue curves indicate charge and discharge of ions, respectively.

Despite the contact between carbon deposition and the quartz is not optimized (which is made by simple drip-coating), both Figure IV-15a and 15b exhibit a characteristic capacitive behavior with rectangular CV profiles, thus confirming previous study^[20] conducted with the same carbons showing that both cations and anions could freely access 1 nm pores. In Figure IV-15a, the potential scan begins first from OCV (0.22 V) down to -0.4 V (vs Ref), and then swept back to the OCV. The simultaneous change of the opposite of the frequency ($-\Delta f$, proportional to the electrode weight increase) versus the potential in Figure IV-15a shows that the mass of the electrode increased during negative scan (orange solid line) and decreased during positive scan (blue solid line). In this potential range, the charge/discharge of the double layer can be considered to be mainly achieved by adsorption/desorption of the cations (EMI^+), in a first approximation. Therefore, the increase of the electrode mass observed during charging (negative scan) is associated with cation adsorption, while during desorption (positive scan), the electrode mass decreases.

In Figure IV-15b, the potential scan was achieved from OCV up to 0.9 V (vs Ref), and then reversed back to OCV; the quartz resonance frequency response ($-\Delta f$) first increased and then decreased. Similarly, from Sauerbrey's equation, the electrode mass increases during charging (positive scan) and decreases during discharging (negative scan); the weight change fits with the adsorption and desorption of TFSI^- anions which is assumed to be responsible of the charge balance at the carbon surface within this potential range.

Figure IV-16 shows the change of the electrode weight (Δm) vs the charge passed in the electrode (ΔQ) during *ion charging* in the cyclic voltammetry: assuming that there is zero polarization at OCV ($\Delta Q = 0$), and the carbon electrode was negatively polarized ($\Delta Q < 0$) from the OCV down to -0.4 V/Ref (Figure IV-15a) and positively polarized ($\Delta Q > 0$) from OCV up to 0.9 V/Ref (Figure IV-15b). The theoretical weight change, indicated as red dashed lines in Figure IV-16, could be obtained by applying Faraday's Law (Equation IV-8) as discussed in Section IV-2.4. It should be noted that the theoretical mass change considers that the charge accumulated on the electrode was compensated *only* by EMI^+ adsorption or TFSI^- adsorption.

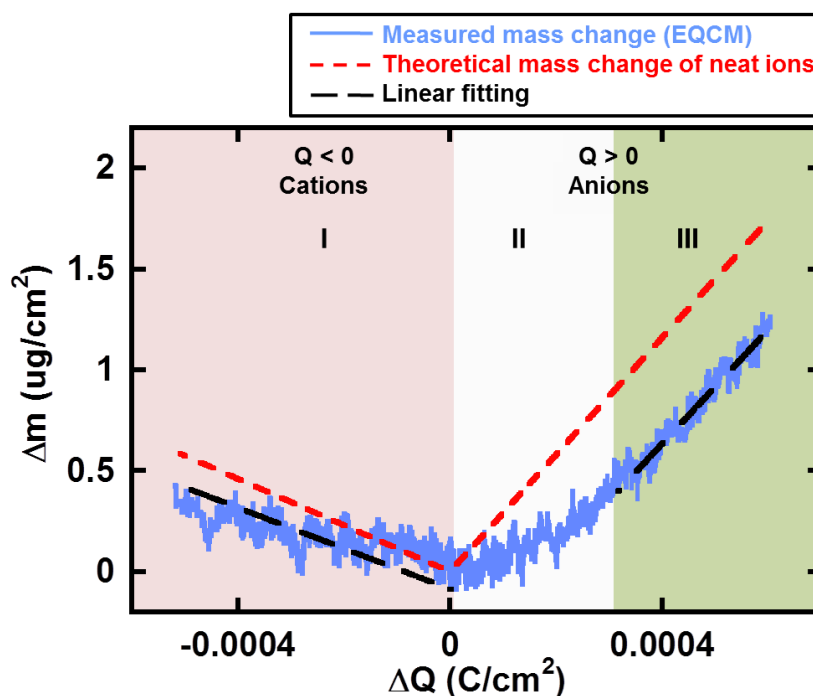


Figure IV-16: Electrode mass change vs charge during the polarization of CDC-1nm in neat EMI-TFSI: Blue solid lines are Red dashed lines are the theoretical mass change of neat ions calculated from Faraday's law. Black dashed line shows the linear fitting of measured mass change.

Furthermore, the apparent molecular weight (M_w') of the species that interact with the electrode during electrochemical measurements could be calculated from the slope of the experimental Δm - ΔQ curve (by Equation IV-9, as shown in Section IV-2.4). Starting from the OCV ($\Delta Q = 0$), the electrode mass change increases steadily during negative polarization in neat EMI-TFSI in CDC-1nm (Figure IV-16, domain I): there is a linear change of the electrode mass with the negative charge accumulated on the electrode. Both the mass change and the mean slope of the experimental plot (black dashed line) are close to those of theoretical ones

over the whole range of charge (ΔQ). The apparent molecular weight (M_w') of the adsorbed species calculated from the experimental slope is 97 g/mol, close to the molecular weight of EMI^+ cation (111 g/mol), showing that in domain I, the charge in the porous electrode was balanced mainly through cation adsorption and no co-ion seems to be involved. Such behavior has been previously reported and described by Levi et al.^[14,15] as perm-selectivity: only the adsorption of the counter-ion balanced the charge at the carbon electrode.

A different behavior is observed during anion adsorption (positive polarization, $\Delta Q > 0$): the electrode mass change first increases slowly for positive charge less than 0.3 mC/cm^2 (domain II), and then reaches a constant slope for charge more than 0.3 mC/cm^2 (domain III). In the linear part of domain III ($\Delta Q > 0.3 \text{ mC/cm}^2$), the calculated apparent molecular weight of the adsorbed species is 270 g/mol, close to that of the bare anions (280 g/mol for TFSI^-). This suggests that, at high polarization, the charge storage mechanism mainly involves anion adsorption in confined nanopores. However, at lower polarization in domain II ($\Delta Q < 0.3 \text{ mC/cm}^2$), the slope of the experimental curve is less than the theoretical one corresponding to the bare anion adsorption (red dashed line), suggesting that TFSI^- anion adsorption is not the only process involved during charging process. This behavior was already reported by Levi et al.,^[15] and corresponds to an ion exchange zone. In this small positive polarization range, the anions enter the nanopores while the cations are expelled from the electrode at the same time, leading to the breaking of the perm-selectivity in the 1 nm micropores.^[15,18] Hence, the net mass change or the apparent molecular weight observed by EQCM are less than that of theoretical ones. Upon subsequent increase of the polarization ($\Delta Q > 0.3 \text{ mC/cm}^2$, domain III), the Δm - ΔQ curve shows that only anion transfer is observed and the perm-selectivity of the electrode is recovered. This also shows that TFSI^- anions need more energy to move, when the energy is small (weak polarization, $\Delta Q < 0.3 \text{ mC/cm}^2$), EMI^+ cations respond faster than TFSI^- anion to compensate the charge, suggesting that EMI^+ cations more mobile than TFSI^- anions in the confined 1-nm nanopores. The difference observed between negative (cation adsorption) and positive polarization (anion adsorption) is consistent with modelling results obtained in neat BMI- PF_6 electrolyte, which showed that more counter- and co-ions were involved during positive polarization.^[7]

3.2.2 CDC-0.65nm

The results of CDCs with smaller pore size (0.65nm) tested in neat EMI-TFSI are presented in Figure IV-17. Since the CDC pore size is smaller than both the cation and anion size, it is expected that the ions have limited access to the pores, as previously shown by Segalini et al.^[36] Both CVs in Figure IV-17a and 17b show slightly-distorted rectangular signature, and the current is an order of magnitude lower than that of CDC-1nm (Figure IV-15a and 15b). The EQCM frequency responses for both positive and negative polarizations exhibit almost no variation, meaning that no mass change on the quartz was observed upon cycling. Both CV and EQCM results are in agreement with the expectation that the pore size of 0.65 nm is too small for both cation and anion to enter or leave without hindrance.

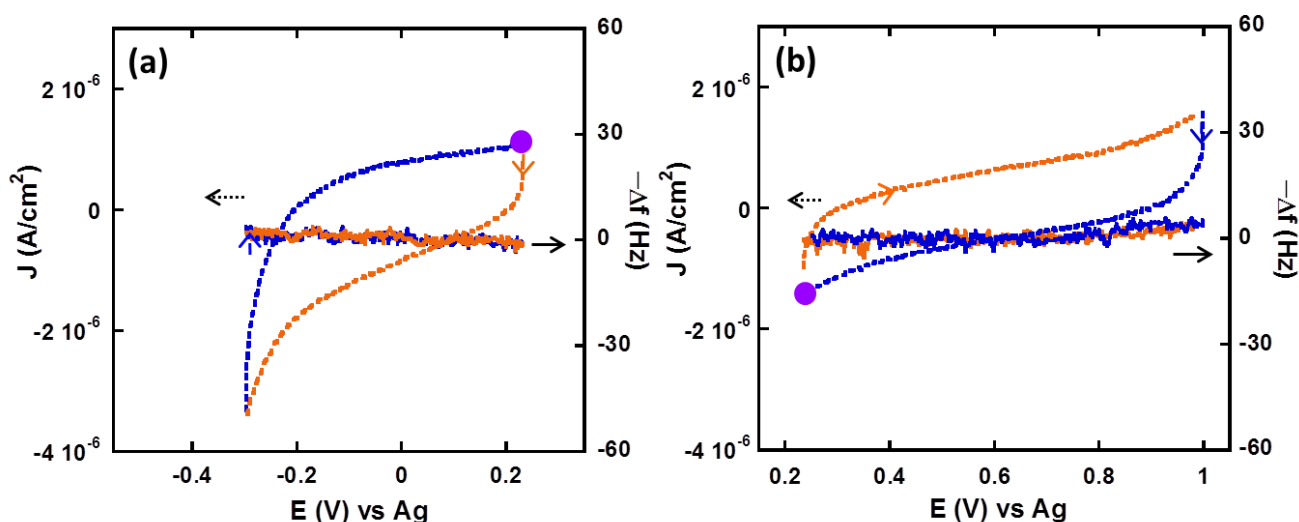


Figure IV-17: CV and EQCM frequency response of CDC-0.65nm in neat EMI-TFSI (a) below OCV and (b) above OCV. Purple dot is where the cycle starts. Orange and blue curves indicate charge and discharge of ions, respectively.

Figure IV-18 presents the electrode mass change measured by EQCM (pastel blue solid line) and theoretically calculated from Faraday's law (red dashed line) versus charge passed in the electrode (ΔQ) during *ion charging* in the cyclic voltammetry. The mass change (Δm) was plotted in the same scale as Figure IV-16. Figure IV-18 gives the same message as Figure IV-17: for both positive and negative polarization, there is much less charge stored on the electrode than that of CDC-1nm and almost no mass change was observed suggesting that both cations and anions have difficulties to access the nanopores. One may question that if no ion enters the pores hence no mass increase observed, but what is the origin of the measured minute current? First, it should be noted that when cycling the blank quartz (only with gold

electrode pad on top of the quartz, without carbon deposition), a tiny current could also be observed with no electrode mass change, arising from the electrical double layer in front of the gold pad as in the conventional planar capacitors. For the carbon electrode, the double layer forms at both interior surface (inside the mesopores and micropores) and exterior surface (outermost carbon layer of the electrode and between carbon particles). Therefore, it is suggested that the current in Figure IV-17 mainly comes from the ion adsorption at the exterior surface of the carbon.

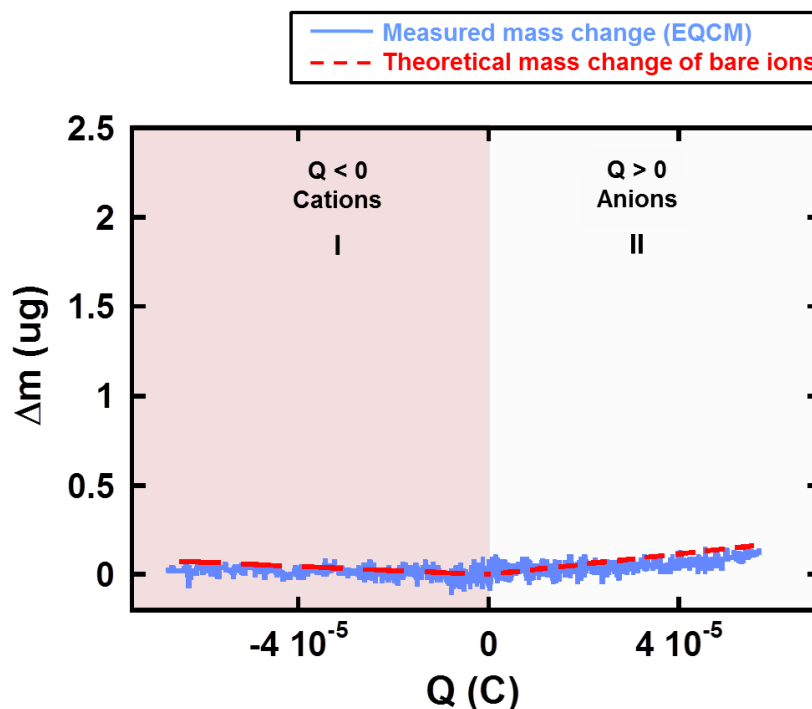


Figure IV-18: Electrode mass change vs charge during the polarization of CDC-0.65nm in neat EMI-TFSI

3.3 Solvated EMI-TFSI

3.3.1 CDC-1nm

The two CDC samples were also tested in 2M EMI-TFSI solvated in acetonitrile to study the effect of solvent. First, the CVs and quartz frequency responses of CDC-1nm in solvated EMI-TFSI are presented in Figure IV-19a and 19b. For both positive and negative polarization, CVs exhibit capacitive behavior with nice rectangular profile, showing that both anions and cations could access the 1 nm-pore without restraint. Regarding the frequency responses, similar trend as in Figure IV-15 (CDC-1nm in neat EMI-TFSI) was obtained: the electrode mass increases during cation/anion adsorption and decreases during cation/anion desorption.

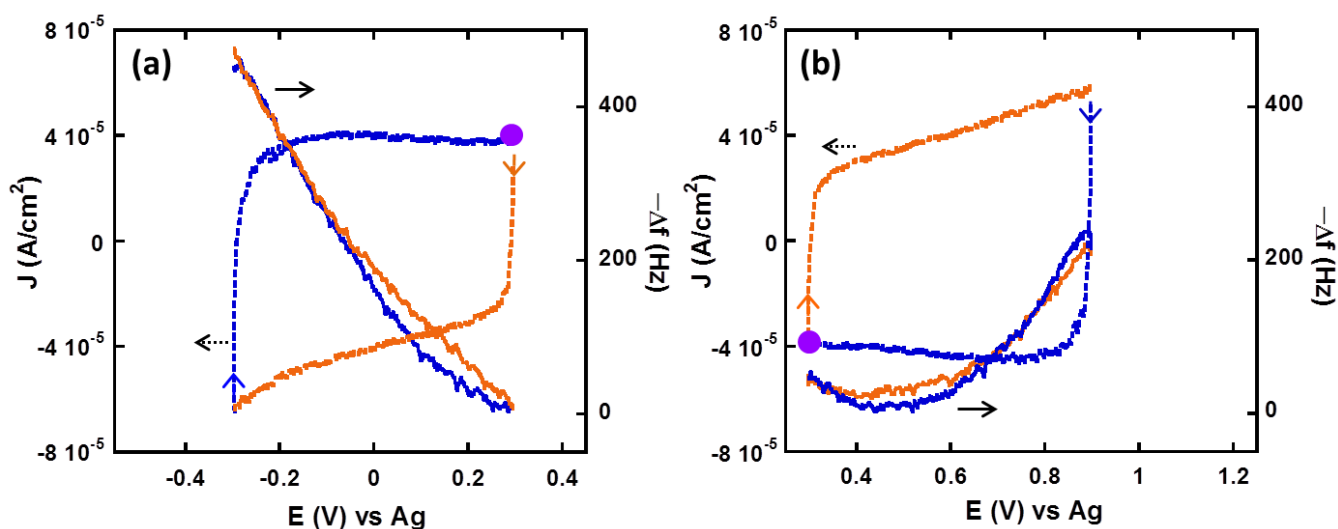


Figure IV-19: CV and EQCM frequency response of CDC-1nm in 2M EMI-TFSI + AN (a) below OCV and (b) above OCV. Purple dot is where the cycle starts. Orange and blue curves indicate charge and discharge of ions, respectively.

The electrode mass change (Δm) vs charge change (ΔQ) during polarization of the CDC-1nm electrode in solvated EMI-TFSI (Figure IV-20) shows similar results to that of neat EMI-TFSI: three different domains could be observed. For negative charge ($\Delta Q < 0$, domain I), the electrode mass change increased linearly with the charge along the whole negative charge range, and slope of the curve is much higher than that of theoretical one (red dashed line). For positive charge ($\Delta Q > 0$), a different behavior is observed. At the beginning of positive polarization (domain II), the slope of the experimental Δm - ΔQ curve is almost zero and increases with charge until 1.4 mC/cm^2 . The slope of the curve then keeps almost constant after reaching 1.4 mC/cm^2 (domain III). Such a behavior can only be explained by the

existence of an cation-anion mixing zone, due to a breaking of the perm-selectivity in the carbon micropores of 1 nm: the adsorption of counter-ions, here TFSI^- , is accompanied by the desorption of co-ions, EMI^+ . But whatever the charge, the slope of the experimental curve is always less than that of theoretical curve which was obtained by considering that the charge stored on the electrode is balanced only by neat (non-solvated) TFSI^- anion adsorption.

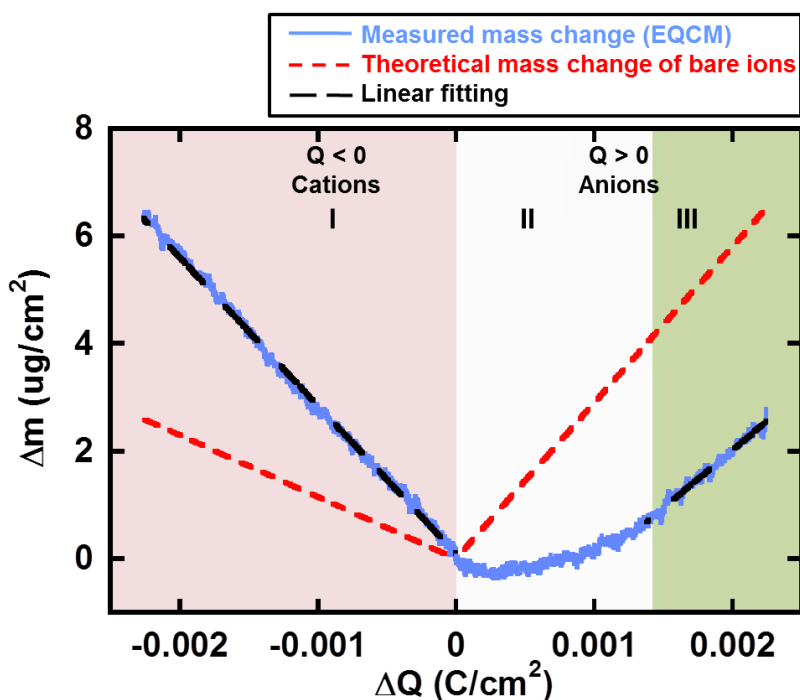


Figure IV-20: Electrode mass change vs charge during the polarization of CDC-1nm in 2M EMI-TFSI + AN: Blue solid lines are Red dashed lines are the theoretical mass change of neat ions calculated from Faraday's law. Black dashed line shows the linear fitting of measured mass change.

The apparent molecular weight of the adsorbed species involved in the charge storage mechanism is proportional to the slope of the $\Delta m-\Delta Q$ curve and could be calculated using Equation IV-9. For positive polarization (domain I), the calculated apparent molecular weight is 265 g/mol which is much higher than bare EMI^+ molecular weight (111 g/mol). Assuming that the stored charge was balanced only by cations with 100% efficiency and that the difference between these two values originates from the presence of solvent molecule surrounding the EMI^+ cation during the adsorption process, the average solvation number of the EMI^+ cations in acetonitrile can then be calculate using Equation IV-10 (Section IV-2.4). Base on the calculation, there are 3.7 acetonitrile molecules entering the pores together with one EMI^+ cation. For negative polarization (domain III), the calculated apparent molecular weight is around 208 g/mol, less than bare TFSI^- molecular weight (280 g/mol). However, this

doesn't suggest that there is no solvated acetonitrile molecule around TFSI⁻ anion. Actually, the slope of the curve increases very slowly with the charge in domain III, but it is not possible to extract the acetonitrile solvation number due to the limited/narrow electrochemical window.

These results indicate that for negative polarization, despite the presence of the solvation shell around the EMI⁺ cations, the 1 nm micropores show a perm-selective behavior since there is no cation-anion mixing in this region. Similar to what was observed in neat EMI-TFSI electrolyte, in presence of solvent molecules, the charge storage in microporous carbons with controlled 1 nm pore size seems to mainly involve cation take-in, different from what was observed with microporous activated carbons in propylene carbonate-based organic electrolytes.^[15] While during positive charging, perm-selectivity of CDC-1nm collapsed at low polarization since cation-anion exchange was observed in this region. These results are in agreement with the higher mobility of cations as compared to anions^[17,37] in neat EMI-TFSI, and with our previous electrochemical study using cavity micro-electrode in solvated EMI-TFSI electrolytes.^[20]

3.3.2 CDC-0.65nm

Regarding the CDC-0.65nm in solvated EMI-TFSI (Figure IV-21a and 21b), both CVs are distorted, and the current is smaller for anion adsorption/desorption process (Figure IV-21b, positive polarization) than that of cation one (Figure IV-21a, negative polarization). Furthermore, the quartz frequency responses show distinct difference between cation and anion adsorptions: an obvious electrode mass change was observed during positive polarization (Figure IV-21a) yet there is almost no mass change during negative polarization (Figure IV-21b). Results show that solvated anions face more difficulties than solvated cations to access the 0.65-nm pores, suggesting that the effective size of anion is larger than that of cation which is in accordance with our previous study.^[20]

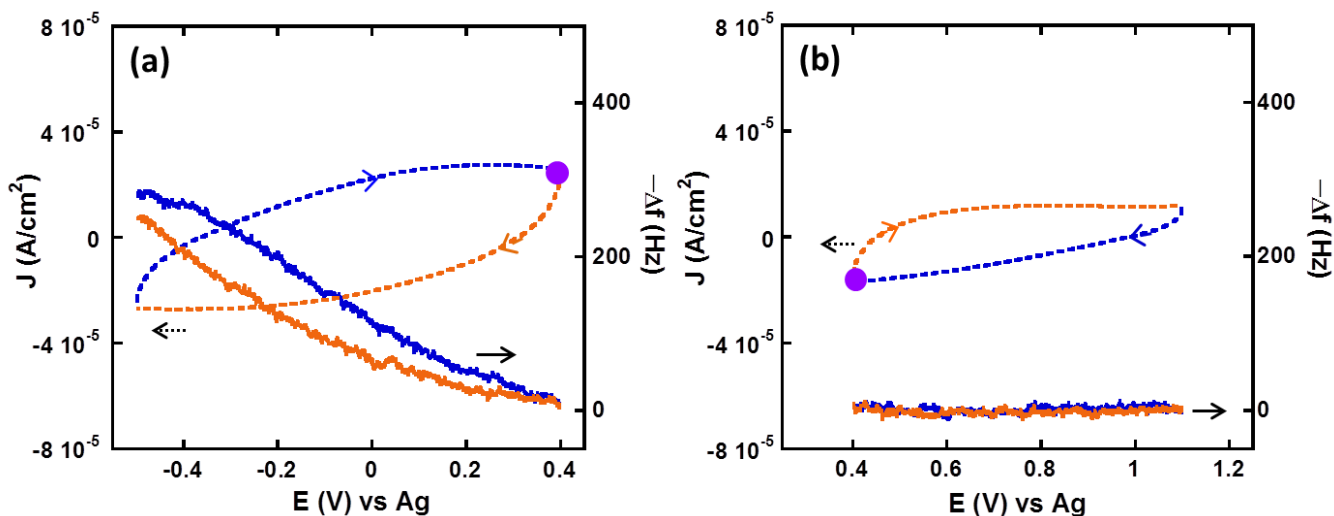


Figure IV-21: CV and EQCM frequency response of CDC-0.65nm in 2M EMI-TFSI + AN (a) below OCV and (b) above OCV. Purple dot is where the cycle starts. Orange and blue curves indicate charge and discharge of ions, respectively.

Figure IV-22 shows the electrode mass (Δm) vs charge change (ΔQ) during the charging of CDC-0.65nm in 2M EMI-TFSI in acetonitrile. As already seen in Figure IV-21b, the Δm - ΔQ curve does not show any mass change during anion adsorption ($\Delta Q > 0$, domain II) which is ascribed to the size effect: pore size is too small for solvated anions to access. For cation

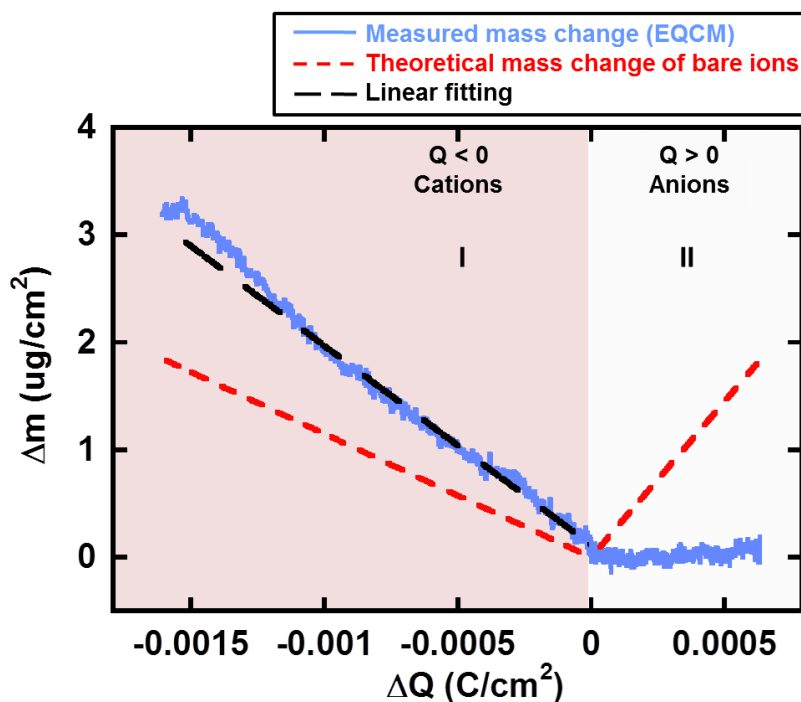


Figure IV-22: Electrode mass change vs charge during the polarization of CDC-0.65nm in 2M EMI-TFSI + AN: Blue solid lines are Red dashed lines are the theoretical mass change of neat ions calculated from Faraday's law. Black dashed line shows the linear fitting of measured mass change.

adsorption ($\Delta Q < 0$, domain I), the same trend as for solvated EMI-TFSI in CDC-1nm is observed, except that the slope of the Δm - ΔQ curve is lower. From the slope of the curve, an average molecular weight of 179 g/mol was obtained, corresponding to a mean solvation number of 1.6. A smaller solvation number has been found for EMI⁺ adsorption in the narrower 0.65-nm pore size as compare in 1-nm pore (with solvation number of 3.7), supporting the partial desolvation of the cations when accessing small pores.

A recent study on charge storage mechanism in confined nanoporous CDC electrodes in another ionic liquid electrolyte (BMI-PF₆) by molecular dynamic simulation shows that at null potential (before polarizing the electrode), no ions are found into the micropores but the acetonitrile molecules are present in all the confined pores. Under polarization, acetonitrile molecules are replaced in the small pores with ions that can access these confined 1 nm pores by partial desolvation, the solvation number moving from 8-9 in bulk electrolyte down to 2-3 in confined pores,^[38] in agreement with the present experimental results.

4. Discussions

The in-situ EQCM study using two CDCs with different pore size in neat and solvated EMI-TFSI electrolytes has unveiled part of the charge storage mechanism in supercapacitor electrodes, and provided some important information on ion transport and ion dynamics during charging process. In both electrolytes, the ions encounter more difficulties in accessing CDCs with 0.65nm-pore than that with 1nm-pore which is in good agreement with our previous studies. Information on the compositional change in the carbon nanopores during the electrochemical incidents could be further derived from in-situ EQCM results. Table IV-2 summarizes the calculated apparent molecular weights and the acetonitrile solvation number in the four systems.

Table IV-2: Apparent molecular weights calculated from the experimental Δm vs ΔQ curves*

	Neat EMI-TFSI (g/mol)		Solvated EMI-TFSI (g/mol)	
	EMI ⁺ (111)	TFSI ⁻ (280)	EMI ⁺ (111+n·AN)	TFSI ⁻ (280+n·AN)
CDC-1nm	97	270 (high Q)	265 (n=3.7)	208 (high Q)
CDC-0.65nm	-	-	179 (n=1.6)	-

*The apparent molecular weights regarding anion adsorption in CDC-1nm for both electrolytes were obtained from Δm vs ΔQ curves at high polarization (high Q). n is the calculated acetonitrile solvation number

From results of CDC-1nm in neat EMI-TFSI, it was found that negative polarization and high positive polarization, the charge storage only involved in counter-ions (EMI⁺ for negative polarization, and TFSI⁻ for positive polarization), suggesting that the adsorption energy is strong enough to screen ion pairing interaction between cations and anions. The co-ions (TFSI⁻ for negative polarization and EMI⁺ for positive polarization) don't seem to participate in the charge storage in these regions.

For CDC-1nm in both neat and solvated EMI-TFSI electrolytes, different behaviors have been observed between EMI⁺ and TFSI⁻ adsorption, as shown in Figure IV-23 (taking neat EMI-TFSI as example). During negative charging, only EMI⁺ cation adsorption is observed, while positive charging, ion exchange was found when polarization was low. When higher

positive polarization was applied, TFSI⁻ anions became the dominating species that balance the charge. The difference between cation and anion adsorption is attributed to the different ion mobility in the system, and the ion exchange process may slow down the transport and adsorption kinetics at the positive porous carbon electrodes.

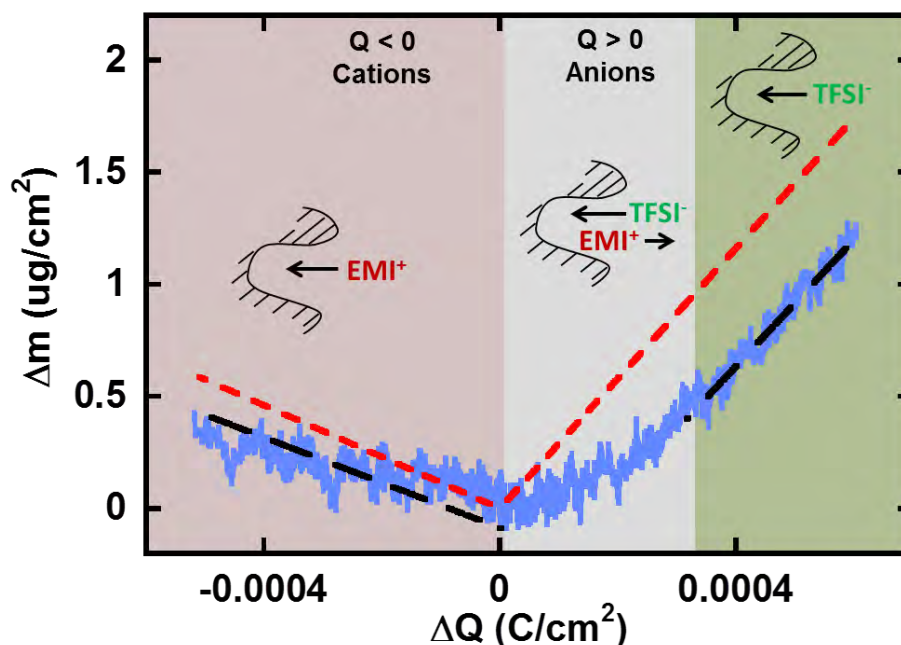


Figure IV-23: Scheme of ion transport in 1-nm pores during different charging states (taking neat EMI-TFSI as example)

It should be noted that EQCM measures the net electrode mass change during the electrochemical tests, but it cannot give quantitative information on each species since it could not distinguish the weight contributed by different molecules. Therefore, regarding the results in solvated EMI-TFSI, it is difficult to point out clearly how the solvent molecules affect the charge storage. Do they screen the charge of counter-ions leading a less efficient charge storage? Or does their solvation help to decrease the interaction between counter-ions and co-ions resulting in a more efficient charge storage? The charge storage efficiency could not be obtained since the exact amount of each ion is unknown; hence these questions were left unanswered. Even though, since at high polarization, no ion-pairing or charge screening by co-ions were observed during charging in confined micropores in neat EMI-TFSI, hence it is reasonable to assume the same for solvated EMI-TFSI – one net charge stored corresponds to one single cation (100% efficiency) – and further calculate the solvation numbers (Equation IV-10). As shown in Table IV-2, by applying the same assumption on the two CDC samples,

it has been found that the cation solvation numbers in 1nm- and 0.65nm-pore were estimated to be 3-4 and 1-2, respectively. These numbers provide important insights into the difference in solvation environment between CDC-1nm and CDC-0.65nm. The less solvated acetonitrile molecules in 0.65nm-pore than in 1nm-pore signify that the ion desolvation more marked in the smaller pores.

Hysteresis was observed in the quartz frequency response between charging and discharging, indicating that charging and discharging involve different processes. It may come from the different difficulties ions face to go in and depart from the micropores. Extended experiments need to be carried out to figure out the origin of the hysteresis.

5. Conclusions

This chapter demonstrates that EQCM can serve as an electrogravimetric probe to study compositional changes in carbon micropores during charging/discharge of supercapacitors, thus making it a powerful tool for understanding the in-situ ion fluxes and the solvation effect. In-situ EQCM study of CDC-1nm and CDC-0.65nm in EMI-TFSI based electrolytes has shown that different charge storage mechanisms are involved for positive and negative polarization.^[39] Experimental acetonitrile solvation numbers were estimated for EMI⁺ cation, and partial desolvation was observed when decreasing the carbon pore size from 1 down to 0.65 nm.

Results also suggested that at high polarization under *dynamic condition*, one net charge stored on the carbon electrode surface corresponds almost to one single counter-ion adsorption. No ion-pairing or charge screening by co-ions are observed during charging in confined micropores. These results provide important information on charge storage mechanisms. However, to get a closer look at the EDL structure and to distinguish the contribution of each electrolytic species, in-situ EQCM alone is insufficient as it cannot probe individual species in the electrolytes. Therefore, in the next chapter, in-situ NMR is coupled with EQCM. The element-selective nature of NMR technique will surely bring more fundamental insights on EDL charging.

6. Reference

- [1] J. Chmiola, G. Yushin, Y. Gogotsi, C. Portet, P. Simon, P. L. Taberna, *Science* **2006**, *313*, 1760.

- [2] J. Huang, B. G. Sumpter, V. Meunier, *Chem. - Eur. J.* **2008**, *14*, 6614.
- [3] R. Lin, P. L. Taberna, J. Chmiola, D. Guay, Y. Gogotsi, P. Simon, *J. Electrochem. Soc.* **2009**, *156*, A7.
- [4] S. Kondrat, N. Georgi, M. V. Fedorov, A. A. Kornyshev, *Phys. Chem. Chem. Phys.* **2011**, *13*, 11359.
- [5] Y. Shim, H. J. Kim, *ACS Nano* **2010**, *4*, 2345.
- [6] P. Wu, J. Huang, V. Meunier, B. G. Sumpter, R. Qiao, *ACS Nano* **2011**, *5*, 9044.
- [7] C. Merlet, B. Rotenberg, P. A. Madden, P.-L. Taberna, P. Simon, Y. Gogotsi, M. Salanne, *Nat. Mater.* **2012**, *11*, 306.
- [8] D. Jiang, J. Wu, *J. Phys. Chem. Lett.* **2013**, *4*, 1260.
- [9] T. Ohba, K. Kaneko, *J. Phys. Chem. C* **2013**, *117*, 17092.
- [10] S. Kondrat, P. Wu, R. Qiao, A. A. Kornyshev, *Nat. Mater.* **2014**, *13*, 387.
- [11] H. Wang, A. C. Forse, J. M. Griffin, N. M. Trease, L. Trognko, P.-L. Taberna, P. Simon, C. P. Grey, *J. Am. Chem. Soc.* **2013**, *135*, 18968.
- [12] M. Deschamps, E. Gilbert, P. Azais, E. Raymundo-Pinero, M. R. Ammar, P. Simon, D. Massiot, F. Beguin, *Nat. Mater.* **2013**, *12*, 351.
- [13] F. W. Richey, B. Dyatkin, Y. Gogotsi, Y. A. Elabd, *J. Am. Chem. Soc.* **2013**, *135*, 12818.
- [14] M. D. Levi, G. Salitra, N. Levy, D. Aurbach, J. Maier, *Nat. Mater.* **2009**, *8*, 872.
- [15] M. D. Levi, N. Levy, S. Sigalov, G. Salitra, D. Aurbach, J. Maier, *J. Am. Chem. Soc.* **2010**, *132*, 13220.
- [16] L. Daikhin, S. Sigalov, M. D. Levi, G. Salitra, D. Aurbach, *Anal. Chem.* **2011**, *83*, 9614.
- [17] M. D. Levi, S. Sigalov, G. Salitra, D. Aurbach, J. Maier, *ChemPhysChem* **2011**, *12*, 854.
- [18] M. D. Levi, S. Sigalov, G. Salitra, R. Elazari, D. Aurbach, *J. Phys. Chem. Lett.* **2011**, *2*, 120.
- [19] C. Largeot, C. Portet, J. Chmiola, P.-L. Taberna, Y. Gogotsi, P. Simon, *J. Am. Chem. Soc.* **2008**, *130*, 2730.
- [20] R. Lin, P. Huang, J. Ségalini, C. Largeot, P. L. Taberna, J. Chmiola, Y. Gogotsi, P. Simon, *Electrochimica Acta* **2009**, *54*, 7025.
- [21] C. Decaux, C. Matei Ghimbeu, M. Dahbi, M. Anouti, D. Lemordant, F. Béguin, C. Vix-Guterl, E. Raymundo-Piñero, *J. Power Sources* **2014**, *263*, 130.
- [22] R. Dash, J. Chmiola, G. Yushin, Y. Gogotsi, G. Laudisio, J. Singer, J. Fischer, S. Kucheyev, *Carbon* **2006**, *44*, 2489.
- [23] M. D. Ward, D. A. Buttry, *Science* **1990**, *249*, 1000.
- [24] D. A. Buttry, M. D. Ward, *Chem. Rev.* **1992**, *92*, 1355.
- [25] C. Steinem, A. Janshoff, Eds. , *Piezoelectric Sensors*, Springer Berlin Heidelberg, **2007**.
- [26] A. A. Vives, Ed. , *Piezoelectric Transducers and Applications*, Springer Berlin Heidelberg, Berlin, Heidelberg, **2008**.
- [27] G. Sauerbrey, *Z. Für Phys.* **1959**, *155*, 206.
- [28] M. D. Ward, E. J. Delawski, *Anal. Chem.* **1991**, *63*, 886.
- [29] M. Rodahl, B. Kasemo, *Sens. Actuators B Chem.* **1996**, *37*, 111.
- [30] F. Josse, Y. Lee, S. J. Martin, R. W. Cernosek, *Anal. Chem.* **1998**, *70*, 237.
- [31] K. K. Kanazawa, J. G. Gordon, *Anal. Chem.* **1985**, *57*, 1770.
- [32] S. J. Martin, V. E. Granstaff, G. C. Frye, *Anal. Chem.* **1991**, *63*, 2272.
- [33] "RQCM - Quartz Crystal Microbalance Research System - INFICON," can be found under http://products.inficon.com/en-us/Product/Detail/CopyOf_P-RQCM?path=Products%2FResearch-QCM, **n.d.**
- [34] M. Urbakh, L. Daikhin, *Langmuir* **1994**, *10*, 2836.
- [35] C. K. O'sullivan, G. G. Guilbault, *Biosens. Bioelectron.* **1999**, *14*, 663.
- [36] J. Segalini, E. Iwama, P.-L. Taberna, Y. Gogotsi, P. Simon, *Electrochem. Commun.* **2012**, *15*, 63.
- [37] A. Noda, K. Hayamizu, M. Watanabe, *J. Phys. Chem. B* **2001**, *105*, 4603.
- [38] C. Merlet, C. Péan, B. Rotenberg, P. A. Madden, B. Daffos, P.-L. Taberna, P. Simon, M. Salanne, *Nat. Commun.* **2013**, *4*, DOI 10.1038/ncomms3701.
- [39] W.-Y. Tsai, P.-L. Taberna, P. Simon, *J. Am. Chem. Soc.* **2014**, *136*, 8722.

***Chapter V:
Further understanding of the EDL
structure by combining in-situ EQCM
with in-situ NMR Spectroscopy***

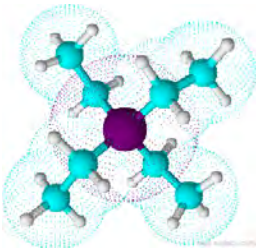
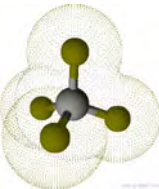
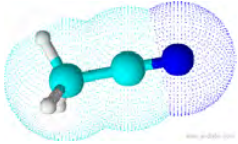
1. Introduction

As EQCM cannot track the individual contribution of each electrolytic species, another in-situ technique that may offer more *quantitative* information of *selected species* is needed for completing the charge storage puzzle. In-situ nuclear magnetic resonance (NMR) spectroscopy is a powerful technique for studying electrochemical mechanisms^[1-4]. As the observed resonance frequencies are sensitive to the local chemical environment, it is possible to distinguish adsorbed and non-adsorbed species within activated carbons^[5-7], further allowing the amount of adsorbed (in-pore) species being quantified. This approach is also element selective, allowing the separate observation of different chemical species in electrochemical system. Therefore, we collaborated with Professor Clare Grey's group (in Cambridge University, England) whose team has been developing in-situ NMR technique to study charge storage mechanisms and the ion dynamics inside the nanopores for supercapacitor application since 2011^[8-10].

In this work, YP-50F activated carbon electrodes in acetonitrile solvated tetraethylphosphonium tetrafluoroborate (PEt_4BF_4) were studied by in-situ EQCM and in-situ NMR. By choosing this salt, the PEt_4^+ cation and BF_4^- anion were tracked in real time *individually* by using in-situ ^{31}P and ^{19}F NMR during charging and discharging of supercapacitor. The electrode mass change during electrochemical measurements was monitored by EQCM to provide further information on solvation. The combination of these two in-situ techniques is expected to provide important insight on the electric double layer structure change during operation of supercapacitors.

Table V-1 summarizes the structures of PEt_4^+ cation and BF_4^- anion and their neat and solvated ion sizes in bulk solution. The solvated BF_4^- anion diameter of 1.16 nm (mentioned in the literature^[11]) is based on the value determined using the Cerius 3.8 program. This assumes a single solvation shell comprising 9 acetonitrile molecules. For the PEt_4^+ cation, no literature data for the solvated ion diameter is available. However, a recent publication by Matsumoto *et al.* provides crystallographic data for PEt_4BF_4 salt, giving a desolvated cation diameter of 0.72 nm^[12]. Assuming the thickness of the solvation shell to be the same as that for the tetraethylammonium (NEt_4^+) cation (calculated in Ref 7 to be 0.32 nm for a solvation shell comprising 7 acetonitrile molecules), the solvated PEt_4^+ cation diameter is thus estimated to be 1.35 nm.

Table V-1: Structure of the electrolytic species, neat and solvated size of the PEt_4^+ cation and BF_4^- anion, and the acetonitrile solvation number in bulk electrolyte

Ions	Structure	Size max/min length (nm)	Solvated ion size in AN (nm) in bulk solution	AN solvation number in bulk slution
PEt_4^+		---/0.72 ^[12]	1.35*	7*
BF_4^-		0.51/0.50 ^[13]	1.16 ^[11]	9 ^[11]
AN		0.58/0.40 ^[13]	---	---

* Estimated from NEt_4^+ cation

2. In-situ nuclear magnetic resonance (NMR) spectroscopy

Nuclear magnetic resonance (NMR) is a physical phenomenon in which atomic nuclei in a magnetic field adsorb and re-emit electromagnetic radiation. This adsorbed energy (and its corresponding resonance frequency) is specific to each nucleus, and also sensitive to the interaction between two nuclei, which arises from either the bonds between them or their special interaction, thus making NMR spectroscopy a powerful technique for studying the electrochemical mechanisms.

2.1 Brief NMR principle

As NMR is not the main topic of this thesis, the NMR principle and NMR spectroscopy will only be described briefly. The fundamental details of this technique were described in reference [14-16].

All the subatomic particles (e.g. electrons, protons, and neutrons) possess the intrinsic quantum property of spin. Just as electrons, the spin of nucleons (protons and neutrons) can pair up when the orbitals are being filled and cancel out. Each nucleus has its characteristic nuclear spin, and only non-zero nuclear spin generates non-zero magnetic moment. Since NMR spectroscopy is based on the interaction between the magnetic moment of atomic nuclei and an external magnetic field, only the nuclei whose spin is nonzero will produce an NMR signal.

Take a nucleus which has a spin of $1/2$ as an example, it has two possible spin states: $+1/2$ or $-1/2$ (also referred to as spin-up and spin-down). These states have the same energy

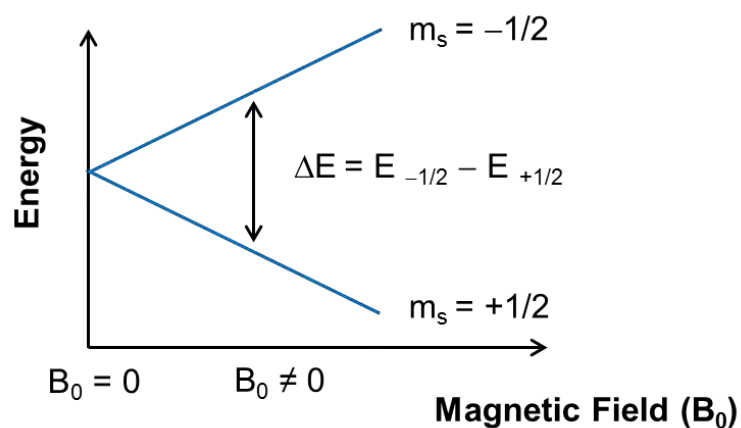


Figure V-1: Splitting of nuclei spin states under an external magnetic field (B_0)

(degenerate) when no external magnetic field is applied. However, if the nucleus is placed in a magnetic field (B_0), the energy of these states differs due to the interaction between the nuclear magnetic moment and the external magnetic field (as shown in Figure V-1).

The energy difference (ΔE) between the two states is described by the following equation:

$$\Delta E = \gamma \hbar B_0 \quad (\text{Equation V-1})$$

Where γ is the gyromagnetic ratio of the nucleus, and \hbar is the reduced Planck constant ($\hbar = h/2\pi$, where h is Planck constant = $6.63 \cdot 10^{-34}$ J.s). It is possible to excite nuclei from the lower to the higher energy level by electromagnetic radiation; in NMR it is often achieved by applying another magnetic field (B_1) which is perpendicular to B_0 . When energy of this electromagnetic radiation matches the energy difference between the two energy states, resonant absorption by nuclear spins will occur, and the nuclei is excited to the higher energy level. It is this energy absorption which is detected in NMR. The energy of the electromagnetic radiation is described as:

$$E = h \nu \quad (\text{Equation V-2})$$

where ν is the frequency. By combining Equation V-1 and V-2, it can then be deduced that the excitement will only occur at a specific frequency where:

$$\omega = \gamma B_0 \quad (\text{Equation V-3})$$

where ω is the angular frequency of the electromagnetic radiation. In NMR, this characteristic frequency is called *Larmor frequency*. When the electromagnetic radiation is given at Larmor frequency, the nuclei that are initially at lower energy level (e.g. spin-up in Figure V-1) will be excited to the higher energy level (e.g. spin-down in Figure V-1), resulting in the so-called *Larmor precession*. The NMR signal intensity is dependent on the energy absorbed, if the energy is low, the NMR signal will be too weak to be detected. Therefore, it is necessary to increase the magnetic field (B_0), which is generally in the range of few Tesla. The resonance frequency where the radiation energy is adsorbed is in the range of radiofrequency (MHz). If an NMR spectrometer is tuned to a particular resonance frequency, only a selected NMR active species is observed. For instance, if a spectrometer is tuned at 400 MHz, only ^1H nuclei are observed, but if the same spectrometer is tuned at 162 MHz, only ^{31}P are observed. This is

similar to tuning a radio and receiving only one station at a time. This element-selective nature is the key of NMR technique, and is different from the nature of EQCM, which measures the net mass change of the system contributed from all the species. However, it is this difference in nature that makes these two in-situ techniques complementary to each other.

As the nucleus is surrounded by electrons, which are also charged species and rotate with a spin to produce a magnetic field opposite to the magnetic field produced by the nucleus, thus generate a “shielding effect”. As a result, the local magnetic field at the nucleus is not equal to the applied magnetic field. The energy gap and the frequency required to achieve resonance adsorption is also reduced. This shift in the NMR frequency due to the electronic molecular orbital coupling to the external magnetic field is called *chemical shift*. It is this chemical shift which depends on the local electronic structure hence chemical bonds that makes NMR a powerful technique to probe the chemical environment of molecules.

In NMR spectra, the NMR signal is often denoted by a chemical shift value (δ):

$$\delta = \frac{(\nu - \nu_0) \times 10^6}{\nu_0} \quad (\text{Equation V-4})$$

where ν_0 and ν are the resonance frequency of reference and interest sample, respectively. As the $(\nu - \nu_0)$ is usually in Hz and ν_0 is in MHz, for convenience, the value is multiplied by 10^6 and the unit of chemical shift is given in ppm (part per million).

2.2 In-situ NMR experimental

Owing to the quantitative and element-selective nature of NMR, the use of this technique for investigating the complex supercapacitor charging process is thought to bring significant insight. It has been demonstrated early by Harris et al that NMR is capable to distinguish between adsorbed and non-adsorbed species within activated carbons [5,17,18]. Other studies have further shown a general trend that regardless of the molecule or nuclear spin studied, the resonances corresponding to the species adsorbed on the carbon surface always shift toward a lower frequency with respect to their non-adsorbed counterparts [6,7,19,20]. Theoretical studies have shown that this characteristic shifts in frequency is originated from the circulation of delocalized electrons in the carbon surface (aromatic ring current effect), which leads to local magnetic field reduction [10,21-23]. This nucleus-independent chemical shift (NICS) thus becomes a measure to identify ions confined in the carbon micropores, and to provide information on ions' local chemical environment (e.g. local curvature of the carbon surface or pore size). Recent study has demonstrated that magic-angle spinning (MAS) technique, in which the NMR samples are spun at the magic angle ($\Theta \sim 54.74^\circ$) with respect to the magnetic field [24], can greatly improve the spectral resolution in ex-situ NMR measurements [25].

In this work, solvated PEt_4BF_4 electrolytes were studied with in-situ NMR, so that the PEt_4^+ cation and BF_4^- anion can be tracked in real time *individually* by using in-situ ^{31}P and ^{19}F NMR during charging and discharge of YP-50F activated carbon electrodes. This section will describe the experimental details of in-situ NMR measurements.

2.2.1 NMR details

In-situ NMR experiments were performed using a Bruker Avance spectrometer operating at a magnetic field strength of 7.05 T, corresponding to ^{19}F and ^{31}P Larmor frequencies of 284.2 and 121.5 MHz, respectively. A Bruker HX double-resonance static probe was used, with a 6.8 mm inner diameter solenoid coil. The “depth” pulse sequence [26] was used for all experiments in order to reduce the background and probe ringing signals. The total delay between excitation of transverse magnetization and acquisition of the free induction decay was 90 μs . A recycle interval of 30 s was used, which was sufficient for spectra to be quantitative. ^{19}F NMR spectra are referenced relative to neat hexafluorobenzene (C_6F_6) at -164.9 ppm, and ^{31}P NMR spectra are referenced relative to 85 wt% $\text{H}_3\text{PO}_{4(\text{aq})}$ at 0 ppm.

2.2.2 Quantification of the adsorbed species at zero applied potential

To be able to quantify the adsorbed species, some calibration tests have been conducted. A series of calibration bag cells were prepared, each containing one 7.4 mg YP-50F film electrode soaked with accurately measured volumes of electrolyte between 2 and 12 μL , and the corresponding ^{31}P and ^{19}F NMR spectra collected from these bag cell samples are shown in Figure V-2. 1.5 M electrolyte concentration was used in the calibration tests due to better resolution.

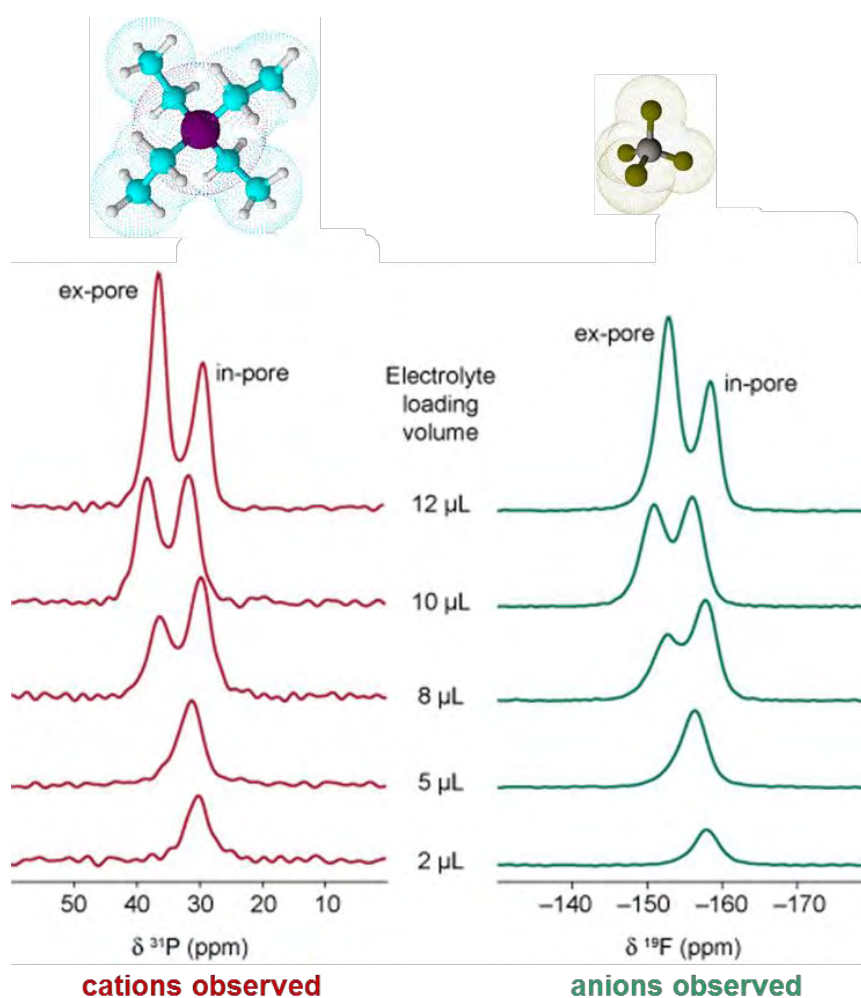


Figure V-2: ^{31}P and ^{19}F NMR spectra of bag cells containing 7.4 mg YP50-F films soaked with different volumes of 1.5 M $\text{PEt}_4\text{BF}_4 / \text{CD}_3\text{CN}$ electrolyte

For low electrolyte loading (2 μL of electrolyte), one single broad peak was observed in both ^{31}P and ^{19}F NMR spectra at 30 and -158 ppm, which is ascribed to strongly bound PEt_4^+

cations and BF_4^- anions (adsorbed in the carbon pores, indicated as “in-pore” in Figure V-2), respectively. As more electrolyte is added, a second peak appears at higher frequency in both spectra, which corresponds to the ions that are weakly affected by the carbon surface (mainly situated at exterior surface of the carbon particles, indicated as “ex-pore” in Figure V-2). These NMR spectra were then fitted with two resonances (corresponding to in-pore and ex-pore environments), and linear fits were performed for the total intensity as a function of electrolyte volume. Since the electrolyte concentrations and total sample volumes are known, it is then possible to quantify the absolute number of ions for a given resonance intensity in the NMR spectrum.

2.2.3 In-situ NMR cell set-up

In-situ NMR Cell Configuration

Two YP-50F electrode films (7.4 ± 0.1 mg each) were prepared as mentioned in Chapter II and laminated on carbon-coated aluminum mesh and a Celgard 2500 (monolayer polypropylene, 25 μm thickness) separator was placed between carbon electrodes. Differently from conventional supercapacitor cell design with two electrodes overlapping each other, an “overlaid” cell design (developed by Wang et al.^[8]) was used where the two electrodes are shifted laterally with respect to each other, as illustrated in Figure V-3. These components were placed inside a plastic bag (3M packaging film), which was first sealed on three sides. The cell was then saturated with 0.75 M PEt_4BF_4 /deuterated acetonitrile (CD_3CN) electrolyte before making the final seal to close the bag. The cell was prepared and assembled under glove box condition (H_2O and O_2 less than 0.1 ppm). The “overlaid” cell design allows *single* electrode to be placed in the NMR detection region for studying the charging process separately in each electrode, and at the same time lower the cell resistance^[8]. Cyclic voltammogram (Figure V-4) of the “overlaid” cell showed capacitive-like signature confirming good electrochemical performance of this design.

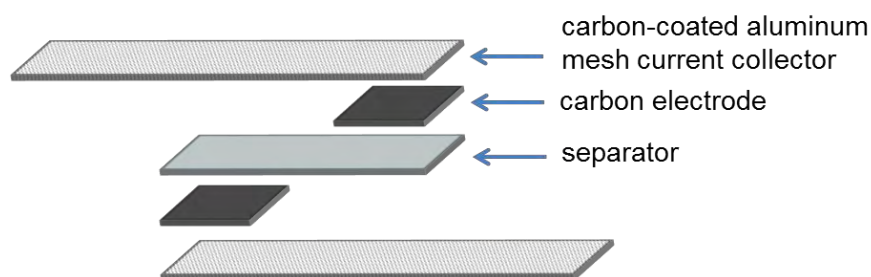


Figure V-3: The “overlaid” supercapacitor configuration used in in-situ NMR measurement (as described in reference^[8])

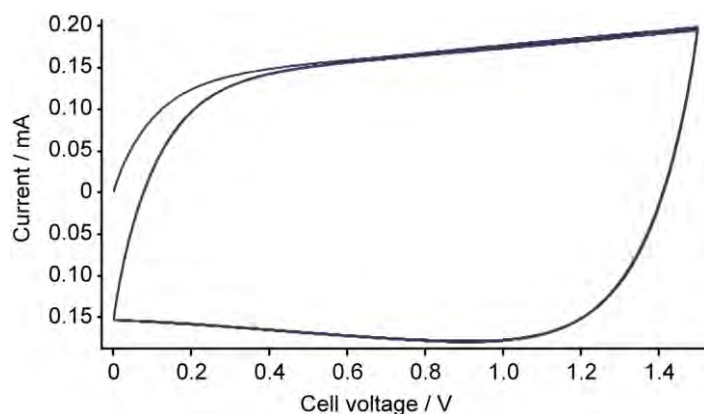


Figure V-4: Cyclic voltammogram of the supercapacitor bag cell with YP-50F electrodes

In-situ NMR measurements

The in-situ NMR cell was placed vertically in the NMR coil ^[8], and charged sequentially to a series of different voltage steps. The cell voltage was controlled by a Bio-logic cycler, and hold as the following sequence: 0, 0.25, 0.5, 0.75, 1, 1.25, 1.5, 0, -0.25, -0.5, -0.75, -1, -1.25 and -1.5 V. Each voltage step was hold for 60 minutes until a steady current was obtained before ¹⁹F and ³¹P NMR spectra were collected. For low voltages the residual current was close to zero at equilibrium; whereas for voltages between 1 – 1.5 V, small constant currents of up to 0.005 mA were observed at equilibrium. For the discharge of the cell (1.5 → 0 V), current relaxations of double duration were used. Spectral fitting was carried out using DMfit software ^[27].

Deconvolutions were carried out using a mixture of Gaussian and Lorentzian lineshapes to describe the different features in the spectra. In each case only the minimum number of components required to model the spectrum were used and a single lineshape was assumed for the in-pore resonance. Some spectra required several lineshapes to describe the free electrolyte / ex-pore resonance. This is ascribed to bulk magnetic susceptibility (BMS) effects and local variations in the magnetic field across the bag cell, which results in a range of different local fields and thus shifts for the same chemical species ^[27]. The spectrum obtained at 0 V was fitted first, as this showed the best resolution of the in-pore resonance. The peak positions and intensities obtained were then used as a starting point to fit the spectrum at the next highest voltage. Fits were repeated up to four times for each series of data in order to estimate errors.

3. In-situ NMR results

3.1 At zero potential

As mentioned previously, with improved in-situ NMR and imaging methods^[9,28], it is possible to observe change in the local environment of the ions in the electric double layer. Figure V-5a and b show respectively ^{31}P and ^{19}F NMR spectrum of individual supercapacitor electrode in the cell when the cell potential was held at 0 V. As observed in Figure V-3, two peaks correspond respectively to strongly and weakly bound ions are observed in both spectra.

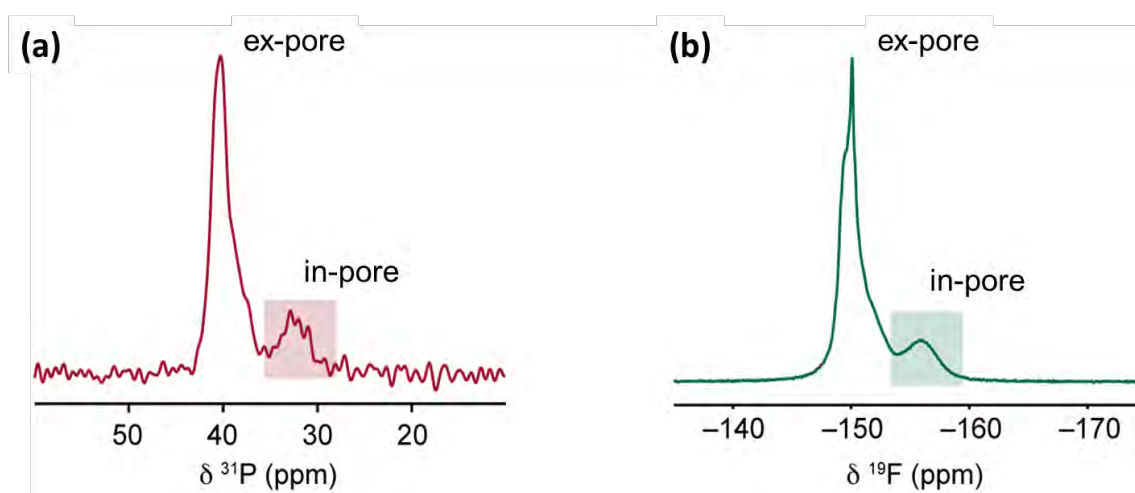


Figure V-5: ^{31}P (a) and ^{19}F (b) NMR spectra of supercapacitor electrodes showing PEt_4^+ cation and BF_4^- anion environments, respectively.

In both spectra, intense “ex-pore” resonances (^{31}P at 40 ppm and ^{19}F at -150 ppm) corresponding the ions resides in voids between carbon particles and bulk electrolytes between two electrodes were observed. For both spectra, the free electrolyte signal appears to contain several superimposed features. It is attributed to bulk magnetic susceptibility (BMS) effects owing to the irregular shape of the sample contained within plastic bag cells.^[8] Weaker “in-pore” resonances, with a lower frequency shift by 5-7 ppm, corresponding to ions inside the micropores close to the carbon surface are also observed. The shift of the in-pore resonance from that of the ex-pore resonance is due diamagnetic nucleus independent chemical shift (NICS) effects (as explained in section V-2.2) associated with the delocalized electrons in the predominantly sp^2 -bonded carbon surface.^[8,10]

Furthermore, the *absolute* number of in-pore species could be obtained through comparison of the in-pore resonance intensities with calibration samples. It has been found that there are almost identical amounts of cations (0.87 mmol per gram of YP-50F) and anions (0.85 mmol/g) confirming that in-pore ionic charges are balanced at 0 V. Moreover, using estimated solvated ion size (Table V-1) and measured ion uptakes, the volume occupied by the solvated ions was found to be 1.12 cm³ per gram of YP-50F. The value is much larger than the measured total pore volume (0.7 cm³/g), indicating that the ions must be partially desolvated or sharing their solvation shells.

3.2 Under polarization

The supercapacitors were charged positively from cell voltage of 0 to 1.5 V in steps of 0.25 V, and then discharged to 0 V before further being charged negatively to -1.5 V with steps of -0.25 V. Each step was hold for 60 minutes until a negligible constant current was obtained. In-situ NMR spectra recorded at different charge states were shown in Figure V-6. For both positive and negative polarization, both in-pore cation and anion resonances move to higher frequency in NMR spectra as the cells were charged, which is due to changes in the NICS that result from the electronic charge that is developed within the carbon electrode.^[8,9] The changes in the in-pore resonance intensities reflect the change in the ion populations within the EDL inside the micropores. The in-pore anion resonance intensity increased during positive polarization; while the in-pore cation resonance intensity increased during negative cell charging. The qualitative picture offered by these results is in agreement with the traditional view of supercapacitor charging: as electronic charge accumulates on the carbon electrode, ions with opposite charge are adsorbed at the electrode/electrolyte surface in the micropores to balance the electronic charge.

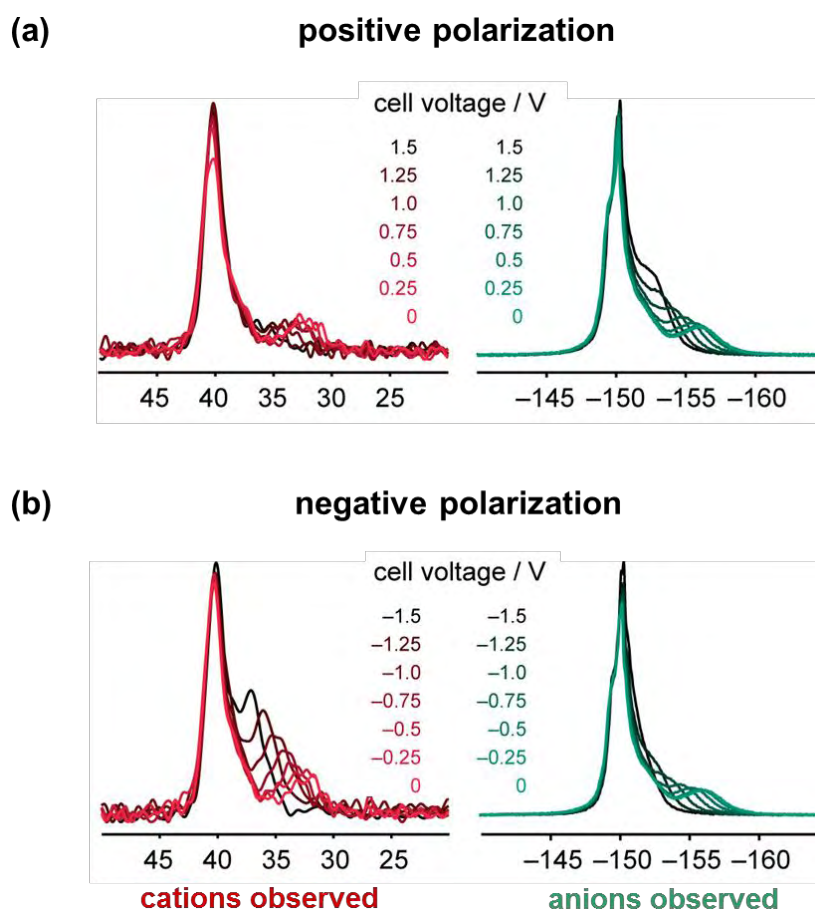


Figure V-6: In-situ ^{31}P (left, in red) and ^{19}F NMR (right, in green) spectra of supercapacitor electrodes at different charge states

3.3 Quantitative information

Figure V-7 shows the absolute in-pore ion populations, obtained from the deconvoluted in-pore resonance intensities, at different charge states. This result further gives detailed compositional information in the EDL structure during charging. For negative cell voltage range (from 0 to -1.5 V), the in-pore cation population increased with charge and the in-pore anion population showed no significant change. Interestingly, a different behavior has been found in positive cell voltage range (from 0 to $+1.5$ V). During positive charging, the in-pore anion population increased with simultaneous decrease of in-pore cation population, and the amount of cation expelled from the pores is approximately the same as anion adsorbed.

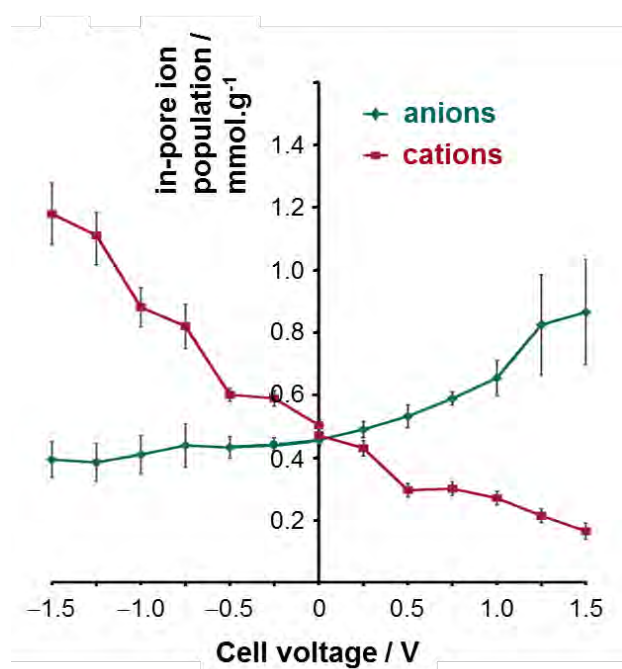


Figure V-7: In-pore ion populations for supercapacitor electrodes at different charges states in the range -1.5 to $+1.5$ V

From the ion populations, it is straight forward to determine the total ionic charge at each voltage steps and compare with the electronic charge stored on the carbon electrode (by integration of the current versus time), shown in Figure V-8. A good overall agreement has been found between ionic charge inside the micropores and the stored electronic charge, suggesting that only ions inside the micropores are responsible for charge storage, the ex-pore ions work as a reservoir for interior and did not play a significant role in the charge storage process. These results also confirm that for negative cell voltage range (from 0 to -1.5 V), cation adsorption dominates the charge storage; whereas for positive range (from 0 to $+1.5$ V), both ions are involved to balance the electronic charge, an ion-exchange was observed, which is similar to the charging mechanisms observed in EMI-TFSI based electrolyte in chapter IV.

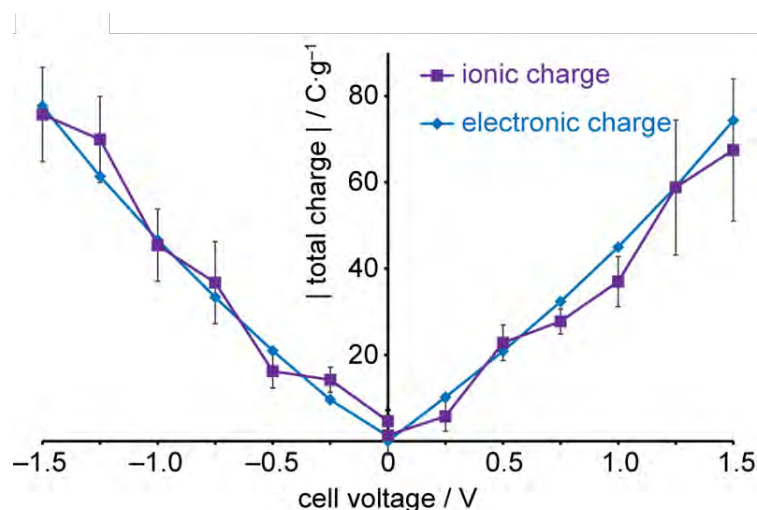


Figure V-8: Comparisons of the magnitudes of ionic and electronic charge stored on supercapacitor electrodes in the range -1.5 to 1.5 V

Although the electrochemical stability window of acetonitrile-based electrolytes can be as large as 3 V, the potential range studied here is limited at 1.5 V due to the significant overlap of in-pore and ex-pore resonance for potential >1.5 V which hampers the result analysis. Therefore, the charging scenarios may change if higher polarization can be achieved. That is to say, for example, anions can be expelled from the pore when the negative polarization is high enough (e.g. cell is charged to -3 V). In this context ion-exchange can also be involved for negative polarization.

Although in-situ ^2H NMR spectra were also collected for probing the solvent molecules (deuterated acetonitrile), the resonances corresponding to in-pore and ex-pore acetonitrile molecules are much broader (probably results from faster exchange process of these highly mobile molecules), so accurate deconvolution of in-pore resonance intensities was precluded. In this case, EQCM study of the same system holds the key for obtaining further information on the charging mechanism and clarifying the role of solvent molecules in the charging process.

4. In-situ EQCM results

In-situ EQCM measurement was used to study the same system (YP-50F activated carbon in 0.75 M $\text{PEt}_4\text{BF}_4/\text{AN}$). The EQCM cell preparation and assembly were carried out as described in chapter IV. The carbon loading on the quartz crystal was controlled in between 35 to 45 $\mu\text{g}/\text{cm}^2$, and the motional resistances of the carbon-coated quartz measured under air and in electrolyte are controlled less than 40 and less than 2300 Ω , respectively. Less than 5 Ω of variation was observed in each cycle, indicating a pure gravimetric behavior thus Sauerbrey equation (explained in section IV-2.1; equation is recalled below) applies for converting between frequency change into mass change:

$$\Delta m = -C_f \cdot \Delta f \quad (\text{Equation V-5})$$

Where Δm is the mass change, Δf is the change in resonance frequency during electrochemical tests in Hertz, and C_f is the calibration constant (13.8 $\text{ng}/\text{Hz}/\text{cm}^2$)

Potential of Zero Charge (PZC)

To fully mimic the in-situ NMR measurements, chronoamperometry measurements were carried out, and separate polarizations were applied to study individual ion contribution. Prior to the EQCM experiments, potential of zero charge (PZC) measurements were conducted using three-electrode Swagelok cell: a YP-50F electrode film with a carbon loading of 7.5 mg/cm^2 as working electrode, silver wire as pseudo-reference electrode (same as in EQCM set-up), and a heavy loading YP-50F electrode film (21 mg/cm^2) as counter electrode. The cyclic voltammogram (at 5 mV/s) of the full window scan in 0.75 M $\text{PEt}_4\text{BF}_4/\text{AN}$ is shown in Figure V-9a. A minimum capacitance is found at around 0.5 V vs reference, highlighted by red frame. Figure V-9b shows an enlarged view of the highlighted part in Figure V-9a, and second order polynomial fitting curves (black line) is also shown. The PZCs (defined at $dC/dE = 0$ which means the minimum of the curves) is at ~ 0.49 V vs reference, close to the measured open-circuit voltage (0.43 V vs reference) in EQCM set-up. Since the reference used in the system is a quasi-reference electrode (Ag wire) without buffer solution, the small difference of 60 mV between PZC and OCV is reasonable and can be ignored. Therefore, OCV was used as reference point to separate positive and negative polarization in this section.

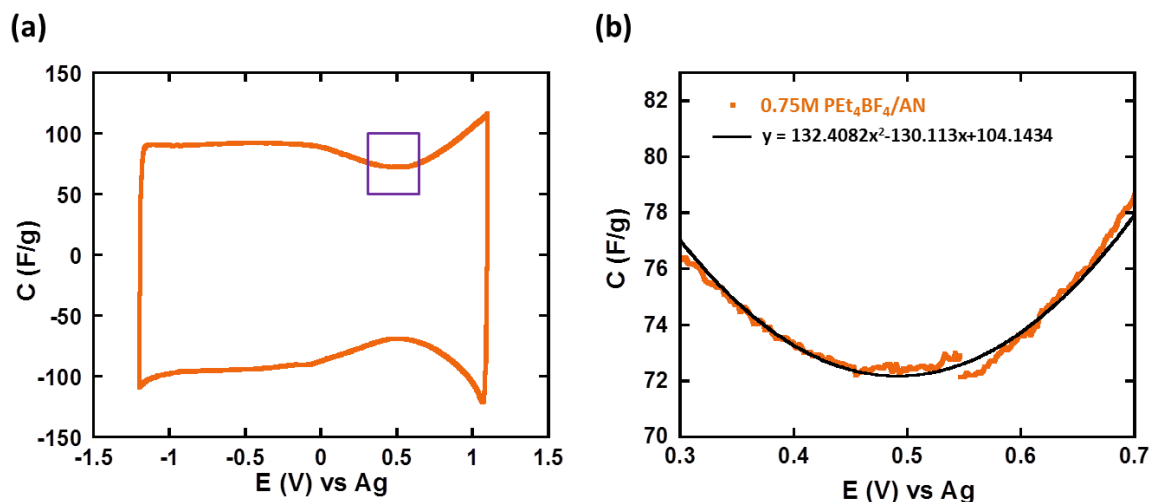


Figure V-9: (a) CVs of YP-50F in 0.75 M $\text{PEt}_4\text{BF}_4/\text{AN}$ at 5 mV/s (3-electrode Swagelok cell); (b) shows the zoomed zone highlighted in (a).

4.1 Primary in-situ EQCM information

The carbon-coated quartz electrode was first positively polarized from the open-circuit voltage (OCV, 0.43 V vs reference) up to 0.8 V vs reference in steps of 0.1 V and reversed back to OCV in steps of -0.1 V during several cycles. The electrode was then polarized negatively from OCV down to -0.1 V vs reference in steps of 0.1 V. The electrode was held at each voltage step for 120 s until a constant residual current was obtained. The quartz resonance frequency was recorded simultaneously with the electrochemical measurement. The potential step profile, the corresponding current response and the in-situ mass variation with time (calculated using the Sauerbrey equation) during positive and negative *charging* are shown in Figure V-10.

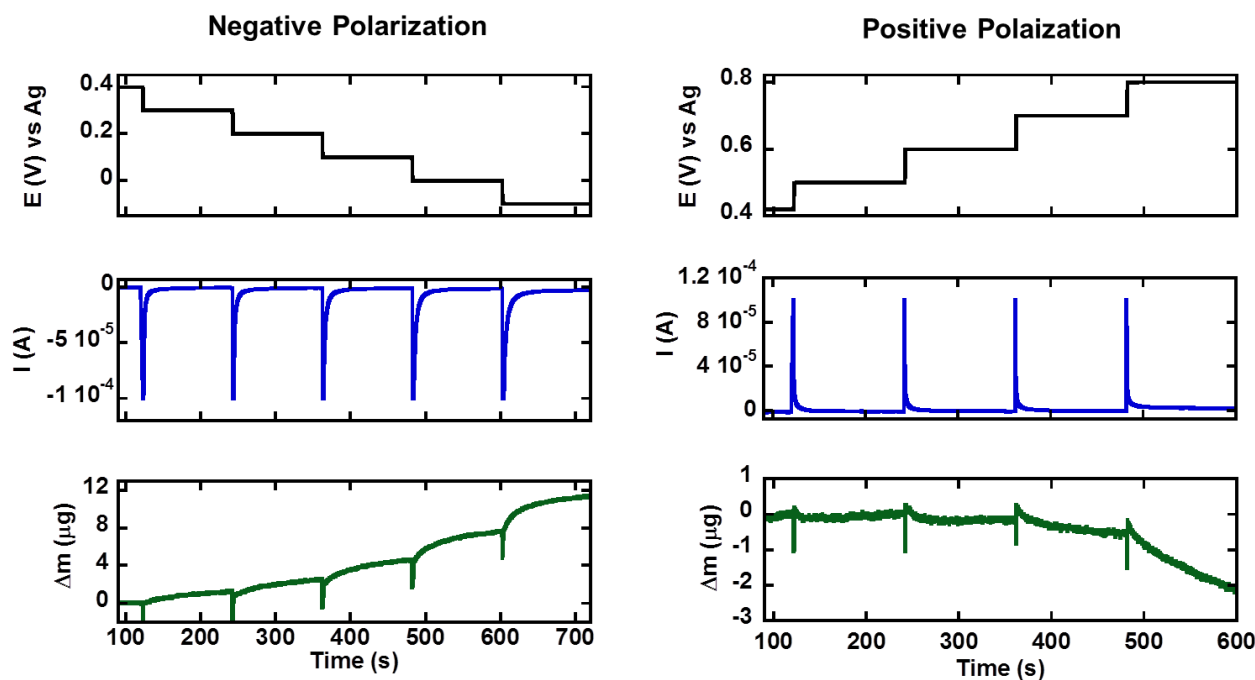


Figure V-10: Chronoamperometry in-situ EQCM test on the YP50F-coated quartz crystal in 0.75 M $\text{PET}_4\text{BF}_4/\text{AN}$ for positive (right) and negative charging (left): the potential step profile (upper part), the corresponding current response (middle) and the in situ mass variation with time

Measured mass changes (normalized by the electrochemically active area of the quartz resonator, 1.27 cm^2) are plotted versus the electrode potential in Figure V-11. At potentials lower than OCV, the mass of the electrode is observed to increase. This behavior is qualitatively consistent with the adsorption-driven charging mechanism inferred from the NMR data – cations are adsorbed while anions are kept constant in the micropores results in an increase in the total number of ions and hence mass of the electrode. For potentials higher than OCV, the electrode mass is found to decrease over the potential range studied. This behavior is consistent with the exchange-driven charging mechanism observed from the NMR data. The adsorption of anions and simultaneous expulsion of cations from the electrode can result in an overall decrease in the total ionic mass since the PET_4^+ cations (molar mass 147 g/mol) have a significantly larger mass than the BF_4^- anions (molar mass 86.8 g/mol).

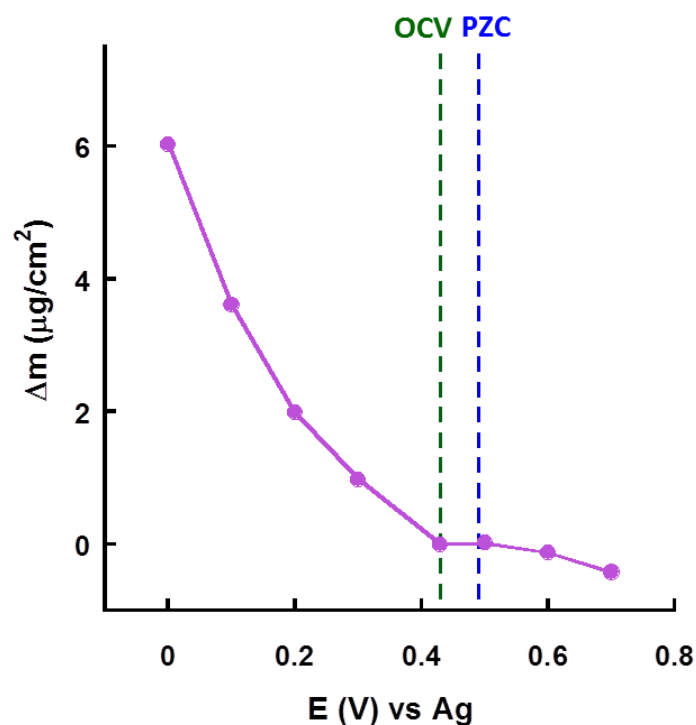


Figure V-11: In-situ electrode mass change (Δm) plotted as a function of potential during polarization of YP50-F in $\text{PEt}_4\text{-BF}_4/\text{AN}$ electrolyte

Further compositional information could be extracted from EQCM results. However, it should be noted that these analyses are based on the calculated capacitive charge which further leads to theoretical mass and the average molecular weight; thus it is essential to verify that the calculated charge only originates from capacitive processes. Figure V-12 presents the current measured at the end of the potential steps shown in Figure V-10 versus the electrode potential during the potential hold. For a constant applied potential, the current passing across an ideal capacitor is null once the equilibrium state is reached; in this case, the presence of electrolyte explains the small – but not null - steady state current ($< 1 \mu\text{A}$) between 0 and +0.7 V vs reference. However, for large polarizations of -0.1 V and $+0.8 \text{ V}$ vs reference (circled in red), the increase of residual current is related to parasitic redox reactions associated with the redox activity of the electrolyte. The potential range where the charge storage can be considered as fully capacitive can thus be defined between 0 and +0.7 V vs reference, again, the restriction of electrochemical window comes from the small carbon loading on the resonator (tens of micrograms) as mentioned in previously.

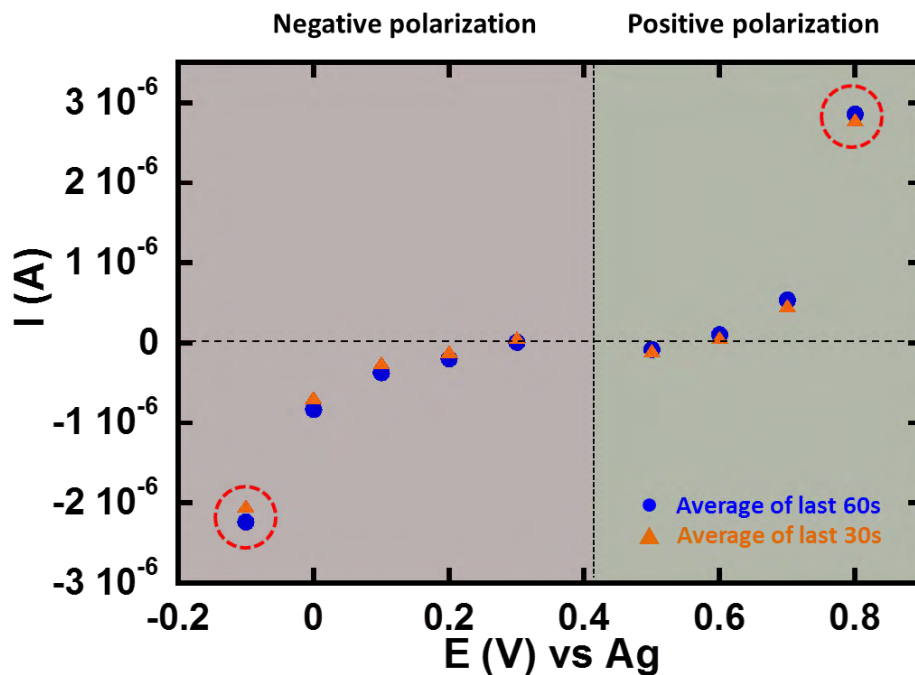


Figure V-12: The average of residual current during the last 60 seconds or 30 seconds of each polarization step versus potential

As mentioned in chapter II, the capacitive charge (Q_c) stored on the electrode in each potential step was obtained by removing the contribution of residual leakage current (I_{leak}) from the total charge (Q_{total} , calculated from integration the current (I) versus step duration time (t) during the potential hold using Faraday's Law), shown as following.

$$Q_c = Q_{total} - Q_{leak} = I \cdot t - I_{leak} \cdot t \quad (\text{Equation V-6})$$

4.2 Quantitative/Qualitative interpretation

A more quantitative interpretation of the EQCM results was obtained by comparing the experimental mass changes to theoretical values based on different models for the charging mechanism. Figure V-13 shows experimental and theoretical mass changes as a function of the capacitive charge stored on the electrode. The theoretical mass changes were calculated based on two different charging mechanisms. For the first model (denoted by red triangles), a purely adsorptive mechanism is considered, based on the traditional assumption that that one negative (positive) charge stored in the electrode is balanced by one single cation (anion) adsorption on

the electrode surface. For negative polarization, the measured mass changes are much higher than the theoretical mass change across the entire potential range. However, it should be noticed that in contrast to the NMR measurements, which selectively observe in-pore cation and anion populations, mass changes measured by EQCM originate from all electrolyte species (including solvent molecules) that enter and leave the porous electrode. The NMR data (Figure V-7) shows that the anion population remains constant during negative polarization; therefore the additional adsorbed species must be solvent molecules. The apparent molecular weight was calculated to be 369 g/mol (by applying Equation IV-9 as discussed in Section IV-2.4), much higher than unsolvated PEt_4^+ cations (147 g/mol). Assuming that the adsorbed species are PEt_4^+ cations and that the extra mass comes from acetonitrile molecules, the cation solvation number is estimated to be 5.4. This value is slightly lower than the solvation number of 7 predicted for chemically similar NEt_4^+ cations in bulk solution^[11], indicating that cations are partially desolvated when they enter the carbon micropores.

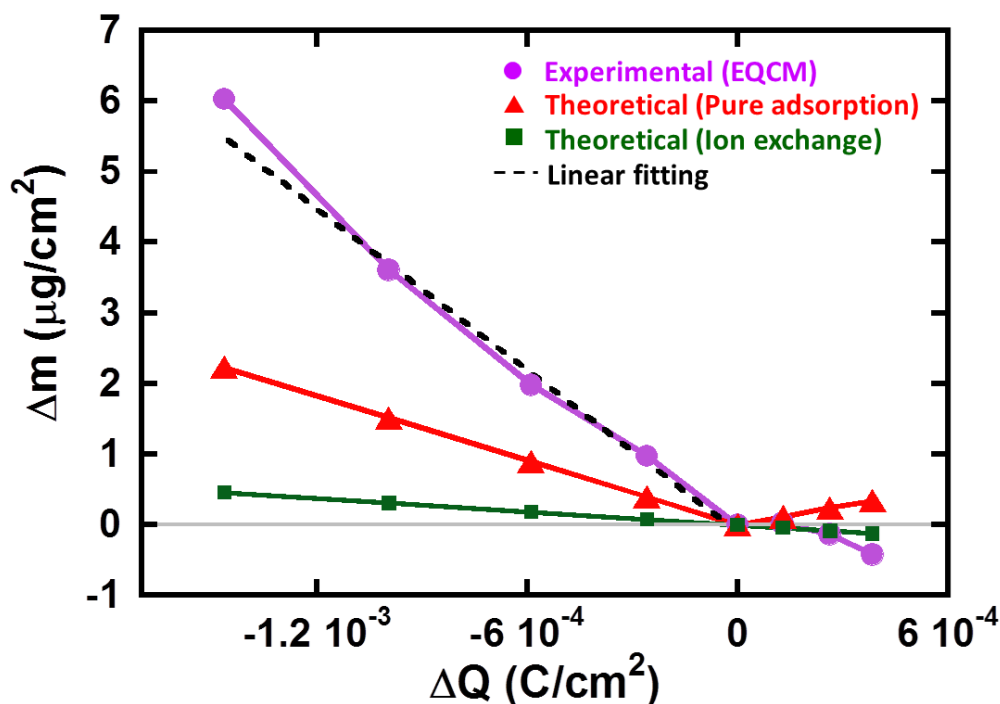


Figure V-13: Comparison of experimental and calculated electrode mass changes based on different models plotted as a function of capacitive charge during charging process.

For positive polarization, Figure V-13 shows that the purely adsorptive model again predicts a mass increase as only BF_4^- anions are absorbed into the micropores. This is not in

agreement with the experimental data, where a slight mass decrease was observed. In view of this, a second model based on the NMR results (Figure V-7) was considered, where for positive (negative) electrode polarization, two charges stored in the electrode surface are compensated by the adsorption of one anion (cation) and the concomitant desorption of one cation (anion). The calculated values based on this model (denoted by green squares) predict a slight decrease in electrode mass during positive charging. This gives better agreement with the experimental values, where a mass decrease is also observed. Although it was not possible to extract clear information regarding the solvation number because of the limited accessible voltage window at positive potentials and low deposited mass of carbon, the fact that change of the electrode mass follows that predicted by the NMR results confirms that the charging mechanism is driven by ion exchange.

5. Discussions

NMR results show that at null potential, charge in the micropores is balanced with the same amount of in-pore anions and cations, and the ions were found partially desolvated or sharing solvation shells with their neighboring ions. Thanks to the element-selective and quantitative nature of NMR, the absolute number of in-pore cation and anion population could be precisely determined. It has been found that the charge storage is predominantly achieved by the in-pore species (as the overall agreement was found between *in-pore* ionic charge and electronic charge). Ions respond differently between positive and negative electrode polarization, as previously observed in EMI-TFSI based electrolyte (chapter IV). The charge storage was mainly dominated by pure cation adsorption when the carbon electrode was polarized negatively; while for positive charging, the positive electronic charge on the carbon electrode was balanced by absorption of anions into the micropores with simultaneous expulsion of cations.

EQCM results not only show excellent agreement with NMR results, moreover, they complement each other. Furthermore, with the help of NMR which confirms that for negative polarization, anion population was kept constant and the additional cation population balances perfectly the electronic charge, cations are found to enter the pores partially desolvated with about 5 acetonitrile molecules. Cations adsorbed in the pore with additional solvent molecules implying that extra space has to be made inside the micropores as the electrode is charged. It is possible that solvent molecules are forced to order so that they take up less space. A recent study using *in-situ* X-ray diffraction has shown the ordering of propylene carbonate (PC) solvent molecules within micropores during charging.^[29] Electron radial distribution function analysis identified a shortening of the average intermolecular distance by approximately 0.05 Å as compared to bulk solution, interpreted as a densification of the packing of the PC molecules through vertical alignment. It is also possible that the micropores may expand during charging to accommodate the additional adsorbed species. Indeed, the expansion of micropores during charging has recently been proposed on the basis of electrochemical dilatometry experiments.^[30]

Although the NMR results show that significant numbers of co-ions remain inside the micropores during charging in both the positive and negative voltages ranges, the nice agreement between electronic charge and in-pore ionic charge implies that the remaining

co-ions do not screen the charge of counter-ion. These results, especially during negative polarization where co-ions population remains constant, highlight that the charge storage can simply be achieved by local re-arrangement of molecules (e.g. co-ions only move slightly further from the carbon surface thus still present in the pore).

Interestingly, BF_4^- anions show different behavior here and in previous in-situ NMR study carried out using YP-50F in $\text{NEt}_4\text{BF}_4/\text{AN}$ electrolyte^[8]. In previous study, the amount of BF_4^- anion kept constant at lower positive-polarized region, and increased abruptly when the polarization was high enough; whereas in $\text{PEt}_4\text{BF}_4/\text{AN}$ electrolyte, the in-pore BF_4^- anions increase constantly over the whole positive charge range. For negative polarization, the BF_4^- anions were ejected from the micropores constantly in $\text{NEt}_4\text{BF}_4/\text{AN}$, however the amount of BF_4^- anion was found constant all along the polarization range in $\text{PEt}_4\text{BF}_4/\text{AN}$ electrolyte. Although the chemical environment for BF_4^- anions seems to be similar in both systems, BF_4^- anions involve in the charging process in different way. This implies that the interaction between cation and anion plays a role in the way how ions respond to the electronic charge.

In this work, the in-situ NMR spectra were not collected from MAS NMR due to different technical limitations, e.g. balance of the plastic bag cell under high speed spinning, and lacking of proper material/design for connecting supercapacitor current collector to potentiostat which needs to withstand the friction and the heat produced by friction under high speed spinning. Once the technical issue will be overcome, the enhancement brought by MAS NMR could reveal deeper insight on the EDL charging process.

Combining in-situ NMR and in-situ EQCM results, one can obtain a better understanding on the role of solvent, and respond to the unanswered questions left in chapter IV. The good agreement between electronic charge and ionic charge (Figure V-8) confirms that the presence of solvent molecules does not affect charge storage efficiency under *steady state* condition.

6. Conclusions

The combination of in-situ NMR and in-situ EQCM study on YP-50F in $\text{PEt}_4\text{BF}_4/\text{acetonitrile}$ electrolyte exhibits that different charge mechanisms have been found for opposite electrode polarizations^[31]: negative charge on the electrode is balanced mainly by counter-ion adsorption (perm-selectivity); on the other hand, positive charge storage is mainly

achieved by ion-exchange (breakdown of perm-selectivity), similar as previously observed in EMI-TFSI based electrolyte. Different from precedent EQCM results of EMI-TFSI based electrolytes, ion-exchange has been found in the whole positive potential range, not only at low degree of polarization. Except the different natures of electrolyte and electrode materials, the distinction may also be attributed to kinetic factor. Under *steady state* condition (chronoamperometry), ions and solvent molecules have sufficient time to move and organize in the confined environment; whereas under *dynamic charging* condition (cyclic voltammetry in EMI-TFSI based electrolytes), the transport and adsorption kinetics can affect the EDL structure. In-situ EQCM with slower scan rate in the future could possibly give an answer regarding the kinetic factor. Furthermore, from both sets of results, it has been found that solvent molecules are involved in the charging process, but they do not affect the efficiency of charge storage, signifying the reorganization of solvent molecules in the micropores.

The results shown in this chapter provide a direct molecular-level insight into the charge storage process, the physics of the ionic adsorption and transport in microporous carbon electrodes. The methodology introduced here opens the way for the study of factors such as relative pore/ion sizes, concentration and solvent effects on the ionic composition of the electric double-layer during charging - questions that are at the heart of current efforts to optimize and improve the energy storage capabilities, which further helps to design the next generation supercapacitors.

7. Reference

- [1] K. Ogata, E. Salager, C. J. Kerr, A. E. Fraser, C. Ducati, A. J. Morris, S. Hofmann, C. P. Grey, *Nat. Commun.* **2014**, *5*, DOI 10.1038/ncomms4217.
- [2] A. Pestov, A. Nazirov, E. Modin, A. Mironenko, S. Bratskaya, *Carbohydr. Polym.* **2015**, *117*, 70.
- [3] M. Letellier, F. Chevallier, F. Béguin, E. Frackowiak, J.-N. Rouzaud, *J. Phys. Chem. Solids* **2004**, *65*, 245.
- [4] J. Xu, J. Hou, W. Zhou, G. Nie, S. Pu, S. Zhang, *Spectrochim. Acta. A. Mol. Biomol. Spectrosc.* **2006**, *63*, 723.
- [5] R. K. Harris, T. V. Thompson, P. R. Norman, C. Pottage, A. N. Trethewey, *J Chem Soc Faraday Trans* **1995**, *91*, 1795.
- [6] K. Shen, T. Pietrass, *J. Phys. Chem. B* **2004**, *108*, 9937.
- [7] R. J. Anderson, T. P. McNicholas, A. Kleinhammes, A. Wang, J. Liu, Y. Wu, *J. Am. Chem. Soc.* **2010**, *132*, 8618.
- [8] H. Wang, A. C. Forse, J. M. Griffin, N. M. Trease, L. Trogno, P.-L. Taberna, P. Simon, C. P. Grey, *J. Am. Chem. Soc.* **2013**, *135*, 18968.
- [9] H. Wang, T. K.-J. Köster, N. M. Trease, J. Ségalini, P.-L. Taberna, P. Simon, Y. Gogotsi, C. P. Grey, *J. Am. Chem. Soc.* **2011**, *133*, 19270.
- [10] A. C. Forse, J. M. Griffin, V. Presser, Y. Gogotsi, C. P. Grey, *J. Phys. Chem. C* **2014**, *118*, 7508.
- [11] Y.-J. Kim, Y. Masuzawa, S. Ozaki, M. Endo, M. S. Dresselhaus, *J. Electrochem. Soc.* **2004**, *151*, E199.
- [12] K. Matsumoto, U. Harinaga, R. Tanaka, A. Koyama, R. Hagiwara, K. Tsunashima, *Phys Chem Chem Phys* **2014**, *16*, 23616.
- [13] C. Decaux, C. Matei Ghimbeu, M. Dahbi, M. Anouti, D. Lemordant, F. Béguin, C. Vix-Guterl, E. Raymundo-Piñero, *J. Power Sources* **2014**, *263*, 130.
- [14] “Wiley: NMR Spectroscopy: Basic Principles, Concepts and Applications in Chemistry, 3rd Edition - Harald Günther,” can be found under <http://eu.wiley.com/WileyCDA/WileyTitle/productCd-3527330046.html>, **n.d.**
- [15] M. J. Duer, in *Solid-State NMR Spectrosc. Princ. Appl.* (Ed.: M.J. Duer), Blackwell Science Ltd, **2001**, pp. 1–72.
- [16] “NMR and MRI Applications in Chemistry and Medicine - National Historic Chemical Landmark - American Chemical Society,” can be found under <http://www.acs.org/content/acs/en/education/whatischemistry/landmarks/mri.html>, **n.d.**
- [17] R. K. Harris, T. V. Thompson, P. R. Norman, C. Pottage, *J Chem Soc Faraday Trans* **1996**, *92*, 2615.
- [18] R. K. Harris, T. V. Thompson, P. R. Norman, C. Pottage, *Carbon* **1999**, *37*, 1425.
- [19] L. Borchardt, M. Oschatz, S. Paasch, S. Kaskel, E. Brunner, *Phys. Chem. Chem. Phys.* **2013**, *15*, 15177.
- [20] S. Mitani, C. Murakami, Y. Korai, Y. Minato, S. Ishimoto, S. Suematsu, K. Tamamitsu, *Electrochimica Acta* **2013**, *94*, 30.
- [21] D. Sebastiani, *ChemPhysChem* **2006**, *7*, 164.
- [22] M. Kibalchenko, M. C. Payne, J. R. Yates, *ACS Nano* **2011**, *5*, 537.
- [23] P. Ren, A. Zheng, X. Pan, X. Han, X. Bao, *J. Phys. Chem. C* **2013**, *117*, 23418.
- [24] J. W. Hennel, J. Klinowski, in *New Tech. Solid-State NMR* (Ed.: J. Klinowski), Springer Berlin Heidelberg, **2005**, pp. 1–14.
- [25] M. Deschamps, E. Gilbert, P. Azais, E. Raymundo-Pinero, M. R. Ammar, P. Simon, D. Massiot, F. Béguin, *Nat. Mater.* **2013**, *12*, 351.
- [26] D. G. Cory, W. M. Ritchey, *J. Magn. Reson. 1969* **1988**, *80*, 128.
- [27] D. Massiot, F. Fayon, M. Capron, I. King, S. Le Calvé, B. Alonso, J.-O. Durand, B. Bujoli, Z. Gan, G. Hoatson, *Magn. Reson. Chem.* **2002**, *40*, 70.
- [28] A. J. Ilott, N. M. Trease, C. P. Grey, A. Jerschow, *Nat. Commun.* **2014**, *5*, DOI 10.1038/ncomms5536.
- [29] M. Fukano, T. Fujimori, J. Ségalini, E. Iwama, P.-L. Taberna, T. Iiyama, T. Ohba, H. Kanoh, Y. Gogotsi, P. Simon, K. Kaneko, *J. Phys. Chem. C* **2013**, *117*, 5752.

- [30] M. M. Hantel, V. Presser, R. Kötz, Y. Gogotsi, *Electrochem. Commun.* **2011**, *13*, 1221.
[31] J. M. Griffin, A. C. Forse, W.-Y. Tsai, P.-L. Taberna, P. Simon, C. P. Grey, *Nat. Mater.* **2015**, In press

General Conclusions and Perspectives

General Conclusions

The aim of this thesis was to improve the energy and power performance of EDLCs, which has been achieved mainly from two different aspects: (1) synthesizing novel electrode materials to increase the energy density as well as improving the electrode/electrolyte interface and electrode microstructure to enhance the power performance; (2) improving fundamental understanding of the double layer charging at the electrode/electrolyte interface, in the confined pores of porous carbons, by using in-situ electrochemical techniques.

Performance Improvement via Carbon Microstructure Design

Based on the concept of adapting electrode materials to electrolyte properties, two carbons with different microstructures have been tested with an ILs mixture – (PIP₁₃FSI)_{0.5}(PYR₁₄FSI)_{0.5} – which possesses a wide stable electrochemical window over extended operating temperature range. In previous work ^[1], this ILs mixture showed outstanding power performance but poor capacitance (30 F/g) with exohedral carbon materials. Therefore, carbons with different micro-architectures have been synthesized to improve the energy performance of this electrolyte. Results are presented in chapter III: hierarchical micro/mesoporous SiC-CDC showed good capacitive behavior down to -40 °C and much better capacitance retention at subzero temperature as compared to a commercial microporous carbon. However, only little improvement in capacitance was found (55 F/g) due to the large amount of mesopores in this carbon. Another carbon material – activated graphene (a-MEGO) presented an exceptionally high capacitance (up to 180 F/g) and wide electrochemical window (up to 3.7 V) over a wide temperature range from -50 °C to 80 °C in ILs mixture. The high SSA, and uniformly situated mesopores (2 to 4 nm), compared with the mesopores of SiC-CDC whose peak ranged from 2 to 10 nm, allow a-MEGO to store the large amount of charge maintaining high ion transport thus high power capability.

EDL Fundamental Understanding via In-situ Techniques (EQCM; EQCM & NMR)

Aside from the development of novel constituent materials, obtaining a fundamental understanding of the charge storage mechanism at molecular scale also holds the key for future design of supercapacitors. Among limited in-situ electrochemical techniques, Electrochemical Quartz Crystal Microbalance (EQCM) technique has been proved to be a powerful in-situ probe

for studying the electrochemical interfacial properties in a porous carbon.^[2,3] Therefore, it has been involved to investigate the EDL charging mechanisms and ion dynamics in the confined carbon micropores in chapter IV. Carbide-derived carbons (CDC) with two different average pore sizes were tested in neat and acetonitrile (AN)-solvated ionic liquid (EMI-TFSI) using in-situ EQCM. Results have shown that different charge storage mechanisms are involved for positive and negative polarization: pure-adsorptive mechanism and ion-exchange mechanism. Despite the strong interaction between cations and anions in neat ionic liquids, at high polarization under *dynamic condition*, almost to one single counter-ion adsorption has been found in response to one net charge stored on the carbon electrode surface. No ion-pairing or charge screening by co-ions has been observed during charging in confined micropores. Experimental acetonitrile solvation numbers were estimated for EMI⁺ cation, and partial desolvation was observed when decreasing the carbon pore size from 1 down to 0.65 nm.

Owing to the nature of EQCM, it cannot distinguish the individual contribution of each electrolytic species. In order to get a more complete picture of double layer charging, in-situ NMR was coupled with in-situ EQCM to study the same electrode/electrolyte system (YP-50F in PEt₄BF₄/AN) in chapter V. Thanks to the quantitative nature of NMR, the amount of cations and anions at different charge states could be determined, and different charging mechanisms have been found for different electrode polarizations under *steady state*: negative charge on the electrode is balanced mainly by counter-ion adsorption; whereas positive charge storage is mainly achieved by ion-exchange, similar as previously observed in EMI-TFSI based electrolyte. In-situ EQCM results showed excellent agreement with the NMR results, and offer important information on ion solvation inside the micropores. The PEt₄⁺ cations are found to enter the pores with ~ 5 acetonitrile molecules corresponding to a slight partial desolvation. Moreover, results have also clarified the role of acetonitrile solvent molecules in EDL charging: although they are involved in the charging process, they do not affect the charge storage efficiency.

These results bring important molecular-level insights to the charge storage process and the EDL structure upon charging, thus further provide the guideline for material design to improve the EDLC performance. To summarize, in the confined micropores, ions are at least partially desolvated and no ion-pairing has been found. Therefore, counter-ions are densely packed in the narrow space, and neither co-ions nor solvent molecules screen the charge, thus

resulting in high capacitance and high charge storage efficiency in this environment. On the other hand, depending on ion nature and cation-anion interaction, charging process can involve pure counter-ion adsorption or co-ion ejection, or both (ion-exchange). Local reorganization and reorientation of the electrolytic species is also necessary to efficiently pack the ions inside the pore. Both molecular reorganization and ion-swapping need some free space, hence materials with only the pore size that matches the maximum capacitance at equilibrium state will not show good performance under dynamical charging since the local reorganization is hindered. In view of this, mesopores might be as important as micropores. However, in this work, large mesopores, in which the pore size is more than 4 nm, are found to decrease the capacitance. Although the charge storage mechanism is still not completely understood, these conclusions highlight the importance of optimizing the electrode/electrolyte interface by the proper electrode architecture design containing appropriate amount and size of micropores and mesopores. Five papers have been published from these results.^[4-8]

Perspectives

As already raised by different studies and confirmed again in this work, optimization of the electrode/electrolyte interface holds the key for future supercapacitors. But questions now are: what is the best microstructure for improving energy density without sacrificing high power features? What is the best volume proportion between pores of different pore size? How do electrolyte properties (e.g. viscosity) affect this proportion? Of course, tremendous efforts need to be put, especially the development of synthesis strategies which can finely control the porous structure and tailor the required pore size and PSD.

From fundamental point of view, lots of work still needs to be done. How the electrolytic molecules re-arrange/re-orient? How the different molecular structures and different interactions between molecules affect this re-orientation? How does the system moves from purely-adsorptive to ion-exchange charging mechanism or vice versa? Will there be different charging pictures between charging dynamically or under steady state? Furthermore, the role of electrolyte permittivity, and the relationship between solvation energy, adsorption energy and charge storage are still poorly understood. To address these points, in addition to improving the in-situ techniques, computational simulations and modeling are definitely needed. What is even more important is that it is important to combine different techniques

for probing the same electrode/electrolyte systems. Only by incorporating the advantages of different techniques, different aspects can be covered hence a more complete scenario of the EDL charge storage can be achieved.

The current in-situ electrochemical techniques are still limited to providing *averaged* information of the whole electrode. The *local* information at the electrode/electrolyte interface at molecular scale still relies on modelling. Recently, in-situ STEM/TEM techniques has been developed for battery-related research.^[9,10] Development of this technique, which allows local observation, in studying EDL charging mechanism will undoubtedly bring important fundamental insights and improve future supercapacitor designs.

-
- [1] R. Lin, P.-L. Taberna, S. Fantini, V. Presser, C. R. Pérez, F. Malbosc, N. L. Rupesinghe, K. B. K. Teo, Y. Gogotsi, P. Simon, *J. Phys. Chem. Lett.* **2011**, *2*, 2396.
 - [2] M. D. Levi, G. Salitra, N. Levy, D. Aurbach, J. Maier, *Nat. Mater.* **2009**, *8*, 872.
 - [3] M. D. Levi, N. Levy, S. Sigalov, G. Salitra, D. Aurbach, J. Maier, *J. Am. Chem. Soc.* **2010**, *132*, 13220.
 - [4] W.-Y. Tsai, P.-C. Gao, B. Daffos, P.-L. Taberna, C. R. Perez, Y. Gogotsi, F. Favier, P. Simon, *Electrochem. Commun.* **2013**, *34*, 109.
 - [5] W.-Y. Tsai, R. Lin, S. Murali, L. Li Zhang, J. K. McDonough, R. S. Ruoff, P.-L. Taberna, Y. Gogotsi, P. Simon, *Nano Energy* **2013**, *2*, 403.
 - [6] P.-C. Gao, W.-Y. Tsai, B. Daffos, P.-L. Taberna, C. R. Pérez, Y. Gogotsi, P. Simon, F. Favier, *Nano Energy* **2014**, DOI 10.1016/j.nanoen.2014.12.017.
 - [7] W.-Y. Tsai, P.-L. Taberna, P. Simon, *J. Am. Chem. Soc.* **2014**, *136*, 8722.
 - [8] J. M. Griffin, A. C. Forse, W.-Y. Tsai, P.-L. Taberna, P. Simon, C. P. Grey, *Nat. Mater.* **2015**, In press
 - [9] “Poseidon 510 In Situ Electrochemistry TEM Holder,” can be found under <http://www.protochips.com/products/poseidon-500.html>, **n.d.**
 - [10] M. E. Holtz, Y. Yu, D. Gunceler, J. Gao, R. Sundararaman, K. A. Schwarz, T. A. Arias, H. D. Abruña, D. A. Muller, *Nano Lett.* **2014**, *14*, 1453.

Résumé de Thèse

Introduction

Un des défis majeurs auquel notre société fait face est la raréfaction d'énergies fossiles, la dégradation écologique ainsi que le changement climatique causé par la consommation de ces énergies. Par conséquent, la recherche a été axée sur le développement de solutions durables et renouvelables, pour obtenir des ressources d'énergie non-exhaustives, comme l'énergie solaire, l'énergie éolienne, l'énergie des vagues, l'énergie géothermique, l'énergie marémotrice, etc. En principe, ces méthodes impliquent la conversion de différentes formes d'énergie (par exemple chaleur, nucléaire, énergie rayonnante, etc...) en énergie électrique (systèmes de conversion d'énergie). Toutefois, l'énergie ne peut pas être produite de façon continue mais doit répondre à une certaine demande en temps utile, soulignant ainsi la nécessité de *systèmes de stockage d'énergie*.

Le diagramme de Ragone (Figure 1^[1]) est couramment utilisé pour présenter et comparer la performance des différents systèmes de stockage d'énergie.^[2] Comme l'indique le diagramme, les batteries, les condensateurs électrochimiques, et les condensateurs sont les trois principaux systèmes qui peuvent être utilisés pour stocker de l'énergie. Chaque système fournit des caractéristiques différentes en termes de puissance spécifique et d'énergie spécifique. L'énergie spécifique indique la quantité d'énergie qui peut être stockée dans le dispositif, et la puissance spécifique détermine la vitesse à laquelle l'appareil peut délivrer son énergie. Les lignes en pointillés du diagramme indiquent le temps nécessaire pour retirer toute l'énergie stockée dans le dispositif ce qui équivaut à la constante de temps des systèmes. Bien que de grands efforts ont été effectués pour développer des batteries lithium-ion et d'autres batteries secondaires, elles souffrent encore d'une faible puissance. Les systèmes de stockage d'énergie ayant de grande puissance sont nécessaires dans un certain nombre d'applications. Par conséquent, les condensateurs électrochimiques, qui sont des dispositifs de puissance et peuvent être entièrement chargés ou déchargés en quelques secondes, sont des systèmes de plus en plus développés.^[3,4]

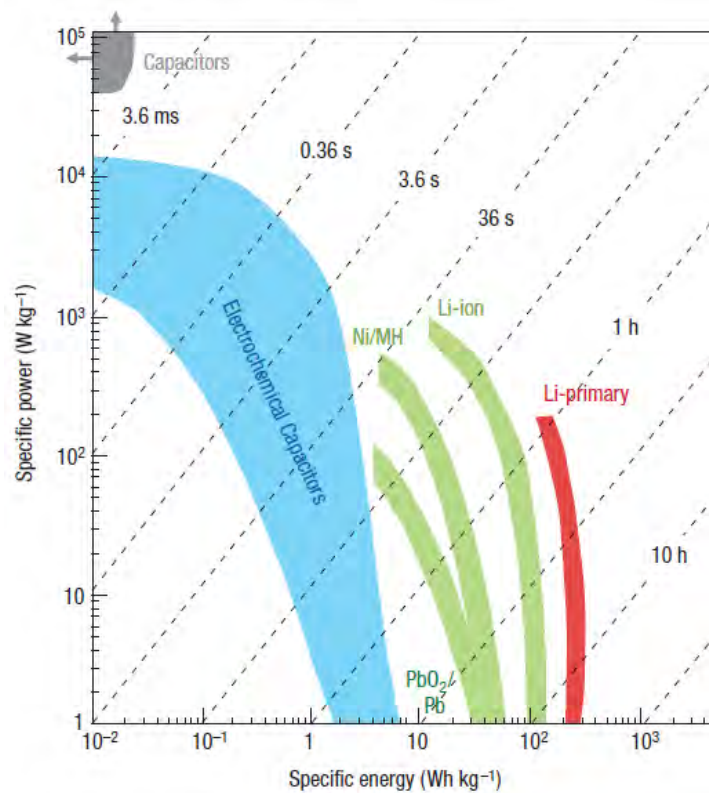


Figure 1: Diagramme de Ragone représentant la puissance spécifique en fonction de l'énergie spécifique de différents systèmes de stockage de l'énergie.^[1]

Comme le montre le diagramme de Ragone (Figure 1), les condensateurs électrochimiques, également connus sous le nom de supercondensateurs ou condensateurs électrochimiques à double couche (EDLC), ont fait le lien entre les batteries et les condensateurs classiques. Ils peuvent fournir une très haute densité de puissance (15 kW/kg) mais avec une énergie plus faible que les batteries (6 Wh/kg). Les batteries, telles que les batteries lithium-ion, ont généralement de fortes densités d'énergie (jusqu'à 200 Wh/kg), mais de faibles puissances (jusqu'à 1 kW/kg).^[1] Ces caractéristiques sont définies par la façon dont l'énergie est stockée dans ces systèmes. En raison de l'attraction électrostatique *non faradique* entre les ions de l'électrolyte et les charges à la surface de la matière active dans les supercondensateurs, le temps pour le stockage et la libération des charges stockées est beaucoup plus rapide par rapport aux batteries. En effet, dans ces dernières, les principaux mécanismes de fonctionnement sont les réactions faradiques dans le bulk des matériaux actifs. En outre, le processus de stockage de charge des EDLCs est très réversible par rapport à d'autres dispositifs de stockage d'énergie qui impliquent des réactions faradiques, ainsi les EDLCs sont en mesure de durer quelques millions

de cycles. En conséquence, les supercondensateurs sont particulièrement intéressants dans les applications où une puissance élevée est nécessaire. Ils peuvent également être considérés comme un complément aux batteries lithium-ion lors d'utilisations à haute énergie (batteries lithium-ion) et à haute puissance (supercondensateurs).

Bien que les supercondensateurs aient une puissance élevée, ils souffrent d'une densité d'énergie relativement faible par rapport aux batteries. Par conséquent, le principal défi aujourd'hui pour les supercondensateurs est d'augmenter leur densité d'énergie. L'objectif de cette thèse est donc d'améliorer leur densité d'énergie et leur puissance, qui peut être réalisé principalement par deux aspects différents: (1) la recherche de nouveaux électrolytes et matériaux d'électrodes pour augmenter la densité d'énergie et améliorer l'interface électrode/électrolyte et la microstructure d'électrode pour améliorer la densité de puissance. (2) Améliorer la compréhension fondamentale de la charge en double couche à l'interface électrode/électrolyte à l'aide d'une technique électrochimique *in situ*.

Chapitre I

Le premier chapitre de cette thèse présente l'étude bibliographique séparée en quatre parties. Dans un premier temps sont présentés le principe de fonctionnement, les applications des supercondensateurs ainsi que le concept général pour améliorer leur performance. Ce travail de thèse est axé sur les supercondensateurs utilisant des matériaux actifs à base de carbone avec une surface spécifique élevée. Plus de 95% de supercondensateurs commerciaux utilisent le charbon actif comme électrode.

La deuxième partie de la bibliographie présente différents types de carbones et d'électrolytes utilisés dans les EDLCs tout en présentant leurs avantages et inconvénients. Des carbones avec différentes microstructures, telles que les oignons de carbone (OLCs)^[5-7], les nanotubes de carbone (NTC)^[8-11], le graphène^[12-16], les carbones dérivés de carbure (CDC)^[17-21], les carbones « template »^[22-24], et les charbons actifs (AC)^[25,26] ont été étudiés comme matériaux d'électrodes pour les EDLCs. D'autre part, les électrolytes utilisés dans les EDLCs peuvent être classés en trois catégories: électrolytes aqueux, électrolytes organiques et liquides ioniques à température ambiante (RTILs). En général, la fenêtre électrochimique (V) est déterminée par la nature des électrolytes. L'augmentation de la fenêtre électrochimique est un moyen efficace pour améliorer les performances des supercondensateurs car les densités

d'énergie (E) et de puissance (P) dépendent du carré de la tension ($E = \frac{1}{2} CV^2$; $P = V^2/4R$). Ceci est la raison pour laquelle la recherche a évolué progressivement des électrolytes aqueux (~ 1 V) vers les électrolytes organiques ($\sim 2,7$ V) puis vers les liquides ioniques à température ambiante (> 3 V). Cette thèse se concentre donc principalement sur les électrolytes organiques et les liquides ioniques.

Bien que des efforts aient été faits sur la recherche de nouveaux matériaux d'électrodes et d'électrolytes, l'amélioration de la densité d'énergie a en revanche été minime en raison du manque de compréhension fondamentale sur les mécanismes de stockage de charge de la double couche électrique. La troisième partie de la bibliographie présente l'état de l'art sur la double couche électrochimique et sur la relation entre la taille des pores et la taille des ions : une découverte importante a été rapportée en 2006^[27] par notre équipe en utilisant des carbones dérivés de carbure (CDCs) avec une distribution de taille des pores finement contrôlée. Il a été constaté que la capacité augmente de façon spectaculaire lorsque la taille des pores de carbone est inférieure à la taille des ions solvatés, ce qui suggère que les ions pourraient perdre une partie de leur couche de solvation pour accéder à ces nanopores confinés (Figure 2). Suite à cette étude, de nombreux travaux ont été dédiés à la compréhension de l'origine de cette augmentation de capacité, ainsi que la physique d'adsorption et le transport des ions dans le carbone microporeux confiné.

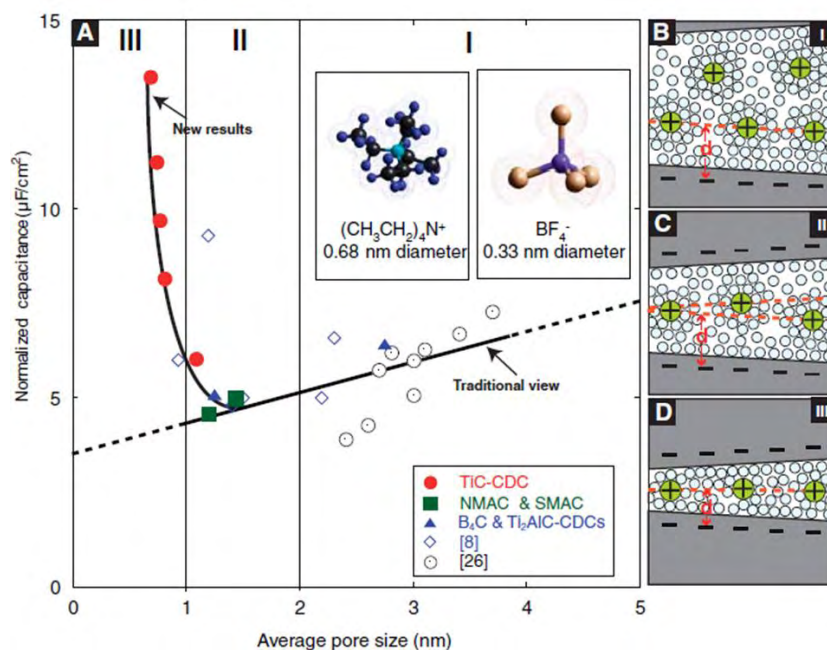


Figure 2: (A) Variation de la capacité spécifique en fonction de la taille des pores de carbone ; Illustration de l'adsorption des ions dans des pores de (B) > 2 nm, (C) 1-2 nm, et (D) < 2 nm.^[27]

De plus, il a été constaté que, dans un électrolyte sans solvant (un liquide ionique), la capacité maximale est atteinte lorsque la taille des pores est proche de la taille de l'ion.^[28] D'un point de vue du design du matériau, tous ces résultats ont souligné la nécessité d'adapter la taille des pores d'électrode à la taille des ions d'électrolyte. Cela indique que les micropores (taille des pores < 2 nm) sont importants pour l'optimisation de la capacité et donc la densité d'énergie. Cependant, d'autres rapports suggèrent également que le carbone contenant uniquement des micropores induit des limitations du transfert des ions, ce qui peut conduire à une diminution de la puissance.^[29] D'autre part, il a été proposé que la présence de mésopores, généralement de 2 à 8 nm, peut accélérer le processus cinétique du transport des ions dans les électrodes et améliorer la puissance.^[30,31] En conséquence, la conception de matériaux d'électrodes possédant de *micro-architectures hiérarchisées* avec une grande quantité de micropores et une haute surface spécifique (SSA), combinées à une courte distance effective pour le transport des ions et une voie de recherche qui se développe.^[32-36] Cependant, pour améliorer les supercondensateurs efficacement, la recherche fondamentale pour comprendre la dynamique des ions dans l'électrode, en particulier dans les micropores confinés, est nécessaire.

Pour obtenir une vision claire du mécanisme de charge, de la dynamique dans l'espace confiné et de la physique fondamentale sur l'augmentation de la capacité, il est nécessaire d'utiliser des *techniques électrochimiques in situ* pour suivre les molécules des électrolytes en temps réel. De nos jours, il nous manque encore des techniques pour étudier la relation entre le degré local de la séparation de charge et la structure locale des pores. Par conséquent, *les simulations et les modélisations* sont aussi importantes pour comprendre ce qui explique l'augmentation de stockage de charge et comment ça se passe. La quatrième partie de ce chapitre résume donc l'ensemble de nos connaissances sur la charge de double couche du point de vue de la modélisation.

Chapitre II

Le deuxième chapitre décrit les différents charbons actifs commerciaux et électrolytes testés lors de ces travaux. Également, les différentes méthodes électrochimiques (voltampérométrie cyclique, chronoampérométrie et spectroscopie d'impédance électrochimique) et configurations de cellules électrochimiques (Swagelok® et microélectrode

à cavité) utilisées pour caractériser les supercondensateurs sont présentées.

Chapitre III

Les matériaux d'électrode présentent des mauvaises performances capacitives dans les liquides ioniques à température ambiante ou à basse température^[18,28,37] en raison de la faible mobilité des ions dans l'électrolyte confiné dans le réseau microporeux. La structure des pores qui contient des micropores *et* des mésopores peut améliorer la cinétique de transport des ions dans les matériaux. Le but de ce chapitre est de construire des supercondensateurs performants qui permettent un fonctionnement sur une vaste plage de la température.

Un mélange de liquides ioniques (LIs), (PIP₁₃FSI)_{0.5}(PYR₁₄FSI)_{0.5}, qui possède une large fenêtre électrochimique stable sur une grande gamme de température est choisi dans cette étude. Dans le travail précédent^[37], ce mélange de liquides ioniques a montré une puissance exceptionnelle mais une faible capacité (30 F/g) avec des carbones exohédraux. Par conséquent, des carbones avec différentes microstructures donc différentes accessibilités des ions sont étudiés afin d'optimiser l'interface carbone/électrolyte et accroître la quantité et la qualité de stockage de charge sur une large plage de température.

III.1 SiC-CDC à porosité hiérarchique micro/mésoporeux

Une voie originale de synthèse de carbures mésoporeux ordonnés a été développée récemment par Favier et al utilisant la réaction de réduction magnésio-thermale sur des composites mésoporeux en carbure de silicium.^[38,39] Cette partie examine la performance électrochimique des carbones dérivés des carbures de silicium ordonnés micro/mésoporeux (SiC-CDC) dans le mélange eutectique de LIs. La synthèse du carbure de silicium et une partie des caractérisations des matériaux ont été menées par l'équipe du Dr. Frédéric Favier (Montpellier, France). La chloration de carbure de silicium a été mise en œuvre par l'équipe du professeur Yury Gogotsi (Drexel University, USA). Les analyses d'isotherme d'adsorption et de MET des SiC-CDCs ont montré que la structure mésoporeuse du carbure de silicium a été conservée après chloration, une fraction importante (~ 70%) des pores ayant des tailles supérieures à 2 nm. En outre, le SiC-CDC contient des micropores étroitement distribué autour de 1 nm. Le charbon actif commercial (YP-50F), qui contient principalement des micropores (92% de pores ont une taille inférieure à 2 nm) sans structure hiérarchique, est testé aux mêmes conditions électrochimiques pour la comparaison avec le SiC-CDC. Les caractéristiques

concernant la porosité des SiC-CDC et YP-50F sont résumées dans Tableau 1.

Tableau 1: Les caractéristiques des SiC-CDC et YP-50F

	SiC-CDC	YP-50F
BET SSA (m²/g)	1619	1732
Volume de pore total (cc/g)	1.59	0.75
Pourcentage de pore < 1 nm (%)	17.5	66
Pourcentage de pore entre 1–2 nm (%)	13.5	26
Pourcentage de pore > 2 nm (%)	69	8
Pic ou moyenne de la taille des pores (nm)	1 and 3-4	0.9

Résultats

Les Figure 3a et b montrent les voltammogrammes cycliques (CVs) du SiC-CDC et du YP-50F à température élevée ($20 \leq T \leq 60$ °C) avec une vitesse de balayage de 20 mV/s jusqu'à 3 V. Tous les CVs conservent des caractéristiques capacitives. La capacité spécifique (calculée à partir de la pente de la courbe de charge (Q) – tension (V) pendant la décharge à 5 mV/s à 20 °C) du SiC-CDC et du YP-50F sont de 55 et 74 F/g, respectivement. Le YP-50F présente une capacité plus élevée en raison de sa teneur élevée en micropores, qui est également responsable de la grande distorsion dans les CVs. Le SiC-CDC présente un comportement électrochimique similaire entre 20 et 60 °C à 20 mV/s. Le YP-50F montre une capacité supérieure à celle du SiC-CDC parmi toutes les températures testées.

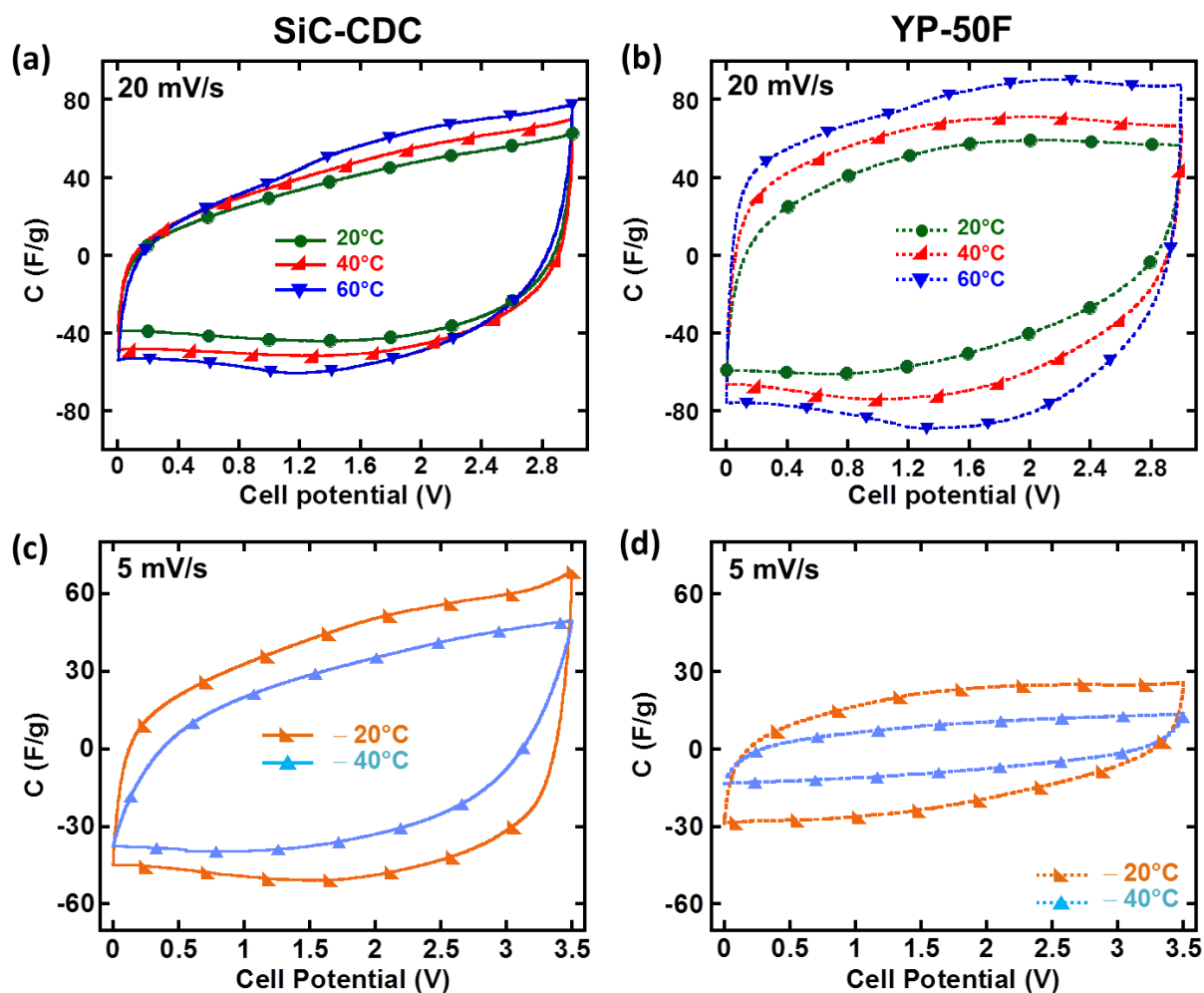


Figure 3: caractérisation électrochimique des SiC-CDC et YP-50F (a, b) à températures élevées ($20 \leq T \leq 60$ °C) – CVs à 20 mV/s et (c, d) températures inférieures à zéro (-20 et -40 °C) – CVs à 5 mV/s

La caractérisation électrochimique des SiC-CDC et YP-50F à des températures inférieures à zéro (-20 et -40 °C) sont présentés sur les Figure 3c et d. Les CVs à 5 mV/s jusqu'à 3,5 V montrent que les deux carbones se comportent différemment lorsque la température diminue. La capacité du YP-50F est réduite de façon considérable (de 25 et 11 F/g pour -20 et -40 °C, respectivement), ce qui correspondent à 34% et 15% de la capacité à la température ambiante, alors que le SiC-CDC à -40 °C garde 70% de la capacité obtenue à température ambiante. Les résultats indiquent que, à basse température, les ions ont une faible mobilité et donc moins d'accessibilité à la microporosité du carbone (YP-50F) comparé à un matériau qui présente un réseau hiérarchique (SiC-CDC).

En ce qui concerne la puissance, le SiC-CDC montre une meilleure rétention de capacité

que celle du charbon actif microporeux lorsque la vitesse de balayage augmente. Il montre également une capacité plus élevée que des carbones exohédraux même à -40 °C . Ces résultats montrent que le SiC-CDC préparé fonctionne correctement dans le mélange de LI à basse température jusqu'à -40 °C , grâce à ses mésopores ordonnés qui servent des réservoirs et des canaux de transport des ions. La capacité a été améliorée par rapport aux carbones exohédraux (de 20 à 30 F/g) grâce à la présence de micropores.

III.2 Oxyde de graphite exfolié par microonde et activé par KOH (a-MEGO)

L'oxyde de graphite exfolié par microonde et activé par KOH (a-MEGO) a été synthétisé et caractérisé par l'équipe du professeur Ruoff (Université du Texas à Austin, États-Unis).^[40,41] Le a-MEGO possède une grande surface spécifique de $1901\text{ m}^2/\text{g}$. Ce matériau contient des micropores (qui lui donnent une haute SSA comme des charbons actifs) et des mésopores (qui facilitent la mobilité des ions lors de la charge et la décharge); tous ses pores sont inférieurs à 5 nm.

Résultats

La Figure 4a montre les CVs mesurés à 100 mV/s à différentes températures. Les profils rectangulaires des CVs confirment la possibilité d'utiliser a-MEGO dans le mélange de LI. Une fenêtre électrochimique maximale de $3,7\text{ V}$ est obtenue à la température ambiante. La capacité spécifique à la température ambiante avec une vitesse de balayage de 20 mV / s est d'environ 160 F / g , ce qui représente une augmentation d'un facteur 5 par rapport aux carbones exohédraux ($\sim 30\text{ F/g}$)^[37] et d'un facteur 3 par rapport au SiC-CDC. Cette augmentation importante peut être attribuée à la surface spécifique élevée et très accessible de ce matériau. L'augmentation progressive de la capacité lors de l'augmentation de la température peut être expliquée par la meilleure conductivité ionique (mobilité ionique) de l'électrolyte à des températures élevées. En outre, la porosité ouverte du a-MEGO permet aux ions de l'électrolyte d'accéder aux pores nanométriques sans limitation de transfert des ions, ce qui peut se produire en utilisant des charbons actifs classiques (conventionnels) avec des rétrécissement de pores ainsi que des pores courbés.^[37]

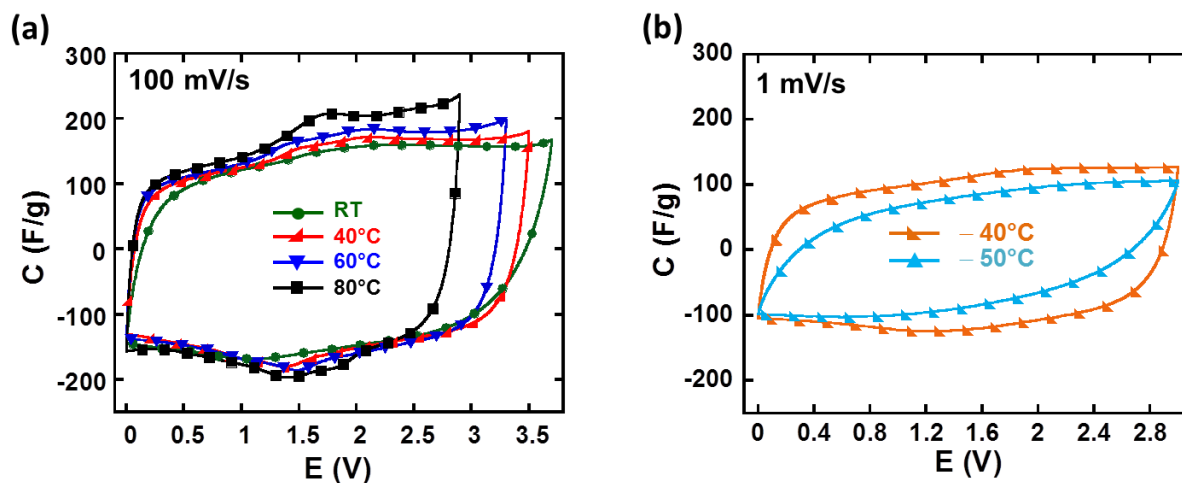


Figure 4: caractérisation électrochimique du a-MEGO (a) à températures élevées ($20 \leq T \leq 80$ °C) – CVs à 100 mV/s et (b) températures inférieures à zéro (-40 et -50 °C) – CVs à 1 mV/s

La Figure 4b montre les CVs obtenus à température inférieure à zéro (-40 et -50 °C). Les CVs présentent un bon comportement capacitif à -40 °C avec des valeurs de capacité élevées de 100 à 120 F/g. Environ 70% de la capacité est conservé à 1 mV/s (ce qui est une vitesse de balayage raisonnable en tenant compte de la mobilité ionique réduit à des températures si basses). Cette rétention de capacité sur cette large plage de température (de -50 à $+80$ °C) avec une capacité toujours au-dessus de 100 F/g n'a jamais été rapportée dans la littérature, à notre connaissance. ^[42-49]

Dans ce chapitre, le SiC-CDC micro/mésoporeux hiérarchisé a montré un bon comportement capacitif jusqu'à -40 °C et une bien meilleure rétention de capacité à basse température par rapport à un carbone microporeux commercial. Cependant, une faible amélioration de la capacité a été obtenue (55 F/g) en raison de la grande quantité de mésopores de ce carbone. Un autre matériau de graphène activé (a-MEGO) a présenté une capacité exceptionnelle (160 F/g) ainsi qu'une large fenêtre électrochimique (jusqu'à 3,7 V) sur une grande plage de températures de -50 à $+80$ °C dans le mélange de LIs. La grande surface spécifique et les mésopores uniformément situés entre 2 et 4 nm permettent au a-MEGO de stocker une grande quantité de charge et de maintenir un transport ionique élevé donc une haute puissance.

Chapitre IV

En dehors du développement de nouveaux matériaux, une meilleure compréhension fondamentale du mécanisme de stockage de charge à l'échelle moléculaire est aussi nécessaire pour concevoir de futurs supercondensateurs. Parmi les techniques électrochimiques in-situ, la microbalance à quartz électrochimique (EQCM) est révélée particulièrement bien adaptée à l'étude in-situ des propriétés interfaciales électrochimiques dans le carbone poreux.^{[50][51]} Par conséquent, la technique EQCM est utilisée pour étudier les mécanismes de charge/décharge de la double couche et la dynamique des ions confinés dans les micropores du carbone. Dans ce chapitre, le liquide ionique EMI-TFSI pur et solvaté dans l'acétonitrile (AN) ainsi que des CDCs microporeux ayant une grande (1 nm) et une petite (0,65 nm) taille de pores sont utilisés pour étudier l'influence de la présence de solvant et l'impact de la taille des pores du carbone.

IV.1 EMITFSI pur

IV.1.1 CDC-1nm

Les résultats de l'EQCM montrent que la masse de l'électrode augmente pendant la charge du supercondensateur et diminue pendant la décharge. La variation de masse peut être considérée, dans une première approximation, comme étant causée par l'adsorption/désorption des contre-ions (ion avec un signe opposé à celui de l'électrode). La Figure 5 montre la variation de masse de l'électrode (Δm) en fonction de la charge accumulée sur l'électrode (ΔQ) au cours de *la charge des ions* (la ligne solide bleu). À supposer qu'il y a aucune polarisation ($\Delta Q = 0$) à OCV (tension de circuit ouvert), l'électrode de carbone est polarisée négativement ($\Delta Q < 0$) lorsque le potentiel est inférieur à OCV et polarisée positivement ($\Delta Q > 0$) lorsque le potentiel est au-dessus de OCV. La variation de masse théorique est indiquée en rouge pointillé sur la Figure 5 (obtenu en appliquant la loi de Faraday). Il convient de noter que le changement de masse théorique considère que la charge accumulée sur l'électrode est compensée par l'adsorption d'EMI⁺ seulement ou l'adsorption d'TFSI⁻ seulement.

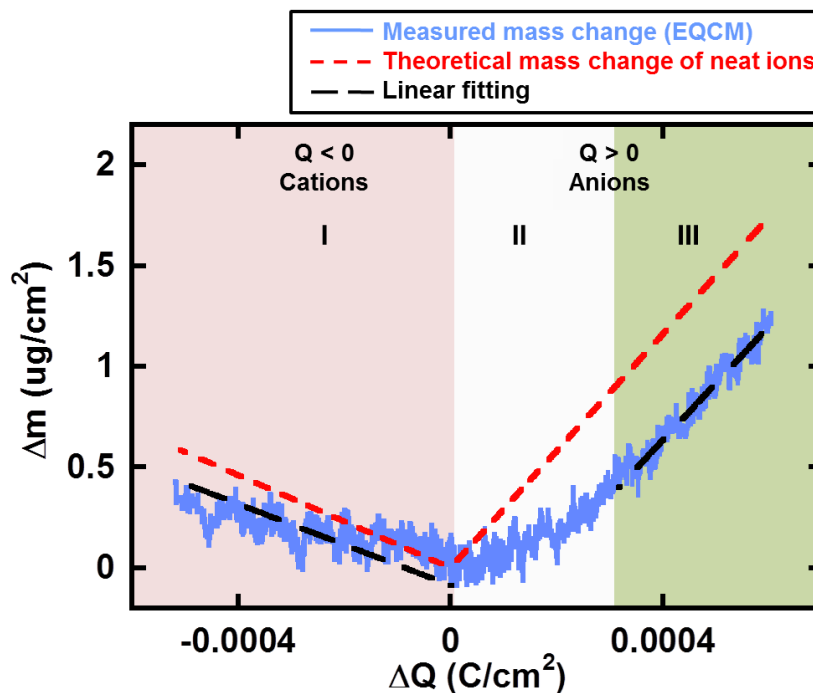


Figure 5: la variation de masse en fonction de la charge du CDC-1nm dans le EMI-TFSI pur.

En outre, la masse moléculaire apparente (M_w') des espèces qui interagissent avec l'électrode pendant les mesures électrochimiques peut être calculée à partir de la pente de la courbe expérimentale de $\Delta m - \Delta Q$. À partir de l'OCV ($\Delta Q = 0$), il y a une variation linéaire de la masse de l'électrode lorsque la charge négative est accumulée (Figure 5, domaine I). La masse moléculaire apparente (M_w') des espèces adsorbées, est calculée à partir de la pente de la courbe expérimentale et correspond à 97 g/mol, ce qui s'approche de la masse moléculaire du cation EMI⁺ cations qui est de 111 g/mol. Cela montre que, dans le domaine I, la charge dans l'électrode poreuse est compensée principalement par l'adsorption de cations. Il semble qu'aucun co-ion (ion avec le même signe à celui de l'électrode) ne soit impliqué. Le même comportement a déjà été signalé et décrit par Levi et al.^[50,51] comme perm-sélectivité: seule l'adsorption de les contre-ions compensent la charge à l'électrode de carbone.

Un comportement différent est observé pendant l'adsorption des anions (polarisation positive, $\Delta Q > 0$) : le changement de masse augmente d'abord lentement pour une charge positive inférieure à +0,3 mC/cm² (domaine II), et puis atteint une pente constante pour une charge de plus de +0,3 mC/cm² (domaine III). Dans la partie linéaire du domaine III ($\Delta Q > +0,3$ mC/cm²), la masse moléculaire apparente des espèces adsorbées calculée est de 270 g/mol, proche de celle des anions nus (280 g/mol pour TFSI⁻). Cela suggère que, pour une polarisation élevée, le mécanisme de stockage de charge consiste principalement en l'adsorption des anions

dans des nanopores confinés. Cependant, pour une polarisation plus faible dans le domaine II ($\Delta Q < +0,3 \text{ mC/cm}^2$), l'adsorption des anions TFSI⁻ n'est pas le seul processus impliqué pendant la charge puisque la pente expérimentale est différente de la pente théorique. Ce comportement a déjà été signalé par Levi et al.,^[51] et correspond à une zone d'échange des ions. Dans cette petite plage de polarisation positive, les anions pénètrent dans les nanopores tandis que les cations sont expulsés de l'électrode en même temps, ce qui conduit à une rupture de la perm-sélectivité dans les micropores de 1 nm.^[51,52] Par conséquent, la variation de masse et la masse moléculaire apparente observé par EQCM sont inférieures à la théorie. Lors d'une augmentation plus importante de la polarisation ($\Delta Q > +0,3 \text{ mC/cm}^2$, le domaine III), la courbe Δm - ΔQ montre que seul le transfert des anions est observé et la perm-sélectivité de l'électrode est récupérée. Cela montre aussi que les anions TFSI⁻ ont besoin de plus d'énergie pour se déplacer. Lorsque l'énergie est faible (polarisation faible, $\Delta Q < +0,3 \text{ mC/cm}^2$), les cations EMI⁺ réagissent plus vite que les anions TFSI⁻ pour compenser la charge. Ce qui suggère que les cations sont plus mobiles que les anions dans les nanopores 1 nm confinés.

IV.1.2 CDC-0.65nm

Les résultats du CDC avec une plus petite taille de pores (0.65 nm) testé dans l'EMI-TFSI pur sont présentés sur la Figure 6. Puisque la taille des pores de CDC est plus petite que celle des cations et des anions (0,76 et 0,79 nm, respectivement), il est prévu que les ions ont un accès limité à la porosité, comme indiqué précédemment par Segalini et al.^[53] La Figure 6 présente la variation de la masse de l'électrode mesurée par EQCM (ligne continue bleue) et théoriquement calculée à partir de la loi de Faraday (ligne pointillée rouge) en fonction de la charge accumulée sur l'électrode (ΔQ) pendant la charge des ions. Il a été constaté que pour la polarisation positive et négative, il y a beaucoup moins de charge stockée sur l'électrode que pour le CDC-1 nm (Figure 5) et presque aucun changement de masse n'est observé. Cela suggère que les cations et les anions ont des difficultés pour accéder aux nanopores.

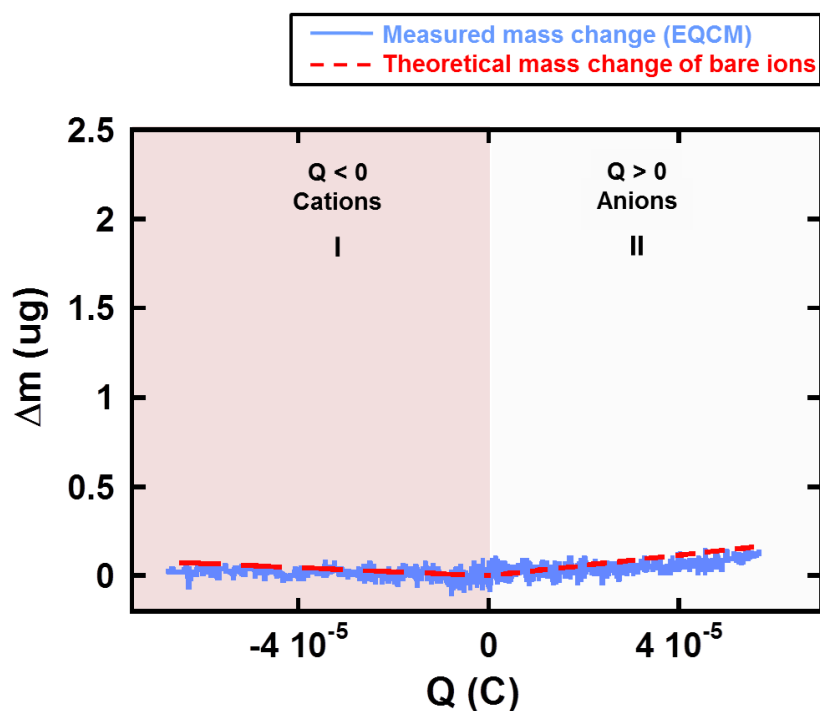


Figure 6: la variation de masse en fonction de la charge du CDC-0.65nm dans le EMI-TFSI pur.

IV.2 2M EMITFSI/acetonitrile

IV.2.1 CDC-1nm

La variation de masse de l'électrode (Δm) en fonction de la charge (ΔQ) au cours de la polarisation de l'électrode CDC-1 nm dans l'EMI-TFSI solvatoé (Figure 7) montre des résultats similaires à celle d'EMI-TFSI pur: trois domaines différents ont pu être observés. Pour une charge négative ($\Delta Q < 0$, domaine I), la variation de masse de l'électrode (ligne continue bleue) augmente linéairement avec la charge sur toute la plage de charge négative, et la pente est beaucoup plus élevée que la pente théorique (ligne rouge pointillée). Pour une charge positive ($\Delta Q > 0$), un comportement différent est observé. La pente de la courbe Δm - ΔQ expérimentale est presque nulle au début de polarisation positive (domaine II), et puis augmente avec la charge. La pente de la courbe reste presque constante après avoir atteint $+1,4 \text{ mC/cm}^2$ (domaine III). Un tel comportement ne peut s'expliquer que par l'existence d'une zone de mélange de cation-anion, en raison d'une rupture de la perm-sélectivité dans les micropores de carbone de 1 nm puisque l'adsorption des contre-ions (TFSI^-) est accompagné par la désorption des co-ions (EMI^+). Mais quelle que soit la charge, la pente de la courbe expérimentale est toujours inférieure à celle de la courbe théorique qui a été obtenue en considérant que la charge stockée sur l'électrode est

compensée seulement par l'adsorption des anions TFSI⁻ non solvatés.

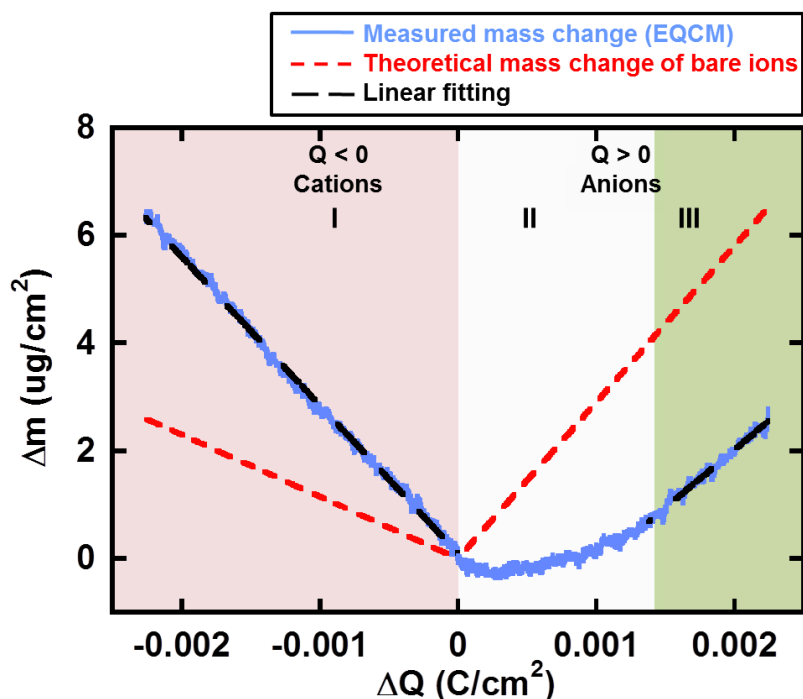


Figure 7: la variation de masse en fonction de la charge du CDC-1nm dans le EMI-TFSI solvaté.

Pour une polarisation négative (domaine I), la masse moléculaire apparente calculée est de 265 g/mol, ce qui est beaucoup plus élevé que la masse moléculaire de EMI⁺ non solvaté (111 g/mol). En supposant que la charge stockée ait été équilibrée que par des cations avec une efficacité de 100% et que la différence entre ces deux valeurs provienne de la présence de molécules du solvant entourant les cations pendant le processus d'adsorption, le nombre de solvation des EMI⁺ cations dans l'acétonitrile peut donc être calculé. Basé sur le calcul, il y a en moyenne 3,7 molécules d'acétonitrile entrant dans les pores avec un cation EMI⁺. Pour une polarisation positive (domaine III), la masse moléculaire apparente calculée est d'environ 208 g/mol, moins de la masse moléculaire de TFSI⁻ (280 g/mol). Toutefois, cela ne signifie pas qu'il n'y ait aucune molécule d'acétonitrile solvatée autour de l'anion TFSI⁻. En fait, la pente de la courbe augmente très lentement avec la charge dans le domaine III, mais il est impossible d'extraire le nombre de solvation d'acétonitrile en raison de la fenêtre électrochimique limitée.

Ces résultats indiquent que pour une polarisation négative, malgré la présence de la couche de solvation des cations EMI⁺, les micropores 1 nm montrent un comportement de perm-sélective étant donné qu'il n'y a pas de zone de mélange cations-anions dans cette

région. De façon similaire à ce qui a été observé dans l'électrolyte EMI-TFSI pur, en présence des molécules du solvant, le stockage de charge dans carbones microporeux avec une taille des pores contrôlée à 1 nm implique principalement l'adsorption des cations. Cependant, pendant la charge positive, la perm-sélectivité du CDC-1 nm s'effondre à faible polarisation puisque un échange cation-anion a été observé dans cette région. Ces résultats sont conformes avec la plus grande mobilité des cations par rapport aux anions^[54,55] dans l'EMI-TFSI pur, et avec notre étude précédente en utilisant le microélectrode à cavité dans l'EMI-TFSI solvate.^[56]

IV.2.1 CDC-0.65nm

En ce qui concerne le CDC-0.65nm dans l'EMI-TFSI solvate (Figure 8), une variation de la masse de l'électrode évidente a été observée lors de la polarisation négative (domaine I) mais il n'y a presque aucun changement de masse au cours de la polarisation positive (domaine II). Les résultats montrent que la taille des pores est trop petite pour les anions solvates et qu'ils ont plus de difficultés que les cations solvates pour accéder aux pores de 0,65 nm. Ce qui suggère que la taille effective des anions est supérieure à celle des cations, ce qui est en accord avec notre étude précédente.^[56]

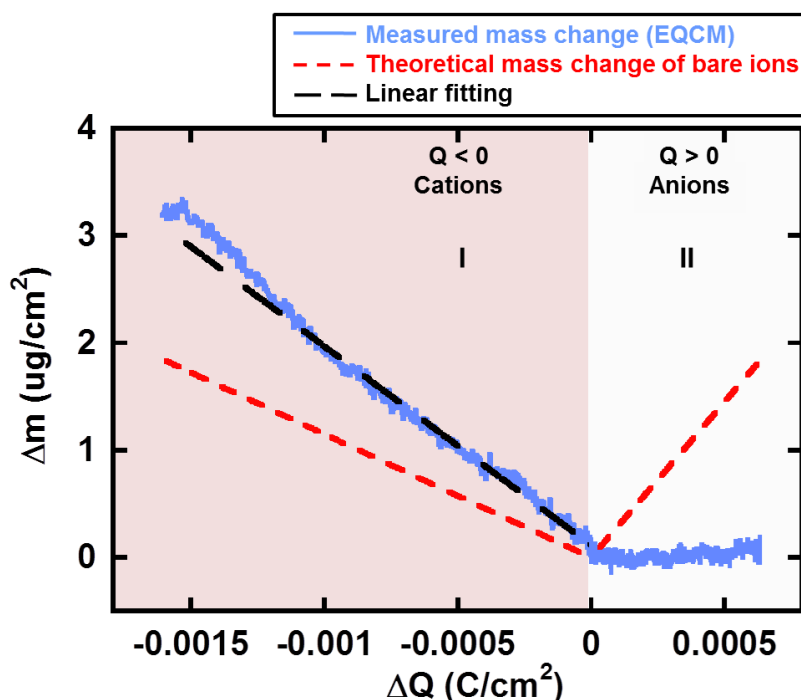


Figure 8: la variation de masse en fonction de la charge du CDC-0.65nm dans le EMI-TFSI solvatoé.

Pour l'adsorption des cations ($\Delta Q < 0$, domaine I), la môme tendance que pour le CDC-1 nm dans le EMI-TFSI solvatoé est observée, sauf que la pente de la courbe $\Delta m - \Delta Q$ est plus faible. De la pente de la courbe, une masse moléculaire moyenne de 179 g/mole a été obtenue, ce qui correspond à un nombre de solvation de 1,6. Un nombre de solvation plus petit a été constaté pour l'adsorption des cations EMI⁺ dans les pores de 0,65 nm que dans celles de 1 nm (nombre de solvation de 3,7), ce qui met en évidence la désolvation partielle des cations lors de l'accès aux petits pores.

Chapter V

Puisque la technique EQCM ne permet pas de suivre la contribution individuelle de chaque espèce électrolytique, une autre technique in-situ permettant de collecter informations *quantitatives* sur des *espèces choisies* est nécessaire pour compléter le puzzle de stockage de charge. La spectroscopie à résonance magnétique nucléaire (RMN) in-situ qui est une technique puissante permettant l'observation et la quantification des différentes espèces chimiques dans les systèmes électrochimiques [57-63] a été choisie pour être associée à l'EQCM in-situ pour étudier le même système électrode/électrolyte dans les mêmes conditions (en chronoampérométrie).

Dans ce chapitre, des électrodes de charbon actif (YP-50F) ont été étudiées dans un électrolyte de tétraéthylphosphonium tétrafluoroborate (PEt₄BF₄) solvatoé dans l'acétonitrile par EQCM in-situ et RMN in-situ. En choisissant ce sel, les cations PEt₄⁺ et les anions BF₄⁻ ont été suivis individuellement en temps réel en utilisant in-situ ³¹P-RMN et ¹⁹F-RMN pendant la charge et la décharge du supercondensateur. La variation de masse de l'électrode pendant les mesures électrochimiques a été mesurée par EQCM pour fournir plus d'informations sur la solvation. La combinaison de ces deux techniques in-situ devrait fournir des informations plus approfondies sur le changement de la structure de double couche pendant le fonctionnement des supercondensateurs.

Résultats de RMN in situ

Les supercondensateurs ont été chargés positivement à partir de la tension de cellule de 0 à 1,5 V par pas de 0,25 V, puis déchargés à 0 V avant d'être chargé négativement à -1.5 V par pas

de -0.25 V. Les spectres RMN enregistrés à différents états de charge sont présentés sur la Figure 9. Pour la polarisation positive et négative, les résonances qui correspondent aux cations et aux anions dans les micropores (marqué « in-pore ») se décalent à une fréquence plus élevée dans les spectres RMN au cours de la charge des cellules. Cela s'explique par des changements dans le déplacement chimique indépendant du noyau (NICS) qui résultent de la charge électronique développée à l'intérieur de l'électrode de carbone.^[64,65] Les variations de l'intensité de résonance « in-pore » reflètent la variation de la population des ions à l'intérieur des micropores. L'image qualitative offerte par ces résultats est en accord avec la vision traditionnelle de la charge du supercondensateur: quand une charge électrique est accumulée sur l'électrode de carbone, les contre-ions sont adsorbés à l'interface électrode/électrolyte dans les micropores pour équilibrer la charge électrique.

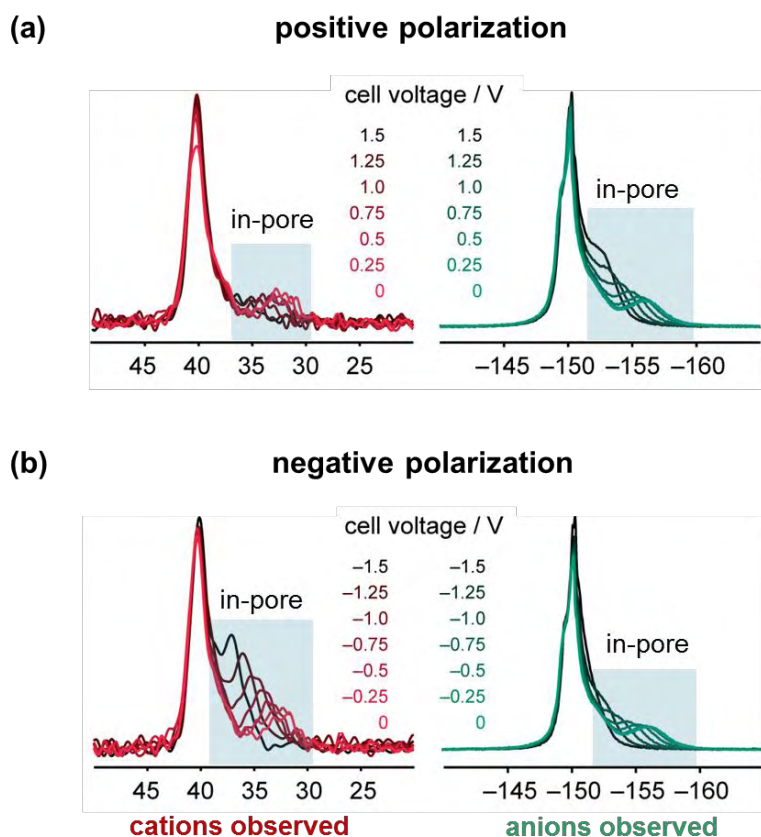


Figure 9: Spectres du ^{31}P -RMN (à gauche, en rouge) et ^{19}F -RMN (à droite, en vert) d'électrode de supercondensateur à différents états de charge.

La Figure 10 montre les valeurs quantitatives d'ions dans les pores, obtenues à partir des intensités de résonance « in-pore » déconvoluées à différents états de charge. Pour une plage de

tension de cellule négative (de 0 à $-1,5$ V), la population des cations dans les pores augmente avec la charge et la population des anions dans les pores ne montre aucun changement significatif. Fait intéressant, un comportement différent a été trouvé dans la plage de tension de cellule positive (0 à $+1,5$ V). Au cours de la charge positive, la population des anions dans les pores augmente tandis que celle des cations diminue, et la quantité de cations expulsés des pores est environ la même que celle des anions adsorbés.

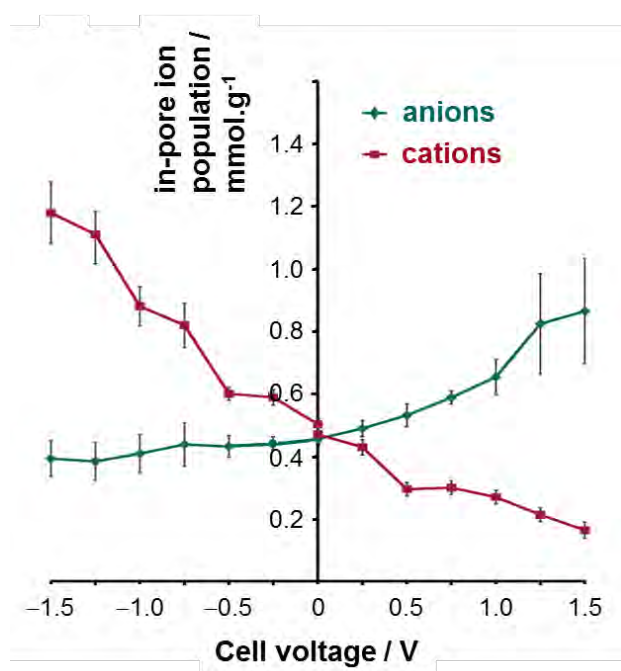


Figure 10: Population des ions aux électrodes de supercondensateurs à différents états de charge de $-1,5$ à $+1,5$ V

A partir des populations des ions, il est relativement simple de déterminer la charge ionique totale à chaque pas de potentiel et de comparer avec la charge électrique stockée sur l'électrode de carbone (par intégration du courant en fonction du temps). Un bon accord global a été trouvé entre la charge ionique à l'intérieur des micropores et la charge électrique stockée. Cela suggère que seuls les ions à l'intérieur des micropores sont responsables du stockage de charge, les ions à l'extérieur des micropores fonctionnant comme un réservoir pour l'intérieur et ne jouant pas un rôle important dans le processus de stockage de charge. Ces résultats confirment également que pour la plage de tensions négatives (de 0 à $-1,5$ V), l'adsorption des cations domine le stockage de charge; tandis que pour la plage positive (de 0 à $+1,5$ V), les deux ions sont impliqués pour équilibrer la charge électronique. Un échange d'ions est observé, ce

qui est similaire aux mécanismes de charge observées dans l'électrolyte à base de EMI-TFSI dans le chapitre IV.

Résultats d'EQCM

La technique EQCM a été utilisée pour étudier le même système (YP-50F charbon actif dans $\text{PEt}_4\text{BF}_4/\text{AN}$). À partir des résultats d'EQCM, une interprétation quantitative a été obtenue en comparant les variations de masse expérimentales aux valeurs théoriques qui sont basées sur différents modèles concernant les mécanismes de charge. La Figure 11 montre les variations de masse expérimentale et théorique en fonction de la charge capacitive stockée sur l'électrode. Les variations de masse théoriques ont été calculées par deux mécanismes de charge différents. Pour le premier modèle (marqué par des triangles rouges), un mécanisme d'adsorption simple est considéré, partant de l'hypothèse traditionnelle qu'une charge négative (positive) stockée dans l'électrode est compensée par l'adsorption d'un seul cation (anion) sur la surface de l'électrode. Pour une polarisation négative, la variation de masse mesurée est beaucoup plus élevée que la variation théorique sur toute la gamme de charge. Cependant, il faut remarquer que, contrairement aux mesures de RMN qui observent sélectivement les populations de cations et d'anions dans les pores, la variation de masse mesurée par EQCM provient de toutes les espèces dans l'électrolyte (y compris les molécules de solvant) qui entrent et sortent de l'électrode poreuse. Les données RMN (Figure 10) montrent que la population d'anions reste constante au cours de la polarisation négative; et par conséquent, les espèces adsorbées additionnelles doivent être des molécules de solvant. La masse moléculaire expérimentale est de 369 g/mol, ce qui est beaucoup plus élevé que celle des cations PEt_4^+ non solvatés (147 g/mol). En supposant que les espèces adsorbées sont des cations PEt_4^+ et que la masse additionnelle provient de molécules d'acétonitrile, le nombre de solvation des cations est estimé à 5,4. Cette valeur est légèrement inférieure au nombre de solvation des cations qui est de 7 (prédit par des cations NEt_4^+ [66]), ce qui indique que les cations sont partiellement désolvatés quand ils entrent dans les micropores de carbone.

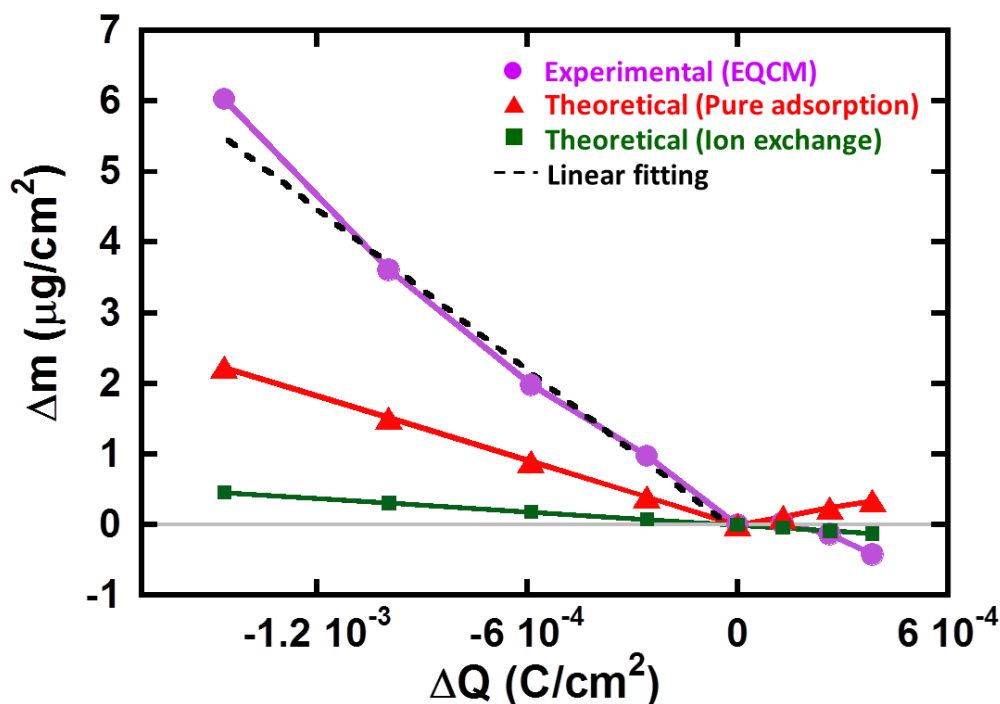


Figure 11: Comparaison des variations de masse d'électrode expérimentale et calculée (basé sur les modèles différents) en fonction de la charge

Pour une polarisation positive, la Figure 11 montre que le modèle d'adsorption simple prédit à nouveau une augmentation de masse puisque seuls les anions BF_4^- sont absorbés dans les micropores. Ceci n'est pas en accord avec les données expérimentales, où une légère diminution de masse est observée. Au regard de cela, un deuxième modèle basé sur les résultats de RMN (Figure 10) est considéré, où pour une polarisation d'électrode positive (négative), deux charges stockées à la surface d'électrode sont compensées par l'adsorption d'un anion (cation) et désorption d'un cation (anion). Les valeurs calculées basées sur ce modèle (carrés verts) prédisent une légère diminution de la masse de l'électrode pendant la charge positive. Cela donne une meilleure corrélation avec les valeurs expérimentales, où une diminution de la masse est également observée. Bien qu'il ne soit pas possible d'extraire des informations claires concernant le nombre de solvation à cause d'une fenêtre électrochimique étroite pour un potentiel positif et une faible masse de carbone déposée, le fait que la variation de masse de l'électrode suive les résultats prédits par RMN confirme que le mécanisme de charge est gouverné par l'échange d'ions.

Conclusions

Ces résultats nous permettent d'approfondir nos connaissances à l'échelle moléculaire du processus de stockage de charge et de la structure en double couche pendant la charge. Ils fournissent ainsi une ligne directrice pour la conception des matériaux afin d'améliorer la performance des EDLCs. En résumé, dans les micropores confinés, les ions sont au moins partiellement désolvatés et aucun appariement d'ions n'est observé. Par conséquent, les contre-ions s'arrangent de façon compacte dans un espace confiné, et ni les co-ions ni les molécules de solvant ne font écran à la charge ce qui entraîne une haute capacité et une efficacité du stockage de charge élevée dans cet environnement confiné. D'autre part, en fonction de la nature des ions et de l'interaction cation-anion, le processus de charge peut soit impliquer l'adsorption des contre-ions, soit l'éjection des co-ions, ou les deux (échange d'ions). La réorganisation et la réorientation locale des espèces électrolytiques sont également nécessaires pour arranger efficacement les ions à l'intérieur des pores. La réorganisation moléculaire et l'échange des ions nécessite un volume libre, ainsi les matériaux qui ont seulement une taille de pore qui correspond à la capacité maximale à l'état d'équilibre ne montrera pas de bonnes performances sous une charge dynamique puisque la réorganisation locale est entravée. Au regard de cela, les mésopores pourraient être tout aussi important que les micropores. Toutefois, dans ce travail, les mésopores dont la taille est supérieure à 4 nm provoquent une diminution de capacité. Bien que le mécanisme de stockage de charge ne soit pas toujours complètement compris, ces conclusions mettent en évidence l'importance d'optimiser l'interface électrode/électrolyte par la conception d'une architecture d'électrode contenant la quantité et la taille des micropores et des mésopores appropriées.

References

- [1] P. Simon, Y. Gogotsi, *Nat. Mater.* **2008**, 7, 845.
- [2] T. Christen, M. W. Carlen, *J. Power Sources* **2000**, 91, 210.
- [3] B. E. Conway, *Electrochemical Supercapacitors: Scientific Fundamentals and Technological Applications*, Springer, **1999**.
- [4] F. Beguin, E. Frackowiak, Eds. , *Supercapacitors: Materials, Systems and Applications - Max Lu, Francois Beguin, Elzbieta Frackowiak*, Wiley-VCH, **2013**.
- [5] C. Portet, G. Yushin, Y. Gogotsi, *Carbon* **2007**, 45, 2511.
- [6] Y. Gao, Y. S. Zhou, M. Qian, X. N. He, J. Redepenning, P. Goodman, H. M. Li, L. Jiang, Y. F. Lu, *Carbon* **2013**, 51, 52.
- [7] J. K. McDonough, Y. Gogotsi, *Electrochem Soc Interface* **2013**, 22, 61.
- [8] D. N. Futaba, K. Hata, T. Yamada, T. Hiraoka, Y. Hayamizu, Y. Kakudate, O. Tanaike, H.

- Hatori, M. Yumura, S. Iijima, *Nat. Mater.* **2006**, *5*, 987.
- [9] S. Dörfler, I. Felhösi, T. Marek, S. Thieme, H. Althues, L. Nyikos, S. Kaskel, *J. Power Sources* **2013**, *227*, 218.
- [10] M. Kaempgen, C. K. Chan, J. Ma, Y. Cui, G. Gruner, *Nano Lett.* **2009**, *9*, 1872.
- [11] M. Noked, S. Okashy, T. Zimrin, D. Aurbach, *Carbon* **2013**, *58*, 134.
- [12] Y. Zhu, S. Murali, M. D. Stoller, K. J. Ganesh, W. Cai, P. J. Ferreira, A. Pirkle, R. M. Wallace, K. A. Cychosz, M. Thommes, D. Su, E. A. Stach, R. S. Ruoff, *Science* **2011**, *332*, 1537.
- [13] M. F. El-Kady, V. Strong, S. Dubin, R. B. Kaner, *Science* **2012**, *335*, 1326.
- [14] P. Tamilarasan, S. Ramaprabhu, *J. Nanosci. Nanotechnol.* **2015**, *15*, 1154.
- [15] W. Li, H.-Y. Lü, X.-L. Wu, H. Guan, Y.-Y. Wang, F. Wan, G. Wang, L.-Q. Yan, H.-M. Xie, R.-S. Wang, *RSC Adv* **2015**, *5*, 12583.
- [16] F. Bonaccorso, L. Colombo, G. Yu, M. Stoller, V. Tozzini, A. C. Ferrari, R. S. Ruoff, V. Pellegrini, *Science* **2015**, *347*, 1246501.
- [17] R. Dash, J. Chmiola, G. Yushin, Y. Gogotsi, G. Laudisio, J. Singer, J. Fischer, S. Kucheyev, *Carbon* **2006**, *44*, 2489.
- [18] V. Presser, M. Heon, Y. Gogotsi, *Adv. Funct. Mater.* **2011**, *21*, 810.
- [19] C. R. Pérez, S.-H. Yeon, J. Ségalini, V. Presser, P.-L. Taberna, P. Simon, Y. Gogotsi, *Adv. Funct. Mater.* **2013**, *23*, 1081.
- [20] H. Wu, X. Wang, L. Jiang, C. Wu, Q. Zhao, X. Liu, B. Hu, L. Yi, *J. Power Sources* **2013**, *226*, 202.
- [21] E. Tee, I. Tallo, H. Kurig, T. Thomberg, A. Jänes, E. Lust, *Electrochimica Acta* **2015**, *161*, 364.
- [22] A. B. Fuertes, G. Lota, T. A. Centeno, E. Frackowiak, *Electrochimica Acta* **2005**, *50*, 2799.
- [23] A. Kajdos, A. Kvit, F. Jones, J. Jagiello, G. Yushin, *J. Am. Chem. Soc.* **2010**, *132*, 3252.
- [24] Y. Korenblit, A. Kajdos, W. C. West, M. C. Smart, E. J. Brandon, A. Kvit, J. Jagiello, G. Yushin, *Adv. Funct. Mater.* **2012**, *22*, 1655.
- [25] A. G. Pandolfo, A. F. Hollenkamp, *J. Power Sources* **2006**, *157*, 11.
- [26] M. Sevilla, R. Mokaya, *Energy Environ. Sci.* **2014**, *7*, 1250.
- [27] J. Chmiola, G. Yushin, Y. Gogotsi, C. Portet, P. Simon, P. L. Taberna, *Science* **2006**, *313*, 1760.
- [28] C. Largeot, C. Portet, J. Chmiola, P.-L. Taberna, Y. Gogotsi, P. Simon, *J. Am. Chem. Soc.* **2008**, *130*, 2730.
- [29] J. Leis, M. Arulepp, A. Kuura, M. Lätt, E. Lust, *Carbon* **2006**, *44*, 2122.
- [30] E. Frackowiak, *Phys. Chem. Chem. Phys.* **2007**, *9*, 1774.
- [31] J. Huang, B. G. Sumpter, V. Meunier, *Chem. - Eur. J.* **2008**, *14*, 6614.
- [32] D.-W. Wang, F. Li, M. Liu, G. Q. Lu, H.-M. Cheng, *Angew. Chem. Int. Ed.* **2008**, *47*, 373.
- [33] D.-D. Zhou, Y.-J. Du, Y.-F. Song, Y.-G. Wang, C.-X. Wang, Y.-Y. Xia, *J Mater Chem A* **2013**, *1*, 1192.
- [34] A. Stein, S. G. Rudisill, N. D. Petkovich, *Chem. Mater.* **2014**, *26*, 259.
- [35] Q. Wang, J. Yan, Y. Wang, T. Wei, M. Zhang, X. Jing, Z. Fan, *Carbon* **2014**, *67*, 119.
- [36] Y. Zhang, M. Ma, J. Yang, W. Huang, X. Dong, *RSC Adv.* **2014**, *4*, 8466.
- [37] R. Lin, P.-L. Taberna, S. Fantini, V. Presser, C. R. Pérez, F. Malbosc, N. L. Rupesinghe, K. B. K. Teo, Y. Gogotsi, P. Simon, *J. Phys. Chem. Lett.* **2011**, *2*, 2396.
- [38] P.-C. Gao, Y. Lei, A. F. C. Pérez, K. Rajoua, D. Zitoun, F. Favier, *J. Mater. Chem.* **2011**, *21*, 15798.
- [39] P.-C. Gao, P. Simon, F. Favier, *Microporous Mesoporous Mater.* **2013**, *180*, 172.
- [40] Y. Zhu, S. Murali, M. D. Stoller, K. J. Ganesh, W. Cai, P. J. Ferreira, A. Pirkle, R. M. Wallace, K. A. Cychosz, M. Thommes, D. Su, E. A. Stach, R. S. Ruoff, *Science* **2011**, *332*, 1537.
- [41] Y. Zhu, S. Murali, M. D. Stoller, A. Velamakanni, R. D. Piner, R. S. Ruoff, *Carbon* **2010**, *48*, 2118.
- [42] R. Kötz, M. Hahn, R. Gallay, *J. Power Sources* **2006**, *154*, 550.
- [43] H. Kurig, A. Jänes, E. Lust, *J. Electrochem. Soc.* **2010**, *157*, A272.
- [44] V. Ruiz, T. Huynh, S. R. Sivakumar, A. G. Pandolfo, *RSC Adv.* **2012**, *2*, 5591.
- [45] E. Iwama, P. L. Taberna, P. Azais, L. Brégeon, P. Simon, *J. Power Sources* **2012**, *219*,

- 235.
- [46] C. Largeot, P. L. Taberna, Y. Gogotsi, P. Simon, *Electrochem. Solid-State Lett.* **2011**, *14*, A174.
- [47] E. Brandon, M. Smart, W. West, *NASA Technical Rep. Serv.* **2010**.
- [48] R. Vellacheri, A. Al-Haddad, H. Zhao, W. Wang, C. Wang, Y. Lei, *Nano Energy* **2014**, *8*, 231.
- [49] R. Väli, A. Laheäär, A. Jänes, E. Lust, *Electrochimica Acta* **2014**, *121*, 294.
- [50] M. D. Levi, G. Salitra, N. Levy, D. Aurbach, J. Maier, *Nat. Mater.* **2009**, *8*, 872.
- [51] M. D. Levi, N. Levy, S. Sigalov, G. Salitra, D. Aurbach, J. Maier, *J. Am. Chem. Soc.* **2010**, *132*, 13220.
- [52] M. D. Levi, S. Sigalov, G. Salitra, R. Elazari, D. Aurbach, *J. Phys. Chem. Lett.* **2011**, *2*, 120.
- [53] J. Segalini, E. Iwama, P.-L. Taberna, Y. Gogotsi, P. Simon, *Electrochem. Commun.* **2012**, *15*, 63.
- [54] M. D. Levi, S. Sigalov, G. Salitra, D. Aurbach, J. Maier, *ChemPhysChem* **2011**, *12*, 854.
- [55] A. Noda, K. Hayamizu, M. Watanabe, *J. Phys. Chem. B* **2001**, *105*, 4603.
- [56] R. Lin, P. Huang, J. Ségalini, C. Largeot, P. L. Taberna, J. Chmiola, Y. Gogotsi, P. Simon, *Electrochimica Acta* **2009**, *54*, 7025.
- [57] K. Ogata, E. Salager, C. J. Kerr, A. E. Fraser, C. Ducati, A. J. Morris, S. Hofmann, C. P. Grey, *Nat. Commun.* **2014**, *5*, DOI 10.1038/ncomms4217.
- [58] A. Pestov, A. Nazirov, E. Modin, A. Mironenko, S. Bratskaya, *Carbohydr. Polym.* **2015**, *117*, 70.
- [59] M. Letellier, F. Chevallier, F. Béguin, E. Frackowiak, J.-N. Rouzaud, *J. Phys. Chem. Solids* **2004**, *65*, 245.
- [60] J. Xu, J. Hou, W. Zhou, G. Nie, S. Pu, S. Zhang, *Spectrochim. Acta. A. Mol. Biomol. Spectrosc.* **2006**, *63*, 723.
- [61] R. K. Harris, T. V. Thompson, P. R. Norman, C. Pottage, A. N. Trethewey, *J Chem Soc Faraday Trans* **1995**, *91*, 1795.
- [62] K. Shen, T. Pietrass, *J. Phys. Chem. B* **2004**, *108*, 9937.
- [63] R. J. Anderson, T. P. McNicholas, A. Kleinhammes, A. Wang, J. Liu, Y. Wu, *J. Am. Chem. Soc.* **2010**, *132*, 8618.
- [64] H. Wang, A. C. Forse, J. M. Griffin, N. M. Trease, L. Trognko, P.-L. Taberna, P. Simon, C. P. Grey, *J. Am. Chem. Soc.* **2013**, *135*, 18968.
- [65] H. Wang, T. K.-J. Köster, N. M. Trease, J. Ségalini, P.-L. Taberna, P. Simon, Y. Gogotsi, C. P. Grey, *J. Am. Chem. Soc.* **2011**, *133*, 19270.
- [66] Y.-J. Kim, Y. Masutzawa, S. Ozaki, M. Endo, M. S. Dresselhaus, *J. Electrochem. Soc.* **2004**, *151*, E199.

Résumé :

L'objectif de cette thèse a été d'augmenter la densité d'énergie des supercondensateurs. La première partie de cette thèse a été consacrée à l'amélioration des performances d'une électrode de carbone pour supercondensateur en étudiant à la fois un mélange de liquides ioniques ainsi que des carbones offrant différents types de microstructures. Une augmentation importante de la capacité spécifique sur une large gamme de températures (-50°C ;100°C) est obtenue en couplant un mélange eutectique de liquides ioniques, (PIP₁₃-FSI)_{0.5} (PYR₁₄-FSI)_{0.5}, avec un oxyde de graphite exfolié par micro-onde et activé par KOH (a-MEGO). Cette première partie de la thèse met ainsi l'accent sur l'importance d'optimiser l'interface carbone/électrolyte afin de maximiser la densité. Dans la deuxième partie, les mécanismes de stockage des charges dans les pores des carbones à l'échelle moléculaire ont été étudiés in-situ grâce à une microbalance électrochimique à cristal de quartz (EQCM). Les études EQCM ont été menées dans deux systèmes électrode/électrolyte : (1) des carbones dérivés de carbure dans des électrolytes à base de EMI-TFSI et (2) un carbone activé dans l'électrolyte PEt₄BF₄. Les résultats d'EQCM et de RMN in-situ montrent comment les ions différents et les molécules du solvant sont impliqués pendant la charge. Ces résultats sont très encourageants et montrent que l'EQCM constitue une sonde dont la sensibilité permet d'étudier la dynamique des ions dans la porosité des électrodes de carbone lors de la charge et de la décharge des supercondensateurs.

Mots-clés : Supercondensateurs, adsorption des ions, carbones poreux, EQCM, solvation

Abstract :

The aim of this PhD work focuses on different approaches to improve the energy density of supercapacitors. First part of this thesis work is to improve the performance of supercapacitor by using ionic liquid mixtures as electrolytes and carbons with different microstructures. A significant increase of specific capacitance over wide temperature range (-50 to 100°C) was obtained by using an eutectic ionic liquid mixture, (PIP₁₃-FSI)_{0.5} (PYR₁₄-FSI)_{0.5}, with an activated microwave exfoliated graphite oxide (a-MEGO). These results evidence that optimization of the carbon/electrolyte interface is of great importance for maximizing the capacitive energy. In the second part of the thesis, the charge storage mechanisms in the porous carbons at molecular scale have been studied using Electrochemical Quartz Crystal Microbalance (EQCM). EQCM studies were conducted on two electrode/electrolyte systems: (1) carbide-derived carbons in neat and solvated EMI-TFSI ionic liquid under dynamic charging condition and (2) YP-50F activated carbon in solvated PEt₄BF₄ electrolyte under steady state charging condition. EQCM and in-situ NMR results showed how different ions and solvent molecules are involved in the charging process. These results provide a direct molecular-level insight into the charge storage process, showing that EQCM is promising electrogravimetric probe to study compositional changes in carbon microspores during charging/discharge of supercapacitors.

Keywords : Supercapacitors, ion adsorption, porous carbons, EQCM, solvation